NEAR THRESHOLD ELECTROPRODUCTION OF THE ω MESON AT MOMENTUM TRANSFER $Q^2 = 0.5$ $(GeV/c)^2$

A Dissertation

Submitted to

the Temple University Graduate Board

In Partial Fullfilment

of the Requirements for the Degree

DOCTOR OF PHILOSOPHY

by

Pawel Ambrozewicz

January, 2002

ABSTRACT

Near Threshold Electroproduction Of The ω Meson

At Momentum Transfer $Q^2 = 0.5$ (GeV/c)^2

Pawel Ambrozewicz

Doctor Of Philosophy

Temple University, 2002

Jefferson Lab kaon experiments *E91016/E93018* produced data on both strangeness and vector meson electroproduction. The latter part of the experiments was focused on the electroproduction of the ω meson for momentum transfer Q^2 near 0.5 (GeV/c)^2. This reaction was selected from the inelastic ep channel, $^1H(e, e'p)X$, by performing involved signal background separation. Tagging the ω meson production only on electron and proton not only introduced appreciable statistical error but also a sizeable systematic uncertainty due to the background removal. Nevertheless, the analysis yielded angular distributions of the differential cross section in the threshold regime extracted with an unprecedented granularity and relatively small errors.

DEDICATION

Dedicated to my dearest

Mom Barbara,

wife Marta

and

daughter Agata

ACKNOWLEDGMENTS

Never in my life had I thought that expressing thanks and gratitude would be that uplifting and heartwarming. First and foremost I thank Jesus Christ the Lord since this is *His* work really.

I want to thank my parents, Barbara and Wiktor Ambrozewicz, for shaping me into a person I am now. They set my priorities by teaching me how to tell left from right and right from wrong.

I cannot even begin to think how to express my thanks to two women I share my life with, my wife Marta and my daughter Agata, the best birthday present I could ever dream of, for not letting me go insane in difficult times and reminding me that there is still a beatiful world out there.

I deeply thank my advisor Jeff Martoff for taking me on board. He steered me into this project and provided me with guidance and support for its duration. I am not the easiest person to put up with. Thank you.

My sheerest thanks go to Ben Zeidman and Keith Baker for they put faith in me, and stuck to it, let me join the collaboration and have a share in their data. In the same breath I must thank a fellow graduate student Chris Armstrong for shedding this project onto me and for “having a minute” when I needed it.

Without a detailed list so no one is forgotten I would like to thank all the Hall C staff, technicians and all the collaborators as their dedicated work made this project possible. In particular, I would like to thank Roger Carlini for extending the support to me when the tough times set in.

Analysis-wise, I benefited tremendously from the knowledge and experience of Jim Dunne, Paul Guéye, Pete Markowitz, Jörg Reinhold, Gaby and Ioana Niculescu, Jinseok Cha, Rick Mohring, Wendy Hinton, Kenneth Gustafsson. Thank you all.

I would like to acknowledge the unceasing support on the part of Hall A leader, Kees de Jager, for the sake of physics. I owe you a great deal.

Many thanks to Donal Day, Rolf Ent and Thia Keppel for reaching out a helping hand just when I needed. I do appreciate it.

Last but by no means least, I would like to express my thanks to Joe Mitchell for his unconditional willingness to share his expertise and unmatched physics intuition, for his determination to see this project through and cracking the whip when it was necessary to do so, for getting me through thick and thin in my scientific and personal life. I cannot thank you enough. **Hats off to you, Joe!**.

TABLE OF CONTENTS

LIST OF TABLES

LIST OF FIGURES

CHAPTER 1

INTRODUCTION AND MOTIVATION

1.1 Introduction

Experimental Hall C of the ***T**homas **J**efferson **N**ational **A**ccelerator **F**acility* (***TJNAF***) [1] is configured in a way that is well suited for coincidence experiments. During these experiments electrons impinge on a fixed target and two emergent particles are detected simultaneously in two magnetic spectrometers. The spectrometers are equipped with sophisticated detector packages for triggering, tracking and particle identification. The kaon electroproduction experiments, *E91-016* and *E93-018*, were coincidence experiments designed for Hall C and intended to investigate the strangeness production via reactions,

[1] formerly known as *CEBAF* - Continuous Electron Beam Accelerator Facility

$$e + p \longrightarrow e' + K^+ + Y \qquad Y = \Lambda\,, \;\; \Sigma^0 \tag{1.1}$$

$$e + d \longrightarrow e' + K^+ + Y + n \qquad Y = \Lambda\,, \;\; \Sigma^0 \tag{1.2}$$

$$e + d \longrightarrow e' + K^+ + Y + p \qquad Y = \Sigma^- \tag{1.3}$$

In these experiments, the simultaneous detection of an electron and a kaon tagged events pertaining to the production of either Λ or Σ hyperons, which were identified employing the missing mass technique - Figure 1.1.

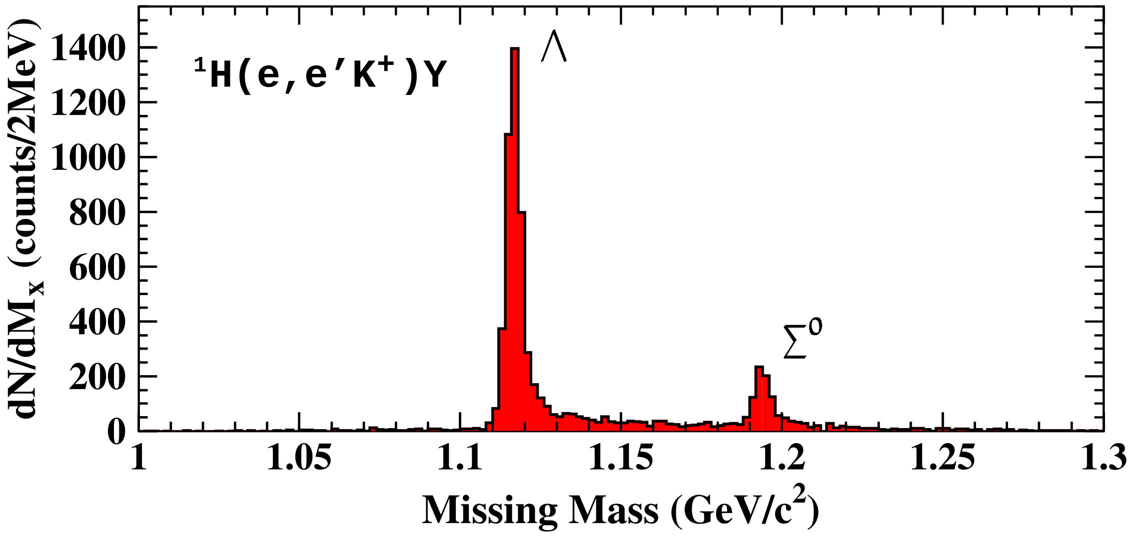

Figure 1.1: ***Kaon Electroproduction.***

Since the spectrometers were set to accept particles of distinct, either positive or negative, polarity the kaons had to be extracted from the background of copiously produced pions and protons. In the case of inelastic electron proton (ep) scattering the missing mass spectrum is shifted toward lower masses (0.6 GeV - 1.0 GeV) enabling the observation of the production of light vector mesons (the $\omega(782)$ and the $\rho^0(768)$) at threshold - Figure 1.2. Particularly interesting is the ω meson, whose discovery and spin and parity assignment is a classic example of a remarkable and exciting analysis (Maglic et al., 1962).

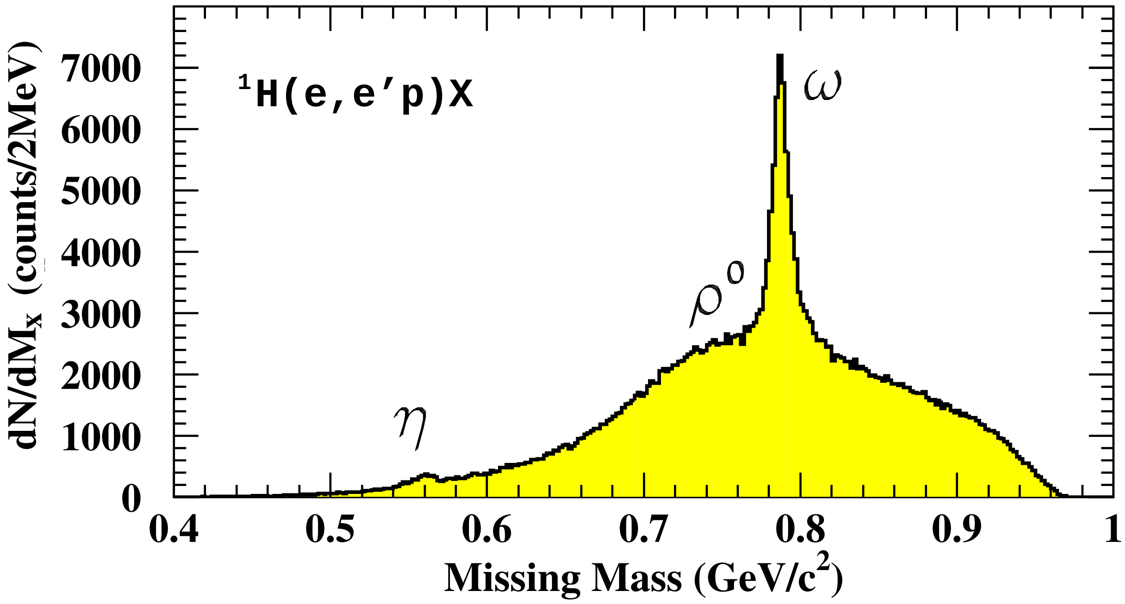

Figure 1.2: ***ω Electroproduction.***

While previous data on the near threshold electroproduction of this meson is rather sparse and suffers from very low statistics, the kaon experiments yielded the largest available, although "parasitic", data set on its production (it exceeds 250,000 events for Q^2 point of 0.5 (GeV/c)^2). Good statistics allowed for a detailed study of the ω cross section angular distribution in the final state $^1H(e, e'p)\omega$. The bulk of the kaon data for $Q^2 = 0.5$ (GeV/c)^2

was taken with the kaon momenta of 0.929 GeV/c and 1.077 GeV/c. Since the magnetic spectrometer is a momentum selective device the protons had the same momenta as the kaons and those corresponded to ω mesons scattered backward in the virtual photon proton Center-Of-Momentum system.

This part of the distribution appears to be most interesting because any departure from the $t-$channel exchange production mechanism would be most apparent there. The possibility of contributions from $s-$channel resonance formation was raised by P. Joos (Joos et al., 1977) in his data analysis of ω electroproduction at *DESY*. This calls for careful scrutiny of the possible candidates since the $N\omega$ channel is now thought to have sizeable couplings to *missing resonances*[2] (Koniuk, 1982; Capstick & Roberts, 1994).

This work presents the analysis and results for the ω meson production at 4-momentum transfer of 0.5 $(\mathrm{GeV/c})^2$ where the extraction of the angular distribution was able to be carried out in fullest detail.

This chapter provides the basic definitions and the theoretical framework for study of the data. It presents the world's data on the production of the ω meson near threshold in conjuction with the Vector Meson Dominance model that was used to describe that data. It also gives a short recapitulation of the Quark Model (Capstick, 1988; Isgur, 1991) with the particular emphasis on the existance of missing resonances in the baryon excitation spectrum.

[2]Missing Resonances - Resonances predicted by quark models but experimentally unobserved. Nowadays, the precise meaning of "missing" is that those resonances are not present in the $N\pi$ data.

Chapter 2 deals with the experimental setup and instrumentation. It briefly describes all parts of the apparatus such as the beamline, cryogenic target, magnetic spectrometers and detectors as well as the data aquisition procedures.

In Chapter 3 the simulation of the experiment is described *in extenso*, as a number of phenomena were implemented in this Monte Carlo program including finite resolution effects, extended target effects (multiple scattering, ionization energy losses) as well as transport of particles through the optical (magnetic) elements of the device. It details all the cross section models used in the simulation, which are vital in subtracting the background coming from other processes leading to the same $(e' p)$ final state.

The details of the analysis of raw data are presented in Chapter 4. That chapter contains an explanation of all the steps of the data reduction and processing including calculation of the detectors efficiencies or other correction factors and detector calibration procedures as well as the ultimate goal of the analysis which is the extraction of the virtual photon cross section.

In Chapter 5 the results and their interpretation are presented along with the estimation of the systematic uncertainities.

1.2 Formalism

1.2.1 Basic Definitions

Throughout this dissertation the Minkowski metric was used to construct the space-time so that the inner product of two for vectors, say P and Q, is given by

$$P \cdot Q = P^0 Q^0 - \vec{\mathbf{P}} \cdot \vec{\mathbf{Q}} = P^0 Q^0 - (P_1 Q_1 + P_2 Q_2 + P_3 Q_3) \tag{1.4}$$

in any reference frame.

Kinematics for all the processes of interest were based on the kinematics for the reaction $p(e, e'p)X$ in the one-photon-exchange approximation in which (see Figure 1.3),

- $k = (E, \mathbf{k})$ is the 4-momentum vector of the incident electron,
- $k = (E', \mathbf{k}')$ is the 4-momentum vector of the emergent electron,
- $q = (E - E', \mathbf{k} - \mathbf{k}') = (\nu, \mathbf{q})$ is the 4-momentum vector of the virtual photon,
- $p_0 = (M_p, \mathbf{0})$ is the 4-momentum vector of the target,
- $p = (E_p, \mathbf{p})$ is the 4-momentum vector of the outgoing proton.

Having defined the above, the Lorentz invariants of the problem are expressed in the laboratory frame of reference, in the massless electron limit ($m_e = 0 \Rightarrow |\mathbf{k}^{(\prime)}| = E^{(\prime)}$), in the following fashion,

- $Q^2 \equiv -q^2 = -(k - k')^2 = 4EE' sin^2(\theta_{e'}/2)$ is the mass (squared) of the virtual photon [3],

[3] Note that $q^2 < 0$ in the chosen metric. However, if the space-time is defined to be pseudo-Euclidean then this quantity is, by definition, positive and there is no need to introduce Q^2.

- $s = W^2 = (p_0 + q)^2 = M_p^2 + 2M_p\nu - Q^2$ is the invariant mass (or, equivalently, center-of-momentum energy) squared of the $\gamma^* p$ system,
- $t = (p_0 - p)^2 = 2M_p^2 - 2M_p E_p$ is the 4-momentum transfer to the target,
- $u = (k - p_0)^2 = M_p^2 - 2M_p E$,
- $M_x^2 = (q + p_0 - p)^2 = W^2 + M_p^2 - 2E_p(M_p + E - E') + 2|\mathbf{q}||\mathbf{p}|cos\theta_{\gamma p}$ is the mass of the particle (or particles) that went undetected with $\theta_{\gamma p}$ being an angle of the scattered proton with respect to the virtual photon direction,
- $s + t + u = 2M_p^2 + M_x^2 - Q^2$ is the relation connecting all the invariants.

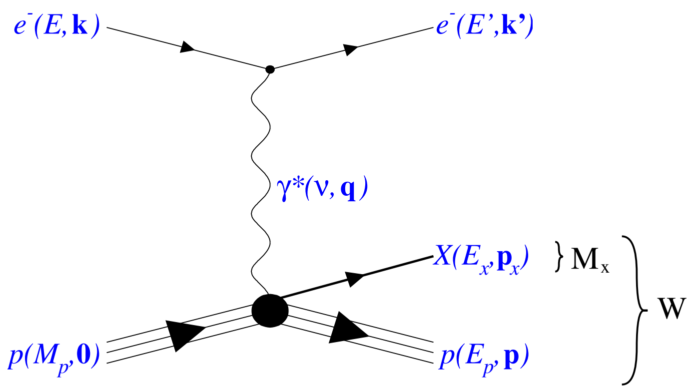

Figure 1.3: ***Kinematics of the*** $\mathbf{p(e, e'p)X}$ ***reaction:*** *Invariant mass W is the mass of the total virtual photon-proton (γ^*p) system, while missing mass M_x is the mass of the particle/particles (X) that remained undetected.*

Kinematically, the initial state is defined by specifying two 4-momenta, k and p_0. This is ensured by chosing the beam energy and the fixed target configuration of the experiment. The three particle final state of the process diagramatically shown in Figure 1.3 is described by three 4-momenta, k', p and p_x, therefore 12 variables. Assuming that the mass of the particle X is not definite, as is the case for resonant particles such as ω meson, while the scattered electron and proton are on thier mass shells and employing the energy-momentum conservation the number of independent variables uniquely describing the final state is reduced to 6 quantities.

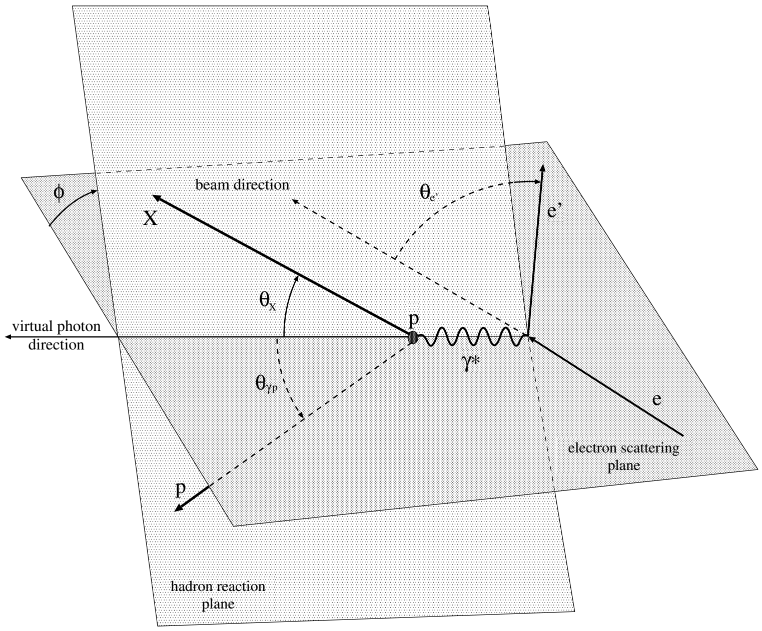

Figure 1.4: ***Electroproduction On A Fixed Target:*** *The diagram of the 2-body electroproduction process in the approximation of one photon exchange. Trajectories of the two electrons span a scattering plane while trajectories of the proton and particle X define the reaction plane. Note that, in general, these planes are not identical meaning they are rotated with respect to one another by a nontrival angle ϕ. By the definition of the center-of-momentum frame this angle will become its azimuthal angle.*

The choice of variables forming this sextuple is arbitrary. One of the conventional choices, for instance, are the components of the momenta $\mathbf{k}'$ and $\mathbf{p}$ in spherical coordinate system. This choice provides the basis for the computation of the natural phase space volume which is identical to the ***Detection Volume***,

$$V_{\text{det}} = \int_{\substack{\text{physical}\\ \text{limits}}} dk'\, d\Omega_{e'}\, dp\, d\Omega_p \tag{1.5}$$

where $\Omega_{e'}$ and Ω_p are the scattered electron and proton solid angles while k' and p are their momenta, respectively.

A different set of quantities was chosen to simulate the reaction of interest, its background and the response of the experimental apparatus to those processes. This set, which is discussed in Section 3.1.2, defined a volume labelled as the ***Generation Volume***. Transition from one set of independent variables to another is facilitated by the use of the appropriate Jacobian. Considering the transformation between the two sets of variables mentioned above it turns out that the electron variables decouple from the proton ones therefore the corresponding Jacobian can be expressed as a product of two Jacobians, first pertaining to the mapping,

$$\{k',\, cos\,\theta_{e'},\, \phi_{e'}\} \xmapsto{\mathcal{J}_{e'}} \left\{Q^2,\, W,\, \phi_{e'}\right\} \tag{1.6}$$

while the other corresponding to

$$\{p,\, cos\,\theta_p,\, \phi_p\} \xmapsto{\mathcal{J}_p} \left\{M_x,\, cos\,\theta_p^{CM},\, \phi_p^{CM}\right\} \tag{1.7}$$

so the total Jacobian is $\mathcal{J} = \mathcal{J}_{e'} \times \mathcal{J}_p$. The details regarding this particular calculation and other Jacobian calculations are presented in the Appendix A.

In order to perform further calculations several frames of reference have to be defined,

Target frame: z_T is along the beam direction ($\mathbf{k}$), x_T is horizontal pointing to the left, y_T is vertical pointing upward, the center of the actual target is located in this frame at $(0, 0, 0)$ point, and extends from $z_T = -2.18$cm to $z_T = 2.18$cm (for further details see Chapter 2),

Spectrometer Transport frame: z_{spec} is along the central ray of the spectrometer, x_{spec} is in the dispersive (vertical) direction pointing downward, y_{spec} is horizontal pointing to the left,

Center-of-Momentum (CM) frame: z_{CM} is along the virtual photon direction ($\mathbf{q}$), y_{CM} is prependicular to the scattering plane (*i.e.* the plane defined by incoming and outgoing electrons (see Figure 1.4)), x_{CM} lies in the scattering plane such that it is perpendicular to y_{CM} and z_{CM}.

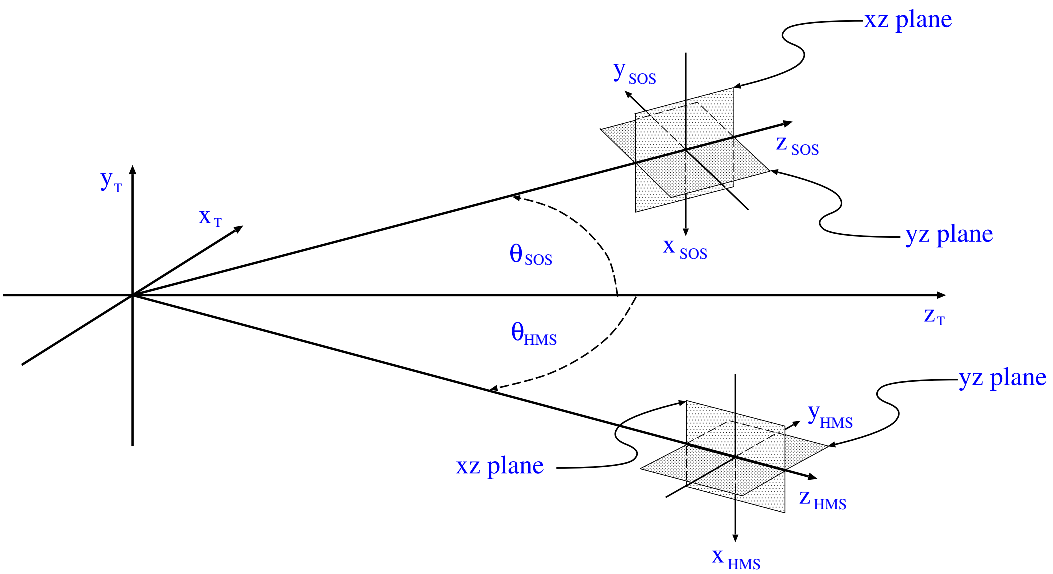

Figure 1.5: ***Spectrometer and LAB coordinate frames:*** *For illustrational purpose the frames where separated. There is no actual separation between the origins of these frames.*

Transformation: LAB $\longrightarrow$ TRANSPORT

The spectrometer frames are related to the lab frame through two simple rotations. Identification of x_{spec} with $-y_T$ and y_{spec} with x_T is equivalent to a 90^o rotation about z_T. The remaining rotation involves the set angle of the spectrometer, that is the angle the central ray of the spectrometer makes with the beam direction. The electron spectrometer frame is rotated by $-\theta_{HMS}$ about x_{HMS} while the proton spectrometer frame is rotated by θ_{SOS} about x_{SOS} (see Figure 1.5).

Transformation: LAB $\longrightarrow$ CM

The transformation from the target frame to the CM frame is a superposition of two rotations and a Lorentz boost. Figure 1.6 shows the angles and axes necessary to define the rotations. The details of the Lorentz boost can be found in the Appendix B. Using unit vectors $\hat{e}_3 \equiv \mathbf{z}/|\mathbf{z}|$, $\hat{e}_2 \equiv \mathbf{y}/|\mathbf{y}|$ and $\hat{e}_1 \equiv \mathbf{x}/|\mathbf{x}|$ the two frames are related via

$$\hat{e}'_3 \equiv \mathbf{z}'/|\mathbf{z}'| = \vec{q}/|\vec{q}| \tag{1.8}$$

$$\hat{e}'_2 \equiv \mathbf{y}'/|\mathbf{y}'| = (\hat{e}_3 \times \hat{e}'_3)/sin\alpha \tag{1.9}$$

$$\hat{e}'_1 \equiv \mathbf{x}'/|\mathbf{x}'| = (\hat{e}'_3 cos\alpha - \hat{e}_3)/sin\alpha \tag{1.10}$$

Given the above definitions the rotation angles are found using scalar products

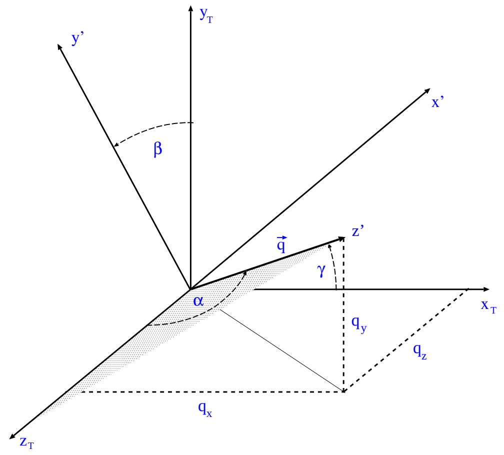

Figure 1.6: ***CM and LAB coordinate frames:*** *Transformation from the lab to the CM frame is achieved by rotating the lab frame by the angle β (see text for the definition) about z axis which is followed by the rotation by the angle α (see text for the definition) about the y' axis.*

$$cos\alpha = \hat{e}'_3 \cdot \hat{e}_3 \quad = \quad \frac{q_z}{|\vec{q}|} \tag{1.11}$$

$$cos\beta = \hat{e}'_2 \cdot \hat{e}_2 \quad = \quad \left(\frac{1}{sin\alpha}\right) \hat{e}_2 \cdot (\hat{e}_3 \text{ x } \hat{e}'_3) \quad = \quad \frac{q_x}{|\vec{q}|sin\alpha} \quad = \quad \frac{cos\gamma}{sin\alpha} \tag{1.12}$$

The decomposition of the proton momentum vector in the rotated frame yields the following components, which eventually will be boosted to the actual CM frame (see the Appendix B),

$$p'_x \quad = \quad \hat{e}'_1 \cdot \vec{p} \quad = \quad \frac{\vec{p} \cdot \vec{q}cos\alpha - |\vec{q}|p_z}{|\vec{q}|sin\alpha} \tag{1.13}$$

$$p'_y \quad = \quad \hat{e}'_2 \cdot \vec{p} \quad = \quad \frac{q_x p_y - q_y p_x}{|\vec{q}|sin\alpha} \tag{1.14}$$

$$p'_z \quad = \quad \hat{e}'_3 \cdot \vec{p} \quad = \quad \frac{\vec{p} \cdot \vec{q}}{|\vec{q}|} \tag{1.15}$$

Figure 1.7 shows schematically how the scattering angle in the CM frame, θ_x^{CM},is defined.

It is the extraction of the cross section with respect to this angle which is the ultimate goal of this work. θ_x^{CM} is very simply related to the invariant 4-momentum transfer t

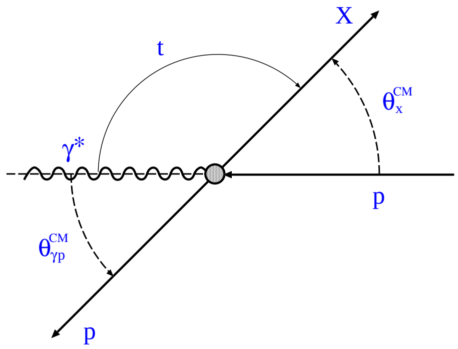

Figure 1.7: ***Scattering in the Center-Of-Momentum system*** *The diagram shows the scattering in the reaction plane (see Figure 1.4 for the definition)*

$$t = (q^{CM} - p_x^{CM})^2 = M_x^2 - Q^2 - 2\nu^{CM} E_p^{CM} + 2|\vec{q}^{\,CM}||\vec{p}_x^{\;CM}|\, cos\theta_x^{CM} \tag{1.16}$$

This expression is convenient in calculating the Jacobian for the transformation $t \longrightarrow cos\theta_x^{CM}$ (for the details refer to the Appendix A) which is necessary to make a transition from the model cross section to the Monte Carlo cross section as the former is differential in t while the latter needs to be differential in Ω_x^{CM} (see Equation (3.6)).

1.2.2 Coincidence Cross Section Framework

The total cross section for a reaction with an N-particle final state can be written in the Lorentz-invariant form (Perl, 1974)

$$\sigma_{TOT} = \frac{(2\pi)^4}{FD} \sum_{f\alpha} \int \left[\prod_{n=1}^{N} |T_{fi}|^2 \delta^{(4)}(P_f - P_i) \frac{d^3p_n}{(2\pi)^3\, 2E_n} \right] \tag{1.17}$$

where

- $FD = 4\left[(P_{i1} \cdot P_{i2})^2 - M_{i1}^2\, M_{i2}^2\right]^{1/2}$ is the flux F of particle 1 multiplied by the density D of particle 2 of the intial state, in the manifestly covariant form; here P_i's are particles 4-momenta and M_i's are their masses,
- T_{fi} is the invariant transition matrix,
- P_i and P_f are total 4-momenta of the initial and final state respectively,
- $d^3p_n/(2\pi)^3 2E_n$ is also Lorentz-invariant (see Appendix C).

Now if N' out of N particles of the final state are detected the cross section (1.17) might be left as a differential cross section, depending on the kinematical coverage, which will no longer be an invariant.

$$\frac{d\sigma}{d^3p_1 \dots d^3p_{N'}} = \frac{(2\pi)^4}{FD} \left[\prod_{n=1}^{N'} \frac{(2\pi)^{-3}}{2E_n} \right] \sum_{f\alpha} \int \left[\prod_{n=N'+1}^{N} |T_{fi}|^2 \delta^{(4)}(P_f - P_i) \frac{d^3p_n}{(2\pi)^3\, 2E_n} \right] \tag{1.18}$$

In the expression (1.18) the dynamics can be separated from the phase space by assuming that the transition matrix T_{fi} does not depend on individual momenta of the final state particles (Fermi, 1950). This assumption leads to the commonly adopted view that the cross section behavior is driven independently by the dynamics of the process of interest and the phase space available to it. It must be noted that four integrations need to be carried out to remove the δ-functions. The differential cross section (1.18), in the case of two body reaction, is most easily evaluated in the center-of-momentum system (see Appendix C for futher details)

$$\frac{d\sigma}{d\Omega^{CM}} = \overbrace{\left(\frac{1}{4p_i^{CM}\sqrt{s}}\right)}^{\text{FD}} \overbrace{\left(\frac{p_f^{CM}}{16\pi^2\sqrt{s}}\right)}^{\text{phase space}} \overbrace{|T_{fi}|^2}^{\text{dynamics}} = \frac{1}{(64\pi^2)\,s}\left(\frac{p_f^{CM}}{p_i^{CM}}\right)|T_{fi}|^2 \tag{1.19}$$

For the electroproduction of particle X (see the diagram in Figure 1.4) the virtual photon cross section is defined through the factorization of the coincidence cross section

$$\frac{d\sigma}{dp_{e'}d\Omega_{e'}d\Omega_X} = \Gamma_T\Big(\frac{d\sigma_v}{d\Omega_X}\Big) \tag{1.20}$$

where the electron variables (virtual photon flux Γ_T) can be separated from proton variables. Since the right-hand side takes on the simplest form in the center-of-momentum frame then the above transforms to

$$\frac{d\sigma}{dp_{e'}d\Omega_{e'}d\Omega_X^{CM}} = \frac{d\sigma}{dp_{e'}d\Omega_{e'}d\Omega_X}\left(\frac{d\Omega_X}{d\Omega_X^{CM}}\right) = \Gamma_T\Big(\frac{d\sigma_v}{d\Omega_X^{CM}}\Big) \tag{1.21}$$

where $p_{e'}$ is the momentum of the outgoing electron, $\Omega_{e'}$ is its solid angle in the target frame, Ω_X^{CM} is the solid angle of the created particle in the virtual photon-proton center of momentum system, σ_v is the virtual photon cross section, in distinction to the real photon cross section, for the production of X, Γ_T is the flux of unpolarized transverse virtual photons.

The original idea of computing the photon polarization by starting in the Breit frame [4] and then transforming to the desired frame comes from L.N. Hand (Hand, 1963). This approach simplifies the calculation because in the Breit frame the emitted photon is an incoherent mixture of +1 and -1 helicity states as a consequence of the fact that relativistic electron preserves its helicity. This, in turn, means that virtual photons will all be transverse and unpolarized and, after performing the transformation back to the lab coordinates, one obtains the following expression for the virtual photon flux

$$\Gamma_T(E, E', \theta_{e'}) = \frac{\alpha}{2\pi^2}\frac{E'}{E}\frac{W^2 - M_p^2}{2M_p^2 Q^2}\frac{1}{1-\epsilon} \tag{1.22}$$

where

$$\epsilon = \left[1 + \frac{2(Q^2 + \nu^2)}{(4EE' - Q^2)}\right]^{-1} \tag{1.23}$$

is a polarization parameter describing both longitudinal and transverse polarizations. In equation (1.22) the Hand convention (Halzen & Martin, 1984)

$$K = \frac{W^2 - M_p^2}{2M_p} = \nu - \frac{Q^2}{2M_p} \tag{1.24}$$

was introduced. K is the laboratory energy of a real photon capable of producing a system with an invariant mass W.

[4]Breit frame - (or brick frame) is the frame where the electron scatters backward without losing any energy.

Finally, the virtual photon cross section can be cast in a form with an explicit dependence on the azimuthal angle ϕ^{CM}

$$\frac{d\sigma_v}{d\Omega_X^{CM}} = \sigma_T + \epsilon\,\sigma_L + \epsilon\,cos(2\phi^{CM})\,\sigma_{TT} + \left[\frac{1}{2}\epsilon(\epsilon+1)\right]^{1/2} cos(\phi^{CM})\,\sigma_{LT} \tag{1.25}$$

where

- ϵ is the virtual photon polarization - see (1.23),
- σ_T is the unpolarized (transverse) cross section,
- σ_L is the longitudinal cross section,
- σ_{TT} is the polarized interference cross section,
- σ_{LT} is the interference cross section.

In the present analysis the last two terms were ignored in the model cross section implemented in the Monte Carlo simulation (see section 3.2.2).

1.3 Physics Motivation

There are only a few measurements of the cross section of electroproduced vector mesons in the near threshold region (Joos et al., 1976; Joos et al., 1977). These experiments suffered from very low statistics. The only published results on the ω electroproduction directly comparable to this work are the *1977* results presented in a paper by P. Joos (Joos et al., 1977). Before reviewing those results however it is beneficial to introduce a theory which was then used to explain them and also the photoproduction data (ABBHHM Collaboration, 1968)

1.3.1 Vector Dominance Model

Before Quantum Chromodynamics (QCD) was widely accepted as the theory of strong interactions J.J. Sakurai (Sakurai, 1960; Sakurai, 1969) had attempted to formulate a theory of strong interactions as a gauge theory with neutral vector mesons ρ^0, ω and ϕ as the gauge bosons ***V**ector **D**ominance **M**odel* (***VDM***). The most interesting content of this theory is related to photon-hadron interactions. The crucial assumption of this approach is that the photon, real or virtual, transmutes into a neutral vector meson before interacting with the hadronic system. Then the VDM predicts that in case of the electron-hadron scattering, which is mediated by the exchange of a virtual photon ($\gamma^* + A \longrightarrow B$), the corresponding amplitude will be given by

$$< B \,|\, T^{\lambda} \,|\, \gamma^* A >= \sum_{V=\rho^0,\,\omega,\,\phi} \frac{\sqrt{\pi\alpha}}{\gamma_V} \frac{m_V^2}{m_V^2 + Q^2} < B \,|\, T^{\lambda} \,|\, V A > \tag{1.26}$$

where

- γ_V is the photon-vector meson coupling constant,
- m_V is the vector meson mass,
- Q^2 is the positive 4-momentum transfer,
- λ represents the helicity,

- A, B stands for the target and all the final state particles, respectively,
- $< B \,|\, T^{\lambda} \,|\, VA >$ is the amplitude for the process $V + A \longrightarrow B$.

This way the vector meson dominance allows the transfer from photon-hadron to hadron-hadron interaction. There are two manifestations of this fact in ω production. Firstly, the virtual photon can fluctuate into an ω which subsequently scatters diffractively from the proton - see diagram (a) on Figure 1.8. Secondly, it can convert to a neutral ρ and then the scattering would occur via the exchange of a neutral pion - second diagram on part (b) of Figure 1.8. The amplitude for the former is governed by

$$< B \,|\, T^{\lambda} \,|\, \gamma^* A >= \frac{\sqrt{\pi\alpha}}{\gamma_\omega} \frac{m_\omega^2}{m_\omega^2 + Q^2} < B \,|\, T^{\lambda} \,|\, \omega A > \tag{1.27}$$

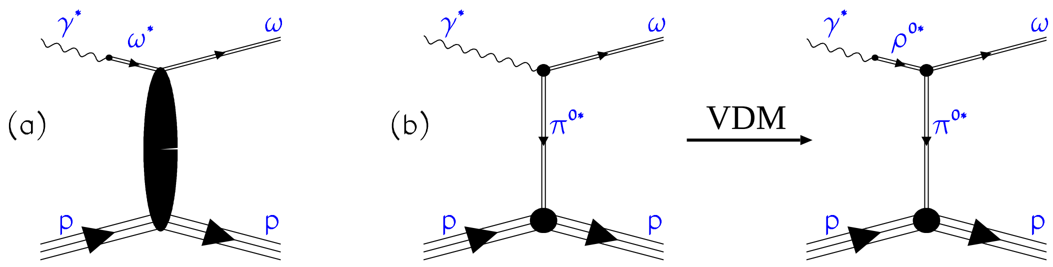

Figure 1.8: ***VDM contributions:*** *(a) diffractive scattering diagram, (b) one pion exchange diagram.*

Justification for the use of the latter is more involved. Employing $SU(3)$ symmetry group for u,d and s quarks the physical ω and ϕ states of the vector (1^-) nonet are expressed in terms of octet-singlet mixing,

$$\phi = \cos\theta \cdot \phi^8 + \sin\theta \cdot \omega^1 \tag{1.28}$$

$$\omega = -\sin\theta \cdot \phi^8 + \cos\theta \cdot \omega^1 \tag{1.29}$$

where θ is the $\omega - \phi$ mixing angle. This, with the aid of the relation between the coupling constants γ_ρ, γ_ω and γ_ϕ

$$\frac{1}{\gamma_\rho} = \frac{\sqrt{3}}{\gamma_\omega}\sin\theta = \frac{-\sqrt{3}}{\gamma_\phi}\cos\theta \tag{1.30}$$

assuming the "ideal mixing", *i.e.* mixing for which $\omega = \frac{1}{\sqrt{2}}(u\bar{u} + d\bar{d})$ and $\phi = s\bar{s}$, (in this case $\tan\theta = 1/\sqrt{2}$) and squaring each coupling constant, yields the ratio estimate that can be directly compared to the experiment (Schildknecht, 1972),

$$\frac{1}{\gamma_\rho^2} : \frac{1}{\gamma_\omega^2} : \frac{1}{\gamma_\phi^2} = 9 : 1 : 2 \tag{1.31}$$

This is indeed in rough agreement with the experimental results,

$$\frac{\gamma_\rho^2}{4\pi} = 0.64 \pm 0.06 \qquad \frac{\gamma_\omega^2}{4\pi} = 4.6 \pm 0.5 \qquad \frac{\gamma_\phi^2}{4\pi} = 2.9 \pm 0.2 \tag{1.32}$$

or,

$$\frac{1}{\gamma_\rho^2} : \frac{1}{\gamma_\omega^2} : \frac{1}{\gamma_\phi^2} = 9 : (1.25 \pm 0.25) : (2 \pm 0.4) \tag{1.33}$$

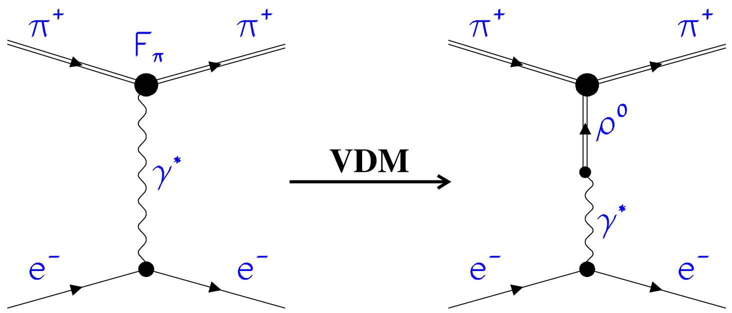

Figure 1.9: ***Pion Form Factor:*** *According to the VDM the electromagnetic structure of the pion arises exclusively from the ρ^0 meson.*

The equation (1.26) can be then simplified by neglecting the ω and ϕ coupling to the photon, by the virtue of the relation (1.31), to give the amplitude for a neutral pion exchange,

$$< B \,|\, T^\lambda \,|\, \gamma^* A >= \frac{\sqrt{\pi\alpha}}{\gamma_\rho} \frac{m_\rho^2}{m_\rho^2 + Q^2} < B \,|\, T^\lambda \,|\, \rho A > \tag{1.34}$$

Using the above arguments and Feynman rules one can calculate the amplitudes for the diagrams at Figure 1.9 (Bhaduri, 1988). Equating them yields a pion form-factor in its simplistic version,

$$F_\pi(Q^2) = \frac{m_\rho^2}{m_\rho^2 + Q^2} \tag{1.35}$$

This prediction says that the pion form factor F_π is entirely due to mediating ρ^0 meson. It stands with remarkable agreement with the data regardless of the regime, either spacelike ($q^2 < 0$) or timelike ($q^2 > 0$) (Brown, 1985), justifying the use of the identification shown on part (b) of Figure 1.8.

1.3.2 ρ^0 Electroproduction Data

The electroproduction of the ρ^0 meson has been found to be predominantly diffractive (Ballam et al., 1973; Joos et al., 1976). During the analysis of the data from the *Deutsches Elektronen-SYnchrotron (DESY)* experiment (Joos et al., 1976) the total cross section was found to have two components with different W behavior. These components were separated by first determining the total cross section for the ρ^0. Then it was supposed that strongly forward peaking (peripheral) component was not present backward of 90^o. The cross section for non-peripheral part of the distribution was integrated over all θ^{CM} range assuming symmetrical behavior about the point of 90^o. The peripheral part was taken to be the difference between the total and non-peripheral cross sections - see Figure 1.10. The peripheral component decreases with increasing Q^2. Also, after taking off steeply from the threshold it is approximately W independent above 2 GeV as would be expected from the diffractive process. On the other hand, similar steep rise from threshold is observed in non-

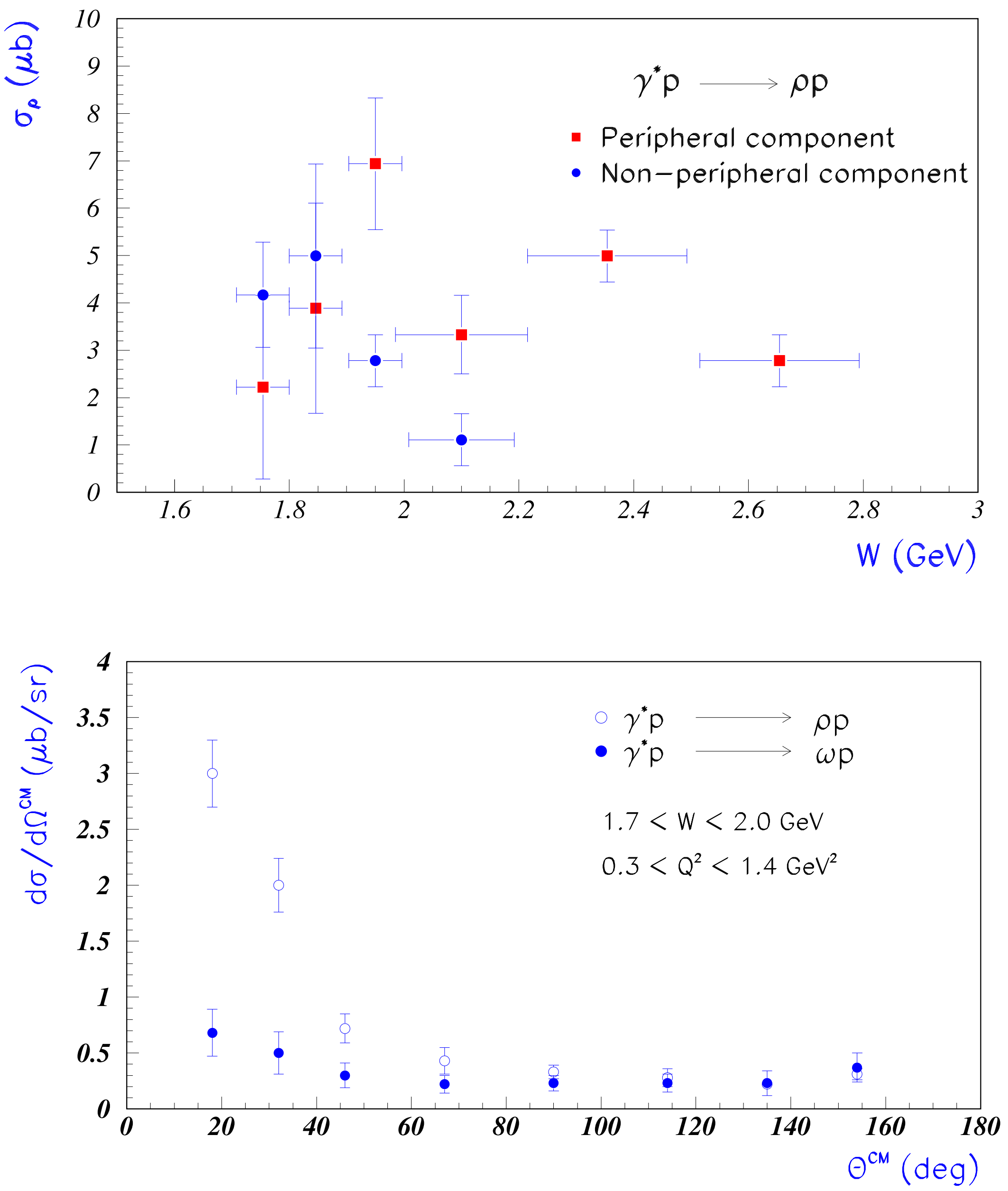

Figure 1.10: ***DESY 1976 data:*** *The total ρ^0 cross section separated into peripheral and non-peripheral. The comparison of the differential cross sections extracted for the ρ^0 and ω mesons productions.*

peripheral component but then it falls off rapidly. The entirely different behavior of these components is seen in the electroproduction of the ω meson - see Section 1.3.4. The t-channel pion exchange is suppressed as the ρ^0 has a marginal $\gamma\pi$ branching ratio ($\Gamma_{\gamma\pi} = 6.8 \times 10^{-4}\%$). The relation (1.31) hints that the ratio of the ω and ρ^0 cross sections would be the same, 1:9, if the production mechanisms were the same. Figure 1.10 is in clear contradiction to that claim, indicating that other contributions have to be accounted for.

1.3.3 ω Photoproduction Data

The natural extension of the model used to describe the ρ^0 data is incorporating the other t-channel process that is the neutral pion exchange. It was prudent to include this process in modeling the ω production (ABBHHM Collaboration, 1968; Joos et al., 1977) since the $\gamma\pi$ branching ratio is fairly large, $\Gamma_{\gamma\pi} = 8\%$. The VMD model including both t-channel processes was then tested against the ω photoproduction data collected by the Aachen-Berlin-Bonn-Hamburg-Heidelberg-München (*ABBHHM*) collaboration during the *DESY* experiment which was performed in 1968. The total cross section was evaluated basing on the statistics of $\sim$6800 events.

The angular distributions at several photon energy ranges were obtained. The lowest two will be discussed here. The first is between 1.1 (threshold) and 1.4 GeV (which is between 1.72 and 1.87 GeV in terms of the CM energies) with the statistics of 420 events. The second is between 1.4 and 1.8 GeV (which is between 1.87 and 2.1 GeV in terms of the

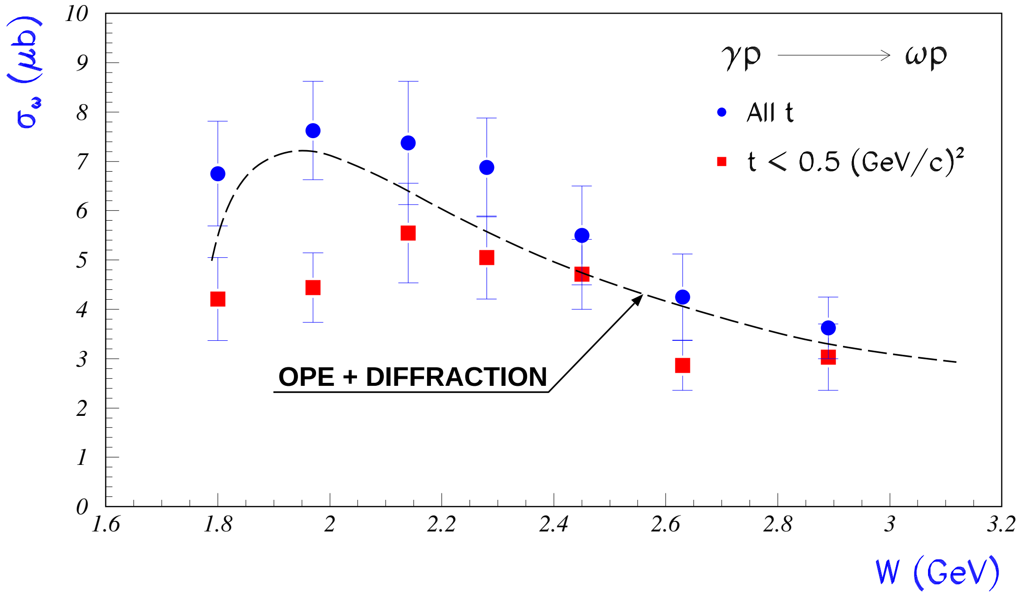

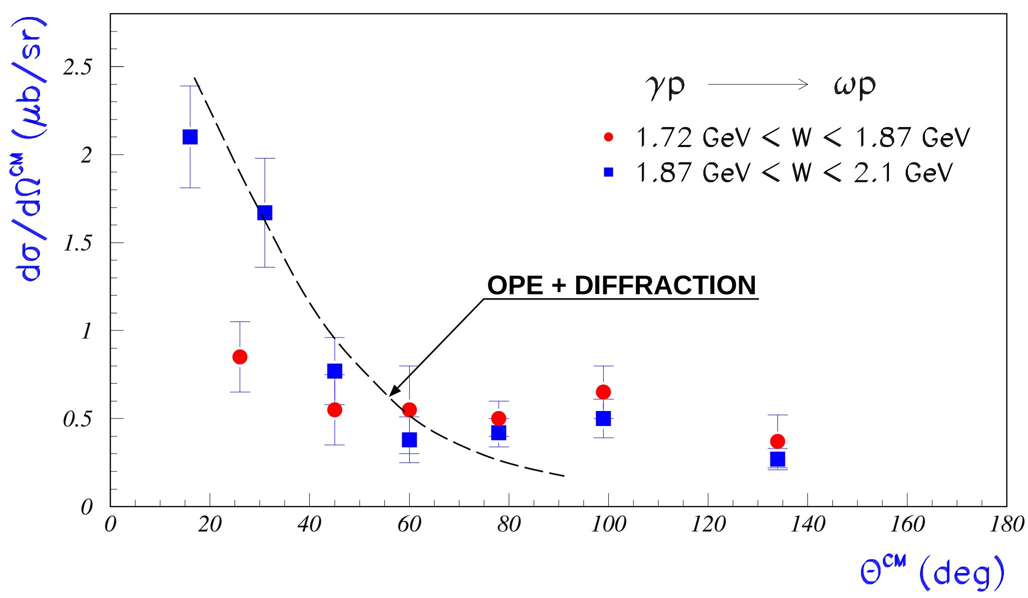

Figure 1.11: ***DESY 1968 Data (ABBHHM Collaboration):*** *Left panel shows the W dependence of the total ω cross section, right panel shows the angular distribution of the differential virtual photon cross section. Worth noting, on the angular distribution plot, is the possible excess of the cross section for the angles backward of 90°.*

CM energies) with statistics of 1166 events. Overlayed on top of Figure 1.11 is the model later used to describe the *DESY 1977* electroproduction data calculated at the real photon limit. The combination of the two described above VDM contributions seems to fit data fairly well for the higher energy interval for which the model curve was calculated. There is, however, visible excess in the differential cross section over the model corresponding to angles backward of 90^o.

1.3.4 ω Electroproduction Data

The results reported in (Joos et al., 1977) come from a streamer chamber experiment carried out at *DESY* in Hamburg, Germany. The data covered center-of-momentum energies, W, from threshold up to 2.8 GeV, 4-momentum transfers, Q^2, from 0.3 to 1.4 (GeV/c)^2 and the full range of scattering angles in the CM system.

The experimental apparatus was capable of detecting all charged particles in the final state ($e'\pi^+\pi^-p$) with nearly 4π angular acceptance. The cross sections were evaluated by normalizing the total number of inelastic ep events to the total inelastic ep cross section determined by the single arm experiment (Stein et al., 1975). The results yielded the dependences of the cross section on Q^2, W and t. To facilitate the studies of the cross section as a function of those variables a t-cut was used to differentiate between peripheral - low t ($|t| < 0.5$ GeV^2/c^2) *i.e.* forward angles in the $\gamma^* p$ CM system - and non-peripheral components (see Figure 1.12). Most interestingly, from the standpoint of the present work,the results indicated that at the

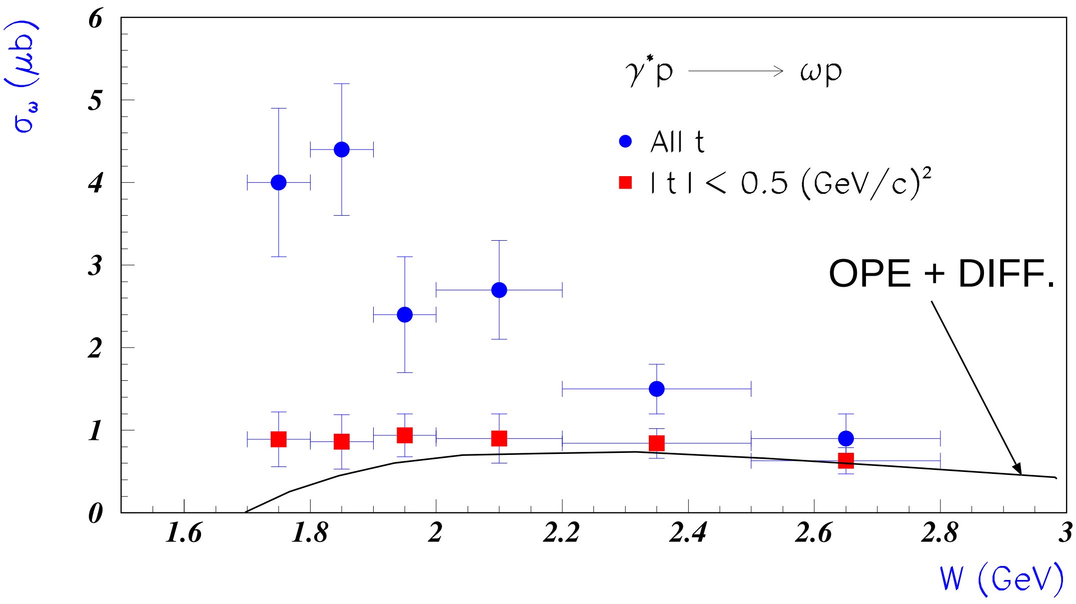

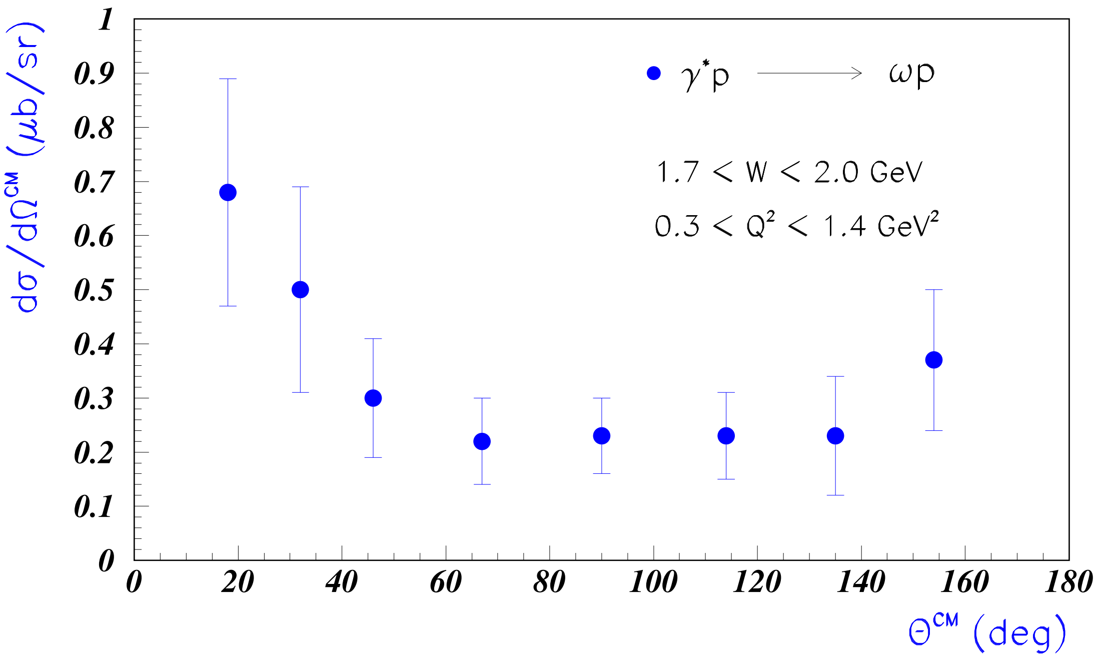

Figure 1.12: ***DESY 1977 data:*** *Left panel shows the W dependence of non-peripheral and peripheral components of the total ω cross section, right panel shows the angular distribution of the differential virtual photon cross section (see text for details).*

ω threshold the cross section was dominated by the non-peripheral production (backward CM angles) and that this non-peripheral component falls off with increasing W while the peripheral component was approximately W independent. The angular distribution of the differential cross section showed that except for a weak forward peak most of the data was of non-peripheral nature. It turned out that the model, based on the derivation by Fraas and Schildknecht (Fraas & Schildknecht, 1969; Fraas, 1971), failed to provide a consistent description of the data, especially for the non-peripheral component (see Figure 1.12). It was concluded that some other production mechanisms must have been contributing, possibly s-channel resonance formation. Diagrams representing the possible contributions are shown in Figure 1.13.

1.3.5 Baryon Spectroscopy

Many excited states of the nucleon have been experimentally observed in ep scattering (see, for instance, (Bartel, 1968)) or πN scattering. A lot of effort was undertaken to construct a theory capable of accounting for the existance of all the nucleon as well as the other baryon spectra.

Quantum Chromodynamics provides the theoretical description of the strong interactions in terms of the fundamental degrees of freedom, quarks and gluons. Motivated by QCD quark models of hadrons were developed (Godfrey & Isgur; Capstick & Isgur) to tackle the problem of baryon spectrum. The ***N****on-****R****elativistic* ***C****onstituent* ***Q****uark* ***M****odel* (***NRCQM***) of Isgur and Karl (Isgur & Karl. 1977; Isgur & Karl, 1978), presented briefly below, will serve as the basis for further discussion.

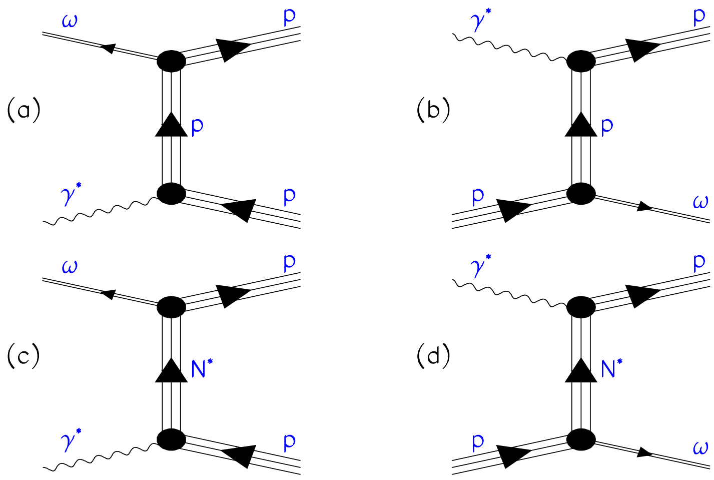

Figure 1.13: ***Nucleon contributions:*** *Intermediate nucleon diagrams in (a) s-channel and (b) u-channel. Formation diagrams for (c) s-channel resonance, (d) u-channel resonance. Note the different direction of the time flow on (a) and (c) as compared to (b) and (d).*

Non-Relativistic Constituent Quark Model

This model treats baryons as systems of three quarks moving in the adiabatic potential generated by the ground state of a three flux-tube junction tying the quarks together in positions $\mathbf{r}_1$, $\mathbf{r}_2$ and $\mathbf{r}_3$ in the center-of-momentum frame of the entire system (Isgur & Paton, 1985). The non-relativistic Hamiltonian consists of the spin-independent and spin-dependent parts,

$$\mathcal{H} \;=\; \mathcal{H}_{s.i.} + \mathcal{H}_{s.d.} \;=\; \overbrace{\sum_i \left(m_i + \frac{p_i^2}{2m_i} \right) + \sum_{i<j} V_{ij}}^{\text{spin}-\text{independent}} \;+\; \overbrace{\sum_{i<j} \mathcal{H}_{hyp}^{ij}}^{\text{spin}-\text{dependent}} \tag{1.36}$$

where the potential V_{ij}, including linear color confinement and Coulomb terms, is given by

$$V_{ij} = C_{qqq} + \frac{1}{2} b r_{ij} - \frac{2\alpha_s}{3 r_{ij}} \tag{1.37}$$

with $r_{ij} = |\mathbf{r}_i - \mathbf{r}_j|$ being a relative distance between i-th and j-th quark and C_{qqq} a constant. The hyperfine interaction term $\mathcal{H}_{hyp}^{ij}$ reads,

$$\mathcal{H}_{hyp}^{ij} = \frac{2\alpha_s}{3 m_i m_j} \left(\frac{8\pi}{3} \mathbf{S}_i \cdot \mathbf{S}_j \delta^{(3)}(\mathbf{r}_{ij}) + \frac{1}{r_{ij}^3} \left[\frac{3 \mathbf{S}_i \cdot \mathbf{r}_{ij} \mathbf{S}_j \cdot \mathbf{r}_{ij}}{r_{ij}^3} - \mathbf{S}_i \cdot \mathbf{S}_j \right] \right) \tag{1.38}$$

In their seminal work Isgur and Karl (Isgur & Karl. 1977; Isgur & Karl, 1978; Karl & Isgur, 1978; Karl & Isgur, 1979) solved the Schrödinger equation ($\mathcal{H} \,|\, \Psi \,\rangle = E \,|\, \Psi \,\rangle$) with the Hamiltonian defined in equations (1.36) through (1.38). The wavefunction Ψ was constructed over four distinct subspaces, spatial (ψ), spin (χ), flavor (ϕ) and color (C),

$$\Psi = \left\{ \sum \psi \chi \phi \right\}_S C_A \tag{1.39}$$

where the subscript A denotes a totally antisymmetric (under the exchange of the three quarks) part of the wavefunction, while the subscript S denotes totally symmetric part of the wavefunction. Solving the problem proceeded in three main steps:

- the Schrödinger equation was solved exactly for the harmonic oscillator Hamiltonian $\mathcal{H}_0$ (to be defined later in the text - see eqn. (1.40)) in two cases:
  - of equal quark masses,
  - when one quark has the mass different from the other two
- perturbation theory was used to calculate the effect of the potential (1.37) on the unperturbed harmonic oscillator states,
- finally, the hypefine interaction was accounted for.

To tackle the task of finding the eigenstates that would be the basis for the subsequent use in the perturbation theory the spin-independent part of the Hamiltonian (1.36) was rearranged to include the harmonic oscillator and the perturbing potential,

$$\mathcal{H} = \overbrace{\sum_i \left(m_i + \frac{p_i^2}{2m_i} \right) + \sum_{i<j} \frac{1}{2} k r_{ij}^2}^{\mathcal{H}_0} + \sum_{i<j} U(r_{ij}) \tag{1.40}$$

where $U(r_{ij}) = V_{ij} - (1/2)kr_{ij}^2$ and k was chosen to minimize the perturbation for the low-lying states. Assuming equal masses for all three quarks ($m_1 = m_2 = m_3 = m$) and transforming to the natural 3-body coordinates (see Figure 1.14),

$$\begin{aligned} \mathbf{R} &= \tfrac{1}{3}(\mathbf{r}_1 + \mathbf{r}_2 + \mathbf{r}_3) \\ \boldsymbol{\rho} &= \tfrac{1}{\sqrt{2}}(\mathbf{r}_1 - \mathbf{r}_2) \\ \boldsymbol{\lambda} &= \tfrac{1}{\sqrt{6}}(\mathbf{r}_1 + \mathbf{r}_2 - 2\mathbf{r}_3) \end{aligned} \tag{1.41}$$

converts the Hamiltonian $\mathcal{H}_0$ to,

$$\mathcal{H}_0 = \frac{P^2}{2M} + \left(\frac{p_\rho^2}{2m} + \frac{3}{2} k \rho^2 \right) + \left(\frac{p_\lambda^2}{2m} + \frac{3}{2} k \lambda^2 \right) \tag{1.42}$$

with $M = 3m$ and $\mathbf{P}$, $\mathbf{p}_\rho$ and $\mathbf{p}_\lambda$ being the momenta conjugate to the respective position vectors.

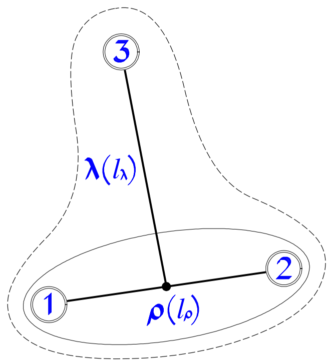

Figure 1.14: ***Constituent Quark Model:*** *Spatial orientation of quarks used in the formulation of the non-relativistic and relativized constituent quarks models, with l_ρ being the relative angular momentum quantum number of the ①–② quark system (ρ-system) and l_λ for the ρ - quark ③ system i.e. λ-system. The relative coordinates $\boldsymbol{\rho}$ and $\boldsymbol{\lambda}$ are defined in the text.*

Ignoring the overall center-of-momentum motion, the eigenstates of the harmonic oscillators were of the form,

$$\psi^{\sigma}_{LM} = \zeta^{\sigma}_{LM}\,\frac{\alpha^3}{\pi^{3/2}}\exp\left(-\frac{1}{2}\alpha^2\left[\rho^2+\lambda^2\right]\right) \tag{1.43}$$

with $\alpha \equiv (3km)^{1/4}$. These states, and the corresponding energies $E = (N+3)\omega$, where $\omega \equiv \sqrt{3k/m}$, yielded the spatial parts of the wavefunctions and the energies of the unperturbed baryonic states of $S = 0$ and $S = -3$ strangeness sectors. For the $S = -1$ and $S = -2$ sectors quark mass difference is taken in to account, so that,

$$m_1 = m_2 = m_d = m_\rho \quad < \quad m_3 = m_s \qquad \text{for } \ S = -1 \ \text{ sector}$$
$$m_1 = m_2 = m_s = m_\rho \quad > \quad m_3 = m_d \qquad \text{for } \ S = -2 \ \text{ sector} \tag{1.44}$$

Performing the same change of variables as in the previous case, the Hamiltonian $\mathcal{H}_0$ reads,

$$\mathcal{H}_0 = \frac{P^2}{2M} + \left(\frac{p_\rho^2}{2m_\rho} + \frac{3}{2}k\rho^2\right) + \left(\frac{p_\lambda^2}{2m_\lambda} + \frac{3}{2}k\lambda^2\right) \tag{1.45}$$

where m_ρ is defined in (1.44), while $m_\lambda = 3m_\rho m_3/(2m_\rho + m_3)$.

The eigenstates of the Hamiltonian $\mathcal{H}_0$ were this time explicitly different for the coordinates ρ and λ.

$$\psi^\sigma_{LM} = \zeta^\sigma_{LM} \left(\frac{\alpha_\rho \alpha_\lambda}{\pi}\right)^{3/2} \exp\left(-\frac{1}{2}\left[\alpha_\rho^2\rho^2 + \alpha_\lambda^2\lambda^2\right]\right) \tag{1.46}$$

where $\alpha_\rho \equiv (3km_\rho)^{1/4}$ and $\alpha_\lambda \equiv (3km_\lambda)^{1/4}$. These states correspond to the energies $E = E_\rho + E_\lambda$ with $E_\rho = (N_\rho + 3/2)\omega_\rho$, where $\omega_\rho \equiv \sqrt{3k/m_\rho}$ and $N_\rho = 2n_\rho + l_\rho$, and similarily for E_λ. Thus introducing different masses in *uds* quark systems removed the ρ-λ degeneracy. In both cases the complete eigenstates were constructed from a antisymmetric color singlet $C_A = \frac{1}{\sqrt{6}}(RBY - BRY + BYR - YBR + YRB - RYB)$ and symmetrized product $\psi \otimes \chi \otimes \phi$ in accordance with the Pauli principle for fermions. For the χ states usual spin multiplets were used ($\uparrow\uparrow\uparrow$, $\frac{1}{\sqrt{2}}(\uparrow\downarrow\uparrow - \downarrow\uparrow\uparrow)$, *etc.*) and the flavor multiplets (uuu, $\frac{1}{\sqrt{3}}(uus + usu + suu)$, $\frac{1}{\sqrt{2}}(udu - duu)$, *etc.*) served the construction of the ϕ states. Complete construction of these states, as well as the analysis, is included in (Isgur, 1991; Karl & Isgur, 1978; Karl & Isgur, 1979).

Once the $\mathcal{H}_0$ eigenstate basis was established performing the first-order perturbation in the anharmonicity U and $\mathcal{H}_{hyp}$ yielded final masses and compositions of the light-quark baryonic states. Even though this model was successful in explaning the data it received criticisms that it, from the theoretical point of view, failed to

- include the glue and sea-quark contributions,
- use the relativistic kinematics and dynamics,
- include the spin-orbit iteraction [5],
- adopt the fundamental QCD parameters [6],
- accomodate also the meson spectra.

The above mentions some of the problems of the NRCQM that challanged theorists to incorporate relativistic effects in the the constituent quark models. These efforts resulted in series of papers by N. Isgur, S. Capstick, S. Godfrey and W. Roberts (Godfrey & Isgur; Capstick & Isgur; Capstick, 1992; Capstick & Roberts, 1994) and others, addressing the issues listed above. The model that emerged from those efforts, sometimes refered to as relativized Constituent Quark Model, describes both mesons and baryons with roughly the same set of parameters with inclusion of naturally small spin-orbit interaction that allows for the use of a strong coupling of a much smaller value ($\alpha_s \simeq 0.6$) simltanenously preserving the N-Δ and Λ-Σ mass splittings, so remarkably predicted by the NRCQM, and the quality of the fits to

[5] Spin-orbit interaction had to be excluded from the model, as producing too large mass splittings.

[6] The parameters used in the model were phenomenological in nature, the strong coupling constant used,for instance, was $\alpha_s \simeq 2$. This fact was the reason behind dropping the spin-orbit interaction out of the model.

the data. Some other efforts using different QCD-based approaches were also undertaken. These are reviewed by S. Capstick and W. Roberts in (Capstick & Roberts, 2000). The spectrum of baryons predicted by the constituent quark models, or other symmetric models, are much richer than that of the naive quark model. Moreover, some of these baryon states have not been experimentally observed yet.

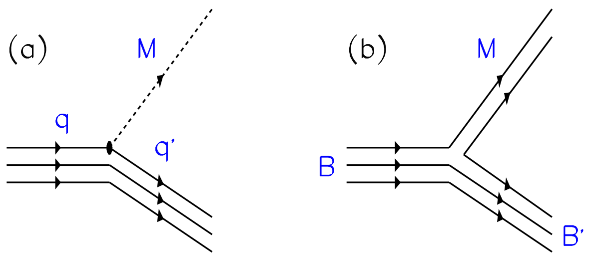

Figure 1.15: ***Baryon Decay:*** *The process seen as (a) an elementary meson emission or (b) a pair creation.*

1.3.6 Missing Resonances

Confirmation of the existance of the states mentioned in the preceding section, called *missing resonances* and populating the energies upto about 2 GeV, would test the validity of the constituent quark or other models. Since the number of the excited states vary from model to model it is very important to observe as many of these states as possible as this would preclude some of the models.

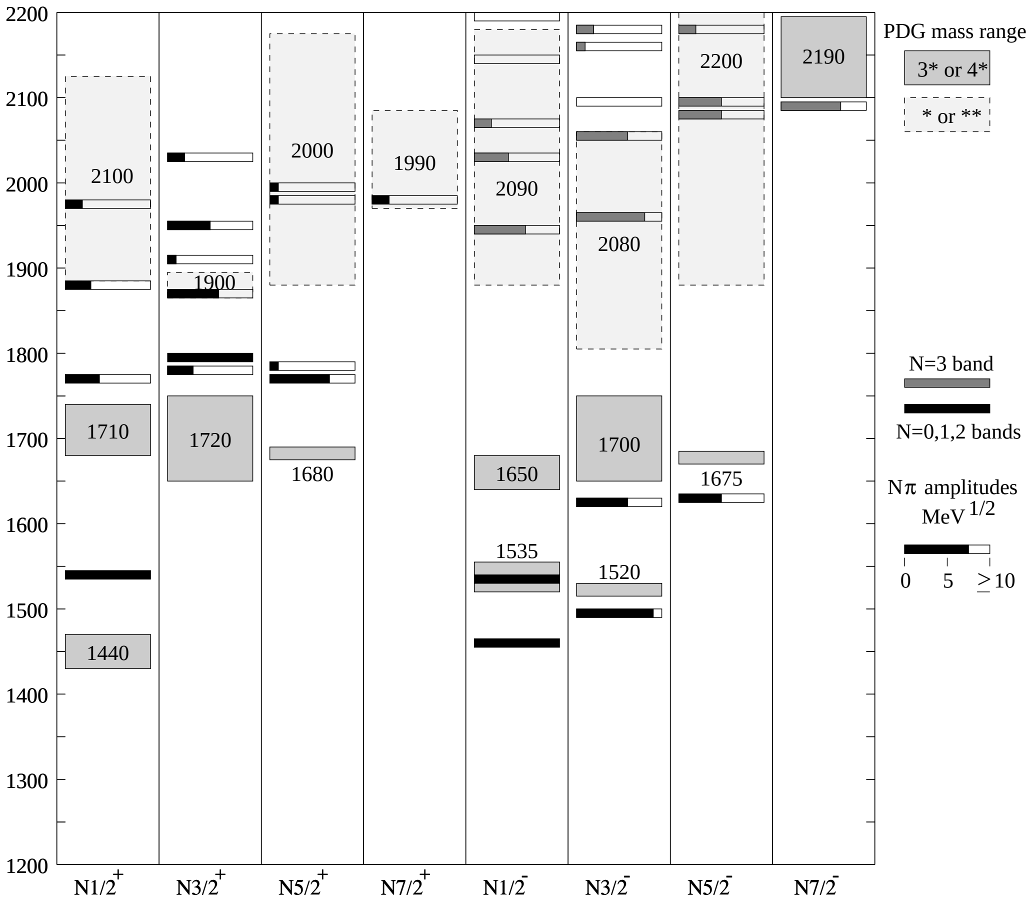

Figure 1.16: ***Missing Nucleon Excited States:*** *Calculated masses and $N\pi$ decay amplitudes for nucleon resonances below 2200 MeV from Refs. (Capstick & Isgur; Capstick & Roberts, 1993), compared to the range of central values for resonances masses from the PDG (Groom et al., 2000), which are shown as boxes. Predicted masses are shown as a thin bar, with the length of the shaded region indicating the size of the $N\pi$ amplitude.*

Moreover, it turns out that it is insufficient to only find a state in a model with a mass similar to one of those found experimentally. since the inability to observe these resonances in the reactions mentioned above does not yet prove the model incorrect. The explanation of this paradox, refered to as the problem of missing resonances, was given by Isgur and Koniuk (Isgur & Koniuk, 1980). Combining their non-relativistic quark model of baryons with the assumption that the baryonic strong decay proceeds via an elementary meson emission (see Figure 1.15 - (a)) they calculated the decay widths for processes with a pseudoscalar meson in the final state.

Remarkably, the couplings of many missing resonances to the πN channel appeared to be very small as a result of strong intra and intermultiplets mixing caused by the hyperfine interaction (see Equation 1.38). This effectively means that these states are either being masked by the neighboring resonances with stronger couplings to that channel or altogether decoupled from that channel. However there are resonance decay modes that have sizeable coupling constants (Capstick, 1992; Capstick & Roberts, 1994). These decay modes include $\Delta\pi$, $N\eta$, $N\eta'$, $N\rho$ and $N\omega$. Table 1.1 and Figure 1.16, taken from (Capstick & Roberts, 2000), show the results of the calculation based on the quark model that included relativistic effects in conjunction with ${}^3P_0$ pair creation model (Le Yaouanc et al., 1978) (see Figure 1.15 - (b)) used for description of baryon decays.

A different approach was presented in (Capps, 1974; Cutkosky & Hendrick, 1977; Forsythe & Cutkosky, 1983). It assumes that a clustering of two quarks within a baryon occurs therefore the number of degrees of freedom of the quarks is reduced which, in turn, leads to fewer baryonic excited states. The two-quark composites, diquarks, are assumed to correspond to the symmetric $SU(6)$ 21-plet and to interact with a sizeable exchange force (Cutkosky & Hendrick, 1977; Lichtenberg, 1969). On this basis the minimal spectrum comprising $(56, L^+_{\text{even}})$ and $(70, L^-_{\text{odd}})$ multiplets was found. It turns out that most of the well established resonances (in Particle Data Group rating $\star\star\star$ or $\star\star\star\star$) are assigned to these multiplets.

Table 1.1: ***Missing Nucleon Excited States:*** *Total widths* Γ *and branching fractions for missing nucleon excited states, from Refs. (Capstick & Roberts, 1993; Capstick & Roberts, 1998; Roberts & Capstick, 1998). States are labeled by their spin, parity, principal quantum number, and model mass (Capstick & Isgur, 1986). Here* $N^*\pi$ *means* $N\frac{1}{2}^+(1440)\pi$, $\Delta^*\pi$ *means* $\Delta\frac{3}{2}^+(1600)\pi$, *and* Σ^*K *means* $\Sigma\frac{3}{2}^+(1385)K$.

State	Γ	$N\pi$	$\Delta\pi$	$N\rho$	$N^*\pi$	$\Delta^*\pi$	$N\eta$	$N\omega$	$\Delta\eta$	ΛK	ΣK	Σ^*K
$[N\frac{1}{2}^+]_4(1880)$	150	.05	.49	.03	.00	.00	.18	.14	.00	.00	.09	.00
$[N\frac{1}{2}^+]_5(1975)$	50	.08	.47	.14	.01	.00	.00	.22	.00	.03	.01	.04
$[N\frac{3}{2}^+]_2(1870)$	190	.20	.12	.02	.01	.02	.26	.11	.00	.00	.26	.00
$[N\frac{3}{2}^+]_3(1910)$	390	.00	.75	.03	.01	.01	.00	.17	.00	.00	.02	.01
$[N\frac{3}{2}^+]_4(1950)$	140	.12	.43	.11	.00	.01	.00	.28	.00	.03	.01	.01
$[N\frac{3}{2}^+]_5(2030)$	90	.04	.57	.15	.00	.01	.00	.16	.00	.01	.00	.06
$[N\frac{5}{2}^+]_2(1980)$	270	.01	.89	.02	.00	.01	.00	.03	.00	.00	.00	.05
$[N\frac{5}{2}^+]_3(1995)$	190	.00	.51	.33	.00	.01	.04	.08	.00	.00	.00	.02
$[N\frac{7}{2}^+]_1(2000)$	50	.13	.53	.03	.00	.02	.21	.06	.00	.00	.02	.00

As mentioned before these baryon states were observed mostly in $\pi N \longrightarrow \pi N$ scattering which would correspond to a simple quark model picture where pion-quark coupling preferably excites a single quark from the ground state. Excitation of two quarks would lead to baryonic states that are decoupled from πN-channel (Bhaduri, 1988). There are indeed some resonances, as $P_{11}(1710) \star\star\star$ and $P_{13}(1870) \star$ both belonging to $70, 0^+$, that escape the above classification. It was predicted that these two states mainly decay via ρN and ωN channels respectively. Therefore the electroproduction of the ω meson may provide the means in the search of the missing resonances. This channel (for which the formation diagrams are shown in Figure 1.13 – (c) and (d)) is also isospin selective since the isoscalar ω can only couple with the proton to $N^*(I = 1/2)$ states, so that the $\Delta^*(I = 3/2)$ resonances are excluded from the considerations thus simplifying the analysis. Any signature of the missing resonance can only be found where the t-channel contributions from one-pion and Pomeron exchange are relatively smaller. This happens to be backward of 90^o in terms of the scattering angles in the hadron Center-Of-Momentum system. The bulk of the data taken during *E91016* and *E93018* pertains exactly to that portion of the angular distribution. However before any conclusions can be drawn the intermediate nucleon terms must be properly accounted for (see diagrams (a) and (b) on the Figure 1.13).

At the time this dissertation was written several theoretical calculations were available for the vector meson photoproduction (Zhao, Li, & Bennhold, 1998; Zhao, 2000) predicting appreciable effects due to the resonance formation for the backward CM angles. The work on the similar model for the electroproduction was in progress (Oh, 2001). This work, although incapable of performing the partial wave analysis and identifying likely contributing resonances, will try to shed some light on the possible intermediate resonant states in the ω electroproduction for the invariant masses from threshold (1.72 GeV) to 1.86 GeV.

CHAPTER 2

EXPERIMENTAL APPARATUS AND DATA ACQUISITION

2.1 Overview

The data for the present analysis were acquired during the kaon electroproduction experiments E91-016 and E93-018 that were conducted in Hall C of Jefferson Lab in late summer and fall of 1996. The CEBAF accelerator capable of delivering high quality **c**ontinuous **w**ave (**CW**) beam with 100% duty factor, provided the electron beam with intensities of up to 30μA and energies ranging from 2.445GeV to 4.045GeV. The beam was aimed at either hydrogen or deuterium targets operating at cryogenic temperatures. The experiments utilized the ***H****igh* ***M****omentum* ***S****pectrometer* (***HMS***) for the detection of the scattered electrons and

S*hort* ***O****rbit* ***S****pectrometer* (***SOS***) for the detection of the short-lived kaons, together with the background protons and pions. Both spectrometers were equipped with similar detector packages whose signals were transmitted to the electronics located in the Counting House for further processing and ultimate recording.

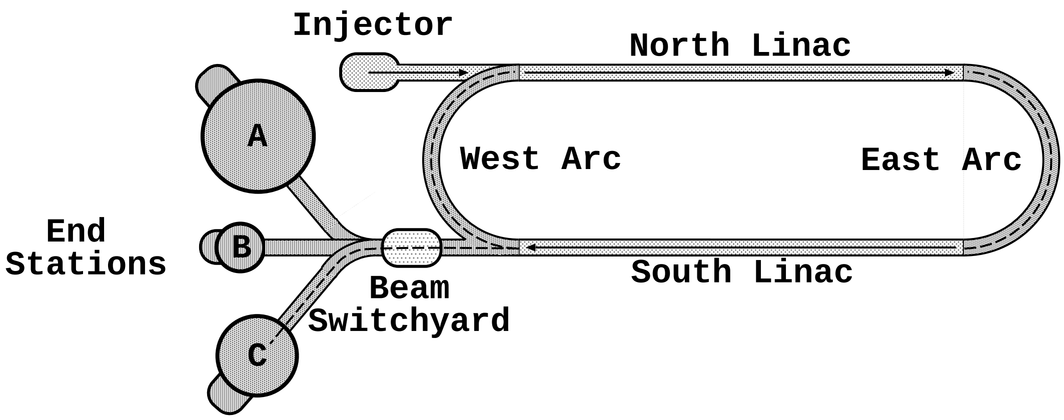

Figure 2.1: ***CEBAF:*** *Top view of the accelerator. The arrows indicate where the acceleration takes place.*

At the time this dissertation was written the accelerator was nominally able to deliver beam of five distinct energies: 0.845, 1.645, 2.445, 3.245 and 4.045 GeV in the standard tune (non-standard tunes resulting in different energies were also possible), however the upgrades to 6 GeV, 12 GeV and beyond were underway. The CEBAF configuration is determined by two linear accelerators coupled by two bending arcs resembling a track-and-field race track. The electrons acquire an energy of 45 MeV in the injector (see Figure 2.1) and are sent into the north linear accelerator (North Linac) where they gain an additional 400 MeV before being bent in the East Arc and accelerated to 845 MeV in the South Linac.

At this point, in the lab jargon, the “one pass” beam can either be directed on the target of any of the experimental halls or recirculated through the accelerator loop to become higher “pass” beam with the energy ramped up by 800 MeV per pass and a maximum of five passes.

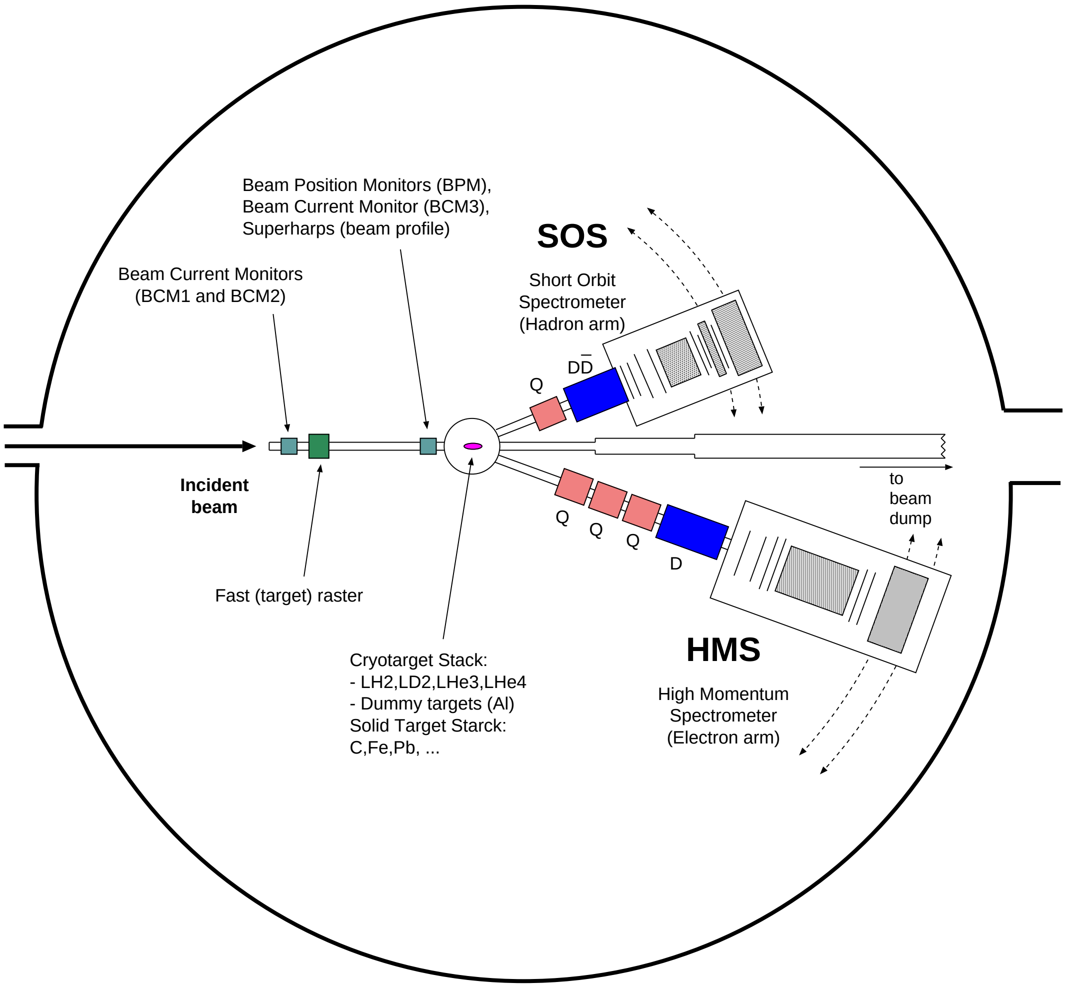

Figure 2.2: ***End Station C:*** *Top view of the Hall.*

CEBAF is capable of simultaneously delivering beam with different energies to different end stations. This is achieved by using separate beamlines in the arcs as the bending fields are energy dependent (the single beamline is used in the linacs) and producing the beam with **r**adio **f**requency (RF) microstructure. Since the beam is generated at the frequency of 1497 MHz (so it, in fact, is not stricly continuous beam) it effectively consists of pulses separated by 668 ps and it can be delivered simultaneously to all three experimental halls by sending from the Beam Switchyard (see Figure 2.1) every third pulse to a given hall. As a result the beam delivered to a hall comes in as bursts every 2 ns (corresponding to 499 MHz frequency). Details regarding the accelerator can be found in (Durham, 1996).

The beamline leading to and in Hall C was instrumented with devices (see Figure 2.2) allowing for the determination of various beam parameters such as:

beam position - **B**eam **P**osition **M**onitors - (**BPM**s) - resonant cavity based monitors provided continuous measurement of the beam position and angle at the target (for details see (Guèye, 1996)). For the duration of the experiments the position of the beam at the target was stable to within ± 1.0mm,

beam current - **B**eam **C**urrent **M**onitors - (**BCM**s) and Unser Monitor - the former, resonant cavities, provided the continuous measurement of the beam current during the data taking while the latter, a parametric current transformer, was used to perform an absolute current calibration (see (Armstrong, 1998)). Using this information the integrated beam charge was evaluated and recorded,

beam energy - superharps and dipoles - allowed for non-concurrent measurements of the beam energy. The former measured the absolute beam position on the entrance to, in the middle and on the exit of the Hall C arc (the arc leading to Hall C which is situated after the Beam Switchyard in Figure 2.1) which combined with the known dispersive characteristic of the arc dipoles (with all nondispersive elements being deactivated) resulted in the beam energy determination (see (Guèye, Tiefenback, & Yan, 1996) for the details) with the accuracy of 10^{-3}. Also noninvasive techniques were used to infer the beam energy and were extensivley described in the theses (Arrington, 1998; Niculescu, 1998).

2.2 The Cryo-target

The target system containing the cryogenic targets as well as solid targets was situated at the pivot common to both spectrometers and enclosed in evacuated scattering chamber. The cryo-target stack was equipped with three independent loops where the cryogenic material was circulated. Each loop consisted of a cell block with 4 and 15 cm target cells. The liquid hydrogen (LH_2) loop is shown schematically on the Figure 2.3.

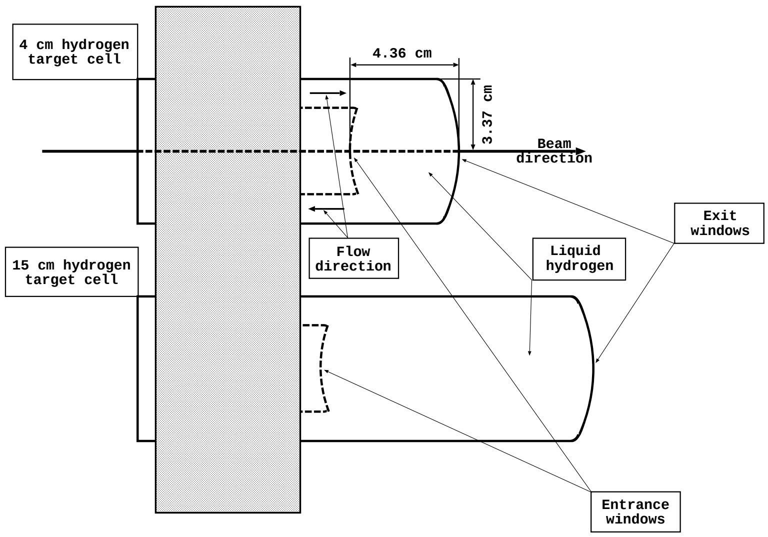

Figure 2.3: ***Cryotarget:*** *Side view of the hydrogen loop (Loop 1).*

It was the 4 cm cell of this (Loop 1) and the deuterium loops (Loop 3), which were the primary targets of the combined E91016/E93018 experiments. The data pertaining to the ω meson production was taken on the 4 cm LH_2 cell (for the dimensions refer to the Table 2.4 and Figure 2.3 as well as to (Dunne, 1997; Meekins, 1999), for an exhaustive description).

Liquid hydrogen circulating through this cell was cooled in a heat exchanger by 15 K gaseous helium and kept at a temperature of (19$\pm$0.2) K and a pressure of 24 psi. The cryo-target stack was remotely operated in two independent directions, either allowing the access to different cryogenic loops and dummy targets (vertical motion) or yielding the room for solid targets by being rotated out of the beamline (horizontal motion). Dummy targets, consising of two aluminum plates mimicking the target entrance and the exit windows and separated by either 15 cm or 4 cm, were mounted on the top and the bottom of the target ladder respectively. These targets were used to subtract out the contribution from the actual aluminum target walls. Solid targets served several purposes, the carbon (^{12}C) targets, for instance, were used for testing and calibrating the optics of the apparatus. To protect the target windows from damage due to small transverse size of the beam spot ($\approx 200\,\mu$m) at the target the beam was rastered using two steering magnets located upstream of the target (fast raster - see Figure 2.2). Using two sinusoidal signals, 24.2 kHz in the horizontal and 17.0 kHz in vertical direction, the beam was deflected in those two directions independently with the amplitudes from $\pm$0.5 to $\pm$1.0 mm.

2.3 The Electron Arm

The combined E91016/E93018 experiments both used the High Momentum Spectrometer to detect scattered electrons and the Short Orbit Spectrometer for outgoing hadrons detection. The main design elements of the HMS, whose operating specifications are presented in the Table 2.1, included,

magnetic elements: HMS consisted of a series of three quadrupoles followed by a dipole (see Figure 2.4 for a schematic of spatial configuration) working in the $Q\bar{Q}QD$ configuration. All the magnets were superconducting. The magnetic fields of the quadrupoles were current regulated while the field of the dipole was controlled by the NMR probe in the feedback loop. All the fields, hence the central momentum, were remotely set and controlled from the Hall C counting room,

entrance slits: the geometrical acceptance of the HMS was defined by a set of three remotely installed apertures: two colimators, large and small, and a sieve slit (Figure 2.6 shows two slits used in the experiment along with relevant dimensions). The large colimator was used during the data taking while with the aid of the sieve slit the finding and optimizing the expansion coefficients of the focal plane to target transformation was facilitated,

detector stack: located in the concrete-shielded hut (see Figure 2.4) consisted of two multiwire drift chambers (DC1 and DC2 in Figure 2.5) followed by two scintilator arrays (S1X and S1Y in Figure 2.5), a gas Čerenkov and two more scintilator arrays (S2X and S2Y in Figure 2.5) and the stack was culminated by a segmented lead glass calorimeter.

The spectrometer worked in the point-to-point tune in both dispersive and non-dispersive (scattering) directions to provide the best interaction vertex reconstruction ($\approx$2-3mm (Niculescu, 1998)).

The central angle of the spectrometer was remotely set from the Hall C counting room. All the ω data was taken with an HMS spectrometer central angle of 17.20^o and a central momentum of 1.723 GeV/c, which, combined with the beam energy of 3.245 GeV, yielded a central Q^2 of 0.5 (GeV/c)^2. At this HMS setting the settings of the hadron arm were varied to cover the full range of scattering angle in the hadron Center-Of-Momentum system (see Table 2.3).

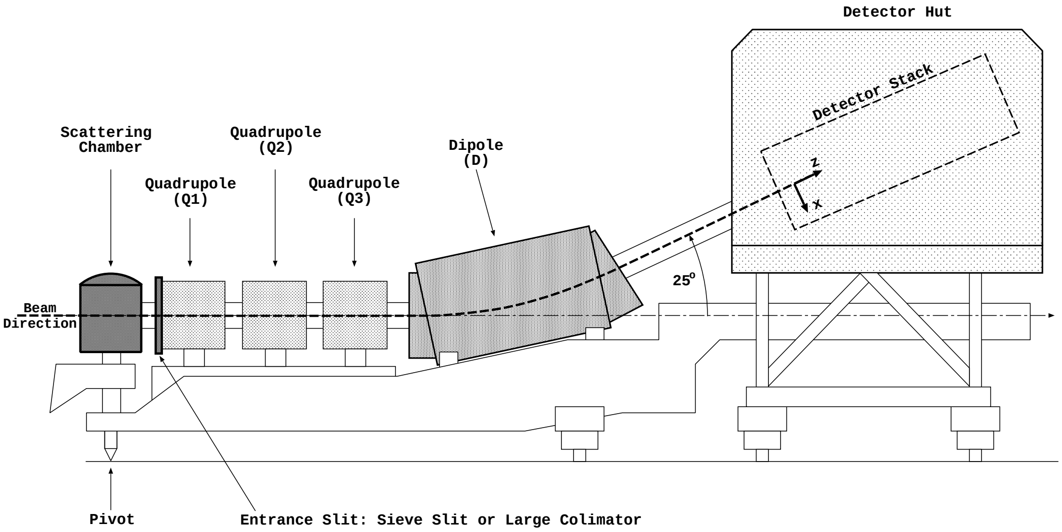

Figure 2.4: ***High Momentum Spectrometer:*** *Schematic side view.*

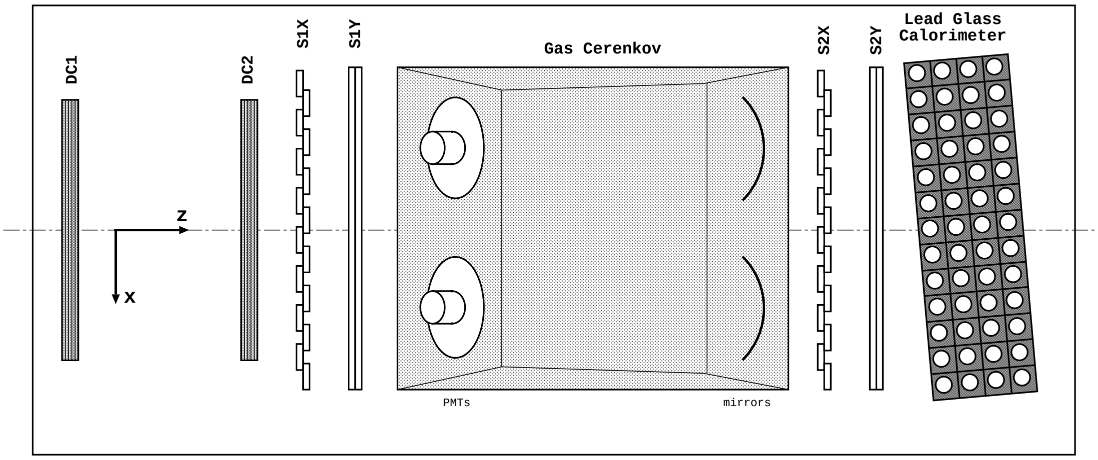

Figure 2.5: ***High Momentum Spectrometer:*** *Detector stack.*

Table 2.1: ***The HMS operating specifications***

Quantity	**Specification**
Minimal Central Momentum	0.5 GeV/c
Maximal Central Momentum	7.5 GeV/c
Minimal Central Scattering Angle	12.5^{o}
Maximal Central Scattering Angle	85^{o}
Momentum Acceptance (Resolution)	18% (0.1%)
Dispersion	$\approx$ 3.9cm/%
Horizontal Opening Angle (Resolution)	56 mrad (1.0 mrad)
Vertical Opening Angle (Resolution)	142 mrad (1.0 mrad)
Solid Angle (4cm target)	$\approx$ 6.5 sr
Optical Length	26.0 m
Upward Bend Angle	25^{o}

The next three sections provide a more detailed description of the detector stack components, as well as their functions.

2.3.1 Tracking: Drift Chambers

The HMS was equipped with a pair of drift chambers separated by about 80 cm and located in front of the detector stack. Each drift chamber consisted of six sense wire planes, which were traversed by the incoming particle in the following order $x \rightarrow y \rightarrow u \rightarrow v \rightarrow y' \rightarrow x'$. The planes labeled x and x', with horizontally extended wires, determined the dispersive coordinate of the particles trajectory while the planes labeled y and y', with vertically oriented wires, determined the coordinate of the particles trajectory in the scattering direction. The wires in the u and v planes were rotated by -15^o and $+15^o$, respectively, with respect to y coordinate (*i.e.* x and x' wires).

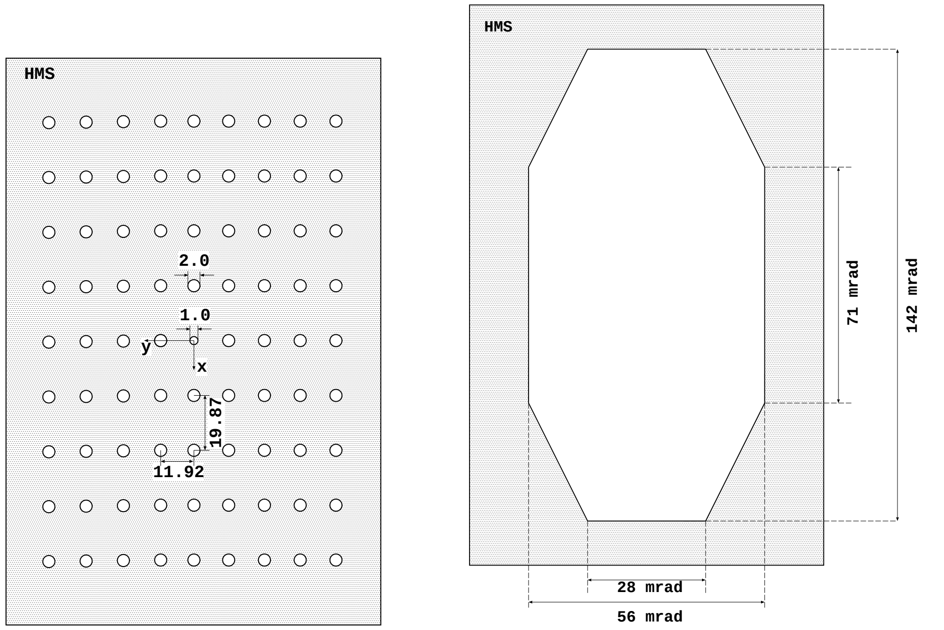

Figure 2.6: ***HMS Entrance Slits:*** *Left panel - sieve slit, right panel - large colimator. All dimensions are in* mrad *assuming 1.262 m distance from the center of the target.*

The primed and unprimed planes were offset with respect to one another by 0.5 cm, in the direction perpendicular to the wire span direction, which was dictated by the need to resolve the left-right ambiguity. The chambers were filled with 1:1 (by weight) mixture of argon and ethane that was circulated at a rate of 400-800 cm^3/min, yielding typical drift times of up to about 100 ns. The HMS drift chamber construction details were presented in various theses and documents (Baker et al., 1995; Niculescu, 1998; Arrington, 1998).

The drift chambers were used to extract the position and orientation of the particle trajectory at the focal plane, which, in turn, facilitated the event reconstruction. From the knowledge of the absolute positions of the senses wire that collected the electrons coming from the ionization due the charged particle passage combined with the drift times extracted from the **T**ime-to-**D**igital **C**onverters (**TDC**s) the positions at each plane of both chambers were determined and then fitted to a straight line (a track) by the tracking software. This procedure yielded vital focal plane information: track position, with the resolution of 200-300 μm, and slopes in the dispersive (xz) and scattering (yz) planes.

2.3.2 Time-Of-Flight & Triggering: Hodoscopes

The electron arm detector package also included two pairs of scintilator hodoscope arrays. Each pair consisted of a plane segmented in the dispersive direction (S1X or S2X on the Figure 2.5) and a plane segmented in the non-dispersive direction (S1Y or S2Y in Figure 2.5) while each segment was composed of long 1cm thick strip of BC404 scintilator on both ends coupled optically via UVT lightguides to photomultipliers (PMTs). It must be noted that all the elements were staggered in such a way that they overlaped by 0.5 cm. This configuration eliminates the gaps between the elements in each plane thus improving the efficiency of the detector.

The signal from the hodoscopes served two purposes. It was used to form the trigger enabling the data acquisition electronics. The raw trigger signal was formed, using a LeCroy 4564 logic module, by

- summing all the discriminated PMT signals (inclusive **OR** logic gate) from one side of each plane thus generating S1X+, S1X-, S1Y+, S1Y-, S2X+, S2X-, S2Y+, S2Y- signals, for instance,

$$\begin{aligned}\mathrm{S1X+} &= (\mathrm{S1X1+})\ \mathbf{OR}\ (\mathrm{S1X2+})\ \mathbf{OR} \cdots \mathbf{OR}\ (\mathrm{S1X16+}) \\ \mathrm{S1Y-} &= (\mathrm{S1Y1-})\ \mathbf{OR}\ (\mathrm{S1Y2-})\ \mathbf{OR} \cdots \mathbf{OR}\ (\mathrm{S1Y9-})\end{aligned}$$

- multiplying signals (**AND** logic gate) from both sides of each plane hence producing S1X, S1Y, S2X and S2Y signals,

$$\begin{aligned}\mathrm{S1X} &= (\mathrm{S1X+})\ \mathbf{AND}\ (\mathrm{S1X-}) \\ \mathrm{S1Y} &= (\mathrm{S1Y+})\ \mathbf{AND}\ (\mathrm{S1Y-}) \\ \mathrm{S2X} &= (\mathrm{S2X+})\ \mathbf{AND}\ (\mathrm{S2X-}) \\ \mathrm{S2Y} &= (\mathrm{S2Y+})\ \mathbf{AND}\ (\mathrm{S2Y-})\end{aligned}$$

- eventually taking final signals in 3 out of 4 coincidence (see Figure 2.10).

Also the signals from each XY pair were combined to form S1 = (S1X) **OR** (S1Y) and S2 = (S2X) **OR** (S2Y) (see Figure 2.10). Thus generated signals were further relayed to the electron pretrigger electronics whose signals were managed by the Trigger Supervisor (see Figures 2.10 and 2.12).

The hodoscopes were also used for the time-of-flight measurements, which were the basis for the velocity determination of the coincident electrons.

2.3.3 Particle Identification: Gas Čerenkov & LGC

As mentioned earlier the entire data set pertaining to the Q^2 point of interest was taken with the HMS central momentum of 1.723 GeV/c. The time-of-flight measurements alone were insufficient to separate electrons from negatively charged pions since their velocities calculated on the basis of those measurements ($\beta_{e^-} = 0.999999956$ while $\beta_{\pi^-} = 0.99672$ for the central momentum given above) were indistinguishable with the achieved resolution. This created the need for additional devices capable of differentiating between the electrons and pions. Therefore the Gas Čerenkov counter and **L**ead **G**lass **C**alorimeter (**LGC**) were incorporated into the detector package.

The Gas Čerenkov detector, a cylindrical tank equipped with two mirrors and two photomultipliers, was filled with carbon dioxide, at room temperature and atmospheric pressure, having refractive index $n = 1.00041$. The threshold velocity for initiating the Čerenkov effect was $\beta_{\check{C}} = 0.999590$ thus the detector was capable of differentiating between the electrons and pions being accepted by the spectrometer. The logic gates generated using the gas Čerenkov analog input formed trigger signals **Č** and **NOT Č** used, in conjunction with the LGC logic signals, for pion supression at the pretrigger level (see Figure 2.10).

The second detector used for e^-/π^- separation was the calorimeter made of TF1 lead glass blocks arranged in four planes, with 13 blocks in each plane. The detector was tilted by an angle of 5° with respect to the central ray of the spectrometer in order to avoid any losses resulting from particles passing through the gaps between the blocks (see Figure 2.5). The thickness of the of the Pb-glass was carefully chosen to ensure that the incident electron lost all the energy in the cascading electromagnetic shower. Light output, which was proportional, in good approximation, to the energy of the primary electron, was collected by the photomultipliers mounted on one side of each block.

Some portion of the pions, which mainly go undetected by the calorimeter, may interact strongly with the nuclei of the lead glass via charge exchange ($\pi^- + p \longrightarrow \pi^0 + n$). The π^0 decay into two photons then triggers an elecromagnetic shower similar to that produced by electrons. This causes pion-electron misidentification. The signals from the calorimeter also contributed in forming the HMS pretrigger (see 2.10).

2.4 The Hadron Arm

The Short Orbit Spectrometer was set to accept positively charged particles such as pions, kaons, protons and deuterons. Therefore constituted the hadron arm of the E91016/E93018 coincidence experiments. Similar to in the HMS case, the main design elements of the SOS, whose operating specifications are presented in the Table 2.2, included,

magnetic elements: SOS QD$\bar{\mathrm{D}}$ design was chosen as the optimal choice for the spectrometer with moderate resolution and large angular and momentum acceptances. As oppose to the electron arm magnets the SOS magnets were cooled with pressurized water. The horizontal focusing quadrupole was followed by a pair of dipoles with the opposite bending directions resulting in the net upward bend of the optical axis of 18^o (see Table 2.2 for exact bend breakdown). Both dipoles were housed in the same iron yoke adding to the compactness of the design much needed in studying unstable particles. All the fields, hence the central momentum, were remotely set and controlled from the Hall C counting room,

entrance slits: the geometrical acceptance of the SOS was defined by a set of three remotely installed apertures: two colimators, large and small, and a sieve slit (Figure 2.9 shows two slits used in the experiment along with relevant dimensions). The large colimator was used during the data taking while the sieve slit was used for optimizing the expansion coefficients of the focal plane to target transformation,

detector stack: located in the concrete-shielded hut (see Figure 2.7) consisted of two multiwire drift chambers (DC1 and DC2 in Figure 2.8) followed by two scintilator arrays

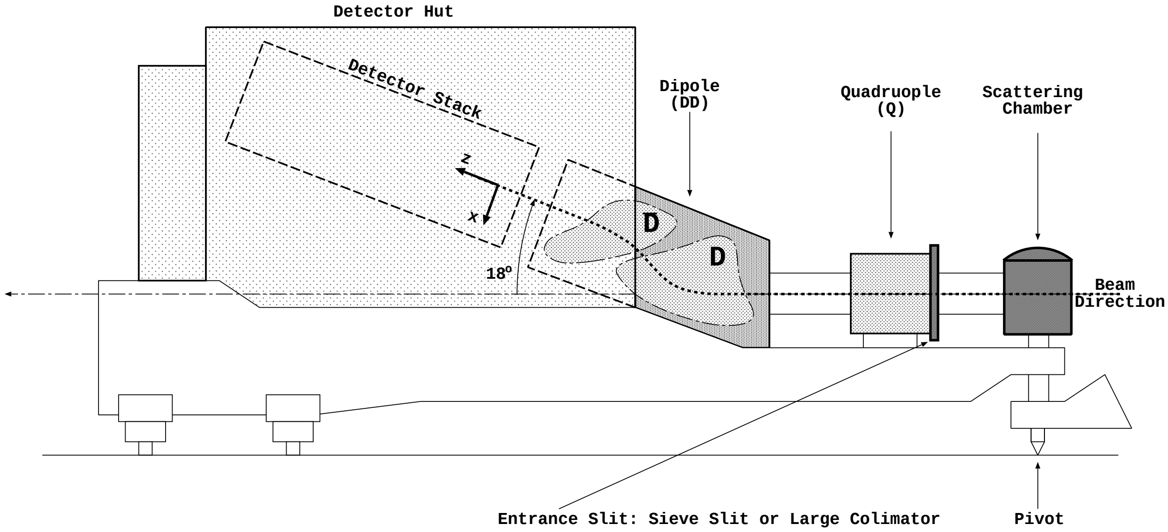

Figure 2.7: ***Short Orbit Spectrometer:*** *Schematic side view.*

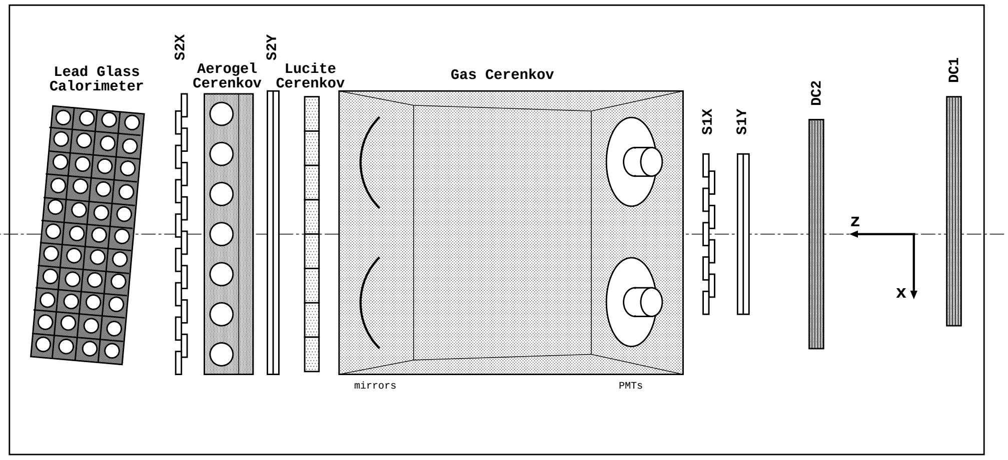

Figure 2.8: ***Short Orbit Spectrometer:*** *Detector stack.*

Table 2.2: ***The SOS operating specifications***

Quantity	**Specification**
Minimal Central Momentum	0.1 GeV/c
Maximal Central Momentum	1.8 GeV/c
Minimal Central Scattering Angle	13.4^o
Maximal Central Scattering Angle	165^o
Momentum Acceptance (Resolution)	40% (0.1%)
Dispersion	¡ 0.92cm/%
Horizontal Opening Angle (Resolution)	114 mrad (3.5 mrad)
Vertical Opening Angle (Resolution)	74 mrad (1.0 mrad)
Solid Angle (4cm target)	$\approx$ 6.5 msr
Optical Length	7.4 m
Net Upward Bend Angle	18^o ($\mathbf{D}$: +33^o, $\bar{\mathbf{D}}$: -15^o)

(S1Y and S1X in Figure 2.8) and a gas Čerenkov. For the duration of the kaon experiments lucite Čerenkov array was installed between gas Čerenkov and S2Y hodoscope array. Two more scintilator arrays (S2Y and S2X in Figure 2.8) were separated by aerogel Čerenkov counter, also not present in the HMS detector package. The stack was culminated, similarily as in the HMS, by a segmented lead glass calorimeter.

This spectrometer was also tuned in the point-to-point fashion in dispersive and scattering directions to provide the best interaction vertex reconstruction ($\approx$1-2mm (Niculescu, 1998)). Changing the central SOS momentum and angle, which was done remotely from the Hall C counting room allowed accessing different regions of the ω scattering angle in the CM system. Table 2.3 shows all the settings of the proton arm pertaining to the Q^2 point of interest. The following subsections provide the description of the components of the detector stack, and their functions.

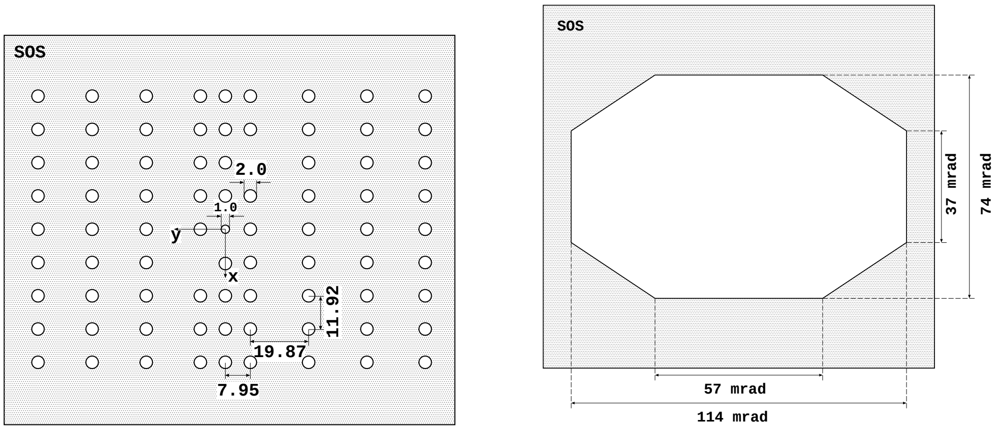

Figure 2.9: ***SOS Entrance Slits:*** *Left panel - sieve slit, right panel - large colimator. All dimensions are in* mrad *assuming 1.262 m distance from the center of the target.*

2.4.1 Tracking: Drift Chambers

The SOS was also equipped with a pair of drift chambers separated by about 49 cm and located in front of the detector stack. Each drift chamber contained six sense wire planes, which the incoming particle traversed in the following order $x \rightarrow x' \rightarrow u \rightarrow u' \rightarrow v \rightarrow v'$. While the planes labeled x and x', with horizontally extended wires, determined the dispersive coordinate of the particles trajectory, unlike in the HMS case, combination of the planes labeled u and v determined the coordinate of the particles trajectory in the scattering direction. The wires in the u and v planes were rotated by -60^{o} and $+60^{o}$, respectively, with respect to y coordinate (*i.e.* x and x' wires). The primed and unprimed planes were offset with respect to one another by 0.5 cm, in the direction perpendicular to the wire span direction, again, to help resolve the left-right ambiguity. Similarily, the chambers were filled with 1:1 (by weight) mixture of argon and ethan that was circulated at a lower rate of $\sim$200 cm^3/min. The description of the SOS drift chambers was presented in several theses (Niculescu, 1998; Arrington, 1998; Mohring, 1999).

The SOS drift chambers played the same role in establishing the particle track as those in the HMS. From the knowledge of the absolute positions of the senses wire that collected the ionization electrons combined with the drift times extracted from the TDCs information the positions at each plane of both chambers were determined and then fitted to a straight line providing, in turn, track position and slopes at the focal plane in the dispersive (xz) and scattering (yz) planes with the resolution, similar to that of the HMS drift chambers, of 150 μm.

2.4.2 Time-Of-Flight & Triggering: Hodoscopes

The SOS detector array included two pairs of scintilator hodoscopes. Each pair consisted of a plane segmented in the dispersive direction (S1X or S2X in Figure 2.8) and a plane segmented in the non-dispersive direction (S1Y or S2Y in Figure 2.8) while each segment was composed of long 1cm thick strip of BC404 scintilator on both ends coupled optically via UVT lightguides to photomultipliers (PMTs). Again, all the elements were staggered in such a way that they overlaped by 0.5 cm.

The signal from the hodoscopes formed the raw trigger in the same way as for the electron (HMS) counterpart (see Section 2.3.2). It was also used to determine the velocity of the scattered protons via the time-of-flight technique.

2.5 Trigger Electronics

At the heart of the Hall C data acquisition network, which was extensively described in numerous theses (Arrington, 1998; Niculescu, 1998; Mohring, 1999; Cha, 2000), was the sophisticated trigger system capable of coping with the high counting rates sustained during the E91016/E93018 experiments due to large pion/proton background. The trigger electronics consisted of three components,

electron trigger electronics: where the HMS raw trigger (or HMS pretrigger) was formed (shown of Figure 2.10),

hadron trigger electronics: where the SOS raw trigger (or SOS pretrigger) was formed (shown on Figure 2.11),

coincidence electronics: where final coincidence trigger signal to the data acqusition system was issued (shown on Figure 2.12),

and was devised to reduce the dead time of the electronics (the time when the electronics is not accepting any signals due to processing the ones it already received) and the data size. Further data reduction was performed offline on the software level.

The vital part in building of either pretrigger signal was the hodoscope information of the respective spectrometer. For the electron arm the scintillator signals were combined into two different gates, **SCIN** and **STOF**. The former was defined as the 3 out of 4 coincidence of the signals coming from the separate hodoscope planes while the latter was defined as simple coincidence of the signals received from either XY-pair of hodoscope planes - S1 **AND** S2 (see Section 2.3.2). The valid **STOF** signal implied that the minimum timing information had been gathered in order to proceed with the time of flight computations.

For the purpose of e^-/π^- separation at the hardware level the signals from the Gas Čerenkov detector (**Č** and **NOT Č**) and shower counter (**PRHI**, **PRLO** - the signals coming from the front layer of the calorimeter discriminated at high and low threshold respectively, and **SHLO** - the discriminated total shower counter signal) were incorporated into the HMS pretrigger.

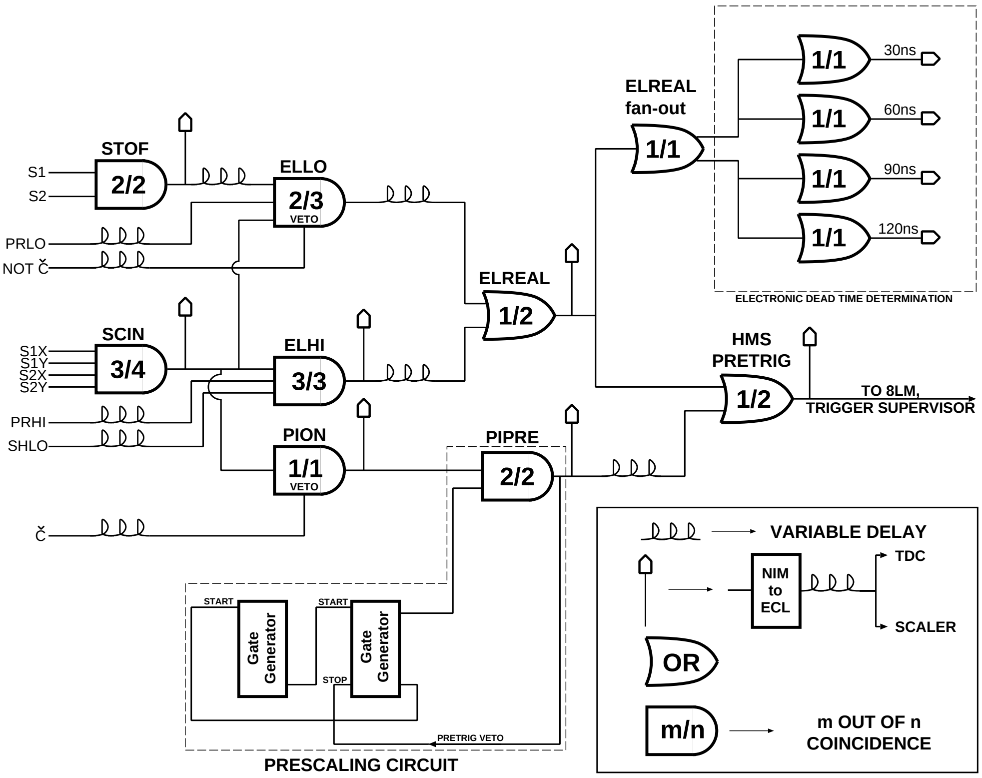

Figure 2.10: ***Electron Trigger:*** *The HMS pretrigger electronics.*

This yielded two separate criteria of identifying an event as a valid electron event, **ELLO** and **ELHI**. The **ELHI** was formed as simple

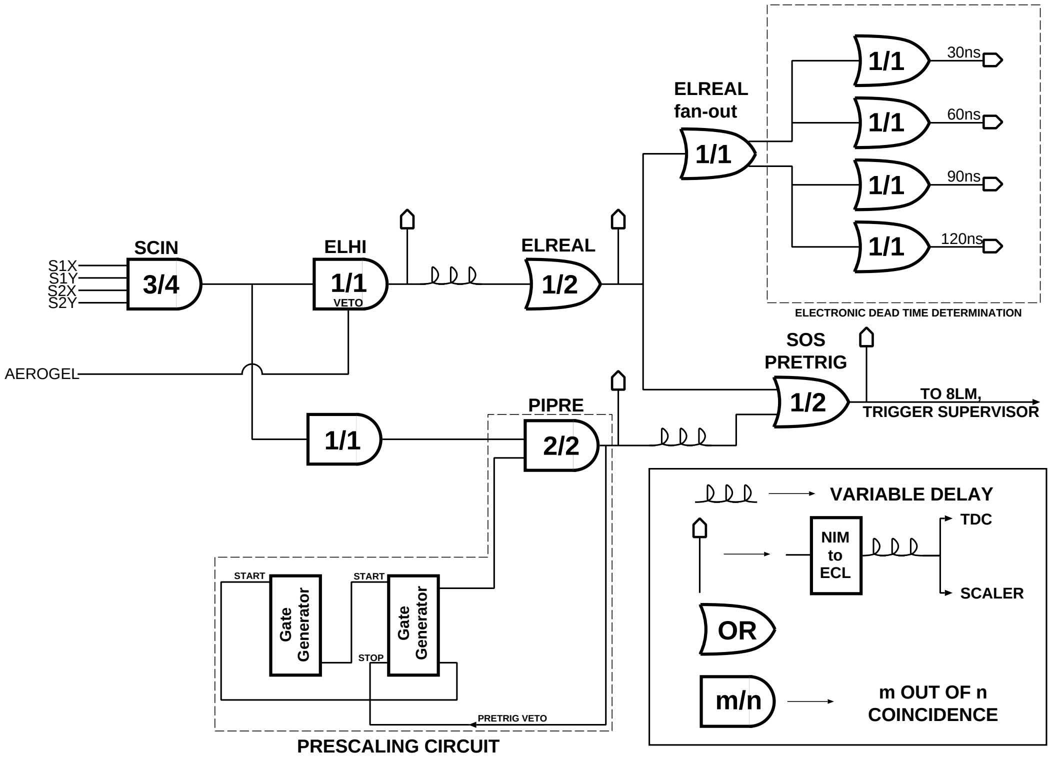

Figure 2.11: ***Hadron Trigger:*** *The SOS pretrigger electronics.*

coincidence of **SCIN**, **PRHI** and **SHLO** while **ELLO** was defined by the quadruple **STOF**, **SCIN**, **PRLO** and **Č** by requiring the first three to form 2 out of 3 coincidence restricted by the **NOT Č** veto. The final electron trigger was the sum of **ELLO** and **ELHI** and was labelled **ELREAL**. For diagnostic purposes some low-rate pion sample was also sent into the data stream by accepting events with valid **PIPRE** signal defined by **SCIN** gate and the absence of the Gas Čerenkov signal **Č** and prescaled. Eventually the HMS pretrigger was formed by summing electron and pion triggers, **ELREAL** OR **PIPRE**.

This design (3/4 hodoscope coincidence, **ELLO**, **ELHI** signals utilizing independent PID signals) and its implementation (discrimination thresholds) aimed at delivering a trigger which is relatively insensitive to always unpredictable hardware problems.

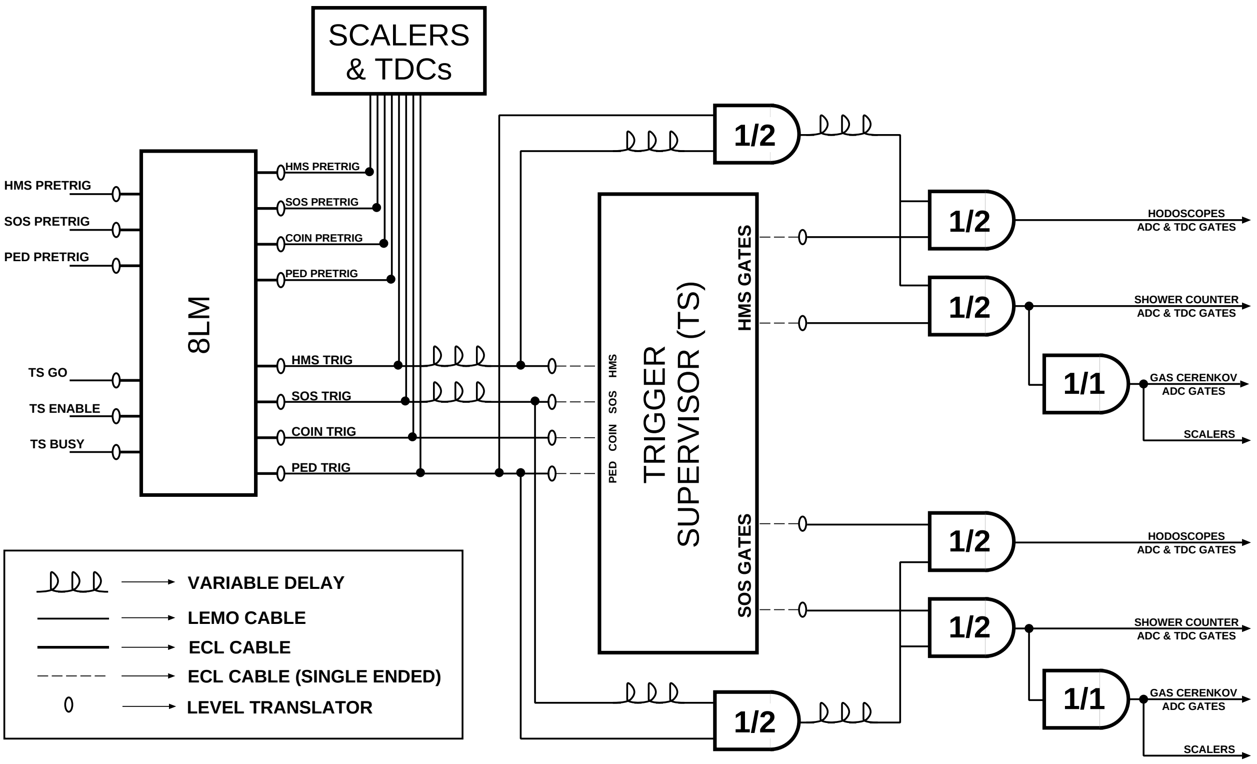

Figure 2.12: ***Trigger Supervisor:*** *The coincidence trigger electronics.*

The hadron trigger logic was a simplified version of that of the electron. There was only one way of identyfying a valid hadron event, similar to the **ELHI** criterion. It required the coincident presence of 3 out of 4 signals from separate scintillator planes. The major difference, that facilitated the pion supression, was the inclusion of the Aerogel Čerenkov signal that was used as a veto on **SCIN** gate. Therefore the final **SOS PRETRIG** was formed for the valid **SCIN** signal provided that the corresponding Aerogel light output did not exceed about 7 photoelectrons (Mohring, 1999).

The single arm pretriggers were subsequently relayed to a programmable logic module 8LM (LeCroy 2365) were the trigger type was determined. If the signals arrived in coincidence, the coincidence trigger signal was issued whenever the TS ENABLE gate, was also present otherwise the trigger was recognized as a single HMS, single SOS (along with TS ENABLE signal) or pedestal signal (along with TS GO) (see diagram on Figure 2.12). In the absence of the TS BUSY gate, which was generated to block accepting new events while processing the accepted ones, the coincidence electronics sent the trigger signal to the Trigger Supervisor. The Trigger Supervisor (the high speed interface with the data acqusition system) after prescaling the trigger (coincidence triggers were prescaled by 1, that means that all the coincidences that reach the Trigger supervisor were accepted), issued two gates to the readout electronics (ADCs and TDCs) via retiming circuits.

The readout electronics were located at FASTBUS and VME crates managed by the Read Out Controllers (ROCs). The ROCs were read by CODA (Cebaf Online Data Acquisition) software, which then, from the pieces of information collected from ROCs managing different detectors, built the complete event written to disk.

2.6 Kinematical Coverage

As mentioned earlier, all the data analyzed in this work was taken with the HMS spectrometer central anlge of 17.20° and central momentum of 1.723 GeV/c. The beam energy was set to 3.245 GeV. Having fixed the HMS position and momentum the settings of the hadron arm were varied to cover the full range of scattering angle in the hadron Center-Of-Momentum system. All the settings are presented in the Table 2.3.

Table 2.3: ***Kinematical settings for the*** $\mathbf{Q^2 = 0.5\ (GeV/c)^2}$ ***point.***

Electron Arm		Proton Arm			
$\mathbf{p_0}$ **(GeV/c)**	$\boldsymbol{\theta_0}$ **(deg)**	$\mathbf{p_0}$ **(GeV/c)**	$\boldsymbol{\theta_0}$ **(deg)**	$\boldsymbol{\theta_{\gamma p}}$ **(deg)**	$\boldsymbol{\theta^{CM}}$ **(deg)**
1.723	17.20	1.077	17.67	0.00	180
			22.00	4.33	∼155
			26.50	8.78	∼135
			31.00	13.3	∼115
		0.929	17.67	0.00	180
			22.00	4.33	∼130
			26.50	8.78	∼110
			31.00	13.3	∼90
			35.00	17.3	∼75
		0.650	17.67	0.00	0.0
			22.00	4.33	∼20
			26.50	8.78	∼30

Figure 2.13 shows the full kinematical coverage of the data set. The sign convention was adopted, according to which the positive sign is associated with scattering angles corre-

sponding to angles greater than the angle of the virtual photon with respect to the incident electron.

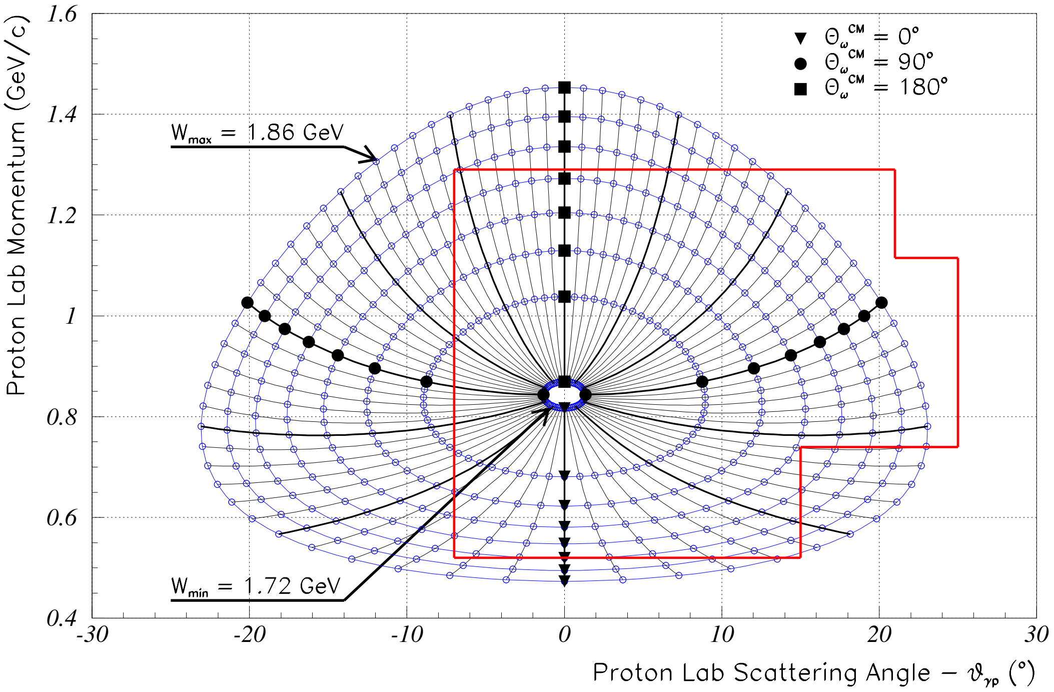

Figure 2.13: ***The kinematics of*** $\mathbf{Q^2 = 0.5}$ ***GeV*** $\mathbf{^2}$ ***point***: *Total kinematical coverage. Gray line defines the acceptance of the experimental apparatus for the all the kinematic settings (see Table 2.3) for the set of cuts used in the analysis. The plot was generated assuming that* $M_x = M_\omega = 0.782$ *GeV*

The result of this, since each consecutive SOS angular setting for a given momentum was further off the beam direction, is shown in Figure 2.13 so the acquired data pertained mostly to positive angles. The grid on the plot of Figure 2.13 represents the points with constant invariant mass W (closed blue lines) and constant scattering angle in the hadron CM frame θ_p^{CM} (black lines converging toward the threshold loop). The open circles denote 20 MeV increments on constant W lines and 5^o increments on constant θ_p^{CM} lines. The CM angles, for the positive part of the plot, for the proton increase clockwise from the top while for the ω counterclockwise from the bottom since they are related by $\theta_p^{CM} + \theta_\omega^{CM} = 180^o$. The plot was generated by

1. fixing M_x and Q^2,

2. expressing $\nu = E - E'$ and $|\mathbf{q}|$, for a given beam energy E, in terms of W and Q^2 (see equalities B.10 and B.2 in the Appendix B),

3. calculating proton energy and momentum E_p^* and p^* (see relations on page 192 in the Appendix B) and the parameters of the Lorentz boost,

4. computing the scattering angle in the lab frame with the aid of the transformation formula on page 196 (see Appendix B),

5. Lorentz-boosting p^* to the lab frame for given θ_p^{CM} and W,

6. stepping through θ_p^{CM} from 0^o to 180^o for given W,

7. eventually looping over W.

The $(\theta_{\gamma p}\ ,\ p_x^*)$-pairs formed this way are shown in Figure 2.14 as open circles located at the intersections of constant W and constant θ_{CM} curves. Relatively small acceptances of the HMS and the SOS introduced strong correlations between many kinematical variables, M_x and W, for instance. Figure 2.14 illustrates how the change in the SOS angular and momentum setting affects the selection of the invariant mass W of the hadron system thus correlating W with the CM scattering angles. The Figure 2.14 displays four plots similar to the one in Figure 2.13 but each plot is generated for a specific SOS setting.

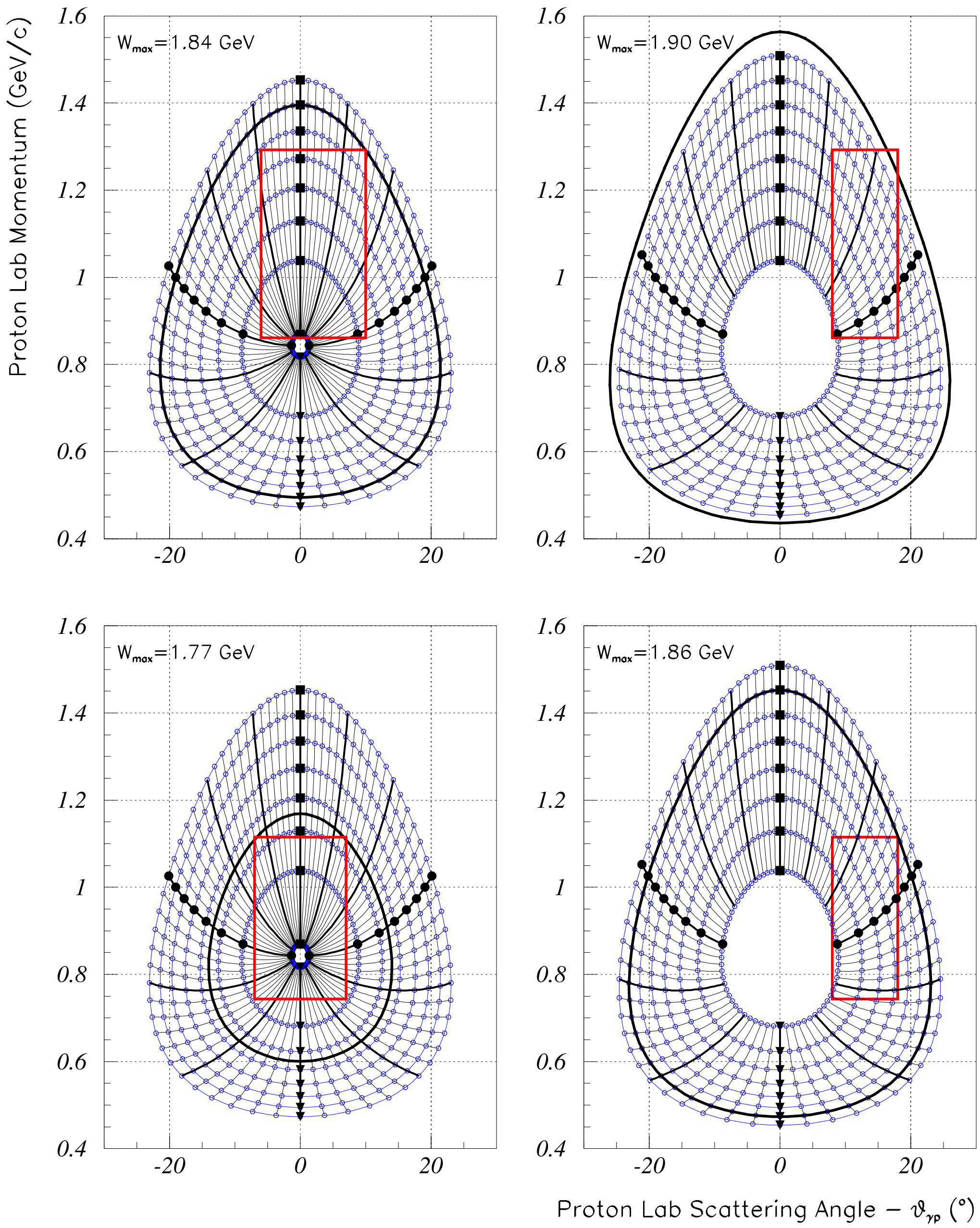

Figure 2.14: ***The kinematics of*** $\mathbf{Q^2 = 0.5}$ ***GeV***$^{\mathbf{2}}$ ***point***: *Correlations introduced by the spectrometer acceptances. The closed black lines indicate the highest W accepted for some of the kinematic settings. Gray lines define the acceptance in proton momentum and proton scattering angle. The solid square, triangle or circle points denote the scattering direction of the ω meson as in Figure 2.13. Refer to the text for full description.*

The top left plot corresponds to the setting for which the central ray is off by $\theta_{\gamma p} = 4.33^o$ from the nominal virtual photon direction and the central SOS momentum is 1.077 (GeV/c)^2. On the second top plot (top right) the SOS momentum is kept the same while $\theta_{\gamma p} = 13.3^o$.

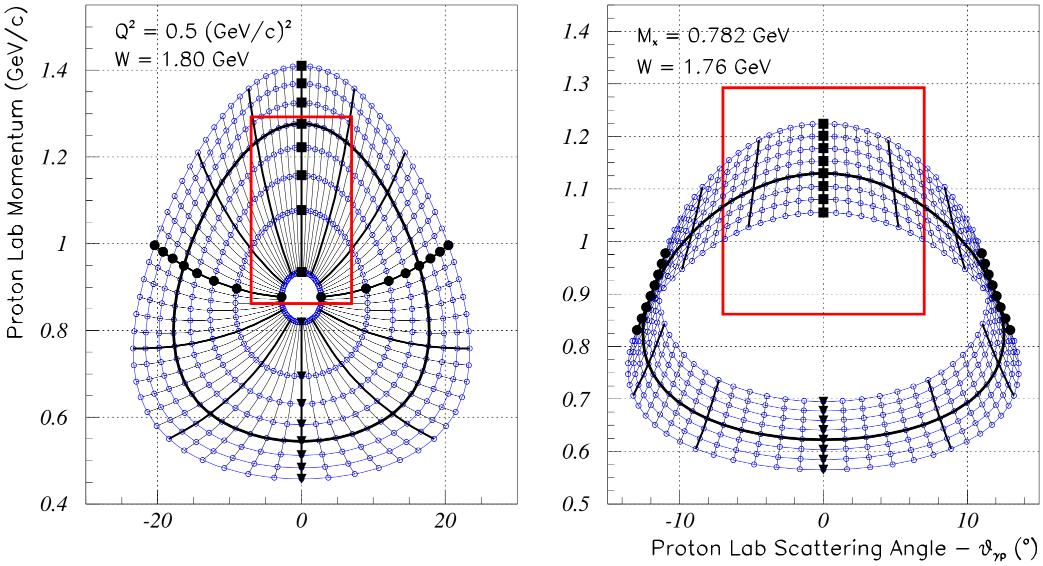

Figure 2.15: ***The kinematics of $\mathbf{Q^2 = 0.5}$ GeV^2 point***: *M_x and Q^2 variations. On the left panel the effect of varying M_x on the fixed W curve is shown. Mass increments of 20 MeV were used. The outermost curve corresponds to a mass of 0.720 GeV while the innermost corresponds to 0.860 GeV. The right panel displays the effect of varying Q^2 on the fixed W curve. The bold black line, on both plots, represents "normal" conditions of the Figure 2.13, i.e. $Q^2 = 0.5\,(GeV/c)^2$, $M_x = 0.782$ GeV and $W = 1.80$ GeV in the case of the plot on the left panel or $Q^2 = 0.5\,(GeV/c)^2$, $M_x = 0.782$ GeV and $W = 1.76$ GeV in the case of the plot on the right panel. The gray box defines the SOS acceptance for the parallel backward kinematics (p_{SOS} =1.077 GeV/c and $\theta_{\gamma p}$ =0.0^o). The solid square, triangle or circle points denote the scattering direction of the ω meson as in Figure 2.13.*

Third plot (bottom right) corresponds to keeping the angular SOS setting the same and lowering its momentum to 0.929 (GeV/c)^2. Eventually the last plot was generated for the

SOS momentum setting of $0.929\,(\mathrm{GeV/c})^2$ but for the parallel kinematics, *i.e.* kinematics for which $\theta_{\gamma p} = 0.0^o$. In order to perform all the calculations when creating those plots the missing mass was fixed at the ω meson mass $M_x = M_\omega = 0.782$ GeV. Since the ω has a narrow intrinsic width, $\Gamma_\omega = 8.43$ MeV, the presented plots describe rather well the actual kinematical correlations. To complete the description of the kinematics using plots introduced above it is necessary to explain what happens if either of the fixed parameters, Q^2 or M_x, is varied. If the mass increases than the threshold for producing a particle of that mass also increases which results in collapsing of the closed W-curves on the threshold point (see Figure 2.15). The effect of changing Q^2, for fixed W and M_x, is shown on the right panel of the same Figure. All the plots on Figures 2.13 through 2.15 were generated with 5^o increments of the proton scattering angle in the CM frame of the virtual photon-proton system which reflected the binning used in the data analysis.

2.7 Setup Materials Specifications

The specifications pertaining to the materials the experimental apparatus was composed of were later used to simulate the phenomena related to the passage through those materials of the detected particles. These phenomena included,

- multiple scattering,
- energy losses,
- external Bremsstrahlung.

Table 2.4 contains all necessary information to facilitate that task.

Table 2.4: *Material specifications of the experimemtal setup.* $\boldsymbol{\rho}$ *is the density,* **t** *is the thickness,* $\mathbf{X}_0$ *is the material specific radiation length while* $\mathbf{X} = \boldsymbol{\rho} \times \mathbf{t}$.

ITEM	Material	ρ (g/cm^3)	t (cm)	X/X_0 (%)
TARGET				
Upstream Window	Al 6061	2.70	0.0069	0.080
Target	Liquid H_2	0.0723	4.36	0.514
Downstream Window	Al 3004	2.70	0.0137	0.157
SOS				
Target Chamber Window	Al	2.70	0.0203	0.228
Target Chamber-SOS Gap	air	0.00121	15.0	0.05
Entrance Window	kevlar	0.74	0.0127	0.017
	mylar	1.39	0.0076	0.026
Exit Window	kevlar	0.74	0.0381	0.051
	mylar	1.39	0.0127	0.044
DC Windows	kapton	1.42	0.0088	0.031
DC Wires	W	19.3	12(0.0002)	12(0.057)
DC Gas	Ar/Ethane	0.0016	16.6	0.261
S1Y Hodoscope	polystyrene	1.03	1.098	2.58
S1X Hodoscope	polystyrene	1.03	1.04	2.45
Gas Čerenkov - Windows	Al	2.70	2(0.05)	1.12
Gas Čerenkov - Gas	Freon 12	0.00493	≈100.0	≈2.08
S2Y Hodoscope	polystyrene	1.03	1.098	2.58
Aerogel Čerenkov - Windows	Al	2.70	2(0.0625)	1.41
Aerogel Čerenkov	Aerogel	-	9.0	≈6.0
S2X Hodoscope	polystyrene	1.03	1.04	2.45
Lead Glass Calorimeter	TF1 lead glass	3.9	40.0	1540
HMS				
Target Chamber Window	Al	2.70	0.0406	0.457
Target Chamber-HMS Gap	air	0.00121	35.0	0.116
Entrance Window	kevlar	0.74	0.0381	0.051
	mylar	1.39	0.0127	0.044
Exit Window	kevlar	0.74	0.0381	0.051
	mylar	1.39	0.0127	0.044
DC Windows	mylar	1.39	4(0.0051)	4(0.018)
DC Wires	Al	2.70	0.0136	0.153
DC Gas	Ar/Ethane	0.0016	30.0	0.472
S1X Hodoscope	polystyrene	1.03	1.067	2.51
S1Y Hodoscope	polystyrene	1.03	1.067	2.51
Gas Čerenkov - Windows	Al	2.70	2(0.05)	2.29
Gas Čerenkov - Gas	N_2	0.00125	150.0	0.494
S2X Hodoscope	polystyrene	1.03	1.067	2.51
S2Y Hodoscope	polystyrene	1.03	1.067	2.51
Lead Glass Calorimeter	TF1 lead glass	3.9	40.0	1540

CHAPTER 3

MONTE CARLO SIMULATION

The Monte Carlo simulation of the experiment was an integral part of the analysis. It consisted of two parts, the first was capable of generating events pertaining to processes of interest, while the other simulated the response of the experimental apparatus to those processes. The latter included detailed modeling of the optics of both spectrometers, multiple scattering and energy losses due to passage through various materials. This part was a combination of two stand-alone, single-arm simulations for the HMS and SOS spectrometers. The event generation modeled vector meson production, electroproduction phase space as well as the ${}^{1}H(e,e'p)$ elastic scattering. This chapter contains a detailed discussion of the Monte Carlo simulation.

3.1 Simulation Overview

The simulation began with defining the kinematics for an event. This was achieved by generating coordinates of a point in the volume spanned by geometrical and kinematical variables described below. Knowing the kinematics and the position of the interaction vertex, the electron and the proton, for the given event, were propagated through the optical elements and the detectors of the spectrometers. Passing of both particles through the fiducial regions of the drift chambers and the hodoscopes of their respective spectrometers constituted a valid coincidence event. For each coincidence event the relevant physics quantities were reconstructed. After generating a required number of such events, typically 250k per process, the simulation terminated.

3.1.1 Modeled Processes

The Monte Carlo aimed at providing a detailed model of the electroproduction of the ω meson on a hydrogen target

$$e + p \quad \longrightarrow \quad e' + p + \omega \tag{3.1}$$

It also simulated reactions giving rise to background for 3.1. These processes were, at first, classified into ones having, in addition to the proton and the electron, only one particle left behind in the final state and the ones with multiparticle final states. There was only one process of the first kind, namely ρ^0 production, that was kinematcally accessible and generation of which paralleled that of the ω,

$$e + p \quad \longrightarrow \quad e' + p + \rho^0 \tag{3.2}$$

The second class consisted of a wide variety of reactions collectively treated as Lorentz invariant electroproduction phase space. In this two-body process, as a result of arbitrary distribution of energy and momentum among the particles in the final state, a ficticious particle of an arbitrary mass, permitted by the conservation laws, was created

$$e + p \quad \longrightarrow \quad e' + p + X \tag{3.3}$$

Finally, for validation and testing purposes, the elastic reactions ${}^1H(e,e')p$ and ${}^1H(e,e'p)$ were also modeled.

3.1.2 Choice of the Generation Volume

In order to fully specify a coincidence event for a given energy of the incident electrons one has to pick the coordinates of the interaction vertex in the target frame (as defined on page 10 in Section 1.2.1) within the interaction volume defined by the target length and the raster amplitudes. This, along with multiple scattering and ionization energy loss, accounted for the extendedness of the target. To complete the event one is free to pick another six independent quantities describing the final state. This sextuple will always be refered to as the ***Generation Volume***.

The choice of the set of variables to build an event from was closely related to the nature of the simulated processes. These included the production of the two vector mesons, ω and ρ^0, as well as the electroproduction phase space. Vector meson masses needed to be generated according to the Breit-Wigner distribution while the phase space mass was assumed to be distributed uniformly. Therefore the missing mass M_x was included in the generation volume. Sometimes it is convenient to express the cross section as differential in the Lorentz-invariant momentum transfer Q^2 and CM energy W, those variables were chosen. Ω_x^{CM} was selected since the ultimate goal was the extraction of the cross section as a function of the scattering angle in the center-of-mass system θ_x^{CM}. The azimuthal angle of the scattered electron, $\phi_{e'}$, naturally completes this set.

The whole simulation process can be divided into three distinct parts:

event generation: the kinematics of an event at the vertex was defined and on that basis the model cross sections were calculated, modification of the kinematics due to radiative effects took place and a corresponding multiplicative weighting was computed,

event propagation: extended target phenomena, including multiple scattering and ionization energy losses incurred during traversing the target material and its windows (for the specifications see Table 2.4 on page 68), were accounted for and the particles were propagated through the spectrometers and their detectors, where again the multiple scattering and energy loss phenomena were simulated (for the list of materials encountered by the detected particles see Table 2.4 on page 68),

event reconstruction: in case of a valid coincidence event, the momentum vectors of the electron and proton were reconstructed, enabling the calculation of all relevant kinematical quantities.

3.2 Event Generation

Generating a complete event proceeded in two stages. The kinematics of the event was generated first and then, on that basis, the dynamics of the event was computed.

3.2.1 Kinematics

For each event, the kinematics was defined the following way

1. since the generation volume did not coincide with the spectrometer detection volume (refer to page 9 for definition), acceptance limits, in Q^2, W, $\phi_{e'}$ and M_x, were calculated based on the initial input information (spectrometers central angles and momenta) and the details of the experimental configuration (dimensions of both collimators - see Figure 2.6 and Figure 2.9) in order to avoid generating events in parts of the phase space not accessible to the measurement; the limits of the generation were chosen to be appropriately larger than the detection volume to well accomodate the Bremsstrahlung related effects and also to ensure that the detection volume was well populated,

2. coordinates of the interaction point - vertex - $(x_{ver}, y_{ver}, z_{ver})$ were picked, as mentioned earlier, within a volume defined by the target length and the fast raster amplitudes. Transvere coordinates x_{ver}, y_{ver} were chosen in accord with the fast raster signals (see Section 2.2) while the longitudinal coordinate z_{ver} was generated randomly over the length of the target,

3. invariant quantities Q^2, W along with $\phi_{e'}$ were generated uniformly over the entire acceptance calculated in **1.**,

4. missing mass M_x was chosen either according to the relativistic Breit-Wigner distribution (with 100% efficiency), in the case of vector mesons ω and ρ^0 or, in the case of the phase space, was generated uniformly, and discriminated against the threshold $(M_x \leq W - M_p)$; in the ω case this way of generating its mass also ensured the proper integration over its line shape in extracting the cross section (refer to Section "Cross Section Reduction" in the Appendix A),

5. energy E_γ of a real photons emitted by the incident electron was chosen, (again with 100% efficiency) according to the inverse power distribution $(1/E_\gamma^x)$ predicted by the Bremsstrahlung calculations (see 3.39),

6. the angles θ_x^{CM} and ϕ_x^{CM} were chosen in such a way that Ω_x^{CM} be populated isotropically, what amounted to generating uniformly ϕ_x^{CM} and $\cos(\theta_x^{CM})$,

7. energy E'_γ of real photons emitted by the emergent electron was simulated with 100% efficiency according to the inverse power distribution (see 3.39), and that concluded the generating of the event kinematics.

$Q^2, W, \phi_{e'}, E_\gamma$ and E'_γ specified the electron momentum vector in the target system which then was transformed to the HMS frame (as defined on page 10 in Section 1.2.1) for subsequent propagation through the optical elements and detectors of this spectrometer.
This set of variables also defined the virtual photon 4-momentum vector thus providing the z-direction of the Center-of-Momentum (CM) frame of the virtual photon proton system and, along with the target mass, specifying the Lorentz boost between target and CM frames.

The proton momentum vector in the CM was found by the use of energy and momentum conservation after $\cos\theta_x^{CM}, \phi_x^{CM}, M_x$ and W were picked. It was then boosted back to the target system, transformed to the SOS frame (as defined on page 10 in Section 1.2.1) to allow for propagation through the magnetic elements and detectors of the SOS spectrometer.

3.2.2 Dynamics

Events pertaining to a given process were also characterized by the appropriate cross section, which was computed on an event-by-event basis and those were used in the subsequent analysis as weights. These calculations were performed in the framework of conventional two-particle coincidence cross section (Akerlof et al., 1969)

$$\frac{d\sigma}{dp_{e'} d\Omega_{e'} d\Omega_x^{CM} dM_x} = \Gamma_T(E, E', \theta_{e'}) \frac{d\sigma_v}{d\Omega_x^{CM} dM_x} \tag{3.4}$$

where Γ_T is the virtual photon flux (as defined in the Section 1.2.2 - see Eqn 1.22). The cross section 3.4 is differential in variables spanning the electron spectrometer phase space, it is therefore necessary to transform it to variables of the generation volume. This is readily achieved by the use of the appropriate Jacobian.

$$\frac{d\sigma}{dQ^2 dW d\phi_{e'} d\Omega_x^{CM} dM_x} = \Gamma_T(E, Q^2, W) \frac{d\sigma_v}{d\Omega_x^{CM} dM_x} \tag{3.5}$$

where the Jacobian for the transformation $(E', \theta_{e'}) \longrightarrow (Q^2, W)$ (for the expression see Appendix A) was absorbed into the virtual photon flux factor. Since the model cross sections for the ω and ρ^0 were formulated in terms of t instead of $\cos\theta_x^{CM}$ therefore a Jacobian correcting for that needed to be applied (see Appendix A), so eventually

$$\frac{d\sigma}{dQ^2 dW d\phi_{e'} d\Omega_x^{CM} dM_x} = \Gamma_T(E, Q^2, W) \left(\frac{dt}{d\,\cos\theta_x^{CM}}\right) \left(\frac{d\sigma_v}{dt dM_x}\right) \tag{3.6}$$

was the starting point for introducing the dynamics of the vector meson electroproduction while the expression 3.5 was the basis for the phase space behavior. In the equation 3.6 the dependence on ϕ_x^{CM} was assumed to be negligibly small therefore it only amounted to a multiplicative factor, appearing in all applications both in the numerator and denominator, so that part was dropped altogether from this and any subsequent expressions.

ω Model

The cross section for the ω meson was calculated in the framework of Vector Dominance Model and included contributions from one pion exchange and pomeron exchange and was differential in 4-momentum transfer t.

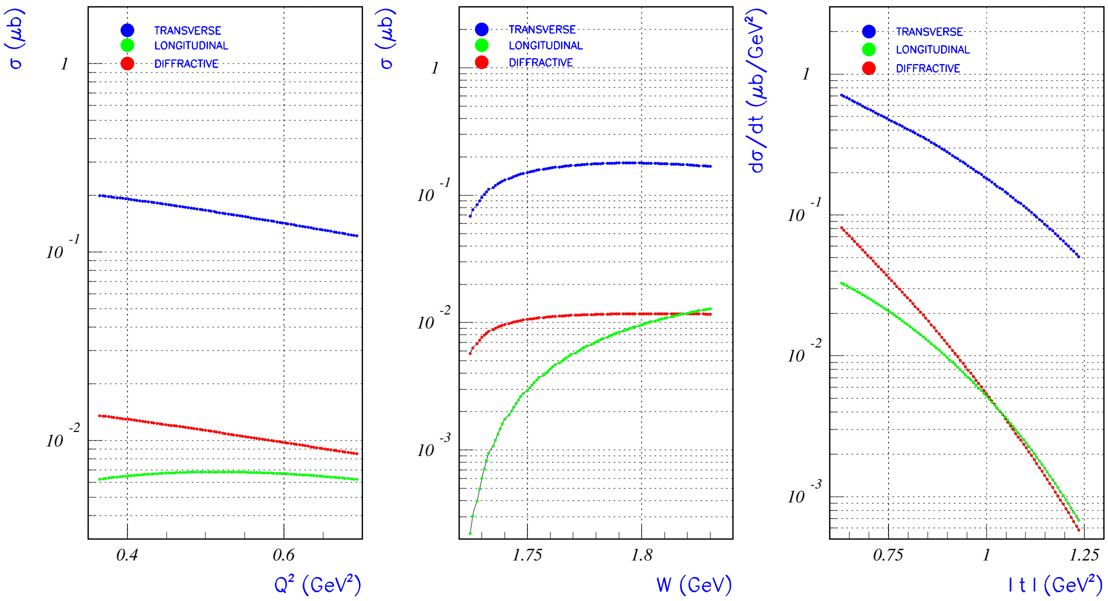

Figure 3.1: ***The ω Cross Section Model:*** *The dependences of different model cross section contributions on the kinematical variables t, W, and Q^2 over the acceptance of the apparatus in these variables for a single setting.*

The one pion exchange (OPE) contribution was expressed as

$$\frac{d\sigma_v}{dt} = \sigma_T^{\pi}(Q^2, W, t) + \epsilon\, \sigma_L^{\pi}(Q^2, W, t) \qquad (3.7)$$

and σ_T^π, σ_L^π were obtained using covariant polarization vectors (Fraas & Schildknecht, 1969; Fraas, 1971) and are given by

$$\sigma_T^\pi = \frac{1}{p(Q^2)\,p(0)\,W^2} G^2 \frac{\Lambda^2_{\omega\pi}}{16} \frac{-t}{(t-m_\pi^2)^2} \frac{1}{\left(1+\frac{Q^2}{m_\rho^2}\right)^2} \frac{4(B+C)^2 - 2Q^2N_3^2}{4(-C)} F_N F_\omega \tag{3.8}$$

$$\sigma_L^\pi = \frac{1}{p(Q^2)\,p(0)\,W^2} G^2 \frac{\Lambda^2_{\omega\pi}}{16} \frac{-t}{(t-m_\pi^2)^2} \frac{1}{\left(1+\frac{Q^2}{m_\rho^2}\right)^2} \frac{Q^2N_3^2}{(-C)} F_N F_\omega \tag{3.9}$$

where $G = \sqrt{14.6}$ is the pion-nucleon coupling,

$$\Lambda^2_{\omega\pi} = 96\pi \left(\frac{M_\omega}{M_\omega^2 - M_\pi^2}\right)^3 \Gamma_{\omega\pi\gamma} \tag{3.10}$$

with $\Gamma_{\omega\pi\gamma} = 0.9$ MeV (Joos et al., 1977) being the $\omega \to \pi\gamma$ partial width. $p(0)$ and $p(Q^2)$ are the real and virtual photon momenta as seen from the hadron Center-Of-Momentum frame. F_N and F_ω are Benecke-Dürr (Benecke & Dürr, 1968; Wolf, 1972) form-factors introduced after P. Joos (Joos et al., 1977). The quantities B, C and N_3 are defined in the following way

$$B = -\frac{1}{2}Q^2(t-2M_p^2) + \frac{1}{4}(M_p^2 - Q^2 - W^2)(M_p^2 - M_\omega^2 - W^2 - t) \tag{3.11}$$

$$C = -\frac{1}{4}[(W-M_p)^2 + Q^2][(W+M_p)^2 + Q^2] \tag{3.12}$$

$$N_3 = \frac{1}{2}[W^2tu - t(M_p^2 + Q^2)(M_p^2 - M_\omega^2) - M_p^2(Q^2 + M_\omega^2)^2]^{1/2} \tag{3.13}$$

The diffractive cross section was normalized to fit the *SLAC-LBL-Tufts* ω production data (Ballam et al., 1973) at the $Q^2 = 0$ and is given by

$$\frac{d\sigma_D}{dt} = \frac{p(0)}{p(Q^2)} \left(1 + 0.4\frac{Q^2}{M_\rho^2}\right) De^{bt} \tag{3.14}$$

where, as in the ρ^0 case, D was a function of W and Q^2

$$D \;=\; \frac{9.3\left(\frac{1.4}{E_\gamma}+1\right)}{(1+\frac{Q^2}{M_x^2})^2} \tag{3.15}$$

with $E_\gamma = (W^2 - M_p^2)/2M_p$ and $b = 6.7$ GeV^{-2}.

This pomeron exchange (diffractive) contribution was typically one order of magnitude lower than the OPE contribution (see Figure 3.1) therefore it did not play any role in cross section extraction even though it was implemented in the code. The final ω meson description was given by

$$\frac{d\sigma_v}{d\Omega_x^{CM} dM_x} = \left(\frac{1}{\pi}\frac{M_\omega\Gamma_\omega}{(M_x^2 - M_\omega^2)^2 + M_\omega^2\Gamma_\omega^2}\right)(\sigma_T^\pi + \epsilon\,\sigma_L^\pi) \tag{3.16}$$

with $M_\omega = 781.94$ MeV and $\Gamma_\omega = 8.41$ MeV (Caso et al., 1998).

ρ^0 Model

In the case of the ρ^0 meson all the results indicate that the reaction is purely diffractive, so that the cross section was assumed to be of the form

$$\frac{d\sigma_v}{dt} = \sigma_D(Q^2, W, t) = De^{bt'} \tag{3.17}$$

where $t' = t - t_{min}$ with t_{min} being the momentum transfer when the scattering occurs along the initial virtual photon direction. D and b (called the exponential slope) are functions of Q^2 and W. D is in fact the photoproduction cross section, with the form suggested by Wolf (Wolf, 1971) (see eqn 3.19). The Q^2 dependence was introduced by the square of the ρ^0 propagator

$$D(Q^2, W) = \frac{\sigma_\rho(Q^2 = 0, W)}{\left(1 + \frac{Q^2}{M_x^2}\right)^2} \tag{3.18}$$

$$\sigma_\rho(Q^2 = 0, W) = \frac{29.4}{E_\gamma} + 9.5 \tag{3.19}$$

$$E_\gamma = \frac{W^2 - M_p^2}{2M_p} \tag{3.20}$$

The exponential slope was parametrized in terms of W and Q^2 to reflect its complex dependence on these variables near threshold (Dunne, 1998),

$$b(Q^2, W) = A\,Q^2 + B\sqrt{Q^2} + C \tag{3.21}$$

$$A = 0.6\,W^2 - 3.62\,W + 5.64 \tag{3.22}$$

$$B = -2.58\,W^2 + 14.93\,W - 23.21 \tag{3.23}$$

$$C = 1.1\,W + 2.6 \tag{3.24}$$

The Söding Model (Söding, 1966) that accounts for the skewing of the ρ^0 meson due to the interference between resonant and non-resonant pion pair production was also implemented. The simple parametrization of this model was adopted in which the distributions of the ρ^0 were weighted by the $(M_\rho/M_x)^n$, with M_x being the mass of the ρ^0 meson for a given event reconstructed from the momenta of the scattered electron (e') and proton (p) while $M_\rho = 768.1$ MeV (Caso et al., 1998).

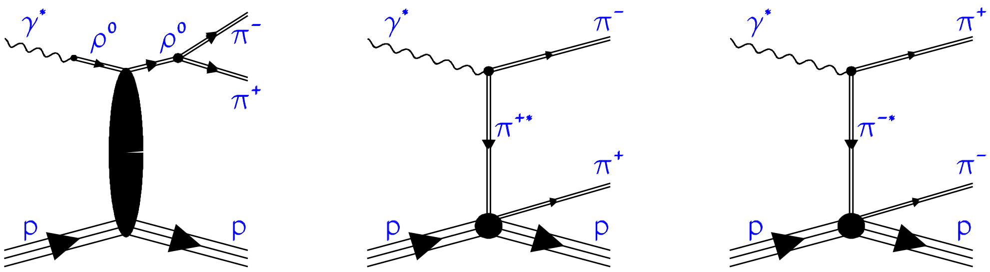

Figure 3.2: ***Söding Model:*** *Resonant and non-resonant pion pair production.*

This parametrization has proved to give an adequate description of the mass shape in photoproduction (Ballam et al., 1972). Previous results from *DESY* (1977) suggested that for the range of W and Q^2 in the present work the exponent should be equal to $n = 5.2$. This value of n was used throughout the background subtraction procedure.

Eventually, the ρ^0 meson production cross section was given by

$$\frac{d\sigma_v}{d\Omega_x^{CM} dM_x} = \left(\frac{M_\rho}{M_x}\right)^n \left(\frac{1}{\pi} \frac{M_\rho \Gamma_\rho}{(M_x^2 - M_\rho^2)^2 + M_\rho^2 \Gamma_\rho^2}\right) De^{bt'} \tag{3.25}$$

with $\Gamma_\rho = 150.7$ MeV (Caso et al., 1998)

Phase Space

Initially the phase space was generated in a non-invariant manner to facilitate a fit in one variable, namely M_x. However, the inspection of other kinematical variables, especially t (see Appendix C for details and Figure 3.3), quickly revealed problems with this approach. The fit was modified to include all relevant kinematical quantities, such as M_x, t, Q^2, W and θ^{CM}, and it proved necessary to start from a Lorentz-invariant phase space factor in deriving the weights that should be applied to phase space events (see Appendix C).

The distributions of those events were generated assuming that the underlying cross section was given by

$$\frac{d\sigma_v}{d\Omega_x^{CM} dM_x} = \frac{1}{16\pi^2} \frac{1}{W\, |\vec{q}^{\,CM}|} \left(\frac{d^2 R_2}{d\Omega_x dM_x}\right) \tag{3.26}$$

which is a conventional differential cross section for a 2-body process in their Center-Of-Momentum frame in the case where $|< f\,|\,T\,|\,i >|^2 = 1$.

Making use of C.28 (see Appendix C for the derivation) the phase space cross section becomes

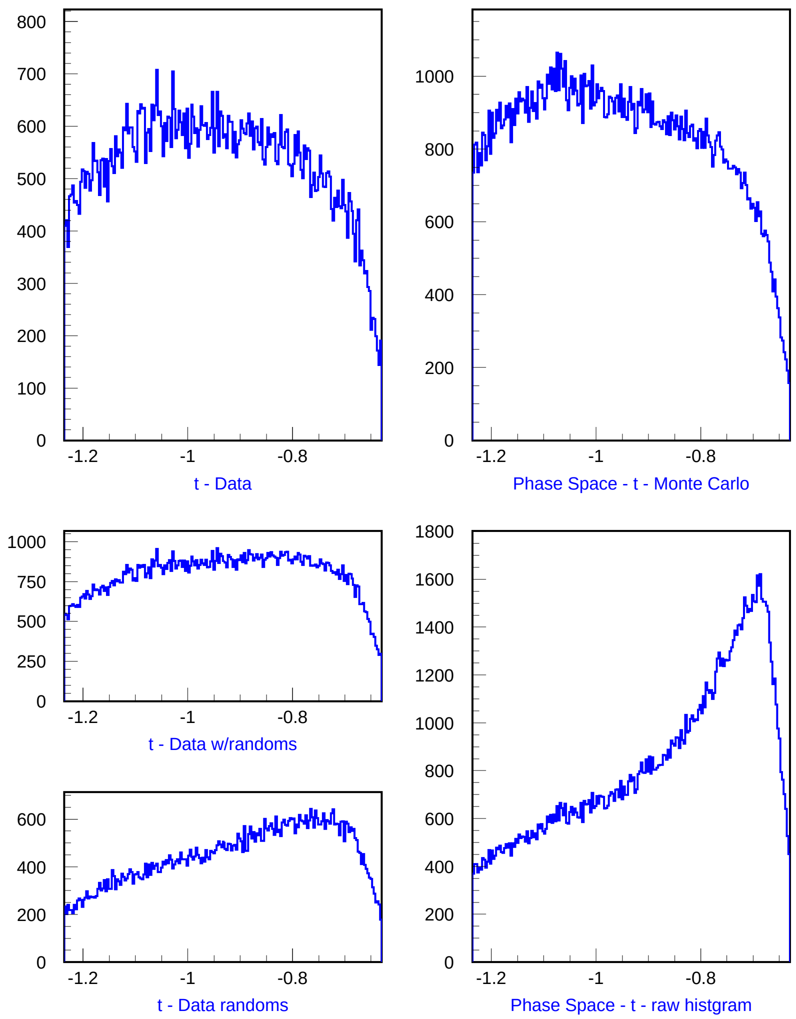

Figure 3.3: ***Phase Space Distributions***: *The left column represents the data while the right one the Monte Carlo. The plot on the left top panel corresponds to the randoms subtracted data distribution. Two plots below the top one correspond to the raw histogram and randoms. The right top plot shows how the application of the derived weights (see Eqn 3.27) changes the shape of the phase space distribution generated according to the noninvariant prescription - right bottom plot. It must be noted that data distributions contain signal plus background (with roughly 1:4 signal to background ratio) while the Monte Carlo is pure phase space. Also, worth noting is the fact that distribution of random events does not provide any insight into how the phase space looks like.*

$$\frac{d\sigma_v}{d\Omega_x^{CM} dM_x} = \frac{1}{32\pi^2} \frac{M_x}{|\vec{q}^{\,CM}|} \frac{p_x^{CM}}{W^2} \tag{3.27}$$

3.3 Event Propagation

After an interaction occured the event entered the propagation stage, which would include simulating effects of multiple scattering, ionization energy losses and propagation through the magnetic fields of the spectrometers.

3.3.1 Multiple Scattering

Emergent electrons and protons underwent multiple scattering while traversing various materials in the target and spectrometers. This phenomenon was simulated by smearing the track slopes in either xz or yz planes (for definition see Figure 1.5) with Gaussians having width θ_0, in the sense of small angle approximation:

$$\begin{aligned} \left(\tfrac{dx}{dz}\right)' &= \tfrac{dx}{dz} + g_1\,\theta_0 \qquad (xz - \text{plane}) \\ \left(\tfrac{dy}{dz}\right)' &= \tfrac{dy}{dz} + g_2\,\theta_0 \qquad (yz - \text{plane}) \end{aligned} \tag{3.28}$$

where g_1 and g_2 are normal deviates distributed around zero with unit standard deviation ($\mu = 0.0$ and $\sigma = 1.0$). The width θ_0 was given by

$$\theta_0 = \frac{0.0136\ \mathrm{GeV}}{\beta cp}\sqrt{\frac{x}{X_0}}\left[1 + 0.088\ \ln\left(\frac{x}{X_0}\right)\right] \tag{3.29}$$

and comes from the fit to Molière distribution of singly charged particles with $\beta = 1$ for all Z, and is accurate to 11% or better for radiation lengths x/X_0 ranging from 10^{-3} to 100. βcp is the product of the velocity and momentum of the particle in question (Caso et al., 1998).

3.3.2 Ionization Energy Losses

The energy losses of the electron and proton due to ionization within the target were also accounted for. The mean energy loss for the proton was computed using the Bethe-Bloch formula in a heavy projectile limit (Leo, 1994),

$$-\frac{dE}{dx} = 0.3071\ \frac{Z}{A}\frac{1}{\beta^2}\left[\ln\left(\frac{2m_e c^2\beta^2}{I(1-\beta^2)}\right) - \beta^2\right] \tag{3.30}$$

where dE/dx is expressed in $\mathrm{MeVg^{-1}cm^2}$ and the mean excitation potential was parametrized in terms of the atomic number Z,

$$\begin{aligned} I &= Z(12 + 7Z^{-1}) \qquad Z < 13 \\ I &= Z(9.76 + 58.8Z^{-1.19}) \qquad Z \geq 13 \end{aligned} \tag{3.31}$$

In the case of the electron the mean energy loss was estimated based on a relativistic approximation of the Bethe-Bloch formula (Leo, 1994),

$$-\frac{dE}{dx} = 0.3071\,\frac{Z}{A}\frac{1}{2}\left[\ln\left(\frac{t}{\rho}\right) + 19.26\right] \tag{3.32}$$

where t is the thickness of the material in g/cm^2 and ρ is its density in g/cm^3.

3.3.3 Spectrometer Models

As the particles left the scattering chamber they were transported through the magnetic fields of their respective spectrometers unless their tracks did not pass through either spectrometer aperture, defined by the geometry of large colimators. After checking the position of either particle against the octogonal colimator slits (for both spectrometers, the entrance and the exit of the slit were located 1.262m and 1.325m away from the pivot respectively), transporting proceeded in either sequential or nonsequential manner. To simulate collimation by the magnets check points were set up at the entrance and the exit of each magnet and additionally at the places where the transverse size of the beam was expected to be the largest - midplane of the SOS quadrupole and 2/3 of first two HMS quadrupoles. At these points, where the positions of the particle were checked against real magnet boundaries, the particles were transported using

- eight 6^{th} order sequential transformations (each transformation began where the previous one ended starting from the pivot), in the case of the SOS,

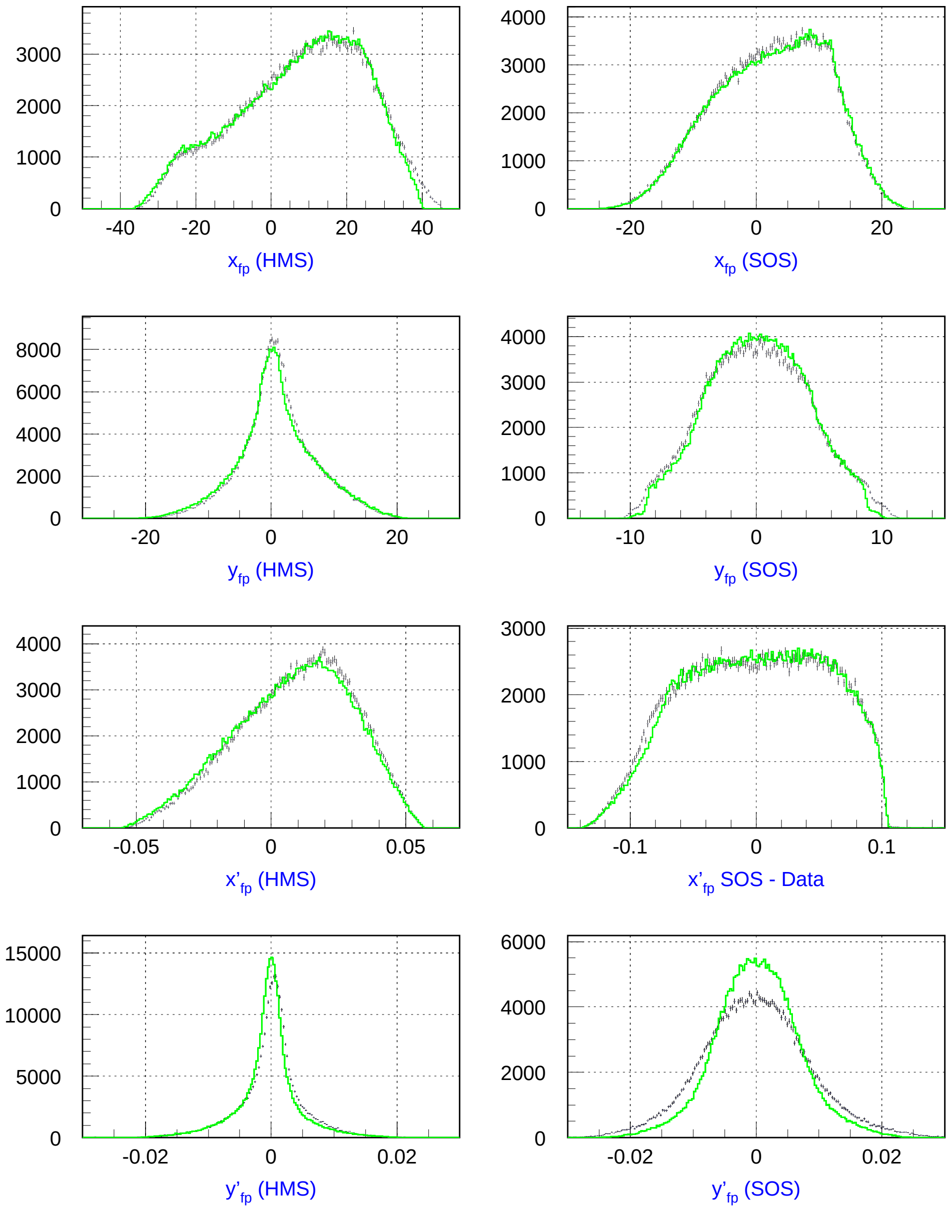

Figure 3.4: ***Data/Monte Carlo Comparison: Event Propagation.*** *Focal Plane Quantities. The data is in black (points) with statistical error bars, full Monte Carlo distribution is in green (solid line) and includes: the ω meson, the ρ^0 meson and the phase space.*

- eleven 5^{th} order nonsequential transformations (each transformation began at the pivot), in the case of the HMS

with each transformation given by

$$q^i_{out} = \sum_{j,k,l,m,n=0}^{N} F^i_{jklm}(x_{in})^j(y_{in})^k(x'_{in})^l(y'_{in})^m(\delta p)^n \tag{3.33}$$

where $q^i_{out} = (x_{out}, y_{out}, x'_{out}, y'_{out})$ are the positions and slopes of the particle's track after each step. The fractional momentum δp remained unchanged by the transformations. The sets of expansion coefficients F^i_{jklm}, called forward maps, were generated using the *COSY INFINITY* (Berz, 1990). This program is capable of simulating the magnetic fields of the existing optical configuration of the spectrometers. N is the order of the expansion. The final step yielded the location and orientation of either particle's track at the focal plane of its spectrometer. To simulate the finite resolution of the wire chambers track positions were smeared by Gaussian distributions with the measured resolution of the wire chambers. As the tracks are projected through the spectrometer huts fiducial cuts on detector sizes were applied. A valid coincidence event was formed by an electron-proton pair for which the tracks met the wire chambers and hodoscopes fiducial cuts. For such an event the smeared track positions were fitted to a straight line to give final focal plane positions and slopes of the particle trajectory. That concluded the propagation of the event.

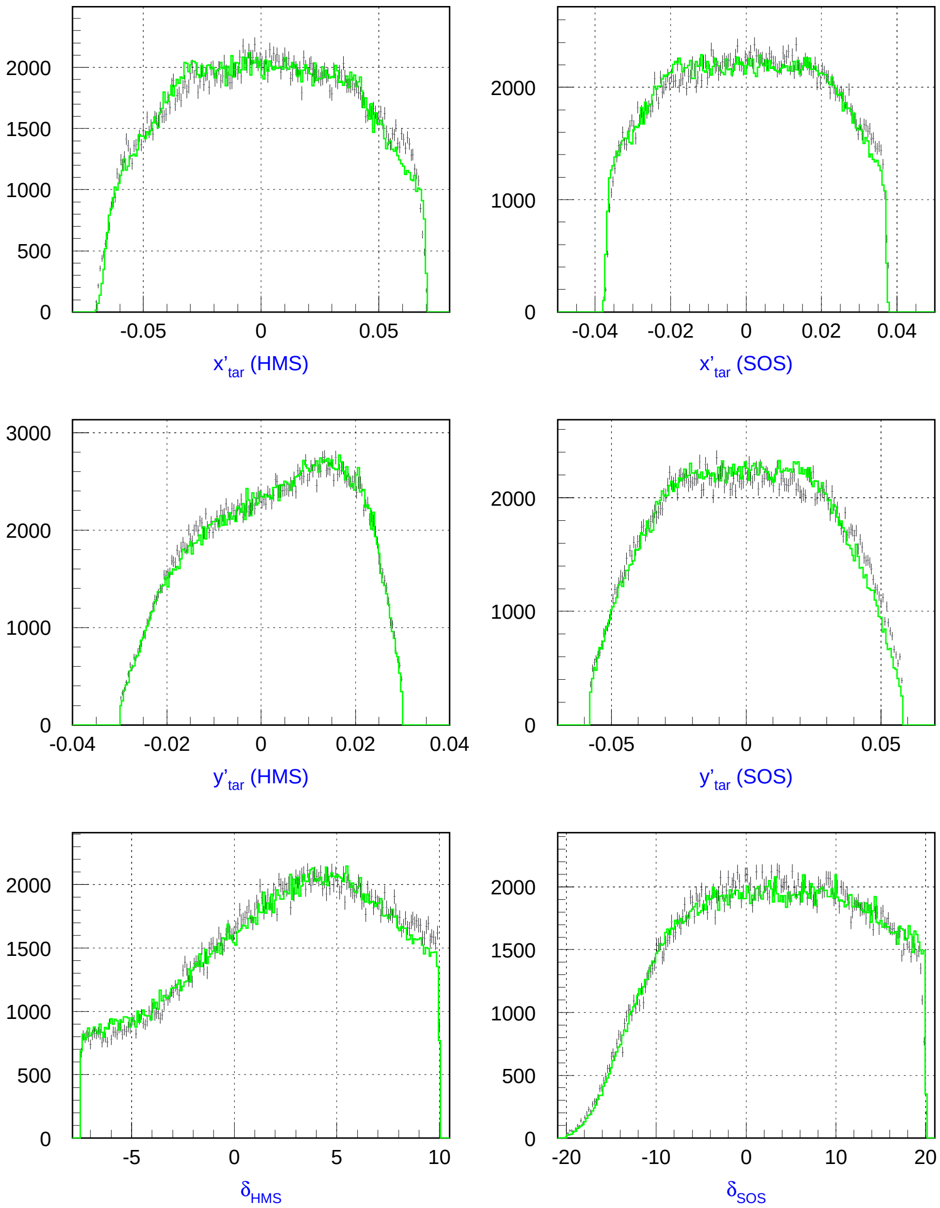

Figure 3.5: ***Data/Monte Carlo Comparison: Event Reconstruction.*** *Target Quantities. The data is in black (points) with statistical error bars, full Monte Carlo distribution is in green (solid line) and includes: the ω meson, the ρ^0 meson and the phase space.*

3.4 Event Reconstruction

Once the focal plane quantities were established for the event its reconstruction began with performing one step transformation to the target quantities, via an expansion similar to the forward one,

$$q^i_{tar} = \sum_{j,k,l,m=0}^{N} R^i_{jklm} (x_{fp})^j (y_{fp})^k (x'_{fp})^l (y'_{fp})^m \tag{3.34}$$

whose coefficients, R^i_{jklm}, called reconstruction matrix elements, were again generated by *COSY INFINITY* program and $q^i_{tar} = (\delta p, y_{tar}, x'_{tar}, y'_{tar})$ are the reconstructed target quantities. Knowing the slopes of the track and the magnitude of the momenta at the interaction vertex one was able to find the components of momentum vectors in the target frame of reference. Combining the results for both spectrometers yields the kinematical quantities, such as Q^2, W, M_x, *etc.*, needed in further analysis.

3.5 Elastic Scattering

A separate goal of the simulation was to reproduce elastic scattering results, which are well known, as a proof of its validity. The exclusive elastic scattering $^1H(e, e'p)$ was also used for testing of the optical part of the Monte Carlo. The Rosenbluth formula provided the dynamical description of this process,

$$\frac{d\sigma}{d\Omega_{e'}} = \frac{\alpha^2 \cos^2(\theta_{e'}/2)}{4E^2 \sin^4(\theta_{e'}/2)} \frac{E}{E'} \left(\frac{G_{Ep}^2 + \tau G_{Mp}^2}{1+\tau} + 2\tau G_{Mp}^2 \tan^2(\theta_{e'}/2) \right) \tag{3.35}$$

where $\tau = Q^2/4M_p^2$ and G_{Ep}, G_{Mp} are Sachs form factors for the proton. The G_{Ep}, G_{Mp} were taken to be of the dipole form,

$$G_{Ep} = \frac{1}{\left(1 + \frac{Q^2}{0.71}\right)^2} = \frac{1}{\mu} G_{Mp}. \tag{3.36}$$

For the several runs taken during the SOS δ-scan the data yield was compared to the simulated yield. The results are shown in Figure 3.6.

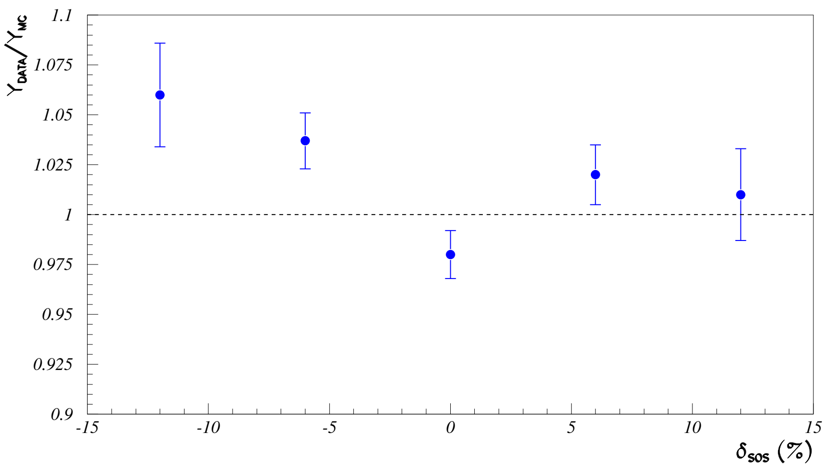

Figure 3.6: ***Elastic Scattering:*** *Comparison of the data and the Monte Carlo yields. The data were taken during the SOS δ-scan.*

3.6 Radiative Processes

The process 3.1, diagramatically represented on the Figure 3.7, is not directly accesible to the measurement. It is mandatory to take into account other (higher order) processes occuring during the primary reaction. These processes are collectively known as the radiative processes (Bremsstrahlung) and can be classified as follows,

external Bremsstrahlung: some energy (real photons) may be radiated by charged particles, taking part in the interaction, in the fields of the nuclei not directly involved in the hard scattering, regardless of whether the particles are incoming or outgoing, this amounts to incoherent summation of appropriate amplitudes,

soft internal Bremsstrahlung: similarily, some number of real (soft) photons may be emitted during the primary scattering process (see Figure 3.8), which amounts to coherent summation of appropriate amplitudes leading to interference terms,

hard internal Bremsstrahlung: finally, also virtual (hard) photons may be emitted and absorbed as shown in Figure 3.9 for the vertex correction and loop diagrams.

3.6.1 Radiative Corrections

This work closely followed the procedure of correcting for radiative processes presented in C.S. Armstrong Ph.D. thesis (Armstrong, 1998) that relied on the results of Wasson *et al.* extensively discussed in papers (Makins, 1994; Wasson, Ent, Makins et al., 1998).

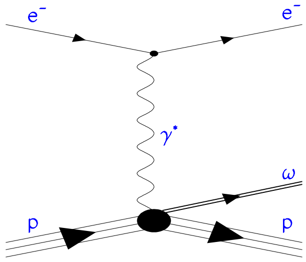

Figure 3.7: ***The ω Electroproduction:*** *First order Feynman diagram - Born term.*

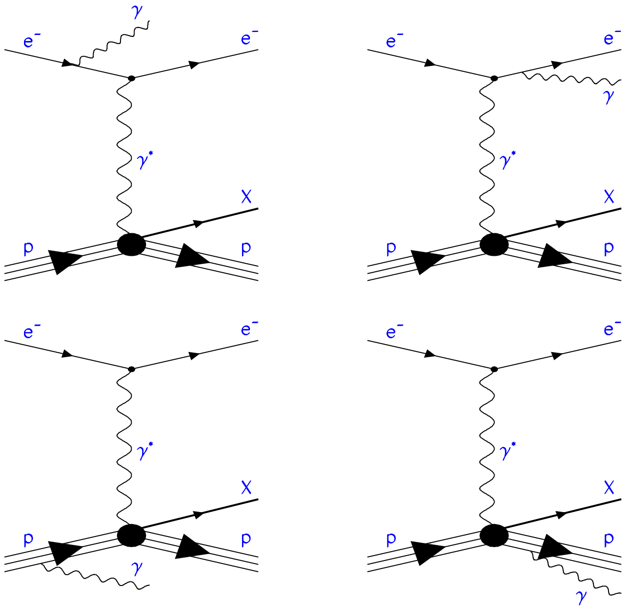

Figure 3.8: ***Radiative Processes:*** *Second order Feynman diagrams for the internal soft Bremsstrahlung corrections (real photons). For the purpose of this analysis only the top two diagrams were implemented.*

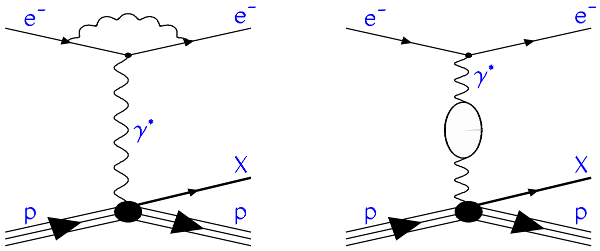

Figure 3.9: ***Radiative Processes:*** *Feynman diagrams for the internal hard Bremsstrahlung corrections (virtual photons).*

There are two aspects of introducing radiative processes in the Monte Carlo simulation apart from the approach adopted in calculating their effects. The first is the fact that radiating a real photon (internal soft Bremsstrahlung) will alter the event kinematics shifting it into or out of the bin of interest changing the cross section for that bin. A multiplicative factor, after appropriate approximations have been made, will have be applied to modify this cross section. The other is that processes involving virtual photons (internal hard Bremsstrahlung) do not change the event kinematics amounting only to the scaling of the cross section being extracted. In order to obtain the Born-level cross section, the one of interest, the radiated cross section had to be integrated over real photon energies. Working in the framework of the soft photon approximation, that assumes that the energy of emitted real photon is just a small fraction of the energy of the particle emitting it, and the extended peaking approximation, for which the angular distribution becomes discrete,

$$A(\Omega_\gamma) = \lambda\,\delta(\hat{\boldsymbol{\gamma}} - \hat{\boldsymbol{k}}) + \lambda'\,\delta(\hat{\boldsymbol{\gamma}} - \hat{\boldsymbol{k}}') + \lambda_p\,\delta(\hat{\boldsymbol{\gamma}} - \hat{\boldsymbol{p}}) \tag{3.37}$$

and defined by the directions of incoming electron ($\hat{\boldsymbol{k}}$) and outgoing electron ($\hat{\boldsymbol{k}}'$) and proton ($\hat{\boldsymbol{p}}$) (with $\hat{\boldsymbol{\gamma}}$ being the direction of the radiated photon), the problem simplifies dramatically.

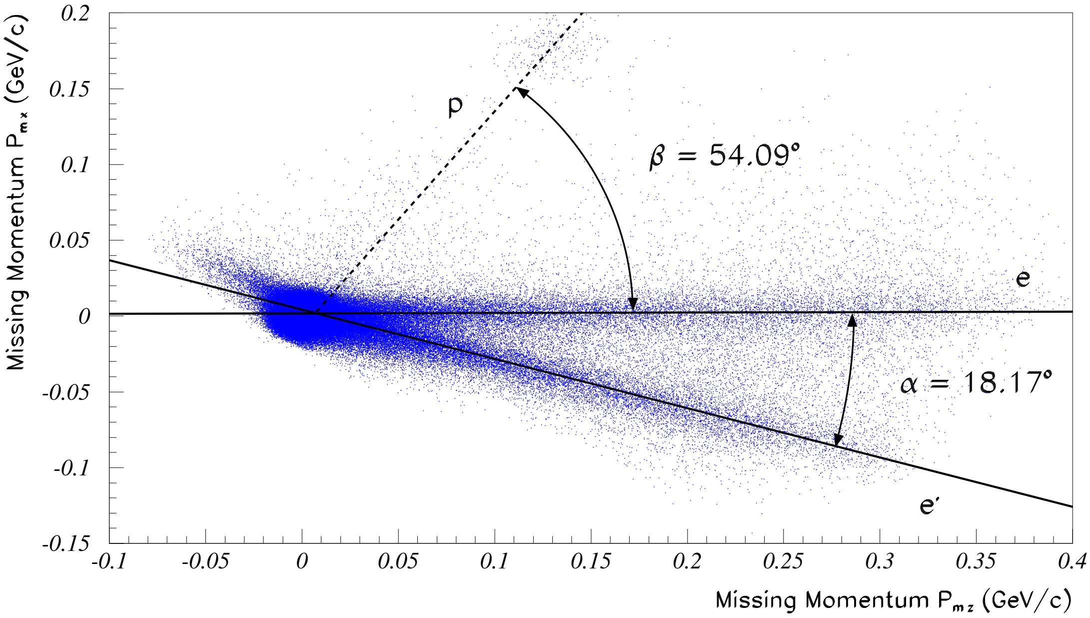

Figure 3.10: ***Peaking Approximation:*** *Missing momentum P_m is decomposed into components in the target frame where z direction is along the beam direction (P_{mz}) and x is the horizontal transverse direction (P_{mx}), xz plane coincides with the Hall C floor plane. The data shown on the plot comes from the SOS δ scan for which the electron arm was located 18.45^o off the z-direction (for the layout of Hall C refer to Figure 2.2). The radiative tails visible on the plot extend along the beam direction and at roughly 18.45^o off that direction. These are the directions of the incoming and outgoing electrons. There is no prominent tail in the direction of the outgoing proton which should sit 54.09^o to the right of the beam. Nevertheless there is some concentration of events along that direction.*

Therefore the integration, where the proton contribution was left out as negligible, can be carried out,

$$\frac{d\sigma^{(Born)}}{dp_{e'}d\Omega_{e'}d\Omega_x^{CM}dM_x} = \int_{E_\gamma^{min}}^{E_\gamma^{max}}\int_{E_\gamma'^{\,min}}^{E_\gamma'^{\,max}} \frac{d\sigma}{dp_{e'}d\Omega_{e'}d\Omega_x^{CM}dM_x dE_\gamma dE_\gamma'} dE_\gamma dE_\gamma' \tag{3.38}$$

where E_γ and E_γ' are the total energies lost via emission of Bremsstrahlung photons by incident and emergent electrons respectively regardless of the creation mechanism (either external or internal). The equation 3.38 can be simplified to

$$\frac{d\sigma^{(Born)}}{dp_{e'}d\Omega_{e'}d\Omega_x^{CM}dM_x} = \int_{\Delta E} M_{\text{corr}}\left(\frac{1}{E_\gamma^x}\right)\left(\frac{1}{E_\gamma'^{\,x}}\right)\frac{d\sigma^{(Born)}}{dp_{e'}d\Omega_{e'}d\Omega_x^{CM}dM_x} dE_\gamma dE_\gamma' \tag{3.39}$$

where the identification $\Delta E \equiv [E_\gamma^{min}, E_\gamma^{max}] \times [E_\gamma'^{\,min}, E_\gamma'^{\,max}]$ has been made as well as $x = 1 - \lambda - bt$ and $y = 1 - \lambda' - (bt)'$. The λ's here are strengths pertaining to soft internal processes, calculated including the interference terms (therefore *extended*), while the material thicknesses bt's play the similar role in the case of the external processes. Finally, the multiplicative correction factor M_{corr} is given by

$$M_{\text{corr}} = (1 - \delta_{\text{hard}})M_{\text{soft}}(\lambda, \lambda', bt, bt', k, k', E_\gamma, E_\gamma') \tag{3.40}$$

where δ_{hard} is the correction due to internal hard processes - Figure 3.9. For the definitions and functional depencences see (Armstrong, 1998).

3.6.2 Kinematics Modification Due To Bremsstrahlung

As stated above, the radiative processes were implemented for the incident and emergent electrons in the peaking approximation in Mo and Tsai approach (Mo & Tsai, 1969). Emission of a real photon by an incident electron modifies the event kinematics. Since it was Q^2 and W (see expressions B.6 and B.10 in Appendix C.25) that were generated initially this modification was introduced in the following way.

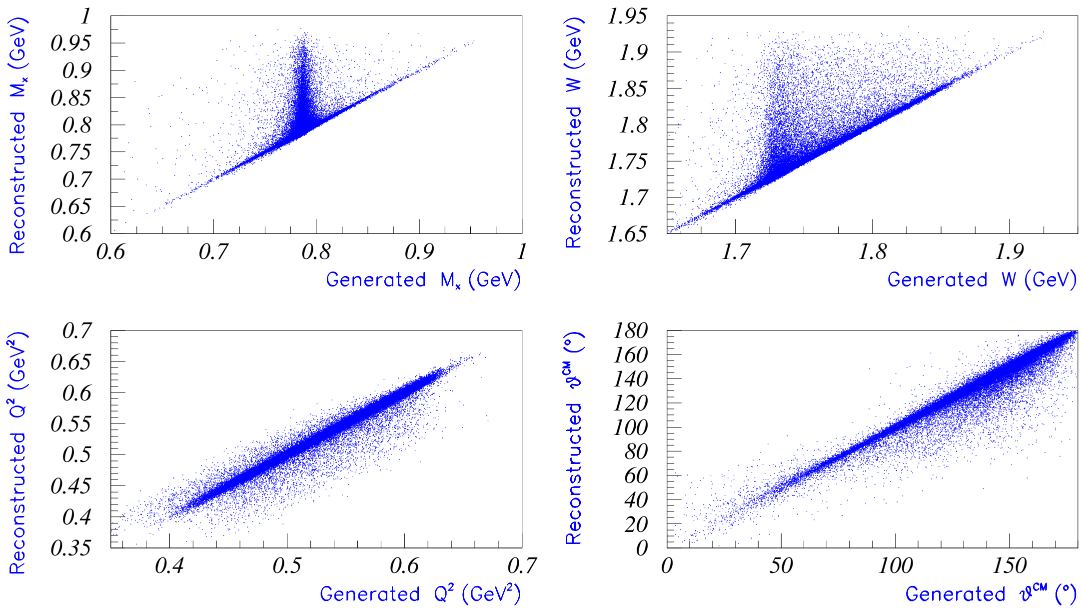

Figure 3.11: ***Kinematics Modification Effects:*** *The effects of applying kinematics modifications, described in the text, on the reconstructed Monte Carlo quantities.*

The set of equations below were solved for E'_{ver} and $\theta_{e'}$,

$$Q^2 = 4(E - E_\gamma)E'_{\text{ver}} \sin^2\left(\frac{\theta_{e'}}{2}\right) \tag{3.41}$$

$$W^2 = M_p^2 + 2M_p(E - E_\gamma - E'_{\text{ver}}) - Q^2 \tag{3.42}$$

finally yielding,

$$E'_{\text{ver}} = \frac{1}{2M_p}[(M_p + E - E_\gamma)^2 - (W^2 + Q^2 + (E - E_\gamma)^2)] \tag{3.43}$$

$$\theta_{e'} = 2 \text{ arcsin}\left(\sqrt{Q^2/(4(E - E_\gamma)E'_{\text{ver}})}\right) \tag{3.44}$$

The emission of a real photon by an emergent electron causes a misidentification of the actual momentum at the interaction vertex,

$$E' = E'_{\text{ver}} - E'_\gamma \tag{3.45}$$

When the initial beam energy E and detected electron momentum E' are used in the calculation of reconstructed quantities such as W or M_x photon emission leads to tails in the distributions of these variables. The effects of Bremsstrahlung are less intuitive in case of other quantities, like Q^2 or θ^{CM} (see Figure 3.11).

3.7 Monte Carlo Yield Evaluation

The Monte Carlo yield N_{MC} (in number of counts) was computed using Monte Carlo integration. This process is represented by the formula:

$$N_{MC} = n_p N_e \int_{\mathcal{A}} \left(\frac{d\sigma_{MC}}{dv'} \right)_{RAD} (v') \; \delta^{(4)}(P_i(v') - P_f(v')) \; dv' \tag{3.46}$$

where the dependence on the particular point of the generation volume is explicitly shown and

- dv' is generation volume spanned by Q^2, W, $\phi_{e'}$, Ω^{CM}, M_x, E_γ and E'_γ (with the last three being integrated out in the course of generation).
- $n_p N_e = \mathcal{L}_{MC}$ is the Monte Carlo luminosity,
- $\mathcal{A}$ is the acceptance of the experimental apparatus for a given bin,
- $(d\sigma_{MC}/dv')_{RAD}$ is the radiated model cross section, differential in variables spanning the generation volume (including Bremsstrahlung photons variables),
- P_i, P_f initial and final total 4-momenta.

The inclusion of radiative effects, as mentioned earlier, was twofold. Initially, the incoming and outgoing electrons were forced to emit real photons with energies picked from a empirically derived intervals and then the outgoing electron was transported through the HMS spectrometer magnetic field and detectors, provided that its momentum was within the acceptance of the spectrometer. The correction to the cross section for radiative effects was done only for incident and emergent electrons in the peaking approximation and as such it factorized from the Born term

$$\left(\frac{d\sigma_{MC}}{dv'}\right)_{RAD} = \frac{d\sigma_{MC}}{dv} \times \mathcal{R}(v') \tag{3.47}$$

Since originally the generation volume (as defined in Section 3.1.2) was populated, with unit multiplicative weighting, the Monte Carlo yield N_{MC} (in counts) for a given bin was calculated using,

$$N_{MC} = n_p N_e \times \sigma_{MC}\mathcal{R} \times \left(\Delta V \frac{N_{accepted}}{N_{tried}}\right) \tag{3.48}$$

or, in a fully blown form,

$$N_{MC} = n_p N_e \times \left(\mathcal{R}\, \frac{\partial(p_{e'}, \Omega_{e'})}{\partial(Q^2, W, \phi_{e'})}\, \Gamma_T(p_{e'}, \Omega_{e'}) \frac{dt}{d\Omega^{CM}} \frac{d\sigma}{dt}\right) \times \Delta v \times \frac{N_{acc}}{N_{tried}} \tag{3.49}$$

where

- $\mathcal{J} \equiv \partial(p_{e'}, \Omega_{e'})/\partial(Q^2, W, \phi_{e'})$ is the jacobian that accounts for the transformation from the lab variables to the invariant variables,
- $\Gamma_T(p_{e'}, \Omega_{e'})$ is the virtual photon flux,
- $dt/d\Omega^{CM}$ accounts for $t \longrightarrow \Omega^{CM}$ transformation of the cross section,

- $d\sigma/dt = \sigma_T + \epsilon\sigma_L$ is the model cross section,

- $\Delta v = 4\pi\Delta Q^2 \Delta W \Delta\phi_{e'}$ total volume within which the events were generated,

- N_{acc} is the number of surviving events, i.e. events that passed all the cuts and were successfully transported through the optical elements and detectors,

- N_{tried} is the number of generated events.

It is worth noting that there are, in principle, two distinct ways of evaluating the Monte Carlo yield related to the nature of the numbers N_{acc} and N_{tried}. The first method, described above, basically aimed at correcting the number of accepted events, N_{acc}, which arose solely from populating the generation volume subject to kinematical and acceptance constraints, by including the physics description of the process via the underlying cross section posterior to the generation.

On the other hand, the dynamics of the process of interest may be taken into account prior to the generation by enlarging the generation volume by one more dimension, the dimension of the cross section, so that the generation volume would read, in the particular case of the analysis presented here, $\Delta v = 4\pi\Delta Q^2 \Delta W \Delta\phi_{e'} \Delta\sigma_{MC}$. The $\Delta\sigma_{MC}$ is the difference between the maximal and minimal value of the cross section calculated over the entire acceptance of the apparatus. Now, the process in question is simulated according to the model cross section implemented in the Monte Carlo program by performing either simple acceptance/rejection test or more complicated importance sampling (James, 1968; Frolov,

1998) which is thus equivalent to correcting the number of tried events N_{tried} (that, again, resulted from populating only the generation volume).

Table 3.1: ***The Monte Carlo yield generation methods.***

	GENERATION METHOD	
	Weighted Phase Space	**Cross Section**
Advantages	highly time efficient	easy yield computation virtually no weightings
Disadvantages	complex yield computation all sorts of weightings incorrect statistical fluctuations	time consuming (unless coupled with importance sampling)

To increase time efficiency of the second method it is convenient to use importance sampling. In this process, however, some weightings are introduced. The method of extracting the Monte Carlo yield in the present work was chosen for its time efficiency.

CHAPTER 4

DATA ANALYSIS

4.1 Analysis Outline

The necessary link between the raw data files (runs), recorded by the Hall C data acqusition system during the data taking, and the data ready for direct off-line analysis was provided by a *FORTRAN* code nicknamed “replay engine”. This program was capable of,

- decoding event information and storing thus obtained ADC and TDC signals in appropriate detector arrays,
- retrieving, upon combination with the initial external input, particles track parameters, from drift chambers and hodoscopes ADC and TDC information, and detector responses to those particles,
- forming, ultimately, the relevant physical quantities (M_x, W, Q^2, t, *etc...*),
- preprocessing the data, if desired, to producea data file of reduced size,
- generating, as the result of the above manipulations, several run-specific output files such as arrays containing either single arm or coincidence data (ntuples), scaler files

with global run information (efficiencies, integarted charge, dead times, *etc*) and diagnostic histogram files.

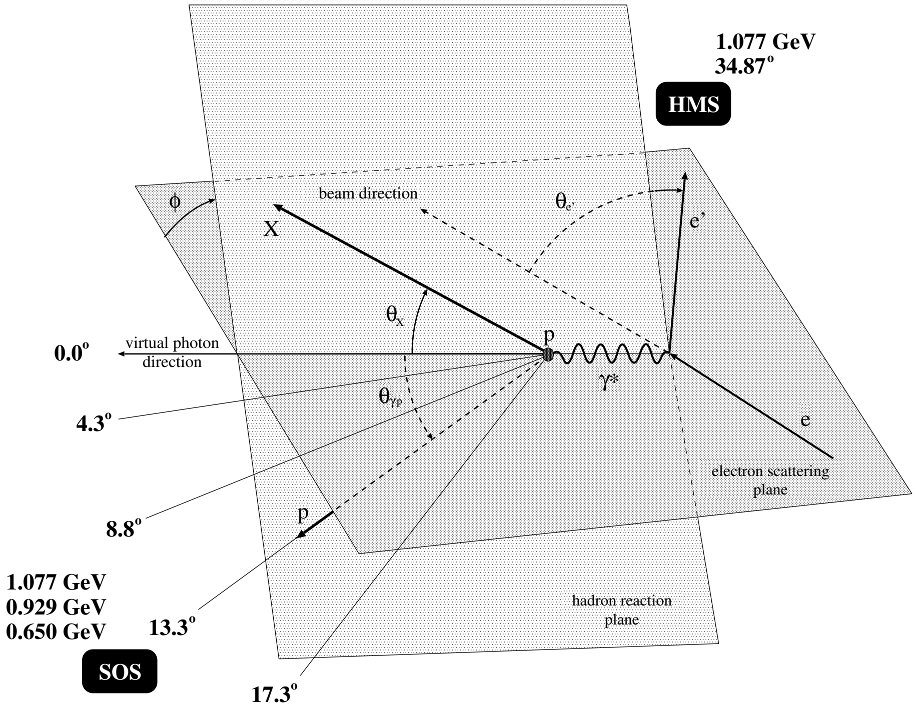

Figure 4.1: ***Ideogram of the Kinematical Settings:*** *To access all angles in the CM frame the momentum and the position of the SOS with respect to the nominal virtual photon direction had to be changed. All the settings are tabulated in Table 2.3 on page 63. All the angles are given with respect to the virtual photon direction.*

These output files for each run and Monte Carlo generated ntuples were the basis for further studies organized as follows,

Data:

- each run was replayed, various histograms checked for the existance of obvious problems or for the validity of the calibrations used,
- if necessary the calibrations were updated and corresponding runs replayed again,
- using loose particle identification (PID) and acceptance cut,s different runs, corresponding to the same kinematical setting, were merged to form final data ntuple.

In this process each event was assigned a multiplicative factor (the same for all the events in a given run) arising from the correction for the detector inefficiencies, dead times and from the normalization to the total charge. These factors were stored in a separate row of the final ntuple array.

Monte Carlo:
- three separate ntuples corresponding to different processes considered (ρ^0, ω and phase space[1]) were created for each setting by populating the generation volume,
- physics quantities (cross sections, jacobians *etc,...*) were also included in the ntuples,

Final Stage:
- data and Monte Carlo were binned in θ^{CM} for each setting (refer to Figure 4.1 or Table 2.3),
- for each bin, after removing the accidental contribution, a multivariable maximum likelihood fit was performed allowing for separation of the ω signal from the background,
- ultimately, the differential cross section was obtained by scaling the model cross section by the data yield normalized to the Monte Carlo yield.

There are two parts of the experimental apparatus that make the extraction of the physics quantities and their studies possible. The first part determines the momenta of the scattered particles. Drift chambers were used to measure the orientation and the position of the hadron (p, K^+, or π^+) and the electron trajectories at the detection (focal) planes of the SOS and HMS spectrometers. Having this information the orientation and the magnitudes of the momenta at the interaction vertex within the target were reconstructed providing six kinematical quantities needed to describe the final state.

However this knowledge itself is insufficient to deduce what particles were involved in the scattering process. The scintilator hodoscopes, Čerenkov detectors and shower coun-

[1]Initially Δ^{++} contribution was also modeled. The evolution of the phase space model made this contribution obsolete since their corresponding distributions were almost indistinguishable from one another.

ters constituted the other necessary part of the apparatus. Using time-of-flight (**TOF**) measurements the velocities of the detected particles were measured thus allowing **p**article **id**entification (**PID**). Eventually, parametrizing the time difference between each trajectory and the central trajectory due to differents pathlengths in either spectrometer in terms of the focal plane quantities allowed the time difference in arriving of the scattered particles at the focal plane of the SOS and the HMS to be determined. This quanitity was crucial in selecting the events pertaining to the process of interest.

4.2 Track Reconstruction

To reconstruct various quantities at the interaction vertex one begins with determining the trajectories of the detected particles. Each spectrometer, as described in Chapter 2, was equipped with a pair of drift chambers that provided the necessary tracking information for each event which was processed by the tracking software during the replay of the data. The goal of the tracking algorithm is to find the parameters of the straight line that yield the best fit to the drift chamber hit coordinates. The starting requirement is that the tracking software attempts to find a track for given event only when at least five (out of six) wire planes registered a hit. The way the track is established is the following. Initially, for a set of hits in a chamber all the intersections of pairs of wires that were hit are identified.

The hit coordinates at each wiire plane are found by adding the distance from the hit position to the position of the wire that detected the passing particle. This distance is calculated

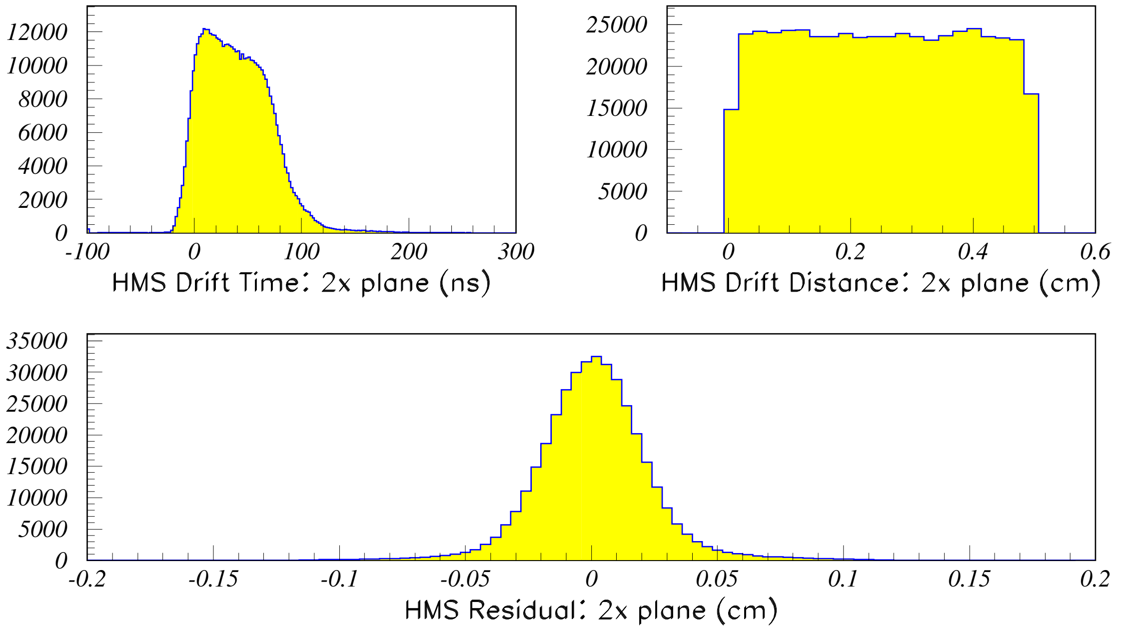

Figure 4.2: ***Tracking Calibrations:*** (Top Right)*: Typical drift time spectrum.* (Top Left)*: Corresponding drift distance distribution calculated using time-to-distance relation.* (Bottom)*: Single residual - the distribution of the differences between the hit coordinates and the fitted track coordinates for one plane.*

from the drift time. If the distances of these coordinates from one another are less than some constant value (1.2cm for *E91016/E93018*), which may vary from chamber to chamber, they are designated as "space points". Linked space points, within a chamber, establish piece of tracks called "stubs" that are likely to be portions of the final track. Collinear stubs from both chambers are linked to form tracks. For each track the χ^2 deviation from a straight line is evaluated. In the case of multiple possible tracks in an event, the χ^2 serves to select the best one.

Drift distance is determined by measuring the difference between the time at which the particle passed through the focal plane and the time the wire detected it passing. Converting drift times to drift distances requires careful mapping of drift time, measured by the drift chamber TDC's and the hodoscope start time, onto the drift distance. The time to distance relation is determined from the integrated time-difference spectrum. Assuming uniform illumination of the chambers the drift time distribution is an unweighted integral of the time-distance relation. The drift distance is then given by,

$$d = \frac{\int_{t_{\min}}^{T} F(t)dt}{\int_{t_{\min}}^{t_{\max}} F(t)dt} \, 0.5\text{cm} \tag{4.1}$$

where

- factor of 0.5cm is the half of the drift cell size,
- $t_{\min}, t_{\max}$ define the range of integration (typically from -25 ns to 250 ns),
- T is the chamber TDC value with the hodoscope time at the focal plane subtracted out.

These time-to-distance maps were periodically checked and regenerated to ensure proper functioning of the tracking software. This procedure yielded the coordinates (x_{fp}, y_{fp}) and orientation (slopes x'_{fp}, y'_{fp}) of the particle trajectory at a specified location in the detector hut. For the sake of consistency this location was defined to be a plane perpendicular to the central ray of the spectrometer situated at its intersection with the spectrometer's optical focal plane. This plane, also refered to as the focal plane (subscripts fp above), was approximately halfway between the two HMS chambers and in front of the first SOS chamber.

4.3 Vertex Reconstruction

The knowledge of the trajectory position and orientation at the focal plane allowed for the reconstruction of this trajectory at the interaction vertex within the target via the power-series expansion,

$$q^i_{\mathrm{tar}} = \sum_{j,k,l,m=0}^{N} M^i_{jklm} (x_{\mathrm{fp}})^j (y_{\mathrm{fp}})^k (x'_{\mathrm{fp}})^l (y'_{\mathrm{fp}})^m \tag{4.2}$$

where the quantities q^i_{tar} are target counterparts of the focal plane quantities (x'_{tar}, y_{tar}, y'_{tar}) with the exception of the x_{tar}, the vertical position at the target, which is replaced by the fractional momentum relative to the central momentum,

$$\delta = \frac{|\mathbf{p}| - |\mathbf{p}_0|}{|\mathbf{p}_0|} \tag{4.3}$$

Here (N is the order of the transformation ($j+k+l+m \leq N$)) the powers j, k, l, m and the coefficients of this expansion, called matrix elements, are based on knowledge of the design, configuration and fields of the magnetic elements of the spectrometers plus a sophisticated optimization procedure (Assamagan, Dutta, & Welch, 1997). Initially, the sets of the matrix elements were generated using *COSY INFINITY* software (Berz, 1990). With the aid of data runs taken specifically for this purpose (sieve slit runs, for instance) the difference between reconstructed and actual values were minimized with the appropriate matrix elements as fit parameters. The procedure was checked using inclusive *ep* elastic data to reconstruct W^2. The W^2 distributions were checked for any dependence on the focal plane quantities.

4.4 Particle Identification

To select events pertaining to the reaction of interest several ways of particle identification were implemented. These included the determination of particle velocity from time-of-flight and the time difference of separate particles arrival at the focal planes of the two spectrometers. This difference is called the coincidence time. The detector stacks, as described in Chapter 2, were also equipped with individual detectors capable of differentiating between particle spieces. In this analysis only the HMS Gas Čerenkov and shower counter were used to ensure that a trigger resulted from an electron in HMS rather than a pion. The proton sample was selected by cutting on the SOS TOF velocity and the coincidence time.

4.4.1 Time-Of-Flight Velocity

The particle velocity, β_{TOF}, was determined by performing a χ^2 minimization of known coordinates, z_{scin}, and hit times, t_{scin}, for the scintillators on the track using for the minimization,

$$\beta_{\mathrm{TOF}} = \frac{1}{c}\frac{z_{\mathrm{scin}}}{(t_{\mathrm{scin}} - t_{\mathrm{fp}})} \tag{4.4}$$

where

- t_{scin} - a single scintillator PMT TDC time that was corrected for the propagation time, time walk associated with the pulse height variation and the offset introduced by the delay electronics and the cables connecting the phototubes with their TDC modules,
- t_{fp} - the time at the focal plane, as determined by the hodoscopes, being an average of the mean (over two PMTs) scintillator times projected back to the focal plane.

This procedure was performed only for tracks having at least one hit per pair of scintillator planes, thus providing minimum information for the fit. For proper operation the time-of-flight software had to be recalibrated (Niculescu, 1998; Armstrong, 1998) whenever any changes were made which affected the timing (changing the central momentum setting, for instance). Histograms in the diagnostic histogram file had to be carefully monitored to ensure quality of the TOF data. In the event of observing inadequate performance of the hodoscopes the parameters for the time-of-flight calculation had to be regenerated using a separate stand-alone code (Armstrong, 1995).

4.4.2 Coincidence Time

Particles originating from the same interaction vertex should arrive at the focal plane in well defined time difference depending on the respective particle properties and the distances they traversed. Measuring this difference was facilited, and implemented in both spectrometers, by using a coincidence trigger, timed by the HMS, to start a TDC which was then stopped by a delayed coincidence trigger, timed by the SOS. The time difference so measured gives the raw time difference, or raw coincidence time.

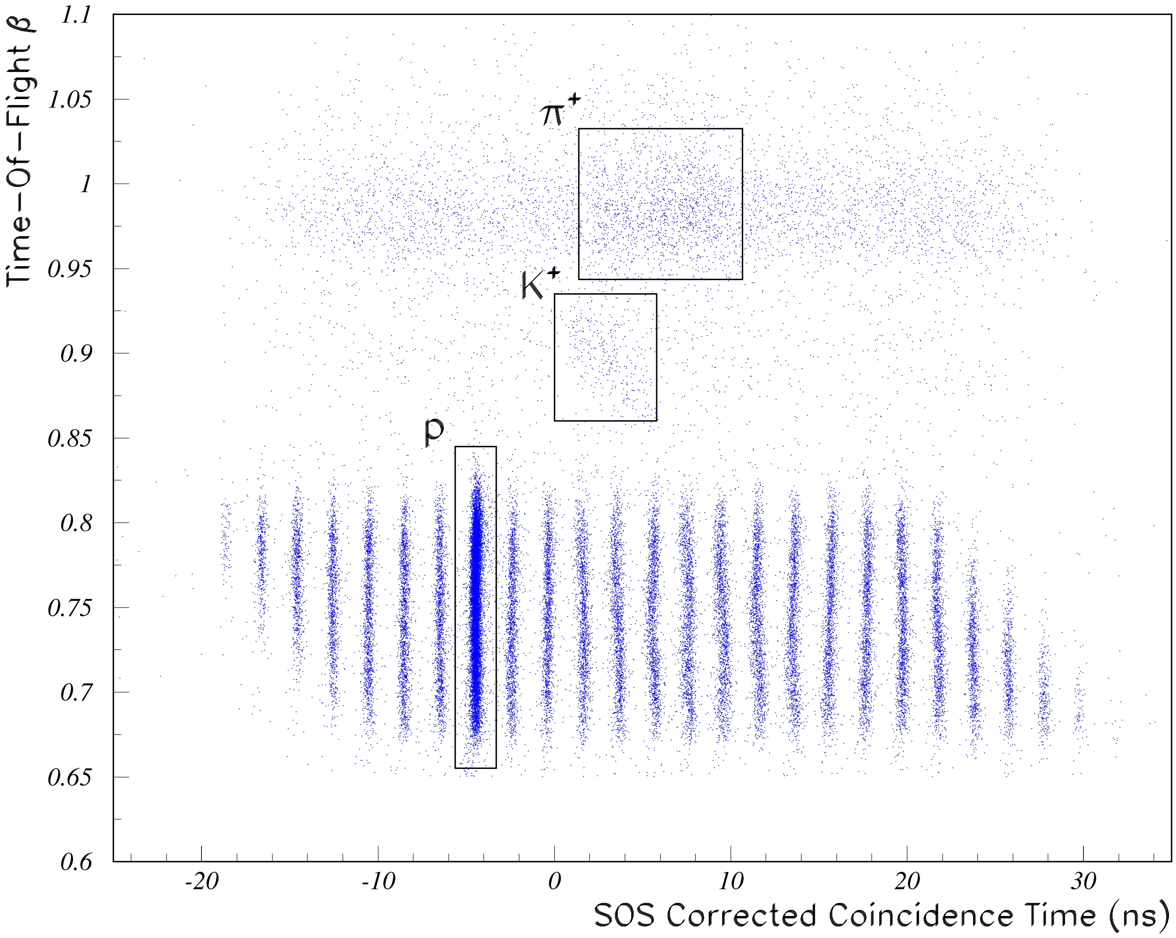

Figure 4.3: ***Proton Identification:*** *Coincident kaons, pions and protons are enclosed in boxes. The box around the protons does not correspond to the coincidence time cut used in the analysis. The actual cut was somewhat larger - see Section 4.6.1*

The raw coincidence time was then projected back to the focal plane and corrected for different pathlengths (Niculescu, 1997) yielding the corrected coincidence time,

$$t_{\mathrm{corr}} = t_{\mathrm{raw}} + (t_{\mathrm{fp}}^{\mathrm{HMS}} + \delta_{\mathrm{pathlength}}^{\mathrm{HMS}}) - (t_{\mathrm{fp}}^{\mathrm{SOS}} + \delta_{\mathrm{pathlength}}^{\mathrm{SOS}}) \tag{4.5}$$

as seen by the SOS coincidence TDC. Similarily, the HMS coincidence TDC measured this coincidence time. This quantity, with the resolution of about $\sigma_{\mathrm{ct}} \approx 180\,\mathrm{ps}$, served two purposes. It was used to select the coincident protons as well as to separate the accidental background from the real coincidence events.

4.4.3 Event Selection

Protons

As already mentioned protons were selected based on their time-of-flight velocity, β_{TOF}, and SOS corrected coincidence time - see Figure 4.3. Distributions in Figure 4.4, being one-dimensional projections of the distribution in the Figure 4.3, illustrate typical time-of-flight velocity and coincidence time spectra. These two plots document the ease of in extracting proton events compared to the evident difficulty encountered for kaon events (see left panel in Figure 4.4). The very small number of pions present in the β_{TOF} distribution is due to the inclusion of the Aerogel Čerenkov veto in the hardware trigger. A remarkable feature of the coincidence time plot is that it so clearly reveals the 499MHz radio frequency structure of the *CEBAF* beam.

To obtain further selectivity from the TOF measurement a cut was imposed on the difference between measured TOF velocity and that calculated from the spectrometer momentum measurement (see Figure 4.5),

$$|\Delta\beta| = |\beta_{\mathrm{TOF}} - \beta_{\mathrm{p}}| = \left| \beta_{\mathrm{TOF}} - \frac{|\mathbf{p}|}{\sqrt{|\mathbf{p}|^2 + M_p^2}} \right| \leq \ 0.05 \tag{4.6}$$

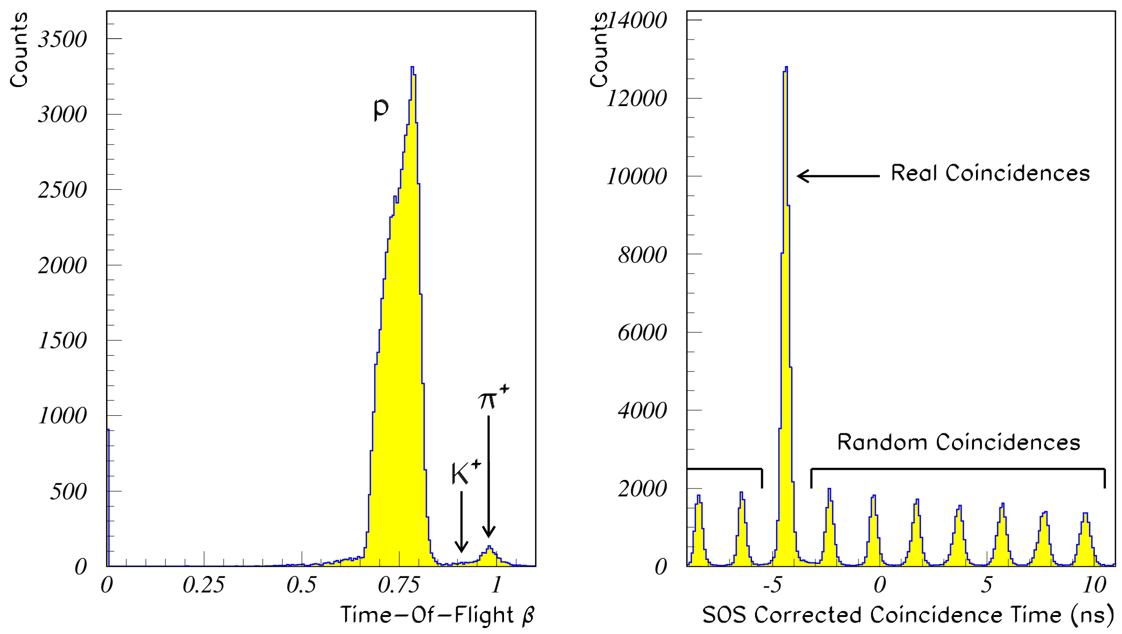

Figure 4.4: ***Proton Identification:*** (Left)*: An example of the β_{TOF} distribution. This plot corresponds to the central SOS momentum of 1.077 GeV and fractional variation of $\pm 20\%$. The TOF software assigns the $\beta_{\mathrm{TOF}} = 0$ value to an event for which it failed to find the velocity, mainly due to the hit scintillator position and track mismatch therefore these events are accumulated in the first bin.* (Right)*: Typical corrected coincidence time distribution - note "in-time" events grouped around $\sim -4.5\,\mathrm{ns}$. The cut on β_{TOF} to select protons was imposed before plotting this histogram.*

The events forming a "tail" extending toward negative values of $\Delta\beta$, atfer subtracting the accidentals, turned out to be legitimate proton events possibly assigned low β_{TOF} due to their interactions in the detecors after passing through the drift chambers. Their fraction ranged from $0.5\% - 1.0\%$ and these events were retained by imposing a rather loose β_{TOF} cut determined for each SOS momentum setting, typically $\beta_{\text{TOF}}^{\max} = 1.25\, p_0^{\text{SOS}}/\sqrt{(1.25\, p_0^{\text{SOS}})^2 + M_p^2}$ and $\beta_{\text{TOF}}^{\min} = 0.6\, p_0^{\text{SOS}}/\sqrt{(0.6\, p_0^{\text{SOS}})^2 + M_p^2}$ - see Table 4.1. The overall β_{TOF} cut efficiency was estimated to be $\sim 98\%$.

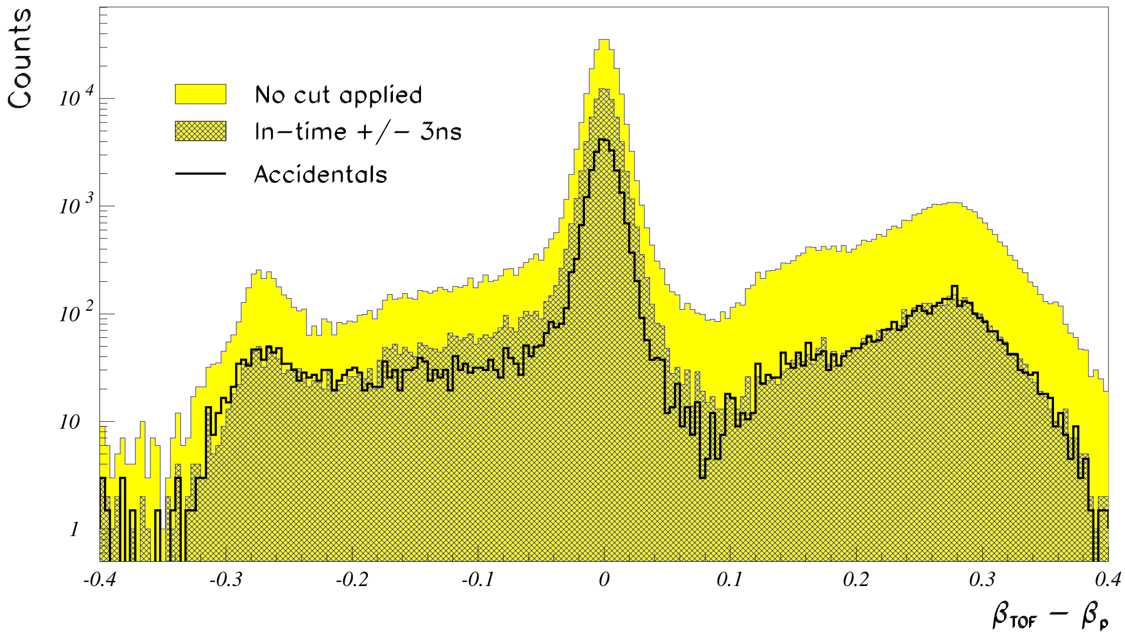

Figure 4.5: ***Proton Identification:*** *Typical spectrum of the difference in the velocities as determined by the Time-Of-Flight technique and proton momentum. Shaded histogram corresponds to data with no coincidence time cut applied, hatched histogram represents the data selected by imposing coincidence cut specified in Section 4.6.1. Eventually, solid black histogram shows the distribution of the random coincidences. (see Section 4.6.1 for determination of random coincidence spectrum).*

Electrons

The measurement of β_{TOF} in the HMS had inadequate resolution to separate electrons from negatively charged pions, therefore the Gas Čerenkov and the shower counter served for pion suppression. Their ADC signals were processed in a similar way. If C_i and S_i are the raw ADC counts from the Gas Čerenkov and shower counter respectively, then the Čerenkov response was converted to a number of photoelectrons while the calorimeter response was converted to energy deposition normalized to the electron momentum as follows,

$$N_{\mathrm{PE}} = \sum_{i=1}^{4} f_i^{\mathrm{G\check{C}}}(C_i - C_i^0) \tag{4.7}$$

$$E_{\mathrm{norm}} = \frac{E_{\mathrm{dep}}}{E'} = \frac{1}{E'} \sum_{i=1}^{52} f_i^{\mathrm{LDG}}(S_i - S_i^0) \tag{4.8}$$

where

- $f_i^{\mathrm{G\check{C}}}$ - Gas Čerenkov conversion factors,
- f_i^{LDG} - shower counter conversion factors,
- C_i^0, S_i^0 - Gas Čerenkov and shower counter pedestals, respectively.

A particle was assumed to be an electron if in the Gas Čerenkov $N_{\mathrm{PE}} \geq 3$ photoelectrons and if the particle deposited more than 70% of its energy (as measured by the spectrometer) in the lead glass calorimeter. Detailed studies (Niculescu, 1997) showed that the combined efficiency was at least 99.8% for the Gas Čerenkov and the shower counter and this number, with assigned error of 0.2%, was used in the analysis.

4.4.4 Physics Quantities

Identification of the real ep coincidence events, using the set of cuts listed in Table 4.1, led to selecting a $^1H(e,e'p)X$ reaction event. In order to calculate any quantity for a given event the laboratory momenta of the detected particles have to be computed first,

$$p_{\mathrm{x}} = p_0^{SOS}(1+\delta_{SOS})\cos\phi_{SOS}^{\mathrm{ev}}\sin\theta_{SOS}^{\mathrm{ev}} \tag{4.9}$$

$$p_{\mathrm{y}} = p_0^{SOS}(1+\delta_{SOS})\sin\phi_{SOS}^{\mathrm{ev}} \tag{4.10}$$

$$p_{\mathrm{z}} = p_0^{SOS}(1+\delta_{SOS})\cos\phi_{SOS}^{\mathrm{ev}}\cos\theta_{SOS}^{\mathrm{ev}} \tag{4.11}$$

where p_{x}, p_{y} and p_{z} are the scattered proton momentum components and

$$\theta_{SOS}^{\mathrm{ev}} = \theta_{SOS}^{0} + \arctan(y'_{\mathrm{tar}}) \approx \theta_{SOS}^{0} + y'_{\mathrm{tar}} \tag{4.12}$$

$$\phi_{SOS}^{\mathrm{ev}} = \arctan(x'_{\mathrm{tar}}) \approx x'_{\mathrm{tar}} \tag{4.13}$$

are the angles defining the orientation of the momentum vector in the lab frame for a given event. The momentum of the electron for that event is calculated in a similar way but its x component is negative since the HMS is to the right of the beam - see the target frame definition on page 10. The knowledge of these six components along with the target mass and the beam energy completely specifies the event kinematics.

Figure 4.6 shows a distribution of the missing mass M_x calculated according to the formula on page 7 for the setting of $p_0^{\mathrm{SOS}} = 1.077\,\mathrm{GeV}$ and $\theta_0^{\mathrm{SOS}} = 17.67^o$ (parallel kinematics -

Table 4.1: ***The standard set of cuts applied to the data***

Quantity	Cut
HMS Fractional Momentum	$\lvert\delta_{\mathrm{HMS}} - 1.25\%\rvert \leq 8.75\%$
SOS Fractional Momentum	$\lvert\delta_{\mathrm{SOS}}\rvert \leq 20\%$
HMS Geometric Acceptance	$\lvert x'_{\mathrm{tar}}\rvert \leq 70\,\mathrm{mrad}$ $\lvert y'_{\mathrm{tar}}\rvert \leq 30\,\mathrm{mrad}$
SOS Geometric Acceptance	$\lvert x'_{\mathrm{tar}}\rvert \leq 60\,\mathrm{mrad}$ $\lvert y'_{\mathrm{tar}}\rvert \leq 40\,\mathrm{mrad}$
Gas Čerenkov PID	$N_{\mathrm{PE}} \geq 3$ p.e.
Lead Glass Calorimeter PID	$E_{\mathrm{norm}} \geq 70\%$
SOS Coincidence Time	centroid $\pm\, 3\,\mathrm{ns}$
TOF velocity	$\beta^{\mathrm{min}}_{\mathrm{TOF}} \leq \lvert\beta_{\mathrm{TOF}}\rvert \leq \beta^{\mathrm{max}}_{\mathrm{TOF}}$

$\theta_{\gamma p} = 0.0^o$). Inspection of this distribution reveals strong ω meson signal atop a complicated background. Contributions to the background include a number of processes, from multi-pion reactions to ρ^0 production to Δ^{++} and Δ^0 resonance formation. It is evident from Figure 4.6 that removing this background will constitute the main source of error in the cross section extraction. This is quite different from the kaon electroproduction channel where there is virtually no background since the kaon is the lightest system containing a strange quark. Selecting a pure kaon sample however, unlike for the protons, is painstakingly difficult. The existance of such a large physics background in the proton case is a consequence of detecting only the electron and proton in the final state. In the other experiments (Joos et al., 1977; Cassel et al., 1981; ABBHHM Collaboration, 1968) on ω production all charged particles in the final states were detected so that the ω channel was identified through its decay products,

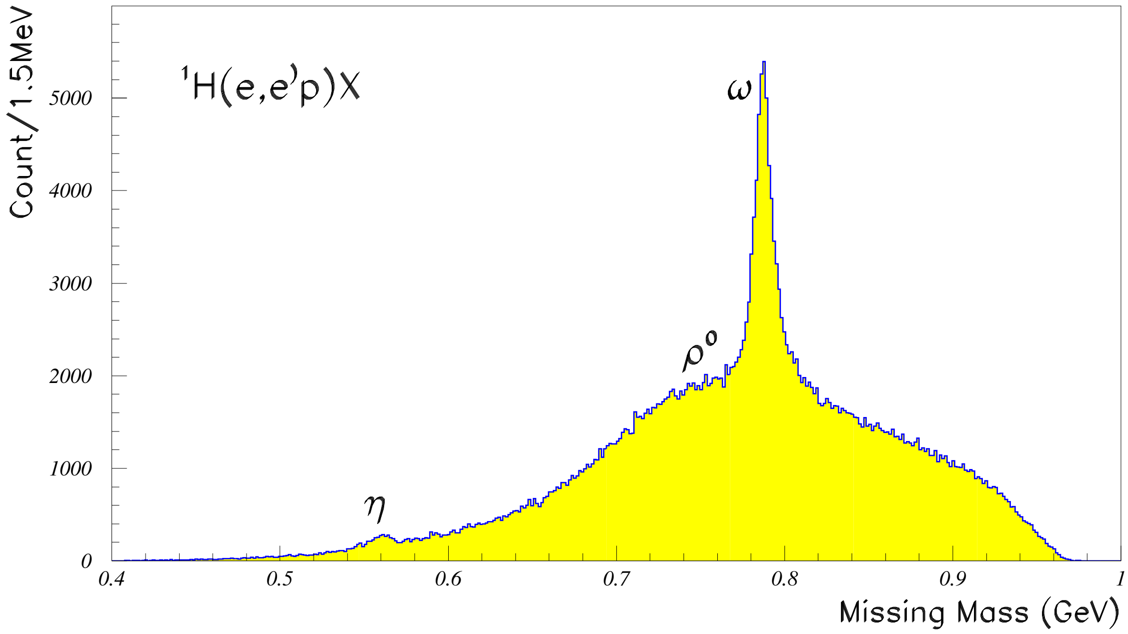

Figure 4.6: ***Inelastic Electron Proton Scattering:*** *A strong ω meson signal is observed along with diversity of other channels forming large physics background. The η channel is later eliminated by appropriate momentum cuts. To generate this plot no momentum cuts were applied.*

substantially reducing the background.

It also turns out that, as described in Section 2.6, the relatively small acceptances of the HMS and SOS impose tight correlations on the kinematical quantities such as M_x, W, Q^2 and $\theta^{\rm CM}$. This fact has two very important consequences. First, it makes binning in W difficult to implement since it would not leave enough phase space to carry out adequate signal-background separation - compare with Figure 4.7. Second, the value of the cross section extracted for a given $\theta^{\rm CM}$ bin at adjacent $\theta_{\gamma {\rm p}}$ settings may reflect averaging over

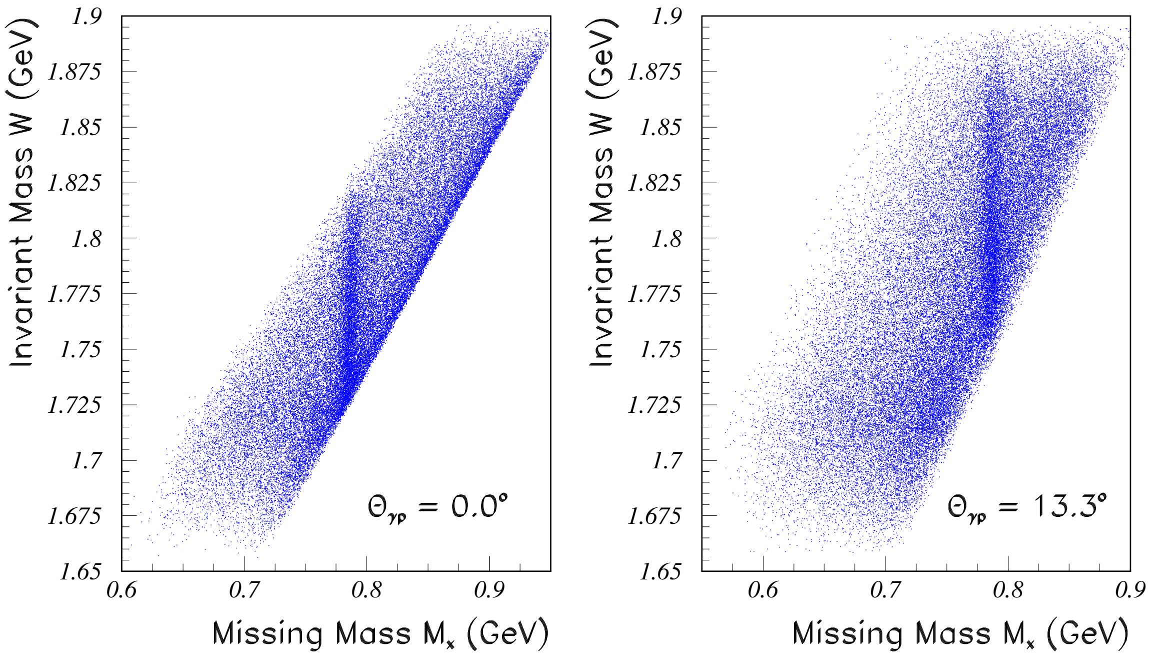

Figure 4.7: ***Kinematical Correlations:*** *Strong M_x and W correlation introduced by relatively small acceptances. As a consequence any binning in W did not leave enough phase space underneath the ω peak to perform a meaningful fit. The lower, clean, edge on the left panel plot corresponds to the threshold production.*

quite different ranges in W and Q^2 - see Figures 4.8 and 4.9.

The histograms in Figures 4.8 and 4.9 were created using a Monte Carlo results of the pure ω meson signal to avoid the background contribution. Imposing a tight cut on the ω mass, say ± 20 MeV, the data was found to display the same behavior. Figure 4.7 shows correlations dervied from the data. Worth noting is the "walk", a shift from the threshold due to the finite acceptance of the apparatus, of the ω from the threshold as $\theta_{\gamma p}$ increases in agreement with the predictions stated in Chapter 2.

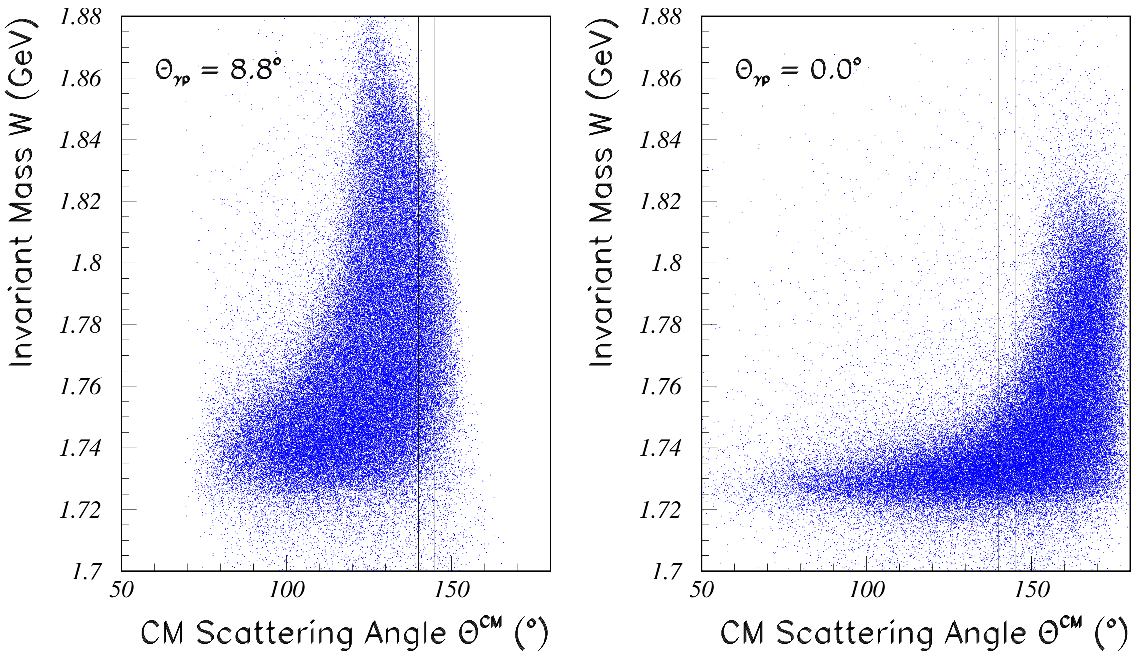

Figure 4.8: ***Kinematical Correlations:*** *θ^{CM} and W correlation shown for two different kinematical settings. Monte Carlo distributions generated for the ω alone at the same momentum ($p_O^{\mathrm{SOS}} = 1.077\,GeV$) but different angle setting.* (Left)*: 8.8^o from the virtual photon direction,* (Right)*: along that direction. At both settings singled out is the bin of $142.5^o \pm 2.5^o$ to illustrate the range of W the cross section will be averaged over.*

Before the physics background can be subtracted from the data several issues have to be addressed. The coincidence time cut, as it is clear from Figure 4.4,passes not only real coincidences but also uncorrelated particles that accidentally produced a coincidence trigger, "random coincidences". The fraction of such events in the total in-time peak can be estimated using a procedure described in Section 4.6.1. Prior to extracting yields, the data have to be corrected for variety of factors including detector efficiencies, live times, *etc*, as outlined

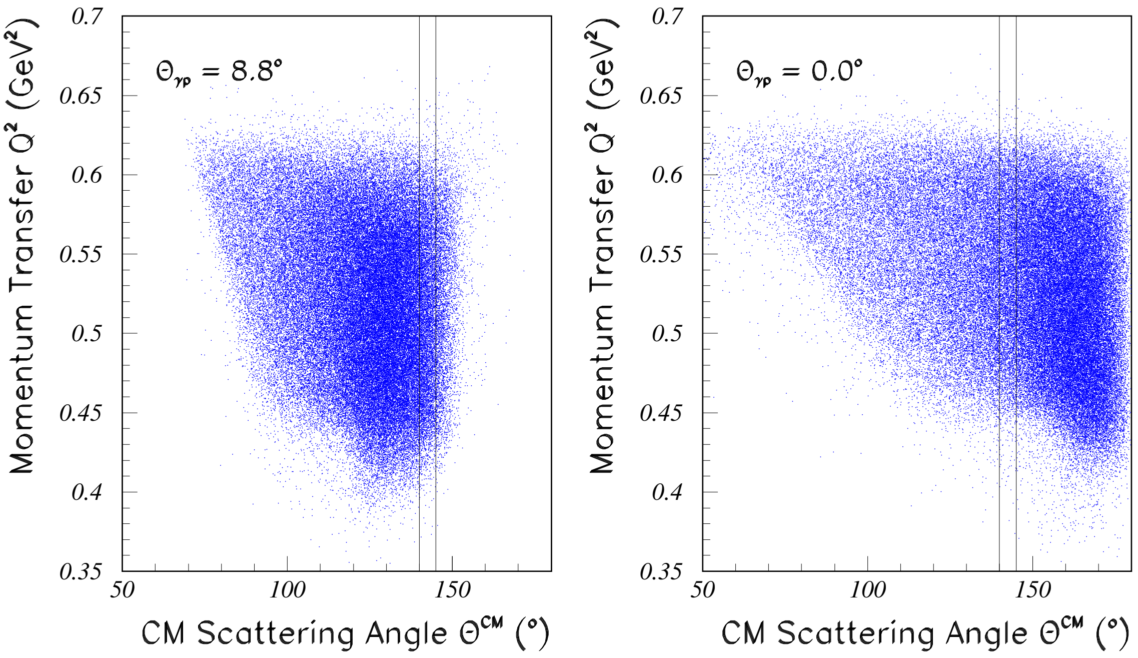

Figure 4.9: ***Kinematical Correlations:*** *θ^{CM} and Q^2 correlation shown for two different kinematical settings. For further details see caption of Figure 4.8.*

in Section 4.6.2. To tackle the task of separating the ω meson signal from the physics background any offsets existing in the setup must be identified and corrected for - Section 4.5

4.5 Offset Determination

An important part of the data analysis was to reconcile the offsets likely exsisting in the experimantal setup. Kinematical overdetermination of the exclusive elastic electron proton scattering (${}^1H(e,e'p)$) provided a tool for this purpose. During the *E91016/E93018* also some elastic data were taken for the SOS and HMS δ-scans which served for extensive optics studies. These studies resulted in obtaining, for each of the spectrometers, an optimal set of coefficients in a multivariable Taylor expansion used to calculating four target variables, fractional momentum δ, slopes of the particles trajectory at the target x'_{tar} and y'_{tar}, and apparent position of the interaction vertex y_{tar}. These coefficients are refered to as the reconstruction matrix elements and their optimization precedure was decribed in (Assamagan, Dutta, & Welch, 1997). The knowledge of the fractional momentum and track slopes of both final state particle combined with the initial information regarding the beam energy (E_0) along with the momentum (p_0) and angular (θ_0) settings of both spectrometers enables calculation of the kinematic variables such as,

- W - the invariant mass of the virtual photon proton system (equals M_p for the elastics),
- E_m - the missing energy of the particle(s) that went undetected (vanishes for the elastics),
- $\vec{p}_m$ - the missing momentum of the particle(s) that went undetected (vanishes for the elastics),
- Q^2 - 4-momentum transfer to the virtual photon,
- t - 4-momentum transfer to the proton (equals Q^2 for the elastics).

as well as other relevant quantities. In the case of the elastic ep scattering, these kinematic quantities should each have definite values as indicated above. If however the measured quantities such as E_0, p_0, θ_0 are subject to offsets from their true values, the kinematic quantities will also deviate from thier expected values. It turned out that significant offsets of measured quantities from their true values were present in the present data. These offsets

Table 4.2: *The set of offsets applied to the data*

Quantity	Offset
Beam Energy	$-3.9\,\mathrm{MeV}$
Scattered Electron Central Momentum	consistent with zero
Scattered Proton Central Momentum	$+4.6\,\mathrm{MeV}$
HMS Central Angle	$-1.2\,\mathrm{mrad}$
SOS Central Angle	$-1.3\,\mathrm{mrad}$

had to be calibrated out in order to allow reliable extraction of ω meson yields. To accomplish this, a minimization procedure described in Appendix D was developed.

These offsets include offsets in the energy of the beam and in the spectrometers central momenta and their in-plane and out-of-plane angles. To reduce the number of offsets that enter the calculations the out-of-plane angles were handled separately before the main procedure was employed.

This treatment is possible because the offsets in out-of-plane angles only affect the out-of-plane component of missing momentum. The optimum out-of-plane offset was set to 2.6 mrad for the SOS (consistent with the effect of sagging in the SOS hydraulic jacks) and its counterpart for the HMS was varied so as to minimize a run-to-run deviation of the corresponding missing momentum component from zero. This yielded an HMS out-of-plane offset of -1.0 mrad. Therefore five offests remained to be determined.

To search for offsets in the measured quantities the procedure was as follows. For each *ep* event, the "expected values" of calculated quantities like W, E_m, *etc* were taken to

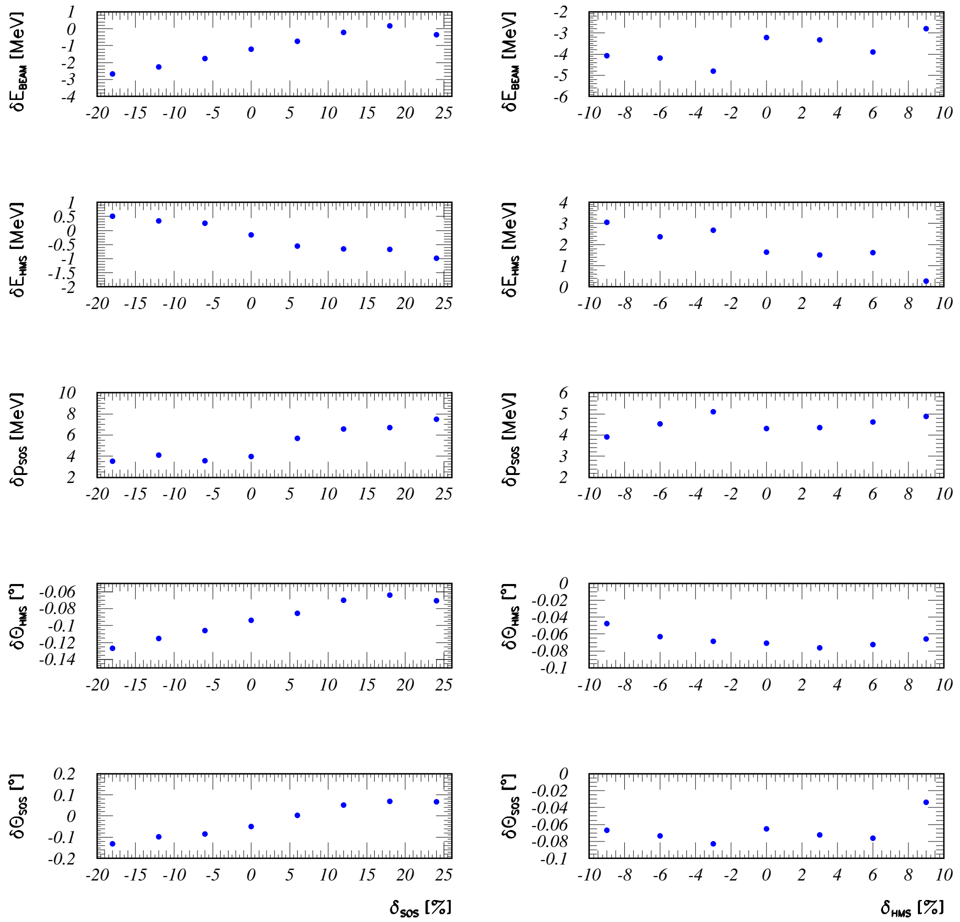

Figure 4.10: ***Offsets:*** *The results shown above correspond to two sets of elastic scattering data: in the left column the SOS δ-scan in which SOS central momentum was varied from 0.883 GeV/c to 1.335 GeV/c, the right column shows the results for the HMS δ-scan in which HMS central momentum was varied from 2.526 GeV/c to 3.025 GeV/c. Worth noting is the fact that for the HMS δ-scan the central momentum setting was originally 2.2 MeV lower than expected from the elastic kinematics - see the plot of δE_{HMS} versus δ_{HMS}. The average offsets, after rejecting the outermost points, for the HMS δ-scan were used in further analysis - see Table 4.2.*

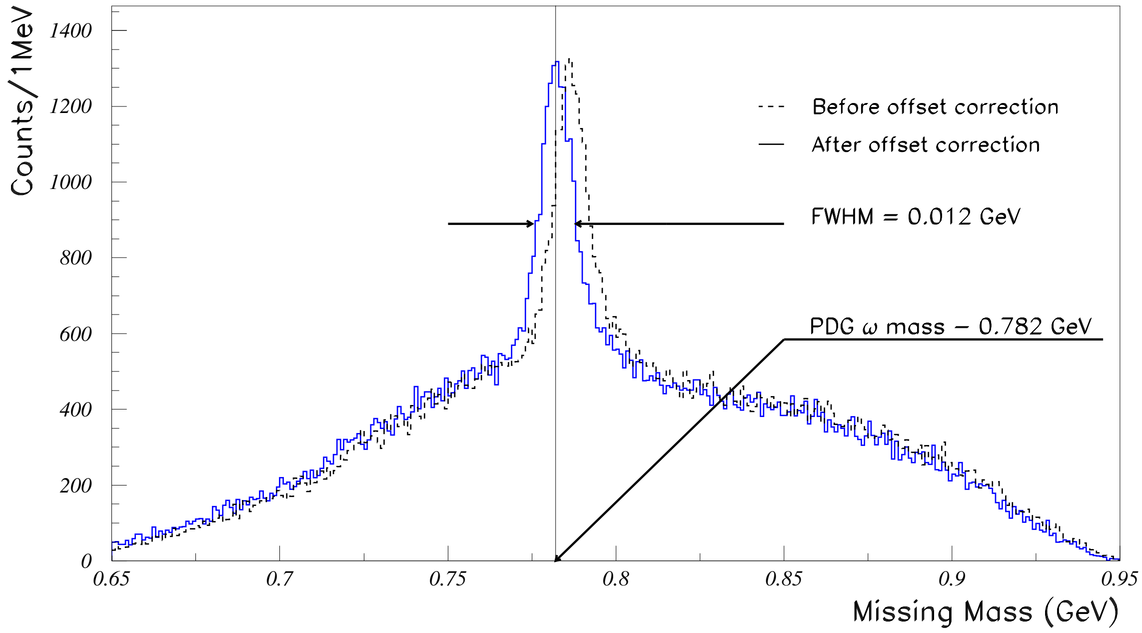

Figure 4.11: ***Reconstructed Missing Mass:*** *The missing mass histograms reflect the application of the found offsets for one kinematical setting. The PDG value of the ω meson full width half maximum, FWHM, is 8.43 MeV. Due to extended target phenomena and radiative effects this width broadens to 12 MeV which is in very good agreement with the simulation, where the PDG value was assumed.*

be the theoretical values for *ep* elastic scattering. The "observed values" were taken to be as calculated from the measured beam energy, θ_{HMS}, p_{HMS}, θ_{SOS}, p_{SOS} according to standard formulae, including parameters representing offsets of the measured beam energy, θ_{HMS}, p_{HMS}, θ_{SOS}, p_{SOS} from their "true" values. A χ^2-like function formed from the squared differences of these "observed" and "expected" values. This function was minimized by varying the offset parameters. The parameter values minimizing the χ^2 were taken to represent the actual offsets of the apparatus. Unfortunately only two sets of elastic runs were taken during the data taking pertaining to the $Q^2 = 0.5 GeV^2$ point. These runs were analyzed using the method just described. The results, which are shown on Figures 4.10, fall within the nominal uncertainties (10^{-3} level) for all the quantities except for the SOS momentum which was estimated to deviate by 0.42%. This last result is consistent with the magnitude of the correction that needs to be applied to the SOS central momentum due to the saturation effects in the SOS magnets (see page 61 in (Volmer, 2000)). The application of thus found offsets results in the mass of the observed ω meson, M_ω, of 782.3±1.3 MeV (compare Figure 4.11).

4.6 Background Subtraction

The goal of the data processing is to extract the ω meson yields and on that basis compute the corresponding cross sections. To be able to do that one has to remove consistently the background present underneath the ω meson peak. This background

can result from either real physical processes leading to the same final state or events that accidentally triggered the data aqcusition electronics - see Figure 4.12. The former requries meticulous modeling of the likely contributing reactions while the later is removed by devising appropriate coincidence cuts.

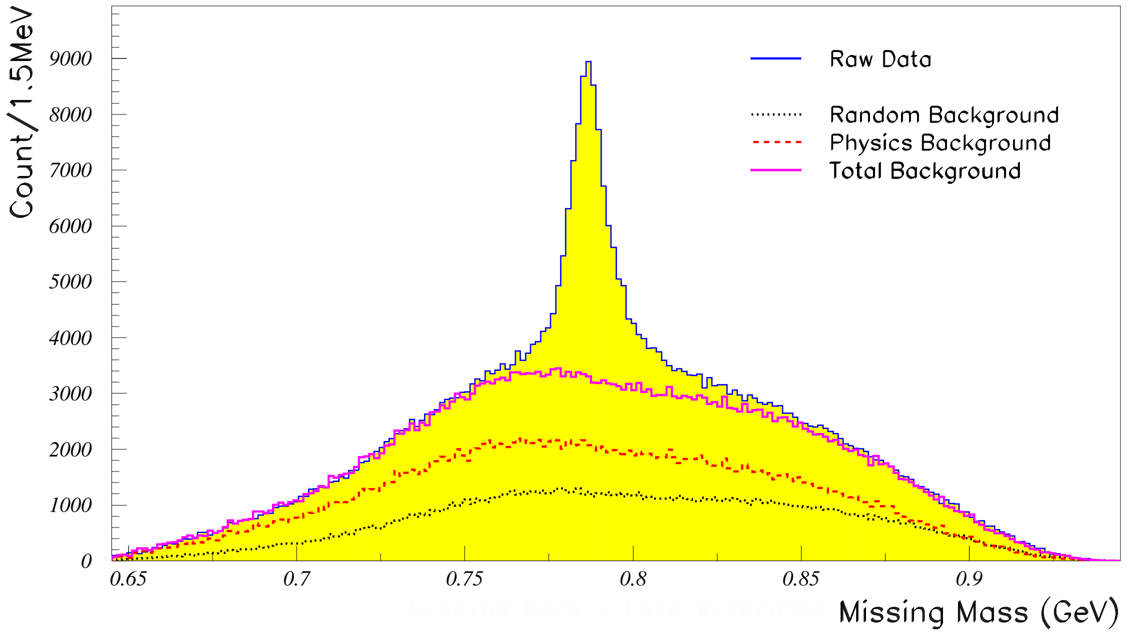

Figure 4.12: ***Backgrounds in Missing Mass:*** *The composition of the total background. Note the radiative tail extending from the ω toward higher masses, enhanced by plotting the background on top of the raw data.*

4.6.1 Accidental Background

There are two main background sources steming from the way the experiment was designed. The first comes from the fact that the coincidence timing accepts random coincidences as valid events. The other is due the interaction of the beam with the aluminum target walls.

The fraction of the events for the former source, ranging from 24% to 44%, is estimated by averaging over five random peaks in the coincidence time spectrum, while the later contri-

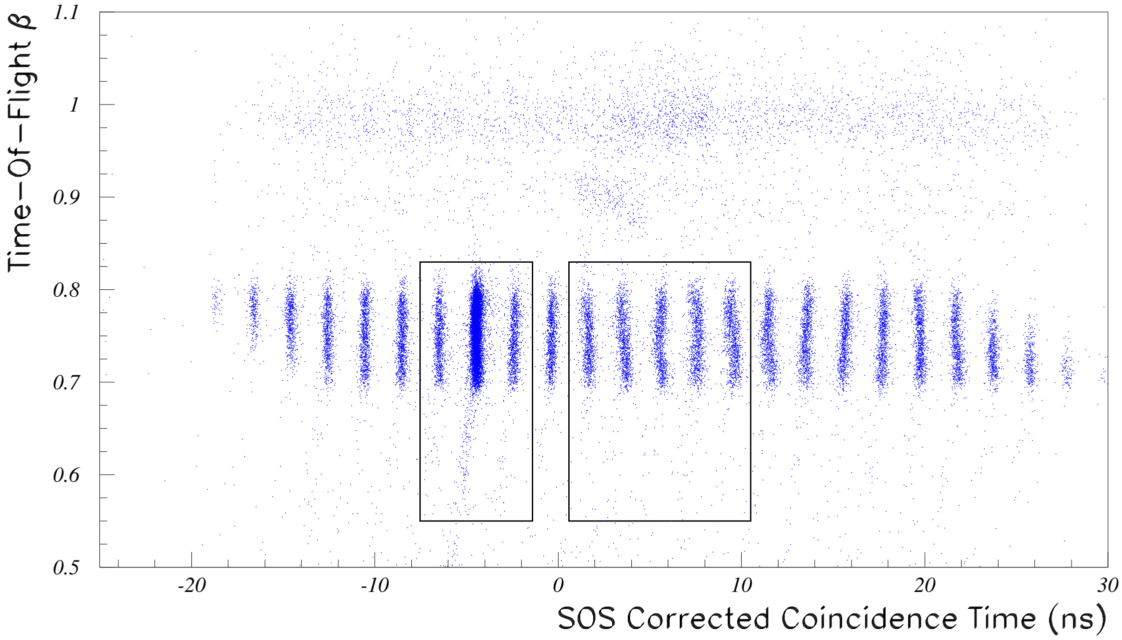

Figure 4.13: ***Random Subtraction:*** *The box containing the sample of random coincidences used in the accidental background subtraction is on the right. The "in-time" coincidence cut extends through* ± 3 *ns to avoid rejecting good events present in the tails below the coincident proton peak* ($\beta_{\mathrm{TOF}} < 0.7$) *and to the right of the peak (coincidence time* > -4 *ns).*

bution, ranging from 0.8% to 1.8%, is removed by methods discussed along with the physics background subtraction in Section 4.6.3. The removal of the accidentals (see Figure 4.13) was handled the following way,

- a coincidence time cut selecting the in-time peak, centroid ± 3 ns (the smaller box in Figure 4.13), was applied and the appropriate histograms, such as M_x, W, *etc*, were filled,

- a coincidence time cut selecting the random events (the bigger box in Figure 4.13) was applied and the same histograms were filled and rescaled by the coincidence time cut range ratio - 3/5,

- finally, the rescaled accidental spectrum was subtracted from the raw data on bin-by-bin basis.

The randoms were sampled over peaks appearing at higher coincidence times because the timing was set for the kaons which were distributed around zero coincidence time (see (Mohring, 1999), for instance).

4.6.2 Corrections Applied to the Data

Before separating the physics background from the ω signal all the runs for each kinematic setting had to be merged. To do so various correction factors to the data, pertaining to a single run, had to be accounted for. Each event was assigned a weight common to all events in the same run and runs for the same kinematics were added together.

Trigger Efficiency

Both the HMS and the SOS triggers required three out of four scintillator planes to fire. Treating the scintillators as independent one can calculate the overall efficiency of four planes,

$$P_{3/4} = P_1P_2P_3P_4 + P_1P_2P_3\ \bar{P}_4 + P_1P_2\ \bar{P}_3\ P_4 + P_1\ \bar{P}_2\ P_3P_4 + \bar{P}_1\ P_2P_3P_4 \tag{4.14}$$

where P_i is the the probability (efficiency estimated on arun-to-run basis) of firing for an individual plane and $\bar{P}_i$ is its inefficiency $(1 - P_i)$. The trigger efficiency calcultated this way was almost always nearly 100%.

Tracking Efficiency

The efficiency of the tracking algorithm was, as for the trigger efficiency, evaluated on a run-to-run basis as follows. A fiducial region was imposed by selecting only events that have passed through the central scintillators of each hodoscope array. This ensures that the particles also went through both drift chambers and should have had a track reconstructed. The ratio of the events that indeed had a good track to all the events in the fiducial region yielded the tracking efficiency, ϵ_{fid}. These efficiencies ranged from 95% to 97% for the HMS while for the SOS they were between 85% and 94%.

Computer and Electronic Live Times

Good events may be missed if they occur during the "busy" time of either the fast electronics or the data acquisition system (Niculescu, 1998; Mohring, 1999). These live times were computed on a run-to-run basis. The electronic live time for the HMS was typically $\sim 99.9\%$ and for the SOS between 98.3% and 99.4%. The computer live time was substantially smaller and ranged from 91% to 95%.

$\boldsymbol{\beta}_{\rm TOF} = 0$ Events

The efficiency of the $\beta_{\rm TOF}$ calculation was $\sim$ 98% efficient meaning that it found $\beta_{\rm TOF} = 0$ for $\sim$ 2% of otherwise legitimate events (see Figure 4.4). This was mostly caused by the fact that scintillator hits did not agree with the reconstructed track. Making an assumption that the effect is particle independent the ratio of protons having good $\beta_{\rm TOF}$ to all other particles should as the ratio of protons to all other particles for the case $\beta_{\rm TOF} = 0$. This leads to a correction varying from 1% to 2%.

4.6.3 Physics Background

The crucial step of the analysis was the subtraction of the processes collectively identified as the physics background. The simultanoeus detection of an electron with a proton, as repeatedly mentioned, may have tagged any of the following reactions,

$$e + p \longrightarrow e' + p\omega \tag{4.15}$$

$$e + p \longrightarrow e' + p\rho^0 \tag{4.16}$$

$$e + p \longrightarrow e' + \Delta^{++}\pi^- \longrightarrow e' + p\pi^-\pi^+ \tag{4.17}$$

$$e + p \longrightarrow e' + \Delta^0\pi^+ \longrightarrow e' + p\pi^+\pi^- \tag{4.18}$$

$$e + p \longrightarrow e' + p + \pi\pi\ldots \tag{4.19}$$

with (4.15) being the reaction of interest and (4.16) through (4.19) being the background processes. The reaction (4.19) stands for production of any number of pions satysfying appropriate selection rules. The production of vector mesons (reaction 4.15 and 4.16) was modeled on the basis of the respective cross sections. The processes (4.17)-(4.19), as well as any physically allowed reaction resulting in more than three particles in the final state (including electron and proton), were collectively modeled as two body, Lorentz-invariant, electroproduction phase space. This step was dictated by the fact that the distributions for these processes, reconstructed only from the electron-proton information, were almost indistinguishable.

Maximum Likelihood Fit

The backgrounds to be subtracted were fitted using maximum likelihood method. The approach incorporated in this method was developed by R. Barlow(Barlow, 1993). This method is appropriate when a sample of data consists of events coming from different sources and one would like to find the proportions (strengths) P_j pertaining to each of them. Moreover, there is no analytic form of the distributions available for these sources as functions of the kinematic variables, only the Monte Carlo generated distributions. This requires the binning of the data. The operation yields set of numbers $d_1, d_2, ..., d_n$, where d_i is the number of the data events in the i-th bin. The number of Monte Carlo events for that bin is given by,

$$f_i = N_D \sum_{j=1}^{m} \frac{1}{N_j^{MC}} P_j a_{ji} \tag{4.20}$$

where $N_D = \sum_{i=1}^{n} d_i$ is the total number of events in the data sample and $N_J^{MC} = \sum_{i=1}^{n} a_{ji}$ is the total number of Monte Carlo events for the j-th source. For convenience, one can incorporate N_D and N_j^{MC} into strengths $p_j = N_D P_j / N_j^{MC}$ to get a simple expression,

$$f_i = \sum_{j=1}^{m} p_j a_{ji} \tag{4.21}$$

Since the data as well as Monte Carlo samples have finite, sometimes low, statistics it is prudent to use Poisson distribution for estimating the probability of observing a particular set of d_i's. There are three contributions to the disagreement between d_i and f_i. These include incorrect p_j, flactuations in d_i and flactuations in a_{ji}. In order to take all three in to account in the maximization process it is necessary to also introduce the probability of finding a particular set of a_{ji}'s. The development leads to constructing a maximum likelihood function or, for convenience, the logarithm of it, in the form,

$$\log\mathcal{L} = \sum_{i=1}^{n} \left(d_i \ln f_i - f_i + \sum_{j=1}^{m} a_{ji} \ln A_{ji} - A_{ji} \right) \tag{4.22}$$

where A_{ji}'s are not actual but predicted number of Monte Carlo events in the i-th bin for the j-th source. This function is to be maximized with respect to the parameters.

This is the approach adpoted in *CERNLib HBOOK*'s `FORTRAN` callable routine `HMCLNL` which results in $m \times (n+1)$ nonlinear, coupled equation to be solved. However this problem can be reduced to a system of n decoupled equations since each unknown A_{ji} can be expressed in terms of d_i, f_i, a_{ji} and p_j. For a given set of strengths p_j the equations for A_{ji}'s are numerically solved using Newton's method (Barlow, 1993). In the present analysis a stand-alone code was used to perform the maximization of the `HMCLNL` function with respect to the strengths p_j using the *CERNLib* `MINUIT` package. It must also be mentioned that this technique, unlike χ^2 minimization is constrained to give the correct overall normalization,

$$N_D = \sum_{j=1}^{m} p_j N_j^{MC} \tag{4.23}$$

making clear the meaning of the p_j's. It also is superior to the χ^2 minimization which assumes that the distribution of the events per bin is Gaussian giving wrong normalization of the χ^2 functional for the bins with low statistics.

Moreover, the `HMCLNL` routine is implemented in a way that allows for maximization in several variables simultaneously. In the present analysis the maximum likelihood fit was performed in five variables including missing mass M_x, invariant mass W, momentum transfers Q^2 and t, and the ω meson scattering angle in the virtual photon-proton Center-Of-Momentum system θ^{CM}.

$$\log \mathcal{L} = \sum_{k=1}^{5} \log \mathcal{L}_k = \sum_{k=1}^{5} \sum_{i=1}^{n} \left(d_{ki} \log f_{ki} - f_{ki} + \sum_{j=1}^{3} a_{kij} \log A_{kij} - A_{kij} \right) \tag{4.24}$$

where the index n corresponds to the number of bins which, in principle, could be different for different quantities. During the final fit this number was the same for all distributions and set to 100.

The fit was performed for each 5-degree θ^{CM} bin for each kinematic setting separately. The number of θ^{CM} bins within a setting varied with a total number of 64 bins divided into two subsets corresponding to different average W. The fit and subsequent background removal was carried out by an external stand-alone program based on *HBOOK* callable routines. The histograms for the fit were prepared using ntuples with the phase space of each contribution populated randomly, except for the masses of the vector mesons. Then each event was appropriately weighted according to Eqn 1.21 and the corresponding cross section determined as defined in Eqns 3.16, 3.25 and 3.27. Although all three modeled processes were included in each fit, at times, the ρ^0 contribution had to be excluded for the bins where the ρ^0 and phase space distribution bore very close resemblance.

The results of the fit for a single θ^{CM} bin within a setting are shown in Figures 4.14 and 4.15. The figures were chosen to illustrate the strong correlations existing due to the relatively small accepatances of the spectrometers. This can be observed on the missing mass plot where the background is moved from the low side of the ω to the higher when θ^{CM} varies from 170^o to 130^o. Also ω itself is produced mostly at threshold, prominent peak in W distribution, for the 130^o bin - compare with Figure 4.8.

Figure 4.16 shows the quality of the fit for all the bins summed together while Figures 4.17, 4.19, 4.21, 4.23, 4.18, 4.20, 4.22, and 4.24 are again intended to document the effect of the acceptance of the apparatus on the data studied. These figures were generated for two adjacent settings ($\theta_{\gamma \mathrm{p}} = 4.3^o$ and $\theta_{\gamma \mathrm{p}} = 8.8^o$) with the same SOS momentum $p_0^{\mathrm{SOS}} = 1.077\,\mathrm{GeV}$ and similar θ^{CM} bins. Inspection of the plots in Figures 4.19 and 4.20 reveals strong correlation between W and θ^{CM} caused, for a fixed electron kinematics, by the finite acceptance of the SOS. For given geometry this acceptance selects protons with lower momentum as the scattering angle changes from 180^o toward forward direction. This can be seen also on the plot in Figure 4.8. The missing mass plots in Figures 4.17 and 4.18 also prove that there exists a correlation between W and θ^{CM} since increasing θ^{CM} causes the background to behave as if there was a W cut present causing a "motion" of the phase space relative to the ω peak - compare with Figure 4.7. The W and Q^2 histograms confirm anti-correlation of these quantities, Eqn B.10, enhanced by the configuration of the spectrometers.

It must also be noted that the background coming from the aluminum target walls, as smoothly distributed low yield background, was absorbed in the phase space and removed upon physics background removal.

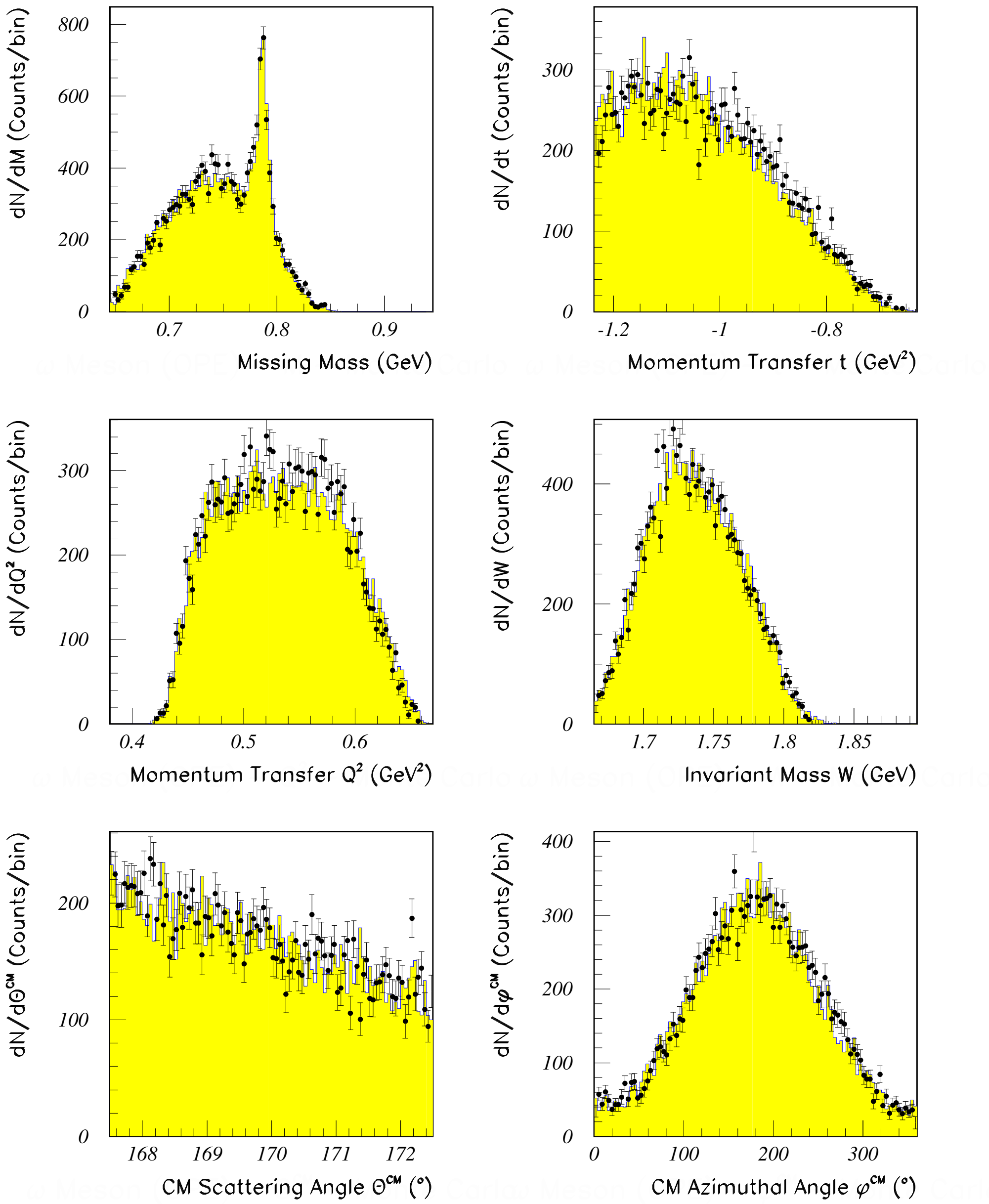

Figure 4.14: ***Fit Results - Single θ^{CM} Bin:*** *The results of the fit for a single θ^{CM} bin ($170^o \pm 2.5^o$), for the setting of 4.3^o relative to the virtual photon direction and $p_0^{\mathrm{SOS}} = 1.077\,GeV$.*

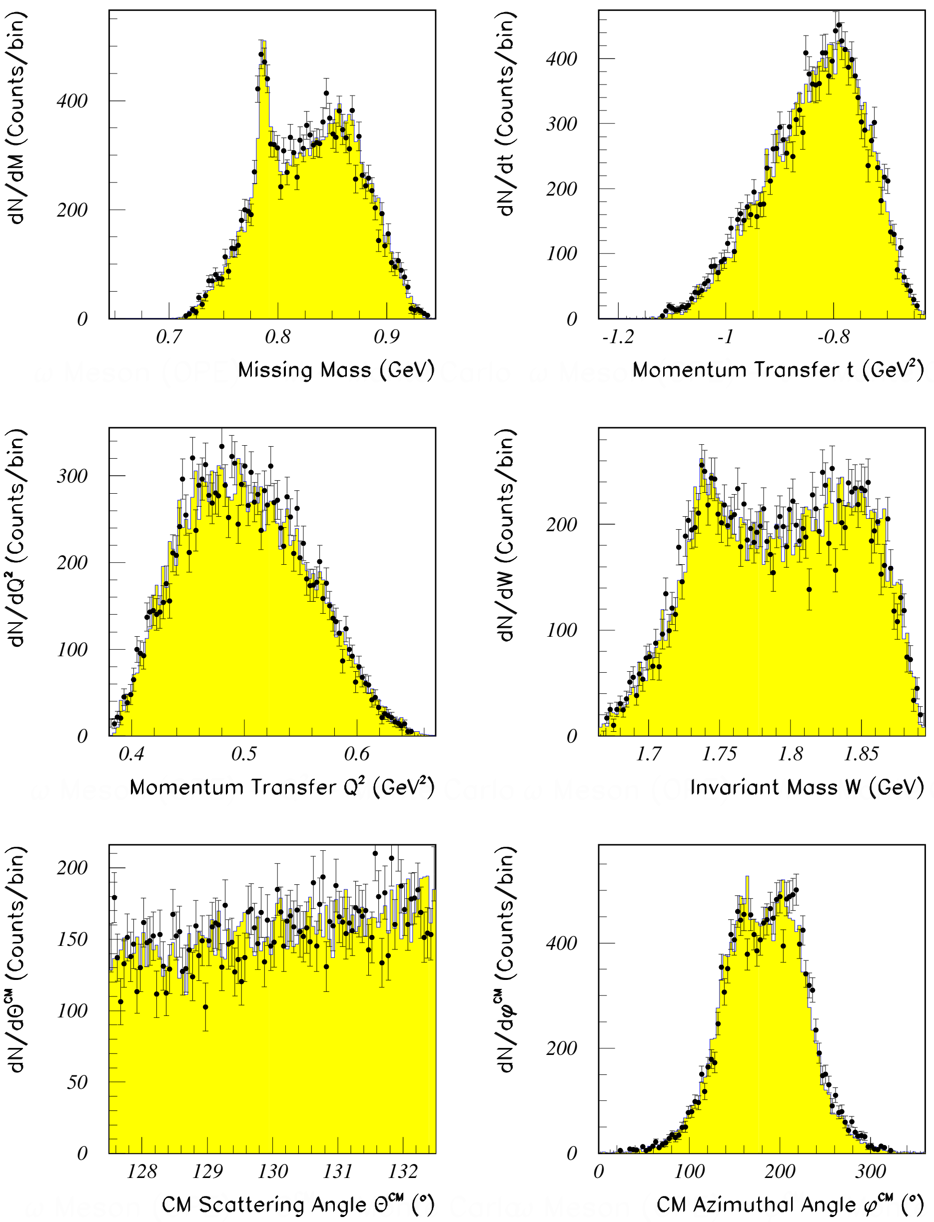

Figure 4.15: ***Fit Results - Single θ^{CM} Bin:*** *All the same as in Figure 4.14 except for the θ^{CM} bin* $(130^o \pm 2.5^o)$.

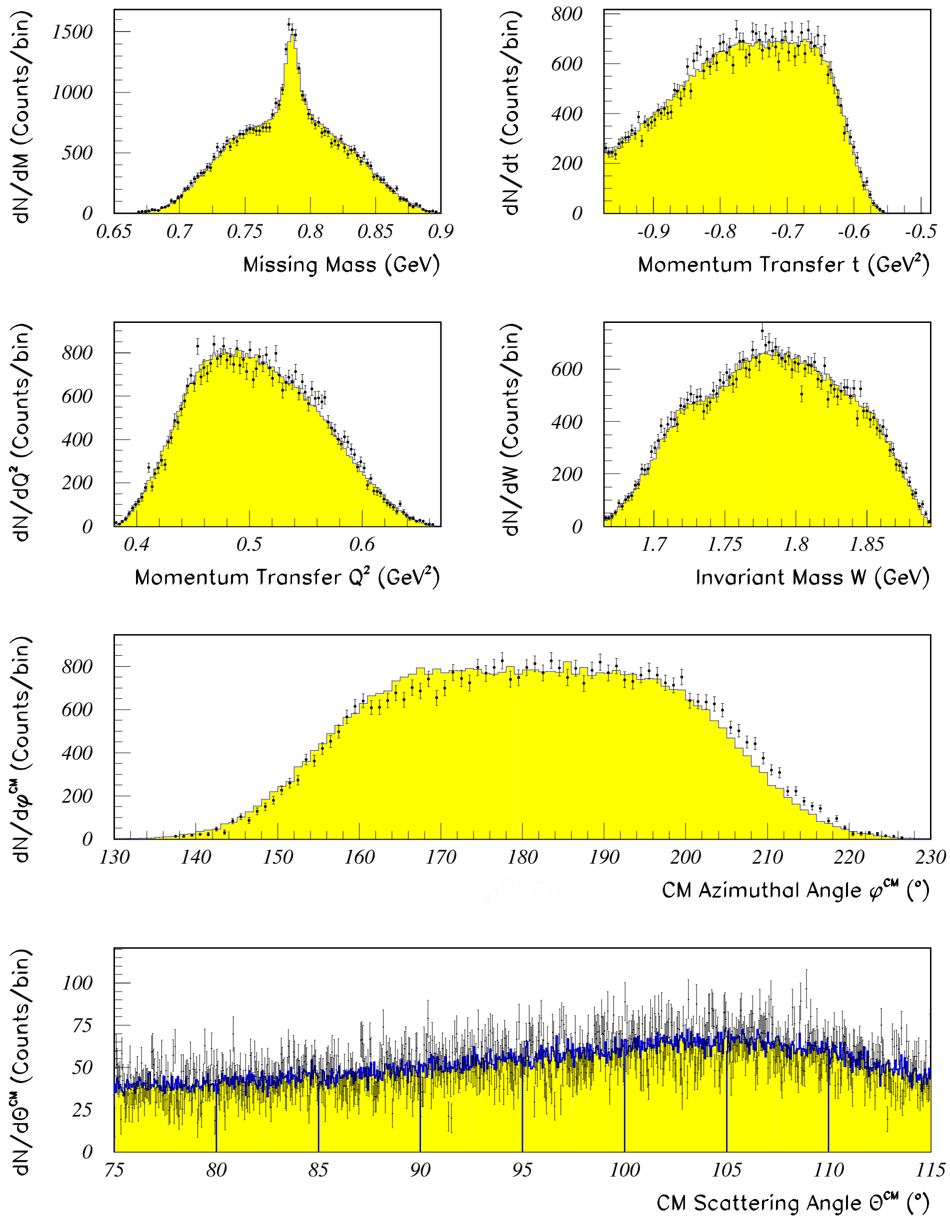

Figure 4.16: ***Global Fit - Single Setting:*** *Single bin fits were summed over all bins for the setting,* $\theta_{\gamma\mathrm{p}} = 13.3^o$ *and* $p_0^{\mathrm{SOS}} = 0.929\,GeV$

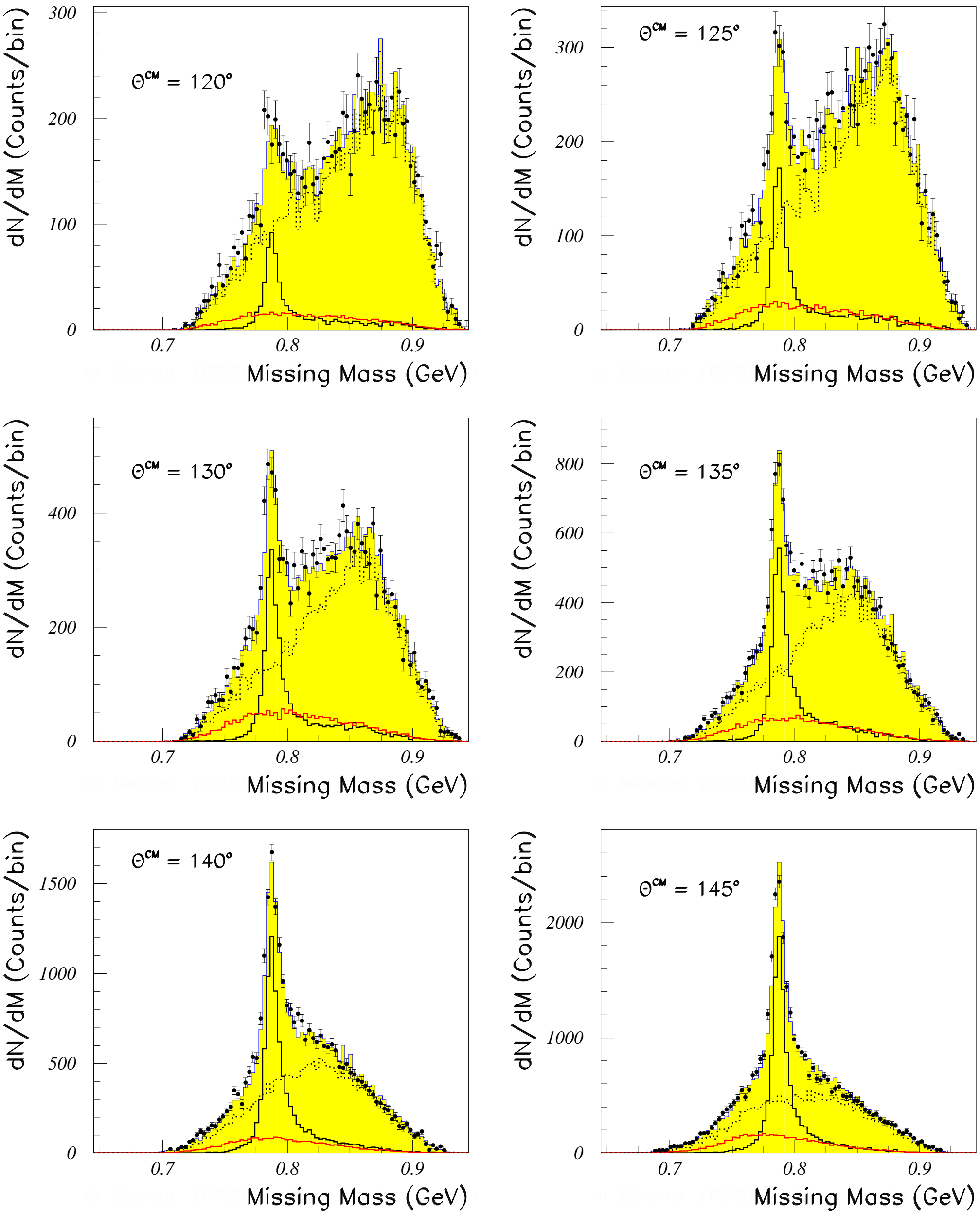

Figure 4.17: **Fit Breakdown In Missing Mass M_x:** *Single bin fit broken down into contributions in the missing mass M_x for $p_0^{\mathrm{SOS}} = 1.077\,\mathrm{GeV}$ and $\theta_{\gamma\mathrm{p}} = 4.3^o$. Solid circles with error bars are the data. The shaded histogram is the full Monte Carlo fit. Dotted histogram is the phase space, solid black histogram is the ω while grey (red) histogram is the ρ^0.*

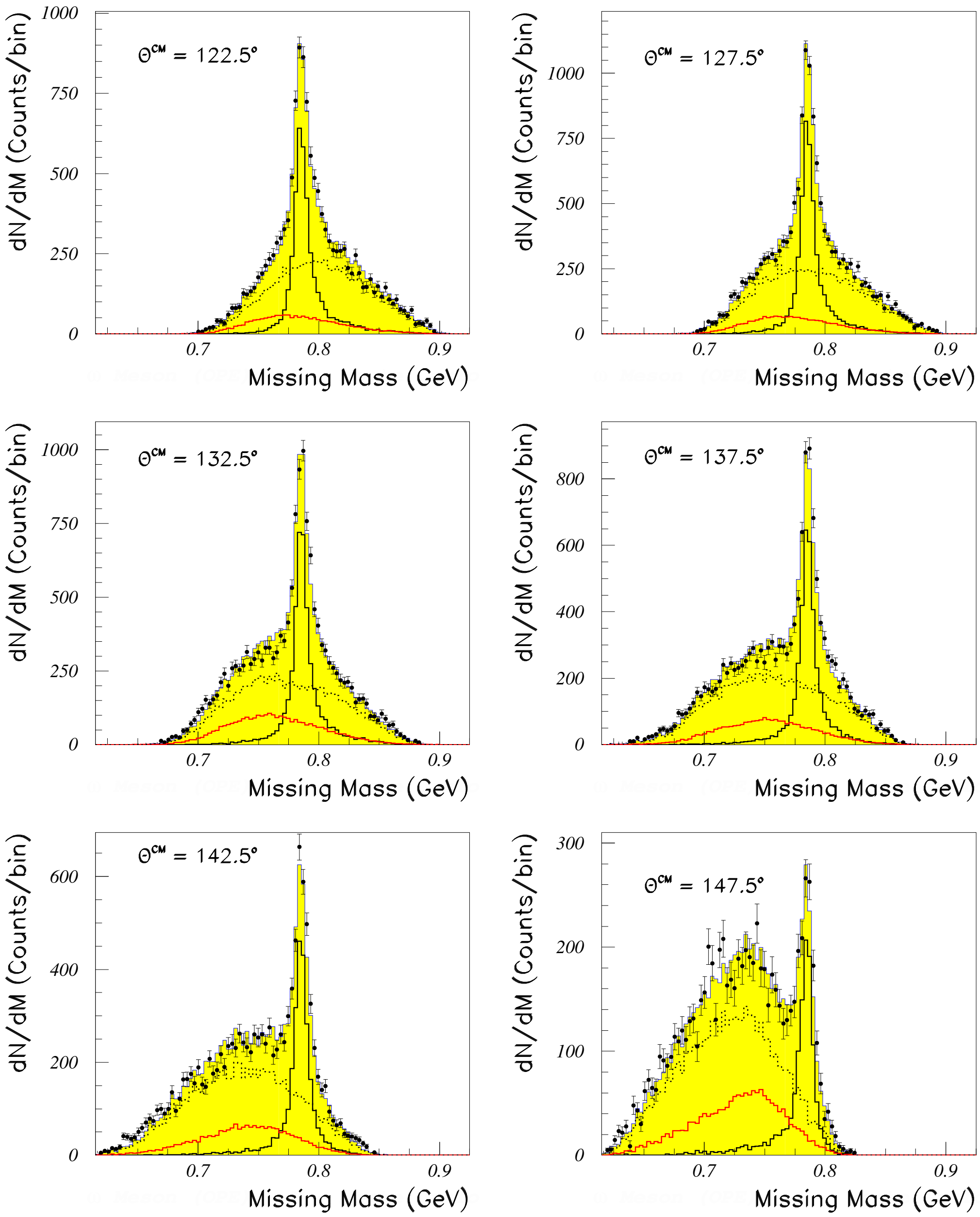

Figure 4.18: **Fit Breakdown In Missing Mass M_x:** *Single bin fit broken down into contributions in the missing mass M_x for $p_0^{\mathrm{SOS}} = 1.077\,GeV$ and $\theta_{\gamma\mathrm{p}} = 8.8^o$. Solid circles with error bars are the data. The shaded histogram is the full Monte Carlo fit. Dotted histogram is the phase space, solid black histogram is the ω while grey (red) histogram is the ρ^0.*

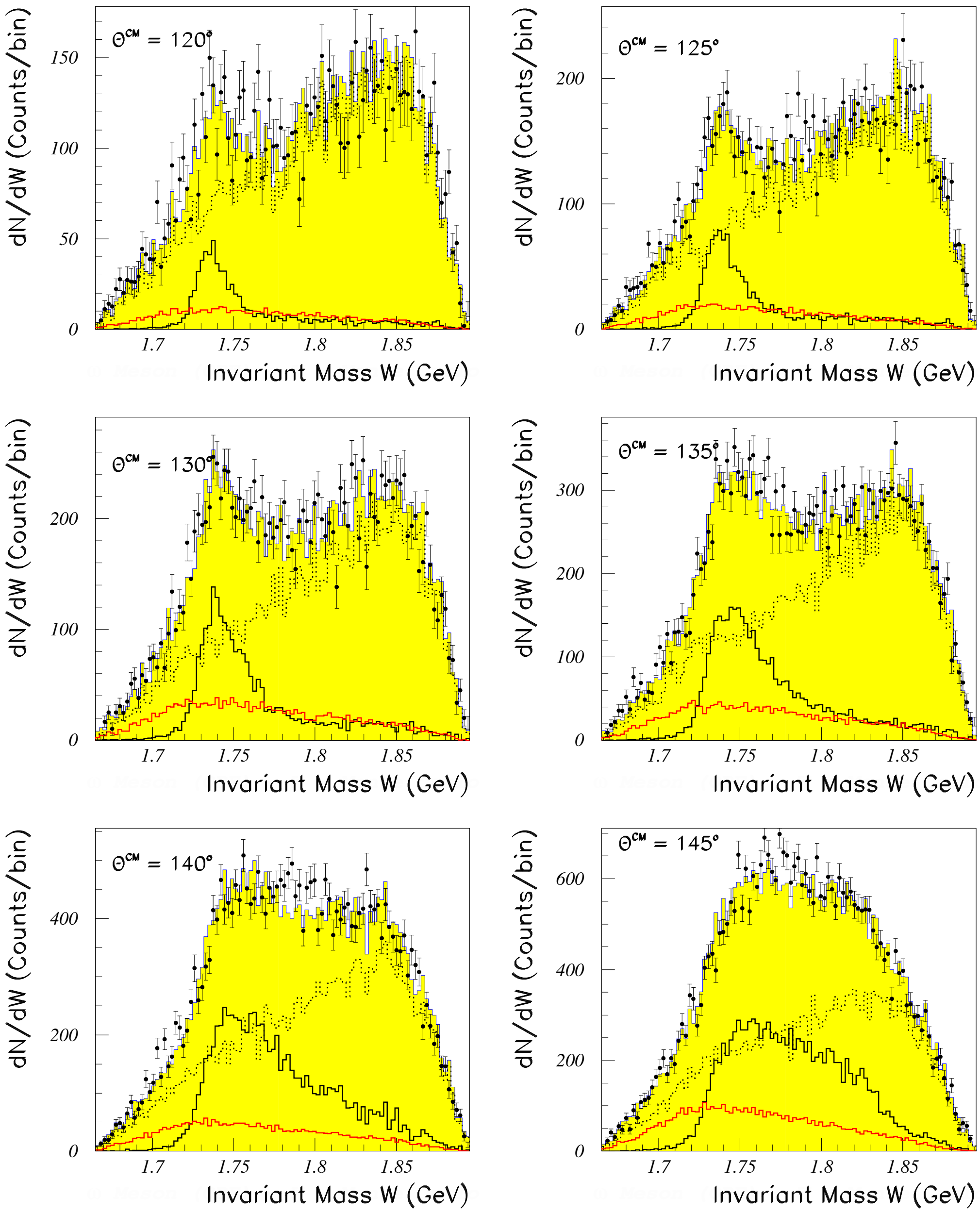

Figure 4.19: **Fit Breakdown In Invariant Mass** W**:** *Single bin fit broken down into contributions in the invariant mass* W *for* $p_0^{\mathrm{SOS}} = 1.077\,GeV$ *and* $\theta_{\gamma\mathrm{p}} = 4.3^o$*. Solid circles with error bars are the data. The shaded histogram is the full Monte Carlo fit. Dotted histogram is the phase space, solid black histogram is the* ω *while grey (red) histogram is the* ρ^0*.*

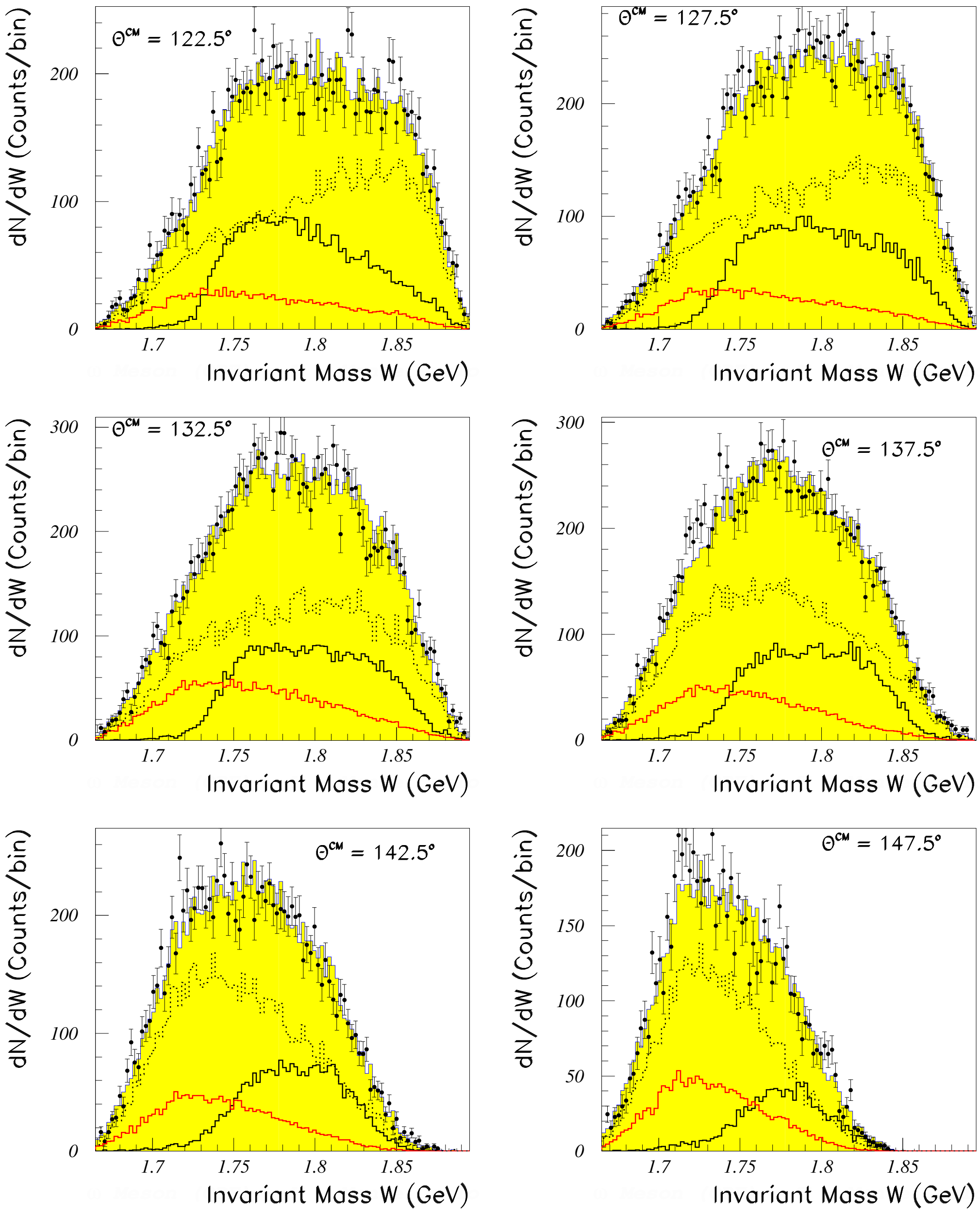

Figure 4.20: **Fit Breakdown In Invariant Mass** W**:** *Single bin fit broken down into contributions in the invariant mass* W *for* $p_0^{\mathrm{SOS}} = 1.077\,GeV$ *and* $\theta_{\gamma\mathrm{p}} = 8.8^o$*. Solid circles with error bars are the data. The shaded histogram is the full Monte Carlo fit. Dotted histogram is the phase space, solid black histogram is the* ω *while grey (red) histogram is the* ρ^0

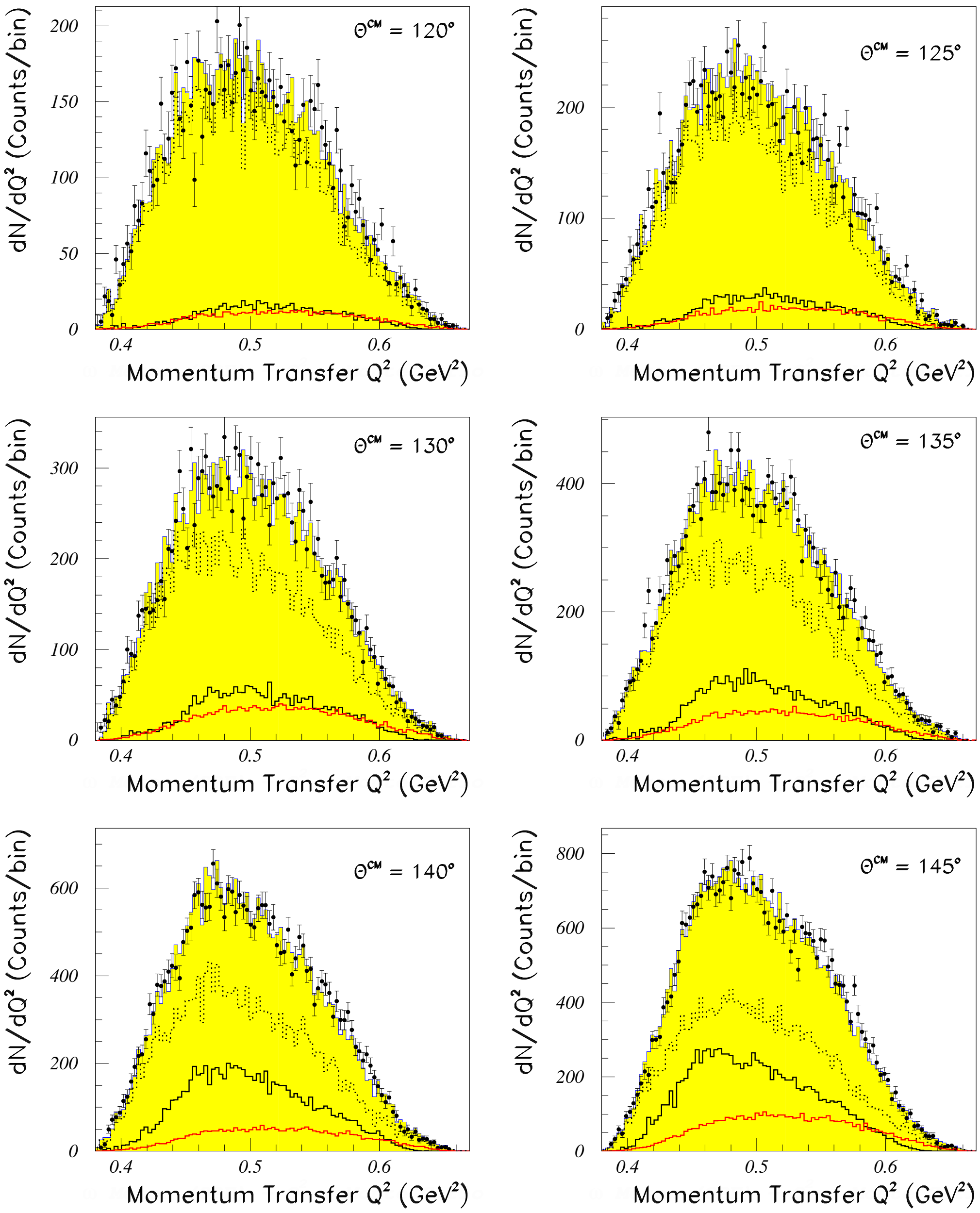

Figure 4.21: **Fit Breakdown In Momentum Transfer Q^2:** *Single bin fit broken down into contributions in the momentum transfer Q^2 for $p_0^{\mathrm{SOS}} = 1.077$ GeV and $\theta_{\gamma\mathrm{p}} = 4.3^o$. Solid circles with error bars are the data. The shaded histogram is the full Monte Carlo fit. Dotted histogram is the phase space, solid black histogram is the ω while grey (red) histogram is the ρ^0.*

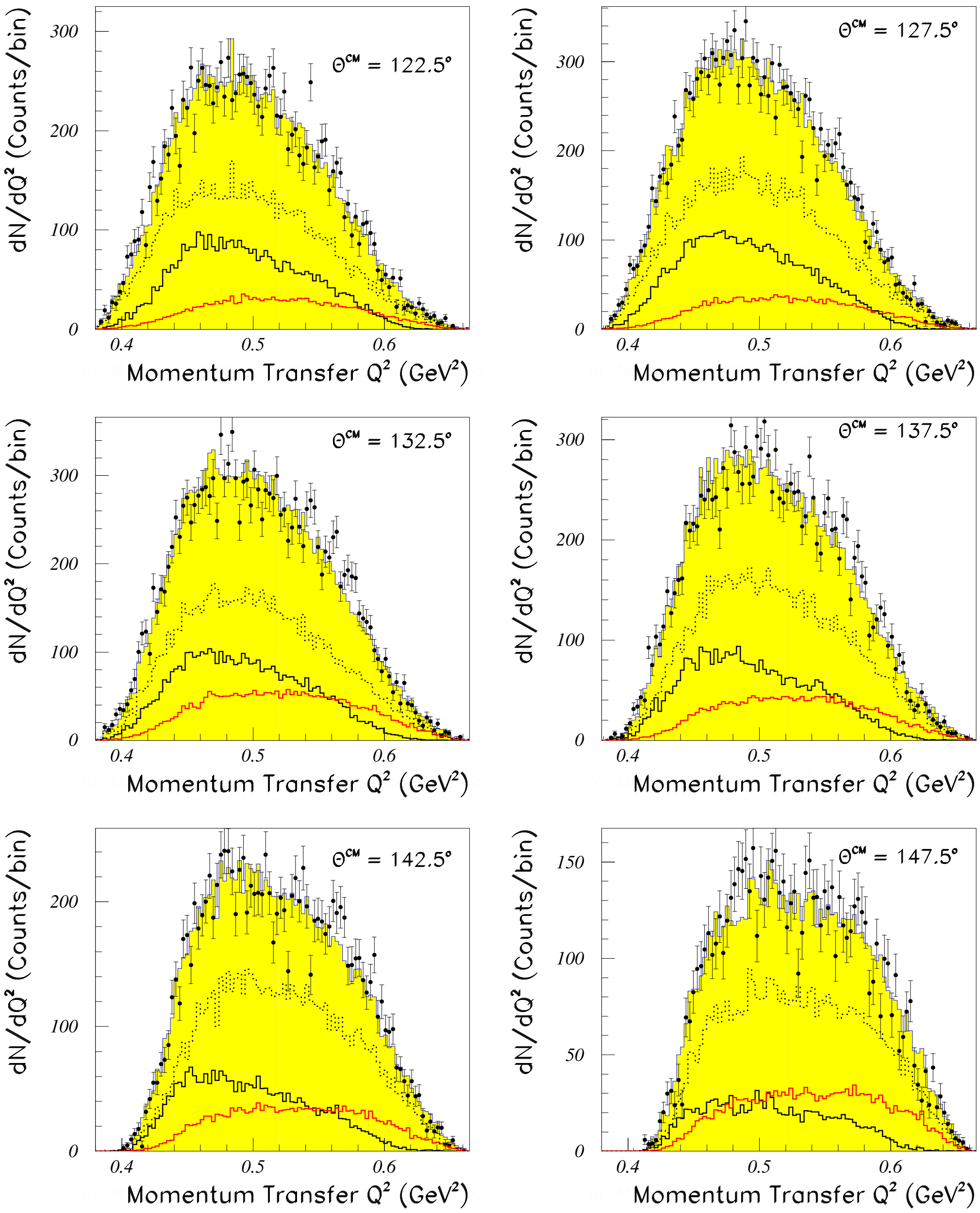

Figure 4.22: **Fit Breakdown In Momentum Transfer Q^2:** *Single bin fit broken down into contributions in the momentum transfer Q^2 for $p_0^{\mathrm{SOS}} = 1.077$ GeV and $\theta_{\gamma\mathrm{p}} = 8.8^o$. Solid circles with error bars are the data. The shaded histogram is the full Monte Carlo fit. Dotted histogram is the phase space, solid black histogram is the ω while grey (red) histogram is the ρ^0.*

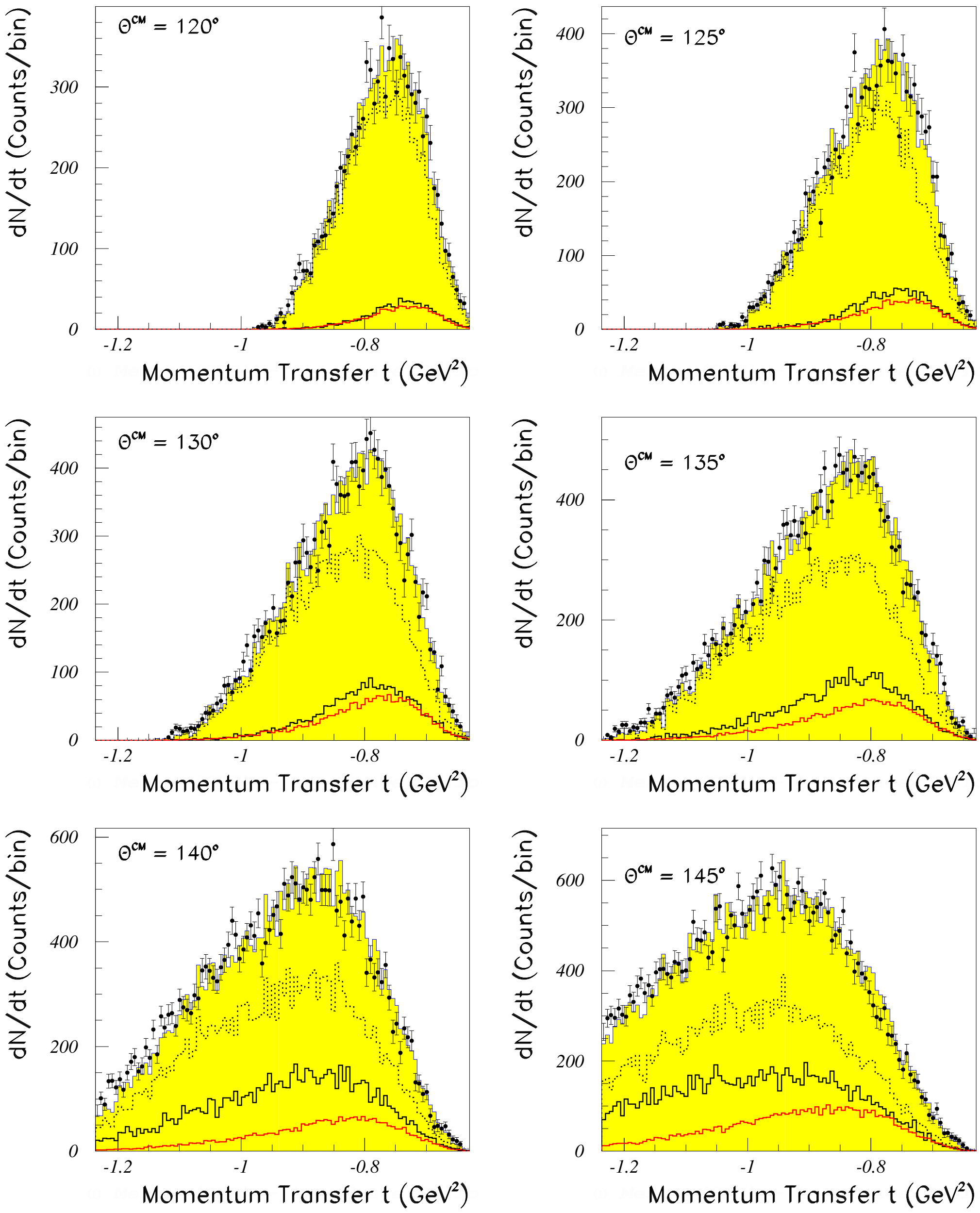

Figure 4.23: **Fit Breakdown In Momentum Transfer t:** *Single bin fit broken down into contributions in the momentum transfer t for $p_0^{\mathrm{SOS}} = 1.077$ GeV and $\theta_{\gamma\mathrm{p}} = 4.3^o$. Solid circles with error bars are the data. The shaded histogram is the full Monte Carlo fit. Dotted histogram is the phase space, solid black histogram is the ω while grey (red) histogram is the ρ^0. The sharp cut off is due to the cut on the SOS momentum.*

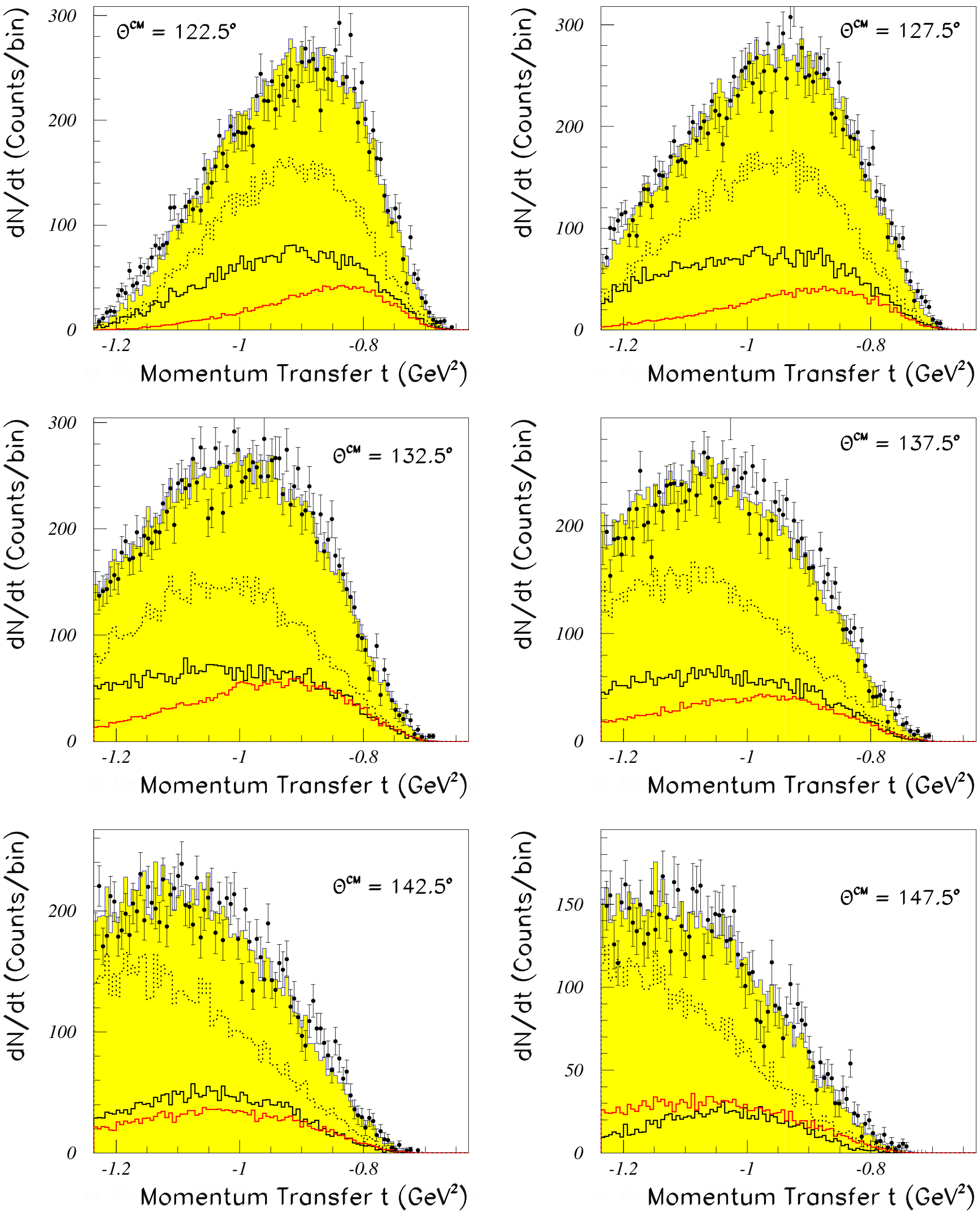

Figure 4.24: **Fit Breakdown In Momentum Transfer** t**:** *Single bin fit broken down into contributions in the momentum transfer* t *for* $p_0^{\mathrm{SOS}} = 1.077$ *GeV and* $\theta_{\gamma\mathrm{p}} = 8.8^o$*. Solid circles with error bars are the data. The shaded histogram is the full Monte Carlo fit. Dotted histogram is the phase space, solid black histogram is the* ω *while grey (red) histogram is the* ρ^0*. The sharp cut off is due to the cut on the SOS momentum.*

4.7 Extraction Of The Differential Cross Section

Figures 4.25 and 4.26 show the data yields and the Monte Carlo fits after background subtraction for two different θ^{CM} bins in low and high statistics runs. These yields were subsequently used to extract the differential vitrual photon cross section with the aid of the formula,

$$\frac{d\sigma_D}{d\Omega^{CM}} = \left(\frac{Y_D}{Y_{MC}}\right) \frac{d\sigma_{MC}}{d\Omega^{CM}} \tag{4.25}$$

where the yields are in μb.

The Monte Carlo yield N_{MC} (in number of counts) is given by

$$N_{MC} = n_p N_e \int_{\mathcal{A}} \left(\frac{d\sigma_{MC}}{dv}\right)_{RAD} (v)\ \delta^{(4)}(P_i(v) - P_f(v))\ dv \tag{4.26}$$

where

- n_p is the number of protons per cm^2,
- N_e is the number of incident electrons,
- $n_p N_e = \mathcal{L}_{MC}$ is the Monte Carlo luminosity,
- $\mathcal{A}$ is the acceptance of the experimental apparatus, either total or fractional,
- $\delta^{(4)}(P_i(v) - P_f(v))$ is the δ-function ensuring the energy-momentum conservation,
- dv is an element of the generation volume,
- v is a point within the generation volume,
- $(d\sigma_{MC}/dv)_{RAD}$ is the radiated model cross section, differential in variables spanning the generation volume.

Converting N_{MC} to Y_{MC}, inserting it into 4.25, and since the concentration of protons per cm^2 is the same for both the data and the Monte Carlo, gives the final formula for extracting the cross section

$$\begin{aligned}
\frac{d\sigma_D}{d\Omega^{CM}} &= \left(\frac{N_D}{N_{MC}}\right)\left(\frac{\mathcal{L}_{MC}}{\mathcal{L}_D}\right)\frac{d\sigma_{MC}}{d\Omega^{CM}} && (4.27)\\
&= \left(\frac{N_D}{N_{MC}}\right)\left(\frac{N_e}{Q^{DATA}/e}\right)\frac{d\sigma_{MC}}{d\Omega^{CM}} && (4.28)
\end{aligned}$$

where

- Q^{DATA} is the integrated beam charge,
- e is the electron charge,
- $d\sigma_{MC}/d\Omega^{CM}$ is the virtual photon model cross section computed at the center of the bin of interest.

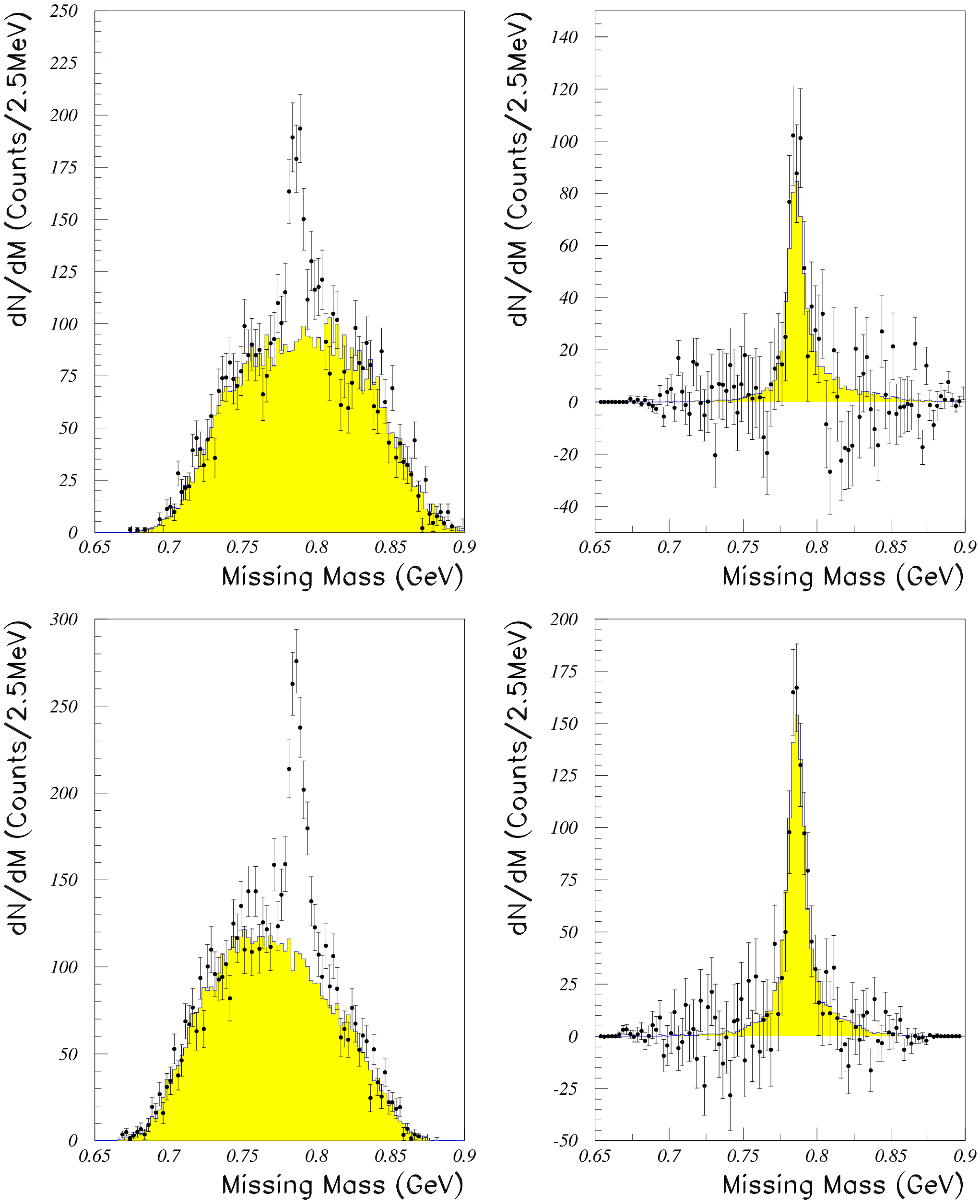

Figure 4.25: **Signal-Background Separation:** *Separation for the low statistics run,* $p_0^{\mathrm{SOS}} = 0.929$ *GeV and* $\theta_{\gamma \mathrm{p}} = 13.3^o$*.* (Top)*:* $\theta^{\mathrm{CM}} = 92.5^o$*.* (Bottom)*:* $\theta^{\mathrm{CM}} = 107.5^o$*.*

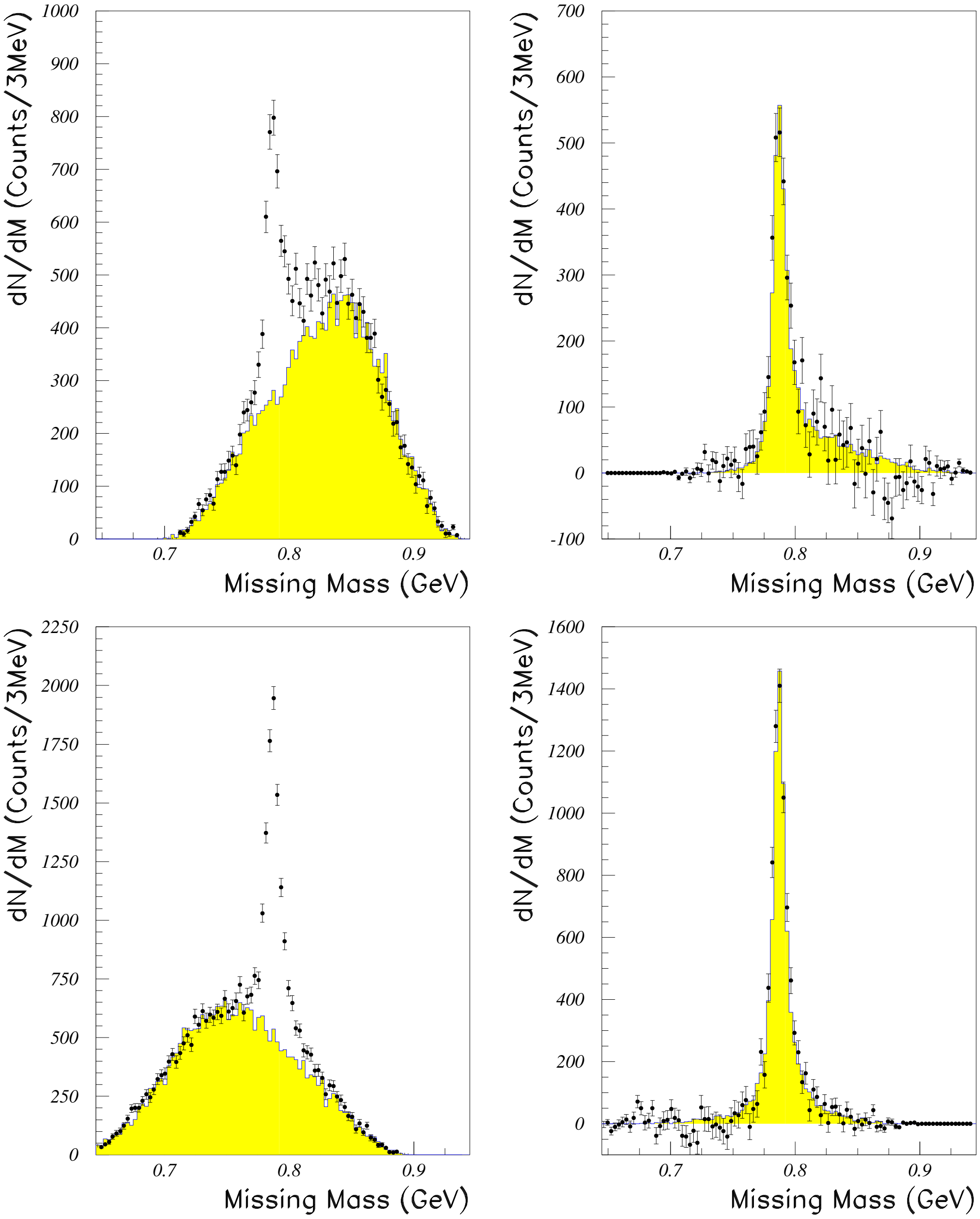

Figure 4.26: **Signal-Background Separation:** *Separation for the low statistics run,* $p_0^{\rm SOS} =$ 1.077 *GeV and* $\theta_{\gamma\rm p} = 4.3^o$. *(*Top*):* $\theta^{\rm CM} = 135^o$. *(*Bottom*):* $\theta^{\rm CM} = 160^o$.

CHAPTER 5

RESULTS AND CONCLUSIONS

5.1 Results & Errors

The differential cross section for the electroproduction of the ω meson at $Q^2 = 0.5\,(\mathrm{GeV/c})^2$ was extracted, as outlined in the preceding chapter, for 60 θ^{CM} bins mostly for backward directions in the virtual photon proton Center-Of-Momentum system. Statistics in these bins varied from several hundred (~ 500) to well over ten thousand (> 11000) events per bin. Two cross section angular distributions were formed. First pertaining to lower average W and comprising the intermediate SOS momentum ($p_0^{\mathrm{SOS}} = 0.929\,\mathrm{GeV/c}$) settings except for the $\theta_{\gamma\mathrm{p}} = 17.3^o$ setting. The latter was incorporated in the angular distribution with higher average W and comprised the high SOS momentum ($p_0^{\mathrm{SOS}} = 1.077\,\mathrm{GeV/c}$) settings (refer to Table 2.3 on page 63).

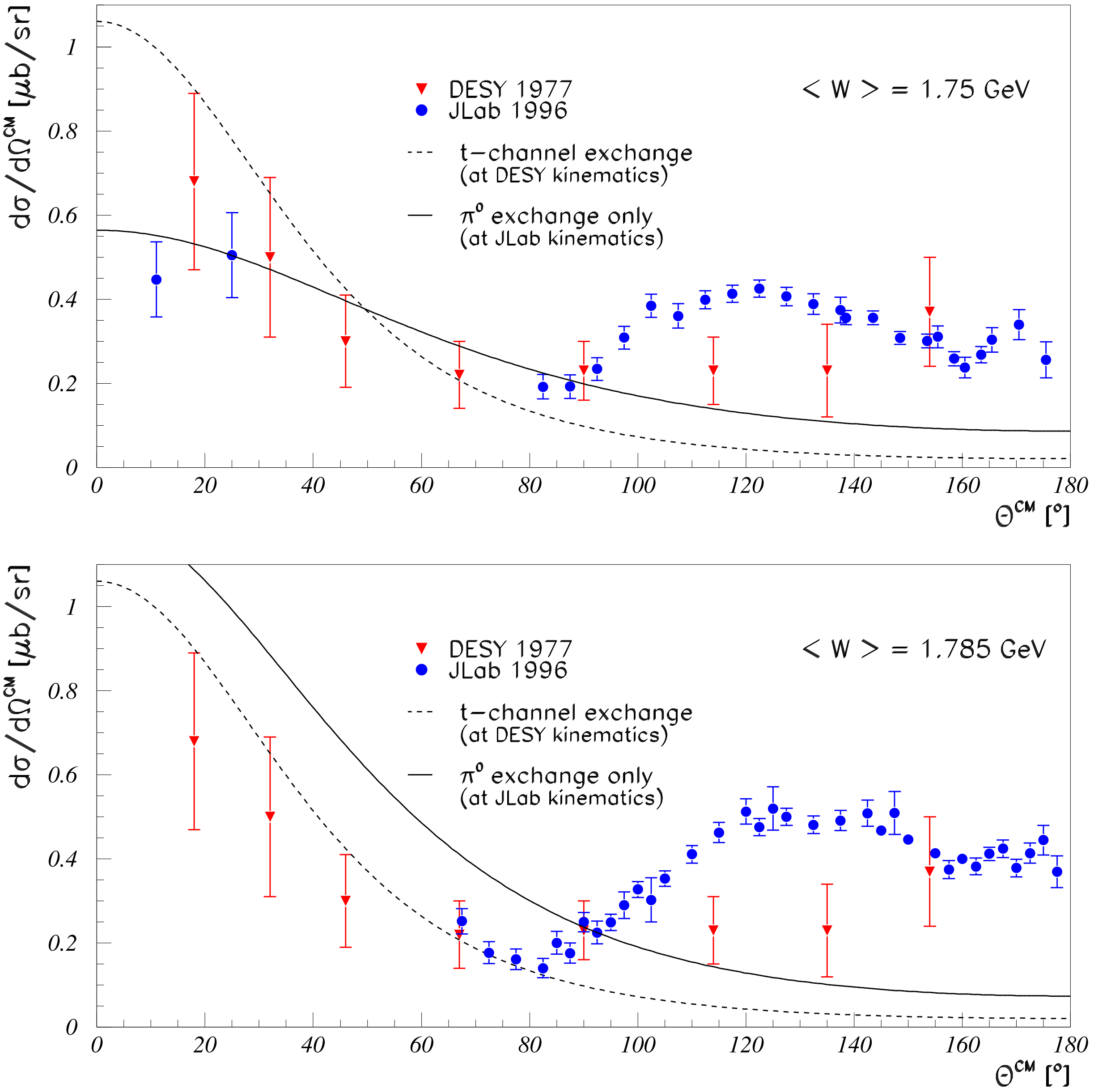

Figure 5.1: $\mathbf{p(e,e'p)}\omega$ ***Results:*** *The angular distributions for different average W.*

This approach was forced by the existance of very tight $W - M_x$ correlation due to relatively small acceptance of the apparatus, as repeatedly mentioned in the previous chapter.

Table 5.1: *Differential cross sections ($\langle \mathrm{W}_{\mathrm{total}} \rangle = 1.75$ GeV).*

θ^{CM} [deg]	$d\sigma/d\Omega^{CM}$ [$\mu b/sr$]	Uncertainty Statistical	Systematic	$\langle \mathbf{W} \rangle$ [GeV]	$\langle \mathbf{Q^2} \rangle$ [$(\mathbf{GeV/c})^2$]
11.00	0.447	0.089	0.015	1.761	0.519
25.00	0.505	0.101	0.017	1.776	0.508
82.50	0.192	0.030	0.006	1.774	0.503
87.50	0.192	0.028	0.006	1.778	0.500
92.50	0.234	0.027	0.008	1.783	0.498
97.50	0.308	0.027	0.010	1.790	0.494
102.50	0.384	0.027	0.013	1.797	0.490
107.50	0.360	0.029	0.012	1.796	0.490
112.50	0.399	0.022	0.013	1.759	0.507
117.50	0.413	0.021	0.014	1.763	0.505
122.50	0.425	0.021	0.014	1.765	0.503
127.50	0.407	0.022	0.013	1.762	0.503
132.50	0.389	0.024	0.013	1.759	0.504
137.50	0.374	0.031	0.012	1.756	0.504
138.50	0.356	0.017	0.012	1.747	0.509
143.50	0.356	0.017	0.012	1.748	0.509
148.50	0.308	0.016	0.010	1.748	0.509
153.50	0.301	0.017	0.010	1.746	0.510
155.50	0.311	0.026	0.010	1.747	0.506
158.50	0.258	0.017	0.009	1.744	0.510
160.50	0.238	0.024	0.008	1.748	0.502
163.50	0.268	0.019	0.009	1.743	0.511
165.50	0.303	0.029	0.010	1.749	0.496
170.50	0.339	0.036	0.011	1.750	0.495
175.50	0.256	0.043	0.008	1.749	0.493

This resulted in an inability to bin the data in W and θ^{CM} and simultaneously perform meaningful fit for signal-background separation. Having not more than 140 MeV of W range

Table 5.2: ***Differential cross sections*** **($\langle \mathrm{W_{total}} \rangle = 1.785\, GeV$).**

θ^{CM} [deg]	$d\sigma/d\Omega^{CM}$ [$\mu b/sr$]	Uncertainty Statistical	Uncertainty Systematic	$\langle \mathbf{W} \rangle$ [GeV]	$\langle \mathbf{Q^2} \rangle$ [$(\mathrm{GeV/c})^2$]
67.50	0.252	0.030	0.008	1.808	0.489
72.50	0.177	0.027	0.006	1.812	0.487
77.50	0.161	0.024	0.005	1.815	0.484
82.50	0.140	0.023	0.005	1.819	0.479
85.00	0.201	0.027	0.007	1.780	0.510
87.50	0.176	0.024	0.006	1.821	0.477
90.00	0.250	0.023	0.008	1.783	0.502
92.50	0.225	0.027	0.007	1.825	0.475
95.00	0.249	0.020	0.008	1.790	0.498
97.50	0.290	0.032	0.010	1.827	0.473
100.00	0.327	0.019	0.010	1.801	0.490
102.50	0.303	0.053	0.010	1.827	0.470
105.00	0.354	0.018	0.011	1.808	0.486
110.00	0.411	0.021	0.014	1.810	0.484
115.00	0.463	0.024	0.015	1.814	0.481
120.00	0.513	0.030	0.017	1.816	0.482
122.50	0.476	0.021	0.016	1.786	0.495
125.00	0.520	0.052	0.017	1.812	0.484
127.50	0.500	0.021	0.017	1.793	0.492
132.50	0.481	0.021	0.016	1.792	0.494
137.50	0.491	0.024	0.016	1.788	0.495
142.50	0.509	0.031	0.017	1.784	0.497
145.00	0.468	0.013	0.015	1.774	0.498
147.50	0.510	0.051	0.017	1.774	0.508
150.00	0.446	0.012	0.015	1.775	0.500
155.00	0.413	0.012	0.014	1.773	0.501
157.50	0.375	0.021	0.012	1.764	0.507
160.00	0.400	0.013	0.013	1.770	0.504
162.50	0.382	0.020	0.013	1.770	0.500
165.00	0.412	0.016	0.014	1.766	0.507
167.50	0.425	0.021	0.014	1.774	0.495
170.00	0.379	0.021	0.013	1.757	0.513
172.50	0.414	0.024	0.014	1.775	0.493
175.00	0.445	0.036	0.015	1.748	0.522
177.50	0.370	0.038	0.012	1.775	0.492

available any $W - \theta^{\mathrm{CM}}$ binning had a profound effect on the background underneath the ω meson. For a number of bins there was not enough background for the appreciable fit, therefore no W binning was implemented. The results are presented in Figure 5.1 and Tables 5.1 and 5.2.

The mass and the width of the ω meson, which are in very good agreement with the values quoted by the Particle Data Group (Caso et al., 1998; Groom et al., 2000), extracted from the data are shown in Table 5.3.

Table 5.3: ***The ω meson parameters.***

	Mass	**Width**
ω meson	$782.3 \pm 1.3\,\mathrm{MeV}$	$8.9 \pm 1.1\,\mathrm{MeV}$

The price one has to pay for observing the ω in the final state in which only scattered electron and proton are detected is relatively large statistical error due to the background subtraction regardless of how good the statistics of the ω meson itself in a given bin is. In addition the signal/background separation introduces a sizeable systematic error. These background related uncertainties are the largest source of errors and combined they exceed by about an order of magnitude any other error. Therefore care had to be exercised when these errors were estimated. The statistical uncertianties of the data and Monte Carlo yields were propagated through the background subtraction and into the final cross section for each bin. The systematic uncertainty due to background removal was estimated by changing the fitting conditions (bin width in fitted histograms and/or bin width in the angular distribution). to the total systematic uncertainty listed in Tables 5.1 and 5.2.

Table 5.4: *Global Systematic Uncertainties.*

Quantity	**Uncertainty (%)**
Total Charge	1.0
Target Length	0.4
Target Density	0.4
SOS Trigger Efficiency	0.1
HMS Trigger Efficiency	0.1
SOS Tracking Efficiency	1.0
HMS Tracking Efficiency	0.5
SOS Electronic Live Time	0.1
HMS Electronic Live Time	0.1
Computer Live Time	0.3
Time-Of-Flight β	1.8
Accidental Subtraction	1.0
Radiative Corrections	2.0
Geometric Sum	3.3

This procedure yielded an estimate of the systematic uncertainty for each bin. All remaining uncertainties were global in nature. The total charge uncertainty was estimated by looking at a variation of the ratio of the charge, as reported by BCM2 and BCM3, as a function of run number. The tracking efficiencies errors were determined from their variations with the incident particle rate. The uncertainty due the random subtraction was estimated by comparing results for different coincidence time cuts used in determining the fraction of the accidentals in the data sample. The uncertainty steming from the correction for the radiative effects was determined by studying the dependence of the data to Monte Carlo yield ratio on the W cut on the elastic peak (Armstrong, 1998). The global systematic errors are listed in the Table while bin dependent errors were added Variation of the cross section with the change of the momentum and geometrical acceptance cuts used in the analysis was also investigated. The uncertainty that stemed from varying the geometrical acceptance cuts, by $\pm 10\%$, was estimated to be $\sim 1.2\%$. The error introduced by changing the momentum cuts (by $\pm 5\%$ and $\pm 2.5\%$ for the SOS and HMS respectively) turned out to be slightly setting dependent and varied from 1.2% to 1.8%.

5.2 Discussion

The energy dependence of the total cross section for the ω photoproduction measured by the *ABBHHM* collaboration was well described by natural and unnatural t-channel parity exchange (ABBHHM Collaboration, 1968). However at the two lowest photon energies, there is an excess of events at large Center-Of-Momentum scattering angles - see Figures 5.2 or 1.11. A similar trend is apparent in the angular distribution of the later electroproduction results from *DESY* (Joos et al., 1977), see Figure 5.3. In that data set the ω meson scattered forward (peripheral component) and backward (non-peripheral component) were separated by employing a cut on the momentum transfer, t - see Figure 1.12.

The non-peripheral component shows strong W dependence. It rises steeply in the vicinity of the ω threshold and quickly decreases for W higher than $\sim 1.9\,\mathrm{GeV}$. Using such a momentum transfer cut in the analysis of the *ABBHHM* photoproduction data reveals not as strong but similar behavior at 150 MeV above the threshold ($1.87\,\mathrm{GeV} < W < 2.1\,\mathrm{GeV}$) - see Figure 5.4 and 5.5.

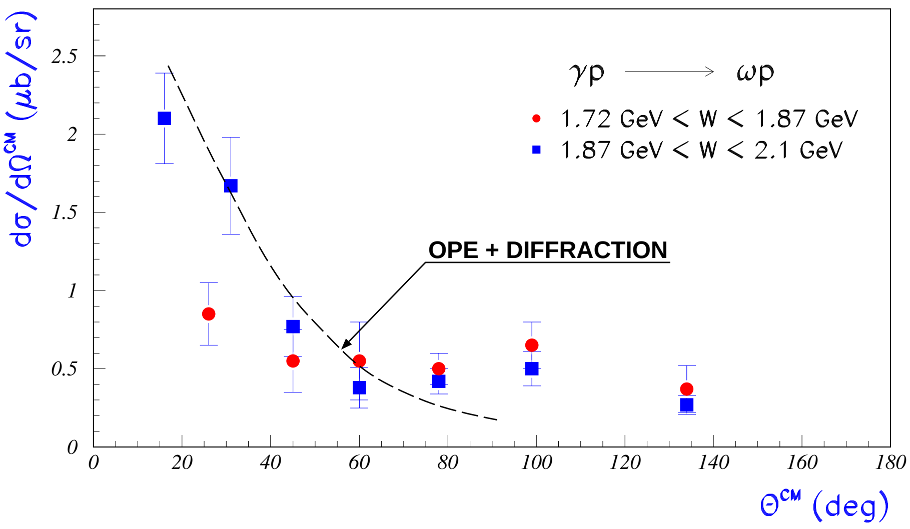

Figure 5.2: ***ω* Photoproduction:** *The angular distribution of the differential cross section. The model curve is an extrapolation to* $Q^2 = 0$ *of the model of Ref (Joos et al., 1976).*

The total cross section follows, to a good approximation, the behavior of the model for this region. It seems rather unlikely, judging from the angular distribution, that the total cross section in the threshold regime (solid circles in Figures 5.2 and 5.3) would be similarily well described by the parity exchange. It is evident that near threshold, regardless of whether it is electroproduction or photoproduction one deals with, there exists an enhancement in the ω meson cross section over the t-channel processes.

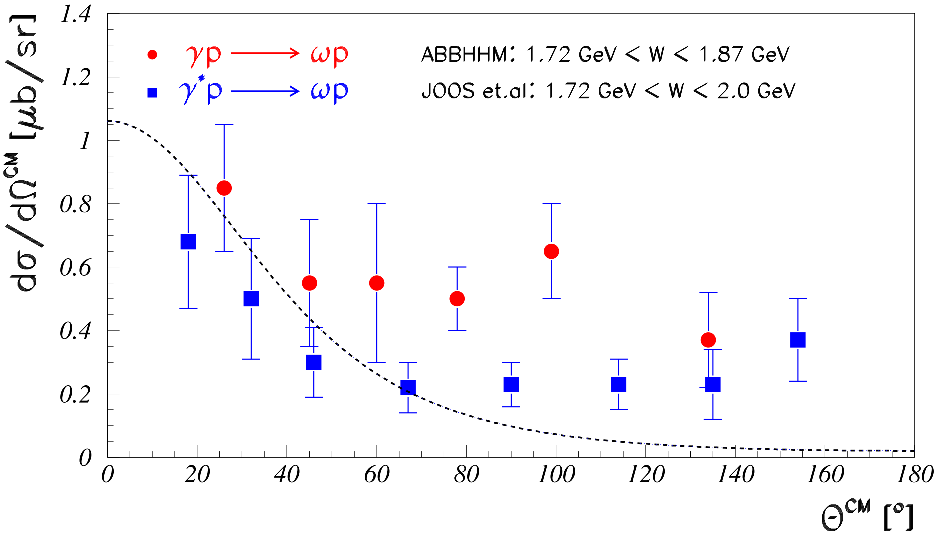

Figure 5.3: **ω *Electro- and Photoproduction:*** *Angular distributions in the threshold regime. Dashed curve represents the t-channel parity exchange electroproduction model described in Ref (Joos et al., 1977).*

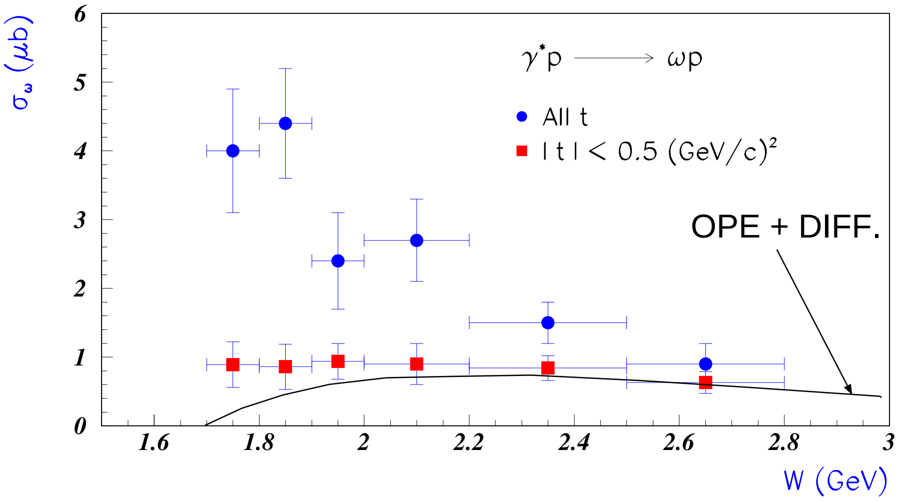

Figure 5.4: **ω *Electroproduction:*** *Total cross section for the electroproduction as a function of the CM energy, for W ranging from* 1.72 GeV *to* 2.0 GeV*.*

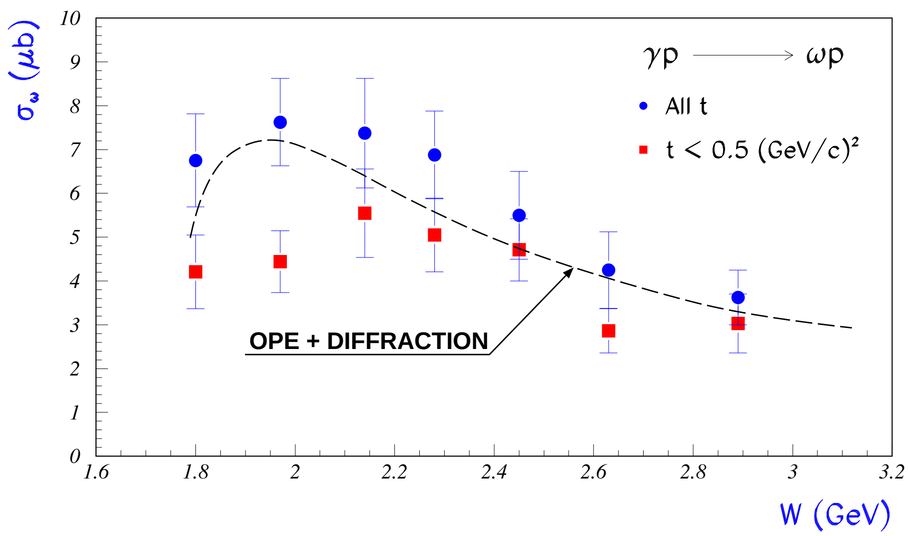

Figure 5.5: ***ω* Photoproduction:** *Total cross section for the photoproduction as a function of the CM energy, for W ranging from* 1.87 *GeV to* 2.1 *GeV.*

This departure from the smooth fall-off of the t-channel processes, either in the angular distribution or t-dependence, has been attributed to formation of s- and u-channel resonances. This is supported by recent theoretical calculations (Zhao, Bennhold, & Li, 1998; Zhao, Li, & Bennhold, 1998; Zhao, 2000; Oh, Titov, & Lee, 2000; Oh, Lee, & Titov, 2000). At the time of writing this dissertation some effort in the electroproduction sector was ongoing (Oh, 2001) and only the photoproduction models were developed and studied. These models were tested mainly against the data from *SAPHIR '94* (Klein, 1996). In Figure 5.6 only nucleon exchange terms (see diagrams (a) and(b) in Figure 1.13), apart from parity exchange, were left in the calculation of the total cross section and t-dependence of the differential cross section (Oh, Titov, & Lee, 2000). The total cross section again suffers a deficiency in strength in the near threshold region.

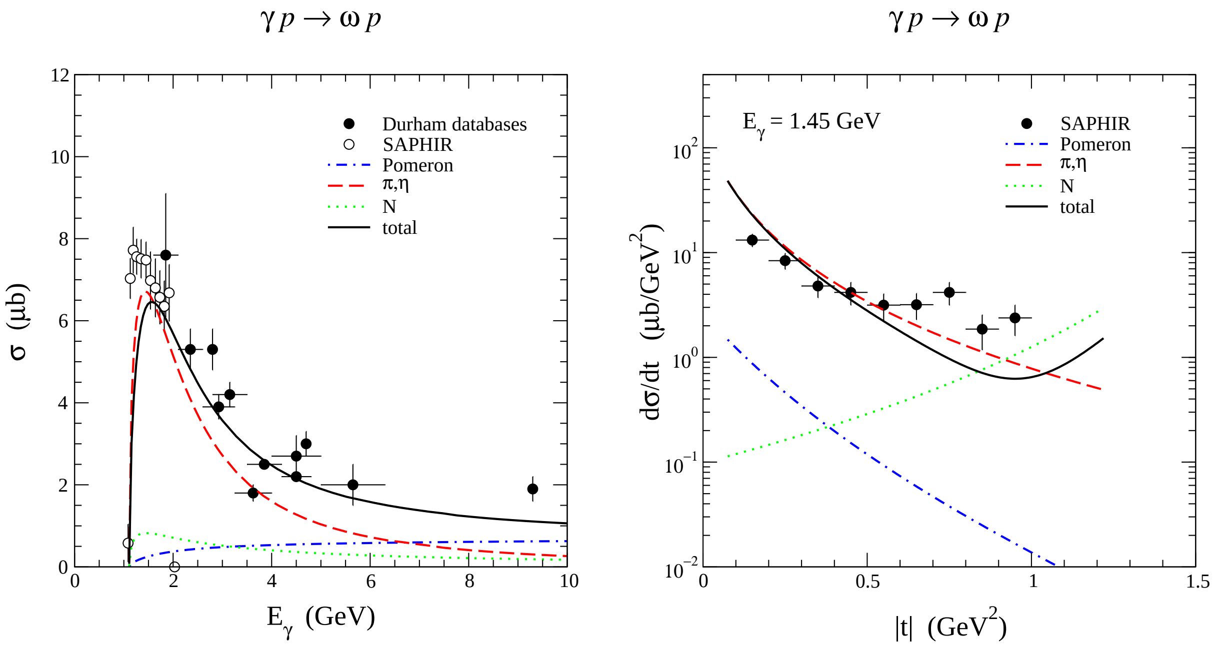

Figure 5.6: ***Photoproduction Theory:*** (Left) - *Total cross section.* (Right) - *Differential cross section. Individual contributions are represented by respective lines, as given on the plots. The nucleon contribution* (dotted *line) only includes the intermediate nucleon exchange diagrams - (a) and (b) on Figure1.13.*

The effect of inclusion of the resonant terms, shown in Figure 1.13 (c) and (d), was studied for different photon energy regimes - see Figure 5.7 (Oh, Titov, & Lee, 2000; Oh, Lee, & Titov, 2000). In this figure, conventionally, the solid line represents the total model behavior. The dotted line corresponds to the $N^\star$ excitation while dashed line corresponds to pseudoscalar meson exchange (π,η). The Pomeron exchange is represented by the dotted-dashed line and the dotted-dotted-dashed curve stands for the nucleon exchange. For low photon energies, or near threshold (see plot (a) in Figure 5.7), the description is still insuf-

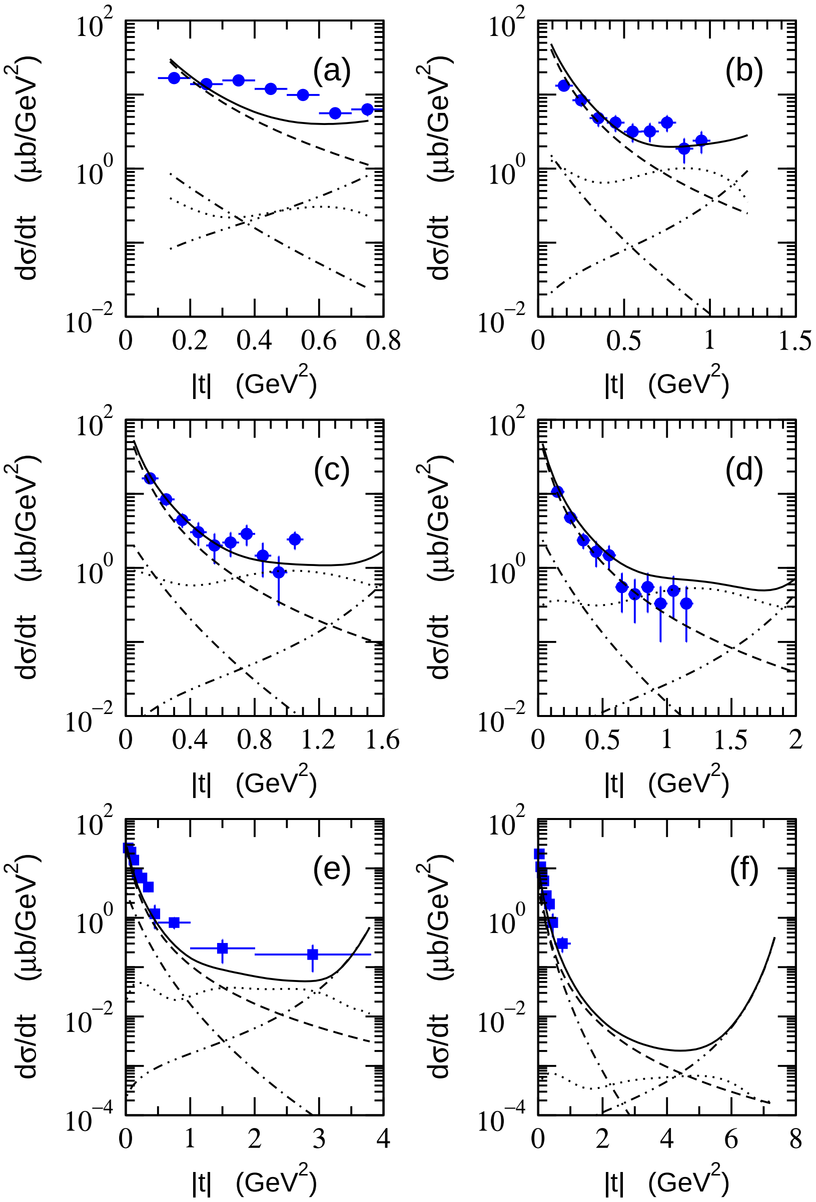

Figure 5.7: ***SAPHIR Data:*** *t-distributions for ω meson photoproduction for different intervals of the photon energy. Increasing $|t|$ corresponds to backward θ^{CM} angles.* (a) $E_\gamma = 1.23\,GeV$, (b) $E_\gamma = 1.45\,GeV$, (c) $E_\gamma = 1.68\,GeV$, (d) $E_\gamma = 1.92\,GeV$, (e) $E_\gamma = 2.8\,GeV$, (f) $E_\gamma = 4.7\,GeV$, *last two plots come from Ref. (Ballam et al., 1973).* Dotted *line represents a s-channel contribution,* dashed *and* dashed-dotted *lines correspond to t-channel parity exchange processes, OPE and Pomeron exchange respectively while* dashed-double-dotted *line represents u-channel processes.*

ficient although the total cross section as a function of W is reproduced rather well - see Figure 5.8.

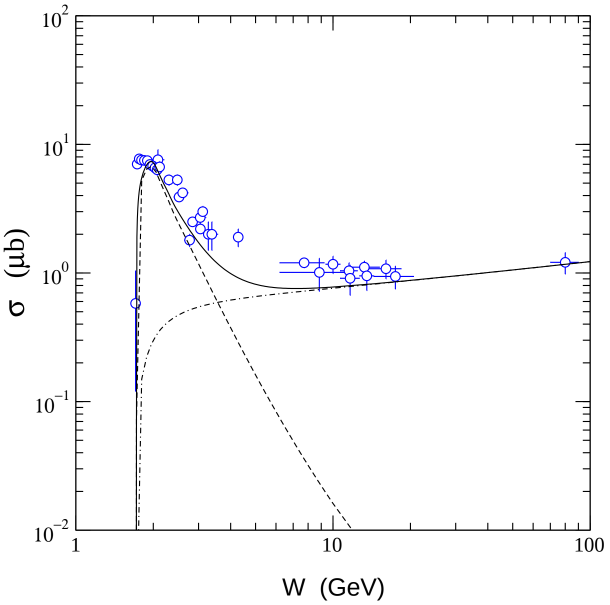

Figure 5.8: ***Photoproduction Theory:*** *Energy dependence of the total cross section* (solid *curve*) *for the model shown in Figure 5.7.* Dashed *curve - calculation without the Pomeron contribution.* Dotted-dashed *curve - Pomeron exchange.*

Table 5.5: *The s-channel nucleon excited states.*

State	L_{2I2J}	Status	Mass	Width
N(1440)	P_{11}	⋆⋆⋆⋆	1440	350
N(1520)	D_{13}	⋆⋆⋆⋆	1520	120
N(1535)	S_{11}	⋆⋆⋆⋆	1535	150
N(1680)	$\boldsymbol{F_{15}}$	⋆⋆⋆⋆	**1680**	**130**
N(1710)	P_{11}	⋆⋆⋆	1710	100
N(1720)	$\boldsymbol{P_{13}}$	⋆⋆⋆⋆	**1720**	**150**
N(1900)	P_{13}	⋆⋆	1900	250
N(2000)	F_{15}	⋆⋆	2000	250

The angular or t distributions are seen to provide a more incisive test of the validity of the model. Within this model (Oh, Titov, & Lee, 2000; Oh, Lee, & Titov, 2000) it was found that the dominant contributions came from a missing resonance, $N^{+}_{3/2}(1910)$, and $N^{-}_{3/2}(1960)$ which is labeled $D_{13}(2080)$ by the Particle Data Group.

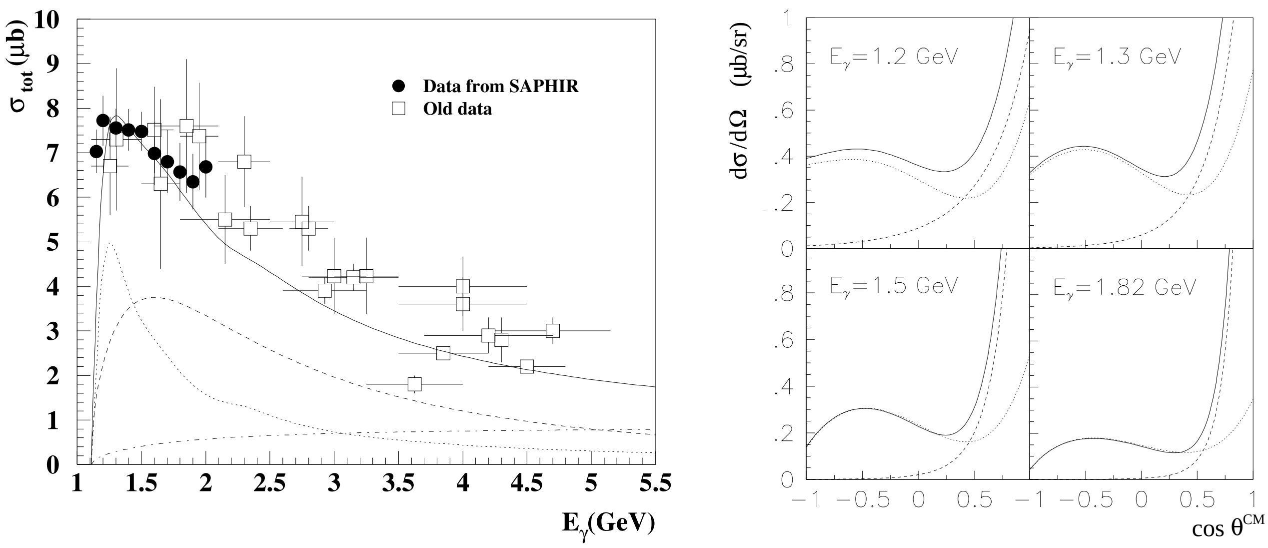

Figure 5.9: ***Photoproduction Theory:*** (Left) - *Total cross section as a function of photon energy overlayed on top of the existing data.* ***solid*** *curve represents the total cross section,* ***dashed*** *curve represents t-channel π^0 exchange while* ***dashed-dotted*** *curve represents t-channel Pomeron exchange, finally* ***dotted*** *curve shows the u- and s-channel resonance contribution.* (Right) - *Predictions for the differential cross section for different photon energies,* ***solid*** *curve represents the total cross section,* ***dashed*** *curve represents t-channel parity exchange,* ***dotted*** *curve shows the u- and s-channel resonance contribution. The above plots were taken from Ref. (Zhao, 2000).*

Other calculations (Zhao, Bennhold, & Li, 1998; Zhao, Li, & Bennhold, 1998; Zhao, 2000) however differ in predictions as to which nucleonic excitations could contribute in the s-channel. All the contributing low-lying states, $n \leq 2$ in the harmonic oscillator basis, are listed in Table 5.5. The states with $n > 2$ were treated as degenerate in this model. It was found that the contribution from two resonances, $P_{13}(1720)$ and $F_{15}(1680)$ (in bold face in Table 5.5), dominated the contributions from the other states. The results of these calculations are shown in Figure 5.9. Although the neutral pion exchange plays a dominant role over large energy regime the resonant contributions govern the total cross section from the threshold, $E_\gamma = 1.11\,\mathrm{GeV}$ (or $W = 1.72\,\mathrm{GeV}$), to about $E_\gamma = 1.5\,\mathrm{GeV}$ (or $W = 1.92\,\mathrm{GeV}$). From the point of view of this work the most interesting finding is that the nucleon excitations produce bump-like structures in the angular distributions of the differential cross section for backward scattering angles. The distributions for the photon energies of $E_\gamma = 1.2\,\mathrm{GeV}$ and $E_\gamma = 1.3\,\mathrm{GeV}$ correspond to energy regime of this analysis. One might expect a similar behavior in the electroproduction channel.

5.3 Conclusions

The kaon experiments *E91016/E93018* produced data on both strangeness and vector meson electroproduction. The latter experiment was focused on the electroproduction of the ω meson for momentum transfer Q^2 near $0.5\,(\mathrm{GeV/c})^2$. This reaction was selected from the inelastic ep channel, ${}^1H(e, e'p)X$, by performing involved signal background separation. Tagging the ω meson production only on electron and proton not only introduced appreciable statistical error but also a sizeable systematic uncertainty due to the background removal. Nevertheless, the analysis yielded angular distributions of the differential cross section in the threshold regime extracted with an unprecedented granularity and relatively small errors.

The inspection of the angular distributions confirms the existance of a substantial enhancement of the cross section over the t-channel processes in the backward angles, as was also found in the *DESY 1977* data (Joos et al., 1977). This result is also similar to the photoproduction results based on the analyses of the *ABBHHM 1968* (ABBHHM Collaboration, 1968) and *SAPHIR 1994* data (Klein, 1996). Comparing the result of this work, in the absence of corresponding electroproduction calculations, to the photoproduction models the similar structure of the angular distribution of the differential cross section is evident. In the view of these findings this result provides a significant evidence of s-channel production mechanism, possibly by formation of the $P_{13}(1720)$ and $F_{15}(1680)$ resonances as intermediate states, in the $\gamma^{\star}p \longrightarrow \omega p$ channel.

Futher extensive resonance studies are being carried out in Hall B of Jefferson Lab where the $N^{\star}$ program is ongoing and a number of experiments intended to investigate the underlying physics with a wide-acceptance system are well underway (Burkert, 1997; Burkert, 2000; Burkert, 2001).

BIBLIOGRAPHY

ABBHHM Collaboration (1968). *Physical Review*, 175, 1669.

Akerlof, C.W., et al. (1969). *Physical Review*, 163(5), 1482-1497.

Armstrong, C.S. (1995). *Hall C time-of-flight fitting code*. JLab Hall C Internal Report (unpublished).

Armstrong, C.S. (1998). *Electroproduction of* $S_{11}(1535)$ *resonance at high momentum transfer*. College of William & Mary.

Arrington, J.R. (1998). *Inclusive electron scattering from nuclei for* $x > 1$ *and high* Q^2. California Institute Of Technology.

Assamagan, K.A., Dutta, D., & Welch, P. (1997). *Hall C matrix elements optimization package*. JLab Hall C Internal Report (unpublished).

Baker, O.K., et al. (1995). *Nuclear Instruments and Methods*, A367, 92.

Ballam, J., et al. (1972). *Physical Review*, D5, 545.

Ballam, J., et al. (1973). *Physical Review*, D7, 3150.

Barlow, R. (1993). Fitting using finite Monte Carlo samples. *Computer Physics Communications*, 77, 219-228.

Bartel, W. (1968) *Physics Letters*, 28B, 148.

Benecke, J., & Dürr, P.H., (1969). *Nuovo Cimento*, 56A, 269.

Berz, M. (1990). *Nuclear Instruments And Methods*, A298, 426-473.

Bhaduri, R.K. (1988). *Models of the nucleon: from quarks to soliton.* Addison-Wesley.

Brown, G.E. (1985). *Nuclear Physics*, A446, 12c.

Burkert, V.D. (1997). The CEBAF N* program. *Nuclear Physics*, A623 (1-2), 59.

Burkert, V.D. (2000). Probing the structure of nucleons in electromagnetic interactions. *Nuclear Physics*, A663-664(1-4), 29.

Burkert, V.D. (2001). Probing the structure of nucleons in the resonance region with CLAS at Jefferson Lab. *Nuclear Physics*, A684, 16.

Byckling, E., & Kajantie, K. (1972). *Particle kinematics.* John Wiley & Sons.

Capps, R.H. (1974). *Physical Review Letters*, 33, 1637.

Capstick, S. (1988). In *Excited Baryons 1988* (pp 32-53). World Scientific.

Capstick, S. (1992). *Physical Review*, D46, 2864.

Capstick, S., & Isgur, N. (1986). Baryons in a relativized quark model with chromodynamics. *Physical Review*, D34, 2809.

Capstick, S., & Roberts, W. (1993). *Physical Review*, D47, 1994.

Capstick, S., & Roberts, W. (1994). *Physical Review*, D49, 4570.

Capstick, S., & Roberts, W. (1998). *Physical Review*, D57, 4301.

Capstick, S., & Roberts, W. (2000). LANL arXiv:nucl-th/0008028 (preprint).

Caso, C., et al. (1998). *The European Physical Journal*, C3.

Cassel, D.G., et al. (1981). *Physical Review D*, 24, 2788.

Cha, J. (2000). *Measurements of kaon electroproduction on hydrogen and deuterium.* Hampton University.

Cutkosky, R.E., & Hendrick, R.E. (1977). *Physical Review D*, 16, 2902.

Dunne, J.A. (1997). *Cryo and dummy target information.* JLab Hall C Internal Report (unpublished).

Dunne, J.A. (1998). Private communication.

Durham, B.M. (1996). *Operating experience at CEBAF*. JLab TechNote PR96-013 (unpublished).

Fermi, E. (1950). *Progress Of Theoretical Physics*, 5, 570.

Forsythe, C.P., & Cutkosky, R.E. (1983). *Zeitschrift für Physik C*, 18, 219.

Fraas, H. (1971). *Nuclear Physics*, B36, 191-204.

Fraas, H., & Schildknecht, D. (1969). Vector meson dominance and diffractive electroproduction of vector mesons. *Nuclear Physics*, B14, 543-565.

Frolov, V. (1998). *Electroproduction of the Δ(1232) resonance at high momentum transfer*. Rensselaer Polytechnic Institute.

Godfrey, S., & Isgur, N. (1985). Mesons in a relativized quark model with chromodynamics. *Physical Review*, D32, 189.

Groom, D.E., et al. (2000). *The European Physical Journal*, C15.

Guèye, P. (1996). *Status of the actual beam position monitors in the Hall C beamline*. JLab Hall C Internal Report (unpublished).

Guèye, P., Tiefenback, M., & Yan, C. (1996). *Hall C beam energy measurement*. JLab Hall C Internal Report (unpublished).

Hagedorn, R. (1963). *Relativistic kinematics*. W.A. Benjamin, Inc.

Halzen, F., & Martin, A.D. (1984). *Quarks & leptons: an introductory course in modern particle physics*. John Wiley & Sons.

Hand, L.N. (1963). *Physical Review*, 129, 1834.

Isgur, N. (1991). An Introduction to the Quark Model for Baryons. In B. Frois, I. Sick (Eds.). *Modern Topics in Electron Scattering* (pp. 2-27). World Scientific.

Isgur, N., & Karl, G. (1977). *Physics Letters*, 72B, 109.

Isgur, N., & Karl, G. (1978). *Physics Letters*, 74B, 353.

Isgur, N., & Karl, G. (1979). *Physical Review*, D19, 2653.

Isgur, N., & Koniuk, R. (1980). *Physical Review*, D21, 1868.

Isgur, N., & Paton, J. (1985). Flux-tube model for hadrons in QCD. *Physical Review*, D31, 2910.

James, F. (1968). *Monte Carlo phase space*. Lectures given in the Academic Training Programme of CERN, (CERN 68-15).

Joos, P., et al. (1976). *Nuclear Physics*, B113, 53-92.

Joos, P., et al. (1977). ω meson production by virtual photons. *Nuclear Physics*, B122, 365-382.

Karl, G., & Isgur, N. (1978). *Physical Review*, D18, 4187.

Klein, F.J. (1996).*Untersuchungen zur photoproduktion von vektormesonen mit dem SAPHIR-detektor*. Bonn University.

Klein, F.J. (1999). *Photoproduction of the ω mesons off protons with linearly polarized photons*. JLab Hall B Proposal - E99013.

Koniuk, R. (1982). *Nuclear Physics*, B195, 452.

Le Yaouanc, A., et al. (1978). *Physical Review*, D18, 1591.

Leo, W.R. (1994). *Techniques for nuclear and particle physics experiments* (2^{nd} ed.). Springer-Verlag.

Lichtenberg, D.B. (1969). *Physical Review*, 178, 2197.

Lyons, L. (1986). *Statistics for nuclear and particle physicists*. Cambridge University Press.

Maglić, B.C., et al. (1962). Spin and parity of the ω meson. *Physical Review*, 125, 687.

Makins, N.C.R. (1994). *Measurement of the nuclear dependence and momentum transfer dependence of quasielastic $(e, e'p)$ scattering at large momentum transfer*. Massachusetts Institute Of Technology.

Meekins, D. (1998). *Coherent π^0 photoproduction on the deuteron.* College of William & Mary.

Mo, L.W., & Tsai, Y.S. (1969). *Review Of Modern Physics*, 41, 205.

Mohring, R.M. (1999). *A comparison ff longitudinal and transverse cross sections in the* $\mathrm{p(e,e'K^+)\Lambda}$ *and* $\mathrm{p(e,e'K^+)\Sigma^0}$ *reactions.* University Of Maryland.

Niculescu, G. (1997). *On pathlenghts and corrected coincidence time.* JLab Hall C Internal Report (unpublished).

Niculescu, G. (1997). *Shower counter and Čerenkov efficiencies.* JLab Hall C Internal Report (unpublished).

Niculescu, G. (1998). *First measurement of the longitudinal and transverse cross section in* $^1H(e,e'K^+)\Lambda$. Hampton University.

Oh, Y. (2001). Private communication.

Oh, Y., Lee, T.-S.H., & Titov, A.I. (2000). LANL arXiv:nucl-th/0006057 (preprint).

Oh, Y., Titov, A.I., & Lee, T.-S.H. (2000). LANL arXiv:nucl-th/0004055 (preprint).

Perl, M.L. (1974). *High energy hadron physics.* John Wiley & Sons.

Roberts, W. & Capstick, S. (1998). *Physical Review*, D58, 074011.

Söding, P. (1966). *Physics Letters*, 19, 702.

Sakurai, J.J. (1960). *Annals Of Physics*, 11, 1.

Sakurai, J.J. (1969). In *Proceedings of the Fourth International Symposium on Electron and Photon Interactions at High Energies (Daresbury Nuclear Physics Laboratory, Daresbury, England).*

Schildknecht, D. (1972). Vector Meson Dominance, Photo- and Electroproduction From Nucleons. *In Springer Tracks In Modern Physics: Vol. 63* (pp.57-97). Springer Verlag.

Stein, S., et al. (1975). *Physical Review*, D12, 1884.

Volmer, J. (2000). *The pion charge form factor via pion electroproduction on the proton.* Vrije Universiteit te Amsterdam.

Wolf, G. (1971). In N.B. Mistry (Ed.). *Proceedings of the 1971 International Symposium on Electron and Photon Interactions at High Energies*.

Wolf, G. (1972). *Physical Review*, 182, 1538.

Zhao, Q. (2000). *Nuclear Physics*, A675, 217.

Zhao, Q., Bennhold C., & Li, Z. (1998). *Physics Letters*, B436, 42.

Zhao, Q., Li, Z., & Bennhold C. (1998). *Physical Review*, C58, 2393.

APPENDIX A

CHANGE OF VARIABLES AND RELATED JACOBIANS

Overview

There are three sets of variables involved in this scattering problem which one is tempted to call "phase space". These deserve careful distinction. The first, consisting of $\{p_{e'}, \cos\theta_{e'}, \phi_{e'}, p, \cos\theta_p, \phi_p\}$, spans the volume in which the particles emerging from the interaction are detected. This volume, in Chapter 1, is called ***Detection Volume*** and is by definition 6 dimensional. The second set of variables, spanned by $\{Q^2, W, \phi_{e'}, M_x, \cos\theta_x^{CM}, \phi_x^{CM}\}$, defines the volume in which the events simulated by the Monte Carlo are generated. That volume, recalling from the Chapters 1 and 3, is called the ***Generation Volume*** and its dimension is determined by the nature of the final state particles. For the reactions of the E91016/E93018 experiments,

$$e + p \longrightarrow e' + K^+ + \text{Hyperon} \tag{A.1}$$

$$e + p \longrightarrow e' + p + \text{Vector Meson} \tag{A.2}$$

this dimension, in the one photon exchange approximation of the Born level diagram (refer, for instance, to the Figure 1.3), is either 5 for the former reaction, since all the final state particles have definite masses, or 6 for the latter reaction due to the reso-

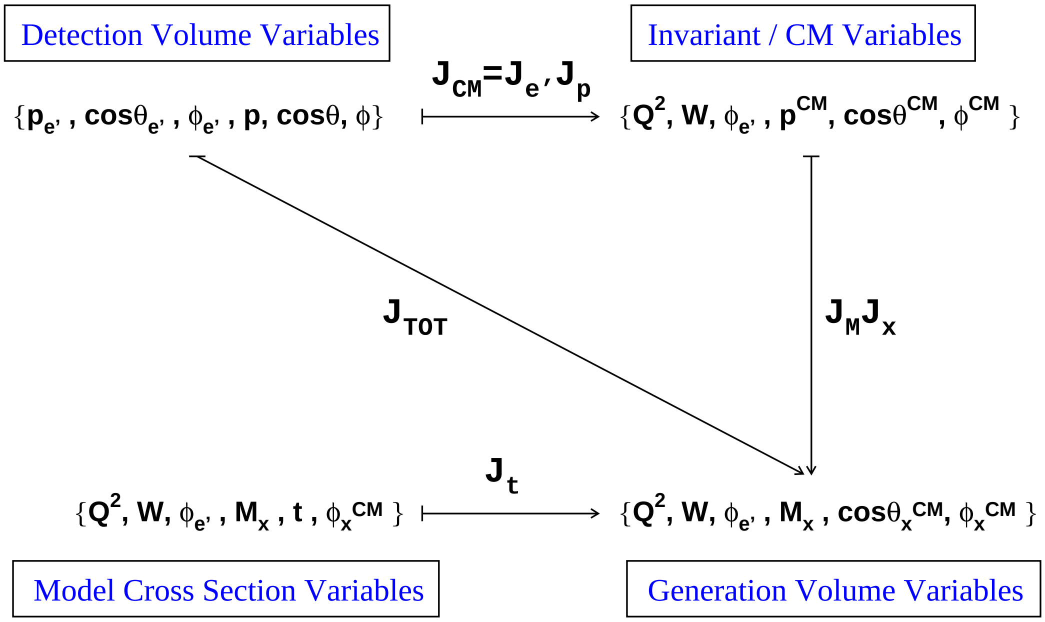

Figure A.1: ***Volume Transformations:*** *The expressions for the Jacobians defined in this figure are described in the text except for the Jacobian, $\mathcal{J}_x$, that transforms proton CM solid angle into ω CM solid angle and is identically equal to one.*

nant nature of the observed vector mesons. Finally, there is a set of variables spanning the volume (***Phase Space Volume***) which enters the cross section calculation that defines the number of states available to the final state particles. The dimension and composition of this set depend on the form of the cross section that is to be extracted but most likely it coincides partially if not entirely with one of the previous sets. The computation of the density of final states conventionally begins in the momentum space therefore any transformation of this natural phase space volume must be compensated by the use of the appropriate Jacobian.

The choice of the variables for the generation volume set is arbitrary. There are however two obvious choices according to which it either coincides with a subset of the variables of the detection volume or with the variables in which the cross section differential. In this work, to facilitate the ω meson line shape integration and futher comparison to the world's data and also to reduce the use of the Jacobians, the second choice was assumed.

The interplay between the volume elements expressed in terms of variables of these sets is described by the use of the appropriate Jacobians. Figure A.1 shows the definitions of several sets of variables and corresponding Jacobians.

Electron-Hadron Decoupling

A very important conclusion can be drawn from the form of the equations B.6 and B.10 relating $p_{e'}$, or equivalently E', and $\cos\theta_{e'}$ to Q^2 and W,

$$Q^2 = 2EE'(1-\cos\theta_{e'}) \tag{A.3}$$

$$W^2 = M_T^2 + 2M_T(E-E') - Q^2 \tag{A.4}$$

They do not include any hadron variables therefore the total Jacobian $\mathcal{J}_{CM}$ of the transformation from the detection to generation variables factorizes into parts corresponding to the electron and hadron quantities respectively (in Figure A.1 this is represented by the factorization of the Jacobian $\mathcal{J}_{CM}$ into $\mathcal{J}_{e'}$ and $\mathcal{J}_p$). This allows separate Jacobian calculations and the electron part is easier to sort out.

Change Of The Electron Variables

Since the transformation of the electron variables leaves the azimuthal angle unchanged the corresponding Jacobian, $\mathcal{J}_W$, is given by the determinant

$$\mathcal{J}_{e'} = \begin{vmatrix} \dfrac{\partial Q^2}{\partial p_{e'}} & \dfrac{\partial Q^2}{\partial \cos\theta_{e'}} \\ & \\ \dfrac{\partial W}{\partial p_{e'}} & \dfrac{\partial W}{\partial \cos\theta_{e'}} \end{vmatrix} = \frac{\partial Q^2}{\partial p_{e'}} \frac{\partial W}{\partial \cos\theta_{e'}} - \frac{\partial Q^2}{\partial \cos\theta_{e'}} \frac{\partial W}{\partial p_{e'}} \tag{A.5}$$

where the individual partial derivatives are given by,

$$\frac{\partial Q^2}{\partial p_{e'}} = 2E(1 - \cos\theta_{e'}) = \frac{Q^2}{E'} \tag{A.6}$$

$$\frac{\partial Q^2}{\partial \cos\theta_{e'}} = -2EE' \tag{A.7}$$

$$\frac{\partial W}{\partial p_{e'}} = -\frac{1}{W}(M_p + E(1 - \cos\theta_{e'})) = -\frac{1}{W}\left(M_p + \frac{Q^2}{2E'}\right) \tag{A.8}$$

$$\frac{\partial W}{\partial \cos\theta_{e'}} = \frac{EE'}{W} \tag{A.9}$$

so that the entire Jacobian $\mathcal{J}_{e'} \equiv \dfrac{\partial(Q^2, W, \phi_{e'})}{\partial(p_{e'}, \cos\theta_{e'}, \phi_{e'})}$ equals to,

$$\boxed{\mid \mathcal{J}_{e'} \mid = \frac{2M_p EE'}{W}} \tag{A.10}$$

This Jacobian is used in the cross section transformation described in the Section 3.2.2 on the page 77 (see the Equation 3.5).

Change Of The Hadron Variables

The transformation from the hadron detection variables to generation ones proceeds in two steps. Initially the hadron lab momentum and angles are mapped on the momentum and angles in the Center-Of-Momentum frame. Then the CM momentum is replaced by the appropriate mass. Performing the operation this way ensures that all the functions differentiated in the Jacobi determinant are single-valued. As a reward of the decoupling of electron and hadron variables one can calculate the jacobian $\mathcal{J}_p$ using the fact that

$$\vec{p} = (p_x, p_y, p_z) = (p\,\sin\theta\,\cos\phi,\, p\,\sin\theta\,\sin\phi,\, p\,\cos\theta) \tag{A.11}$$

and computing the jacobian for a transformation from cartesian to spherical coordinate system,

$$\frac{\partial(p_x, p_y, p_z)}{\partial(p, \cos\theta, \phi)} = p^2 \tag{A.12}$$

where the above relation is sometimes cast in a differential form $d^3p = p^2 dp d\Omega$. Eventually, recalling that the quantity d^3p/E (see the Equation C.10 in the Appendix C) is a Lorentz invariant one gets [1],

$$\frac{\partial(p_x^*, p_y^*, p_z^*)}{\partial(p_x, p_y, p_z)} = \frac{d^3p^*}{d^3p} = \frac{E^*}{E} \tag{A.13}$$

[1] * - will, for brevity, denote the Center-Of-Momentum quantities in the remaining part of this Appendix.

Upon combining all these facts and using the properties of the jacobian calculus one obtains

$$\mathcal{J}_p \equiv \frac{\partial(p^*, \cos\theta^*, \phi^*)}{\partial(p, \cos\theta, \phi)} = \frac{\partial(p^*, \cos\theta^*, \phi^*)}{\partial(p^*_x, p^*_y, p^*_z)} \cdot \frac{\partial(p^*_x, p^*_y, p^*_z)}{\partial(p_x, p_y, p_z)} \cdot \frac{\partial(p_x, p_y, p_z)}{\partial(p, \cos\theta, \phi)} \tag{A.14}$$

which, in the straightforward differential notation, reads,

$$\mathcal{J}_p = \frac{dp^* d\Omega^*}{dp d\Omega} = \left(\frac{p}{p^*}\right)^2 \frac{d^3p^*}{d^3p} \tag{A.15}$$

Employing the result of the expression A.13 the final form of the Jacobian $\mathcal{J}_p$ is,

$$\boxed{\mathcal{J}_p = \left(\frac{p}{p^*}\right)^2 \left(\frac{E^*}{E}\right)} \tag{A.16}$$

To carry out the second step of this transformation the missing mass is expressed in terms of Center-Of-Momentum quantities

$$M_x^2 = W^2 + M^2 - 2WE^* = M_x^2(p_e, \theta_e, E^*(p^*)) \tag{A.17}$$

therefore the result for $\mathcal{J}_M$ is

$$\boxed{\mathcal{J}_M = \frac{1}{2M_x} \frac{\partial M_x^2}{\partial E^*} \frac{\partial E^*}{\partial p^*} = -\frac{W\beta^*}{M_x}} \tag{A.18}$$

Eventually one arrives at the expression for the full Jacobian corresponding to the transformation from the hadron detection to generation variables as defined in Figure A.1,

$$| \mathcal{J} |= \left(\frac{W\beta^*}{M_x}\right)\left(\frac{E^*}{E}\right)\left(\frac{p}{p^*}\right)^2 \tag{A.19}$$

where $\beta^* = p^*/E^*$ is hadron's velocity in the center of momentum frame.

Cross Section Reduction

The coincidence cross section computed for the process in which all three final state particles have definite masses can be naturally generalized to the situation when the undetected particle has indefinite mass (like the vector mesons for instance). This procedure was outlined in Section "Non-definite Mass Particles" of the Appendix C and it amounts to the replacement,

$$\frac{d\sigma}{dp_{e'}d\Omega_{e'}d\Omega_x^*} \xrightarrow{d\sigma(M_x)} \frac{d\sigma}{dp_{e'}d\Omega_{e'}d\Omega_x^* dM_x^2} \tag{A.20}$$

The Monte Carlo yield, corresponding to the reaction A.2 and used in the cross section extraction, was integrated over the mass variable assuming a relativistic Breit-Wigner line shape of the ω meson. This operation was performed using Monte Carlo integration which is nicely preseneted in (Lyons, 1986) and may be formally written as,

$$\begin{aligned} \frac{d\sigma}{dp_{e'}d\Omega_{e'}d\Omega_x^*} &= \int \frac{d\sigma}{dp_{e'}d\Omega_{e'}d\Omega_x^* dM_x} dM_x & \text{(A.21)} \\ &= \frac{1}{\pi}\int \Gamma_T \frac{M_\omega \Gamma_\omega}{(M_x^2 - M_\omega^2)^2 + M_\omega^2 \Gamma_\omega^2} \left(\sigma_T(M_x) + \epsilon\, \sigma_L(M_x)\right) dM_x & \text{(A.22)} \end{aligned}$$

where the relation 3.6 was used after implicit transformation to appropriate variables was carried out. The reaction A.1 can be treated on the same footing by noting that trivially,

$$\frac{d\sigma}{dp_{e'}d\Omega_{e'}d\Omega_Y^*} = \int \frac{d\sigma}{dp_{e'}d\Omega_{e'}d\Omega_Y^* dM_Y^2} dM_Y^2 \tag{A.23}$$

$$= \int \frac{d\sigma}{dp_{e'}d\Omega_{e'}d\Omega_Y^*} \delta\left(p_Y^2 - M_Y^2\right) \, dM_Y^2 \tag{A.24}$$

and this is in clear agreement with the fact that the phase space volume for this type of reaction is five-fold. The above equation can also be viewed as a common ground for two approaches to the cross section extraction in the case of definite mass particles (as in the reaction A.1, for instance),

$$\frac{d\sigma}{dp_{e'}d\Omega_{e'}d\Omega_Y^*} = \int \frac{d\sigma}{dp_{e'}d\Omega_{e'}dp_{K^+}d\Omega_{K^+}} \left(\frac{dp_{K^+}d\Omega_{K^+}}{dp_{K^+}^*d\Omega_{K^+}^*}\right)\left(\frac{dp_{K^+}^*}{dM_Y}\right) dM_Y \tag{A.25}$$

where the equality of the hyperon and kaon solid angles in their CM frame was used. This establishes the equivalence between two different ways of extracting the cross section of the electroproduced Λ or Σ^0. First one assumes that the particle left undetected in the final state is either Λ or Σ^0 and uses five dimensional phase space (Mohring, 1999; Cha, 2000) while the other starts from the six dimensional detection volume and, with the aid of appropriate Jacobians, transforms it to the natural phase space volume and integrates the cross section corresponding to the Born term over the appropriate mass range (Niculescu, 1998). The former approach allows for relatively easy but model dependent analysis and the latter one achieves model independence at the expense of very high degree of sophistication.

Cross Section Transformations

There are also two Jacobians that must be introduced that ease the transition from the theory to application. The first one connects the volume elements expressed in terms of the CM scattering angle θ^* and momentum transfer to the target t. Most theoretical papers derive cross sections in terms of the invariants Q^2, W and t. The form of this Jacobian simply follows from the Equation 1.16,

$$\frac{dt}{d\cos\theta_x^*} = 2|\vec{q}^*||\vec{p}_x{}^*| \tag{A.26}$$

The second relates solid angles in the lab and CM frames. The starting relation to derive that Jacobian (see the Equation B.35 in the Appendix B) is

$$\tan\theta = \frac{\sin\theta^*}{\gamma^*(\cos\theta^* + (\beta^*/\beta_p^*))} \tag{A.27}$$

where $\beta_p^* = p^*/E_p^*$ and β^* and γ^* are defined in equations B.28 and B.29 respectively. The chain rule, for the derivative of $\partial\cos\theta^*/\partial\cos\theta$, gives,

$$\frac{\partial\cos\theta}{\partial\cos\theta^*} = \frac{\partial\cos\theta}{\partial\tan\theta} \cdot \frac{\partial\tan\theta}{\partial\cos\theta^*} = -\sin\theta\cos^2\theta\frac{\partial\tan\theta}{\partial\cos\theta^*} \tag{A.28}$$

Taking a partial derivative of the expression A.27 and putting $\alpha = \beta^*/\beta_p^*$ one gets,

$$\frac{\partial \tan\theta}{\partial \cos\theta^*} = -\left(\frac{\cos\theta^*}{\gamma^*\sin\theta^*(\cos\theta^*+\alpha)} + \frac{\sin\theta^*}{\gamma^*(\cos\theta^*+\alpha)^2}\right) \tag{A.29}$$

employing A.27 once again and working out the algebra this yields,

$$\frac{\partial \cos\theta}{\partial \cos\theta^*} = \sin^2\theta\cos\theta\left(\frac{\cos\theta^*}{\sin^2\theta^*} + \frac{1}{\cos\theta^*+\alpha}\right) \tag{A.30}$$

Since perpendicular components of the momentum do not change with the boost along virtual photon direction one may use $p^*\sin\theta^* = p\sin\theta$ to get the formula,

$$\frac{\partial \cos\theta}{\partial \cos\theta^*} = \left(\frac{p^*}{p}\right)^2\cos\theta\left(\cos\theta^* + \frac{\sin^2\theta^*}{\cos\theta^*+\alpha}\right) \tag{A.31}$$

If one proceeds further it is easy to simplify $\partial\cos\theta/\partial\cos\theta^*$ by using A.27 in the formula,

$$\frac{\partial \cos\theta}{\partial \cos\theta^*} = \left(\frac{p^*}{p}\right)^2\left(\cos\theta\cos\theta^* + \gamma^*\cos\theta\frac{\sin\theta^*}{\gamma^*(\cos\theta^*+\alpha)}\sin\theta^*\right) \tag{A.32}$$

and simple algebra leads to the final relation between the cosines of the lab and CM angles and, in turn, to the relation between the corresponding solid angles,

$$\boxed{\frac{\partial \cos\theta}{\partial \cos\theta^*} = \left(\frac{p^*}{p}\right)^2(\cos\theta\cos\theta^* + \gamma^*\sin\theta\sin\theta^*)} \tag{A.33}$$

$$\frac{\partial(\cos\theta,\,\phi)}{\partial(\cos\theta^*,\,\phi^*)} \equiv \begin{vmatrix} \dfrac{\partial\cos\theta}{\partial\cos\theta^*} & \dfrac{\partial\phi}{\partial\cos\theta^*} \\[2ex] \dfrac{\partial\cos\theta}{\partial\phi^*} & \dfrac{\partial\phi}{\partial\phi^*} \end{vmatrix} = \frac{\partial\cos\theta}{\partial\cos\theta^*}\frac{\partial\phi}{\partial\phi^*} = \frac{\partial\cos\theta}{\partial\cos\theta^*} \tag{A.34}$$

As noted in the Appendix B caution should be exercised when using this Jacobian. Depending on the kinematics (different values of the α parameter - refer to the Appendix B for the definition) it may be only piecewise invertible which means that the inverse Jacobian would be singular for some angle as a consequence of double-valuedness of the function $\theta^* = \theta^*(\theta)$ (refer to the Figure B.5 in the Appendix B). Therefore this Jacobian should only be used to transform five-fold cross sections pertaining to appropriate portion of the data. At the six-fold level cross sections are safely transformed using A.19.

It must be mentioned that the Jacobians presented in this Appendix may by no means be generally applicable. Each reaction or kinematics calls for calculation of its own appropriate Jacobians.

APPENDIX B

DETAILED KINEMATICS OF THE PROCESS $\gamma^* + A \longrightarrow B + C$

Definitions

This calculation assumes Minkowski's structure of the space-time and a fixed target in the lab frame. A complete treatment of the kinematics can be found in (Byckling & Kajantie, 1972; Hagedorn, 1963). Electron variables define the virtual photon 4-momentum,

$$(e - e', \vec{\mathbf{k}} - \vec{\mathbf{k}'}\,) = (\nu, \vec{\mathbf{q}}\,) \tag{B.1}$$

and, as will turn out, with the aid of the target mass, M_T, the invariant mass, W, of the system. The scattering process, along with the definitions of the electron vertex variables, is schematically shown in the Figure B.1. Variables of the hadron vertex are defined in Figure B.2.

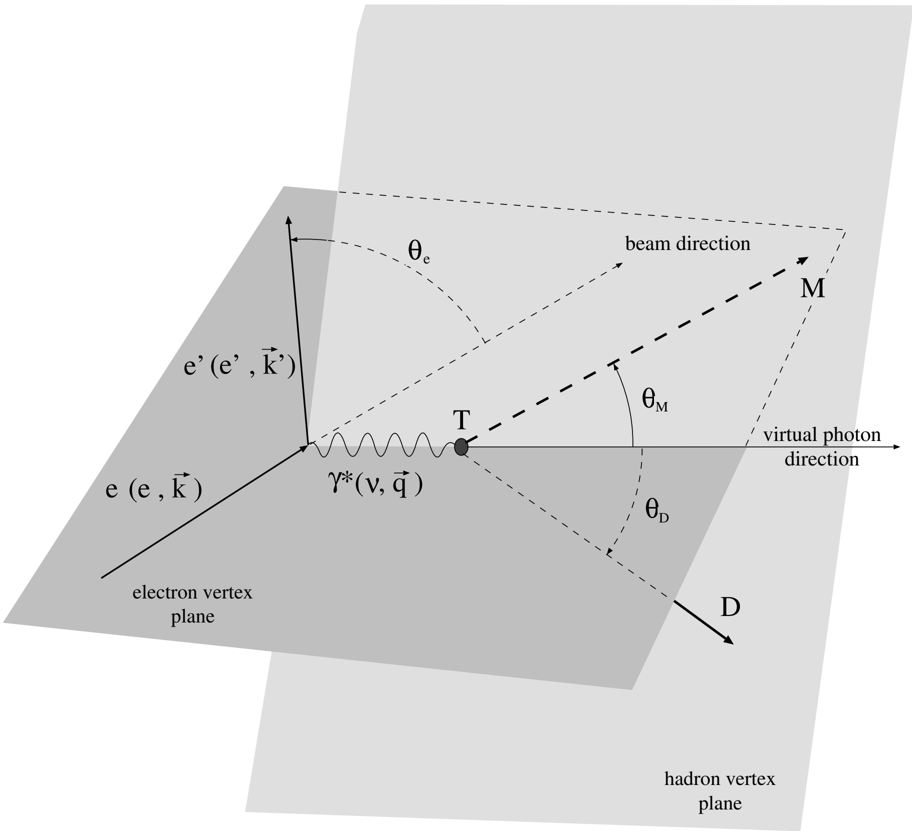

Figure B.1: *General overview of the kinematics*

Masses of particles involved are defined by squares of the corresponding four-vectors,

$$Q^2 = -(\nu, \vec{\mathbf{q}}\,)^2 = \ |\vec{\mathbf{q}}|^2 - \nu^2 \quad - \ 4 - \text{momentum transfer} \tag{B.2}$$

$$M_D^2 = (E, \vec{\mathbf{p}}\,)^2 = E^2 - |\vec{\mathbf{p}}|^2 \quad - \ \text{detected particle mass} \tag{B.3}$$

$$M_M^2 = (\varepsilon, \vec{\boldsymbol{\pi}}\,)^2 = \varepsilon^2 - |\vec{\boldsymbol{\pi}}|^2 \quad - \ \text{"missing" particle mass} \tag{B.4}$$

Q^2 can be expressed in terms of electron variables in the following way,

$$Q^2 = -(\nu, \vec{\mathbf{q}}\,)^2 = (e' - e, \vec{\mathbf{k'}} - \vec{\mathbf{k}}\,)^2 = 2m_e^2 + 2(ee' - |\vec{\mathbf{k}}||\vec{\mathbf{k'}}|\cos\theta_e) \tag{B.5}$$

with the approximation that $m_e \approx 0$ [1] one obtains,

$$Q^2 = 2ee'(1 - \cos\theta_e) = 4ee'\sin^2\left(\frac{\theta_e}{2}\right) \tag{B.6}$$

Fixed Target Case

In lab frame and Center-Of-Momentum (CM) frame the initial total momenta are given by,

$$k_i \quad = \quad (\nu, \vec{\mathbf{q}}\,) \quad + \quad (M_T, \vec{\mathbf{0}}\,) \quad = \quad (M_T + \nu, \vec{\mathbf{q}}\,) \tag{B.7}$$

$$k_i^* \quad = \quad (\nu^*, \vec{\mathbf{q}}^*) \quad + \quad (E_T^*\,, -\vec{\mathbf{q}}^*) \quad = \quad (\nu^* + E_T^*\,, \vec{\mathbf{0}}\,) \tag{B.8}$$

From the Lorentz invariance of the four vector length it follows that,

$$k_i^2 = (M_T + \nu)^2 - (\vec{\mathbf{q}}\,)^2 = (\nu^* + E_T^*)^2 = (E_{TOTAL}^*)^2 = W^2 \tag{B.9}$$

therefore,

$$W^2 = M_T^2 + 2M_T\nu - Q^2 \tag{B.10}$$

[1] This approximation holds whenever $e, e' \gg m_e$.

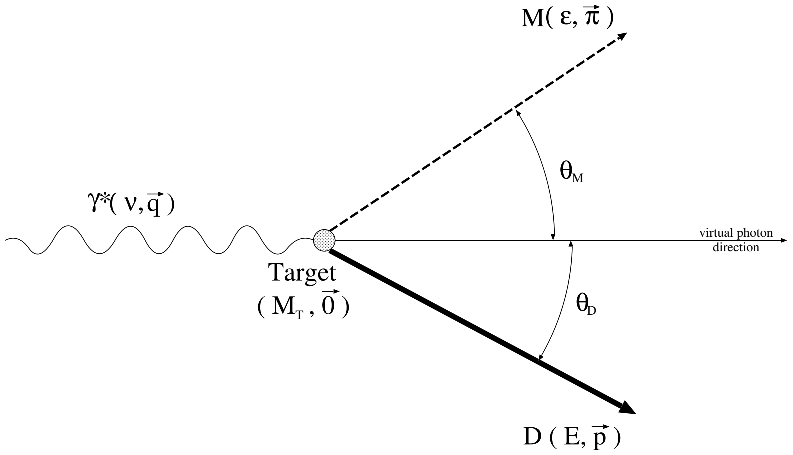

Figure B.2: ***Reaction Plane Scattering - Lab Frame:*** *Hadron vertex in the lab frame of reference.*

To compute the initial energies in the CMS one uses the Lorentz invariance of the scalar product to get,

$$(\nu, \vec{\mathbf{q}}\,) \cdot (M_T + \nu, \vec{\mathbf{q}}\,) = (\nu^*, \vec{\mathbf{q}}^*) \cdot (\nu^* + E_T^*, \vec{\mathbf{0}}\,) \tag{B.11}$$

so that the initial energy of the virtual photon equals,

$$\nu^* = \frac{M_T\nu - Q^2}{W} \tag{B.12}$$

Employing the same fact again gives,

$$(M_T, \vec{\mathbf{0}}\,) \cdot (M_T + \nu, \vec{\mathbf{q}}\,) = (E_T^*, \vec{\mathbf{q}}^*) \cdot (W, \vec{\mathbf{0}}\,) \tag{B.13}$$

Therefore the initial energy of the target is,

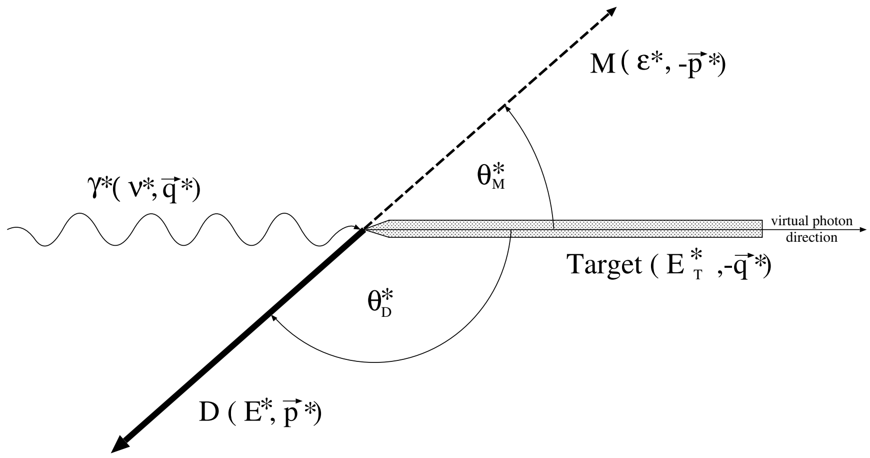

Figure B.3: ***Reaction Plane Scattering - CM Frame:*** *Hadron vertex in the Center-Of-Momentum (CM) frame of reference.*

$$\boxed{E_T^* = \frac{M_T(M_T+\nu)}{W}} \tag{B.14}$$

Moreover,

$$E_T^{*2} - |\,\vec{\mathbf{q}}^*|^2 = M_T^2 \tag{B.15}$$

which yields,

$$|\,\vec{\mathbf{q}}^*|^2 = \frac{M_T^2((M_T+\nu)^2 - W^2)}{W^2} = \frac{M_T^2(\nu^2 - q^2)}{W^2} \tag{B.16}$$

which is equivalent to saying that,

(B.17)

$$\boxed{|\,\vec{\mathbf{q}}^*| = \frac{M_T}{W}|\vec{\mathbf{q}}|\ .}$$

In order to calculate the energies of the particles D and M in the CMS, it is convenient to use the following scalar products equalities,

$$(\varepsilon^*, -\vec{\mathbf{p}}^*) \cdot (W, \vec{\mathbf{0}}\,) = (\varepsilon, \vec{\boldsymbol{\pi}}\,) \cdot (\varepsilon + E, \vec{\boldsymbol{\pi}} + \vec{p}\,) \tag{B.18}$$

$$(E^*, \vec{\mathbf{p}}^*) \cdot (W, \vec{\mathbf{0}}\,) = (E, \vec{\mathbf{p}}\,) \cdot (\varepsilon + E, \vec{\boldsymbol{\pi}} + \vec{p}\,) \tag{B.19}$$

Since,

$$(\varepsilon + E, \vec{\boldsymbol{\pi}} + \vec{\mathbf{p}}\,)^2 = (\varepsilon^* + E^*, \vec{\mathbf{0}}\,)^2 = W^2 \tag{B.20}$$

Equality B.18 yields,

$$\begin{aligned} \varepsilon^* W &= (\varepsilon, \vec{\boldsymbol{\pi}}\,)((\varepsilon, \vec{\boldsymbol{\pi}}\,) + (E, \vec{\mathbf{p}}\,)) = \\ &= (\varepsilon, \vec{\boldsymbol{\pi}}\,)^2 + (\varepsilon, \vec{\boldsymbol{\pi}}\,) \cdot (E, \vec{\mathbf{p}}\,) \\ &= M_M^2 + \tfrac{1}{2}[(\varepsilon + E, \vec{\boldsymbol{\pi}} + \vec{\mathbf{p}}\,)^2 - (\varepsilon, \vec{\boldsymbol{\pi}}\,)^2 - (E, \vec{\mathbf{p}}\,)^2] \\ &= \tfrac{1}{2}[W^2 + M_M^2 - M_D^2] \end{aligned} \tag{B.21}$$

so that eventually,

$$\boxed{\varepsilon^* = \frac{W^2 + M_M^2 - M_D^2}{2W}} \tag{B.22}$$

Similarly, using equality B.19 one gets,

$$E^* = \frac{1}{2}[W^2 + M_D^2 - M_M^2] \tag{B.23}$$

and finally,

$$\boxed{E^* = \frac{W^2+M_D^2-M_M^2}{2W}} \tag{B.24}$$

To find the magnitude of the momentum after collision in the CMS one writes,

$$|\,\vec{\mathbf{p}}^*|^2 = E^{*2} - M_D^2 \tag{B.25}$$

which gives,

$$\boxed{p^* \equiv |\,\vec{\mathbf{p}}^*| = \frac{\sqrt{(W^2+M_D^2-M_M^2)^2-4M_D^2W^2}}{2W}} \tag{B.26}$$

CMS-to-Lab Scattering Angle Transformation

To proceed further the above quantities have to be transformed to the lab system. This transformation takes place through the Lorentz boost defined by β^* and γ^*. These can be found by noting that,

$$\begin{aligned} \vec{\mathbf{q}}^* &= \gamma^* M_T \vec{\boldsymbol{\beta}}^* \\ E_T^* &= \gamma^* M_T \end{aligned} \tag{B.27}$$

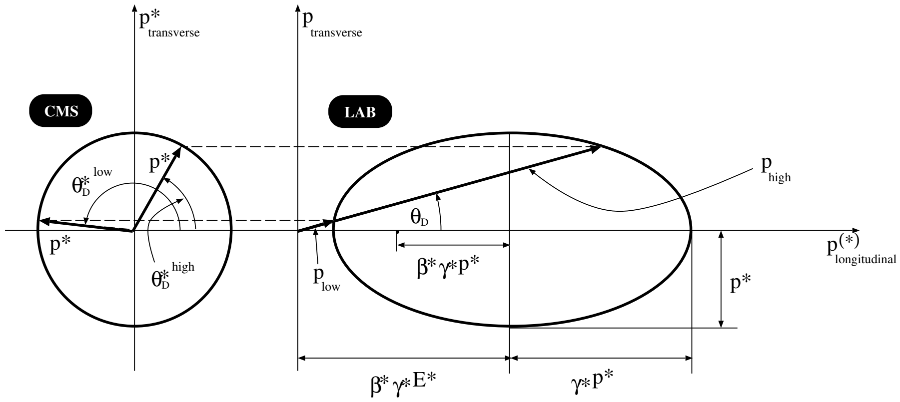

Figure B.4: *Lorentz boost from the center-of-momentum system to the lab.* $p_{\rm low}$ *and* $p_{\rm high}$ *are the solutions of the equation* $E^* = \gamma^*(p\,\cos\theta_D - \beta^* E)$

Combining with the results for $|\,\vec{\mathbf{q}}^*|$ and E_T^* one gets,

$$\beta^* = \frac{q}{M_T + \nu} \tag{B.28}$$

$$\gamma^* = \frac{M_T + \nu}{W}\ . \tag{B.29}$$

Chosing the z direction along the initial virtual photon direction and assuming that the momentum vectors lie in the yz plane the Lorentz boost for timelike components is given by,

$$\begin{aligned} E &= \gamma^*(E^* + \beta^* p^* \cos\theta_D^*) \\ \varepsilon &= \gamma^*(\varepsilon^* + \beta^* p^* \cos\theta_M^*) \end{aligned} \tag{B.30}$$

where $\theta_M^* = \pi - \theta_D^*$ as is easily verified from Figure B.3. Spacelike components transform like,

$$
\begin{aligned}
p_z &= \gamma^*(p^* \cos\theta_D^* + \beta^* E^*) \\
p_y &= p^* \sin\theta_D^* \qquad \text{(B.31)} \\
p_x &= p_x^* = 0
\end{aligned}
$$

$\vec{\pi}$ is given the same way, i.e.,

$$
\begin{aligned}
\pi_z &= \gamma^*(\pi^* \cos\theta_M^* + \beta^* \varepsilon^*) \\
\pi_y &= \pi^* \sin\theta_M^* \qquad \text{(B.32)} \\
\pi_x &= \pi_x^* = 0
\end{aligned}
$$

but since $\vec{\boldsymbol{\pi}}^* = -\vec{\mathbf{p}}^* = (0, -p^* \sin\theta_D^*, -p^* \cos\theta_D^*) = (0, p^* \sin\theta_M^*, p^* \cos\theta_M^*)$,

$$
\begin{aligned}
\pi_z &= \gamma^*(-p^* \cos\theta_D^* + \beta^* \varepsilon^*) \\
\pi_y &= -p^* \sin\theta_D^* \qquad \text{(B.33)} \\
\pi_x &= \pi_x^* = 0
\end{aligned}
$$

Relation between scattering angles in both frames can be found by dividing p_y by p_z and using expressions B.31,

$$
\frac{p_y}{p_z} = \tan\theta_D = \frac{p^* \sin\theta_D^*}{\gamma^*(p^* \cos\theta_D^* + \beta^* E^*)} \qquad \text{(B.34)}
$$

By defining $\alpha = \beta^*/\beta_D^*$ where $\beta_D^* = p^*/E^*$ one arrives at,

$$\tan\theta_D = \frac{\sin\theta_D^*}{\gamma^*(\alpha+\cos\theta_D^*)} \tag{B.35}$$

This expression constitutes a functional dependence of $\theta_D = f(\theta_D^*)$, the behavior of which is shown in the Figure B.5.

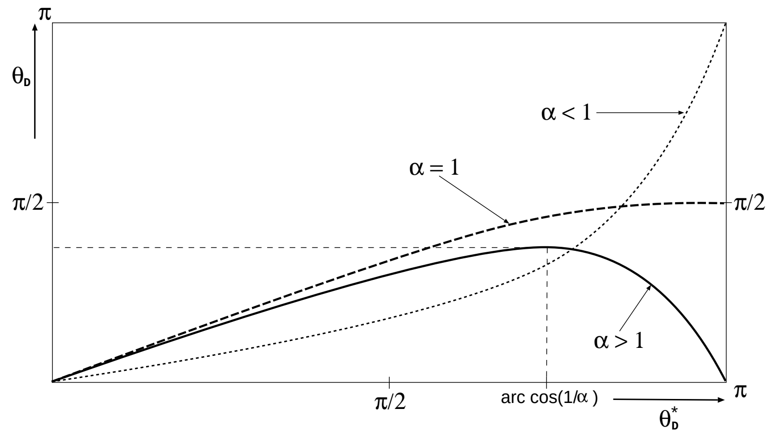

Figure B.5: ***Relation Between Lab And CMS Scattering Angles.****Lab scattering angle θ_D as a function of CMS scattering angle θ_D^* for different beta ratios.*

Worth noting is the fact that if the velocity of the detected particle in the CMS is smaller than that of Lorentz boost ($\alpha > 1$) there are two different scattering angles in the CMS that correspond to only one scattering angle in the lab frame. This dictates cautiousness when inverting this function. The relation between scattering angles and corresponding momenta in both frames for the case ($\alpha > 1$) is shown in Figure B.5. For ($\alpha < 1$) the ellipsoid encircles the origin of the lab coordinate frame and for ($\alpha = 1$) it is tangent to the $p_{transverse}$ axis at the origin. If $\alpha = 1$ this, again, poses an inversion problem at $\theta_D^* = \pi$.

APPENDIX C

GENERATION OF THE HADRON ELECTROPRODUCTION PHASE SPACE

In order to define the hadron phase space for the process,

$$e + p \longrightarrow e' + p' + X \tag{C.1}$$

the starting point is the following formula that serves to reduce the 3-body problem to an equivalent 2-body one,

$$\frac{d^4\sigma}{dp_{e'}d\Omega_{e'}d\Omega_x^{CM}dM_x} = \Gamma_T\Big(\frac{d^2\sigma_v}{d\Omega_x^{CM}dM_x}\Big) \tag{C.2}$$

Assuming that the matrix element for the underlying process is independent of the final state particles momenta one may write,

$$\frac{d^2\sigma}{d\Omega_x^{CM} dM_x} \propto |M.E.|^2 \times \frac{d^2 R_2}{d\Omega_x^{CM} dM_x} \tag{C.3}$$

where R_2 is Lorentz-invariant two-body phase space factor.

Definite Mass Particles

The general expression for the invariant phase space R_n of the n final state particles is the following,

$$R_n(P, m_1, ..., m_n) = \int \prod_{i=1}^{n} d^4 p_i \, \delta(p_i^2 - m_i^2) \times \delta^{(4)} \left(\sum_{j=1}^{n} p_j - P \right) \tag{C.4}$$

In order to carry out the integrations over δ functions it is necessary to reduce the quadratic expression in $\delta(p_i^2 - m_i^2)$ to the linear one. This is done by applying the identity,

$$\delta(f(x)) = \sum \frac{\delta(x - x_i)}{|df/dx|_{x=x_i}} \tag{C.5}$$

where $f(x_i) = 0$. With the identification of $f(p_0) = p_0^2 - \mathbf{p}^2 - m^2$, where $p_{0i} = \pm\sqrt{\mathbf{p}^2 + m^2} = \pm E$, the derivatives are,

$$\left|\frac{df}{dp_0}\right|_{p_0=p_{0i}} = 2E \tag{C.6}$$

so that,

$$\delta(p_i^2 - m_i^2) = \frac{1}{2E}\left(\delta(p_0 - E) + \delta(p_0 + E)\right) \tag{C.7}$$

with $E = \sqrt{\mathbf{p}^2 + m^2}$

Application of the above formula amounts to replacing,

$$\delta(p_i^2 - m_i^2)d^4p_i \longrightarrow \delta(p_0 - E)\left(\frac{\mathbf{p}_i^2}{2E_i}\right) dp_{0i}dp_id\Omega_i \tag{C.8}$$

where the δ-function with the positive root was used as the only physical solution. This allows the integration over p_{0i}'s. Therefore the expression for the R_n becomes,

$$R_n(P, m_1, ..., m_n) = \int \prod_{i=1}^{n} \frac{d\mathbf{p}_i}{2E_i}\, \delta\left(\sum_{j=1}^{n} E_j - E\right) \delta^{(3)}\left(\sum_{j=1}^{n} \mathbf{p}_j - \mathbf{P}\right) \tag{C.9}$$

The above expression is still the Lorentz invariant since $dp_1 = dp'_1$, $dp_2 = dp'_2$ and,

$$dp_3 = \gamma(dp'_3 + \beta dE') = \gamma dp'_3\left(1 + \beta p'_3 E'\right) = dp'_3\frac{E}{E'} \tag{C.10}$$

Combining gives $d\mathbf{p}/E = d\mathbf{p}/E'$.

To find the differential phase space factor it is simpler to perform the calculation in the Center-Of-Momentum frame of the virtual photon proton system,

$$d^6R_2 = \delta(W - E_p - E_x)\,\delta^{(3)}(\,\vec{p} + \vec{p}_x)\left(\frac{d^3p}{2E_p}\right)\left(\frac{d^3p_x}{2E_{p_x}}\right) \tag{C.11}$$

where the subscript p refers to the proton variables while x refers to the missng particle variables.

By integrating over the scattered proton momenta, employing the fact that $\vec{p} + \vec{p}_x = 0$, and using a spherical coordinate system this reduces to,

$$d^2R_2 = \delta(W - E_p - E_x)\left(\frac{{p_x}^2}{4E_xE_p}\right)dp_x d\Omega_x \tag{C.12}$$

where

$$\begin{aligned} E_p &= \sqrt{|\vec{p}_x|^2 + M_p^2} \\ |\vec{p}_x| &= \sqrt{E_x^2 - M_x^2} \end{aligned} \tag{C.13}$$

Finally one has to perform the integration over momenta p_x to get the only relevant differential for the 2-body process,

$$\frac{dR_2}{d\Omega_x} = \frac{1}{4}\int \delta(W - E_p - E_x)\left(\frac{{p_x}^2}{E_xE_p}\right)dp_x \tag{C.14}$$

However, in order to integrate the δ-function out it is necessary to change the integration variable to E_x. This is readily done using $E_x = \sqrt{(\mathbf{p}_x)^2 + M_x^2}$ since it gives,

$$p_x dp_x = E_x dE_x \qquad \Longrightarrow \qquad dE_x = \left(\frac{p_x}{E_x}\right) dp_x \tag{C.15}$$

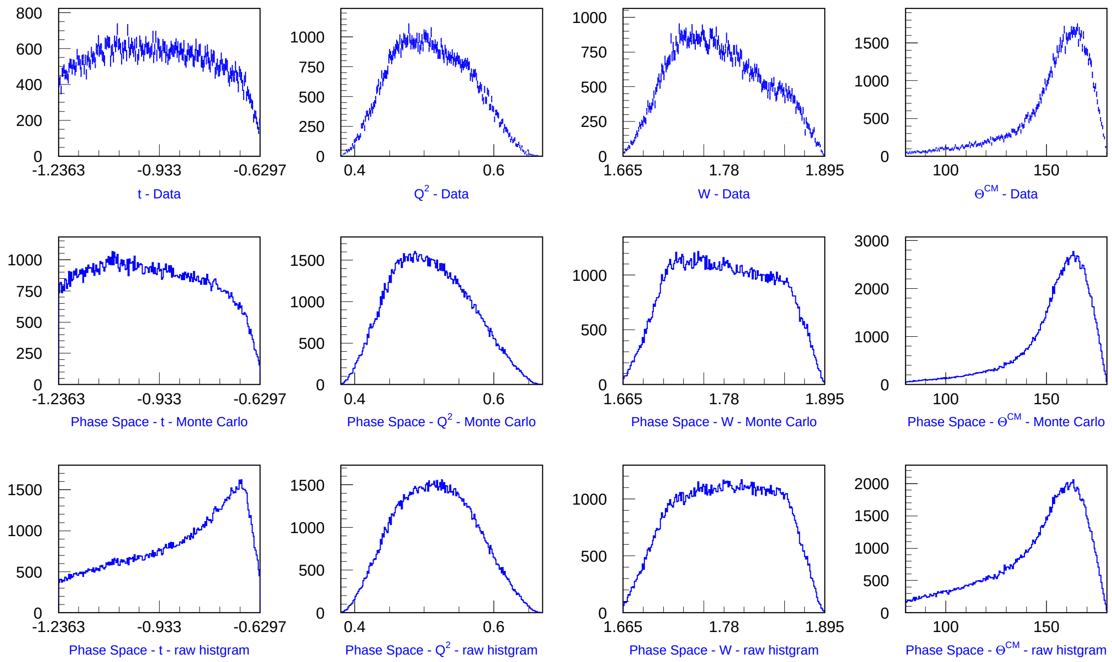

Figure C.1: ***Phase Space Distributions:*** *The first row of plots shows experimental data after random coincidence subtraction. It is desired to model this using the weighted phase space. The plots of the second row were generated using the derived weights (see C.28 and the text that follows it). Finally, the third row plots are the ones with no weighting applied.*

which yields,

$$\frac{dR_2}{d\Omega_x} = \frac{1}{4}\int \delta(W - E_p - E_x)\left(\frac{p_x}{E_p}\right) dE_x \tag{C.16}$$

Now, to perform the integration it is imperative to remember that $E_p = E_p(E_x)$ therefore

$$\delta(W - E_p - E_x) = \delta(f(E_x)) \tag{C.17}$$

so one needs to use C.5 once more. This time around

$$f(E_x) = W - \sqrt{(\mathbf{p}_x)^2 + M_x^2} - E_x \tag{C.18}$$

so that

$$f(E_x) = 0 \qquad \Longrightarrow \qquad E_x^0 = \frac{W^2 + M_x^2 - M_p^2}{2W} \tag{C.19}$$

$$\left|\frac{df}{dE_x}\right|_{E_x = E_x^0} = \frac{E_p + E_x}{E_p} \tag{C.20}$$

This transforms C.16 to

$$\frac{dR_2}{d\Omega_x} = \frac{1}{4}\int \delta\left(E_x - E_x^0\right)\left(\frac{p_x}{E_p + E_x}\right) dE_x \tag{C.21}$$

so after integration one gets. Combining, however, the results of these integrations, eqns C.13 and C.19,

$$\frac{dR_2}{d\Omega_x} = \frac{1}{4}\left(\frac{p_x}{E_p + E_x^0}\right) \tag{C.22}$$

Combining, however, the results of the above integrations, eqns C.13 and C.19, yields

$$E_p + E_x^0 = \sqrt{(E_x^0)^2 - M_x^2 + M_p^2} + E_x^0 = W \tag{C.23}$$

thus arriving at the expression for the two-body hadron phase space,

$$\frac{d^2R_2}{d\Omega_x} = \frac{1}{4}\frac{p_x}{W} \tag{C.24}$$

The above result is valid for two particles with definite masses, which is not the case for the missing particle X. Therefore a modification to the equation C.4 must be made before the energy integrations can be carried out.

Non-definite Mass Particles

In the specific case of 2-body process the phase space factor reads,

$$R_2 = \int d^4p\, d^4p_x\, \delta(p^2 - m^2)\, \delta^{(4)}\,(p + p_x - P) \tag{C.25}$$

In order to be able to integrate over time-like componenets of the 4-vector p_x one needs to use the identity

$$\int \delta(p_x^2 - M_x^2) dM_x^2 = \mathbf{1} \tag{C.26}$$

Inserting the above into C.25 and performing the appropriate integrations leads to the modified expression C.11 which now reads

$$d^7 R_2 = \delta(W - E_p - E_x)\, \delta^{(3)}(\vec{p} + \vec{p}_x) \left(\frac{d^3 p}{2E_p}\right) \left(\frac{d^3 p_x}{2E_{p_x}}\right) dM_x^2 \tag{C.27}$$

so that all the previous calculation can be repeated and eventually the differential phase space factor is given by

$$\frac{d^2 R_2}{d\Omega_x dM_x} = 2M_x \frac{d^2 R_2}{d\Omega_x dM_x^2} = \frac{1}{2} \frac{M_x}{W} p_x \tag{C.28}$$

This means that if one wants to generate a hadron phase space for the process C.1 using uniform generation in M_x and Ω_x it has to be weighted by the factor on the right-hand side of C.28. Full electroproduction phase space is then, according to equation C.2, a product of the flux of transverse virtual photons Γ_T and $d^2 R_2 / d\Omega_x dM_x$. The application of these weights to raw Monte Carlo, or in other words, to noninvariant phase space histograms is presented in the figure C.1.

APPENDIX D

DETERMINATION OF OFFSETS VIA $^1\mathrm{H(e,e'p)}$ REACTION

Coincidence experiments with two spectrometers do provide the means to control most of the offsets in measured quantities which are inevitable in any experimental setup. Exclusive elastic scattering data $^1H(e,e'p)$ is employed to fix the offsets. This reaction is kinematically overdetermined since all the particles of the final state are detected. This, in turn, imposes strong correlations on the reconstructed quantities. The most obvious consequence of the fact that reaction is elastic is that no particle was additionally created in the final state so that the missing mass is zero (compare with Figure 1.3). Vanishing missing mass, or vanishing missing energy and momentum for that matter, results in the Center-Of-Momentum energy W being equal to the mass of the proton. This fact also is evident from the elastic kinematics calculations. All these and other constraints, described later on in this Appendix, make the corresponding distributions have well defined centroid values. Deviations from these values can be casued by the actual phenomena occuring during the experiment and by the existence of offsets in,

- beam energy (E_0),
- scattered electron energy (E'_0) and its angle ($\theta^0_{e'}$),
- scattered proton momentum (p'_0) and its angle ($\theta^0_{p'}$).

It must be noted that the above are not, in general, the only sources of the visible shifts in the mentioned centroid values. The effects of these other contributions can be taken into account in the final formulation of the fitting problem. To define the problem a short review of the kinematics of $^1\mathrm{H}(\mathrm{e},\mathrm{e}'\mathrm{p})$ process is needed.

Kinematics of $^1\mathrm{H}(\mathrm{e},\mathrm{e}'\mathrm{p})$ Scattering

In the rest frame of the proton target 4-momenta of the particles involved in the scattering are defined as follows (see Figure D.1),

- $p_e = (E_0, \vec{k}_0) \equiv k$ - incoming electron 4-momentum,
- $p_{e'} = (E'_0, \vec{k}'_0) \equiv k'$ - outgoing electron 4-momentum,
- $p_i = (M_p, \vec{0}) \equiv p$ - incoming proton 4-momentum,
- $p_f = (E_{p0}, \vec{p}_0) \equiv p'$ - outgoing proton 4-momentum.

The subscript "0" denotes the nominal, unaffected by the offsets, elastic kinematics. The energy-momentum of the initial virtual photon proton system is given by

$$(k - k' + p)^2 = (q + p)^2 = q^2 + p^2 + 2(q \cdot p) = M_p^2 - Q^2 + 2\,\nu_0\, M_p = W_0^2 \qquad \text{(D.1)}$$

which is equal to the invariant mass of the system, W. The final 4-momentum reads,

$$p'^{\,2} = (k' - k - p)^2 = M_p^2 \qquad \text{(D.2)}$$

which on the other hand yields, by squaring what is in the parenthesis, the expression in terms of E_0, E_0',

$$(k' - k - p)^2 = 2m_e^2 + M_p^2 - 2k' \cdot p - 2k' \cdot k + 2k \cdot p \qquad \text{(D.3)}$$

$$(k' - k - p)^2 = 2m_e^2 + M_p^2 - 2M_p(E_0' - E_0) - 2E_0' E_0 + 2|\vec{k}\,||\vec{k}\,'|\,\cos\theta_{e'} \qquad \text{(D.4)}$$

In the ultra relativistic limit ($E_0, E_0' \gg m_e$) the above formula reduces to

$$(k' - k - p)^2 = M_p^2 - 2M_p(E_0' - E_0) - 4E_0' E_0 \sin^2\left(\frac{\theta_{e'}}{2}\right) = M_p^2 \qquad \text{(D.5)}$$

This means, in the sense of Eqns B.2 and B.6 (on page 189 and the following), that,

$$Q^2 = 2\,(E_0 - E_0')\,M_p \qquad \text{(D.6)}$$

or equivalently using Eqn D.1,

$$\boxed{W_0^2 - M_p^2 = 0} \tag{D.7}$$

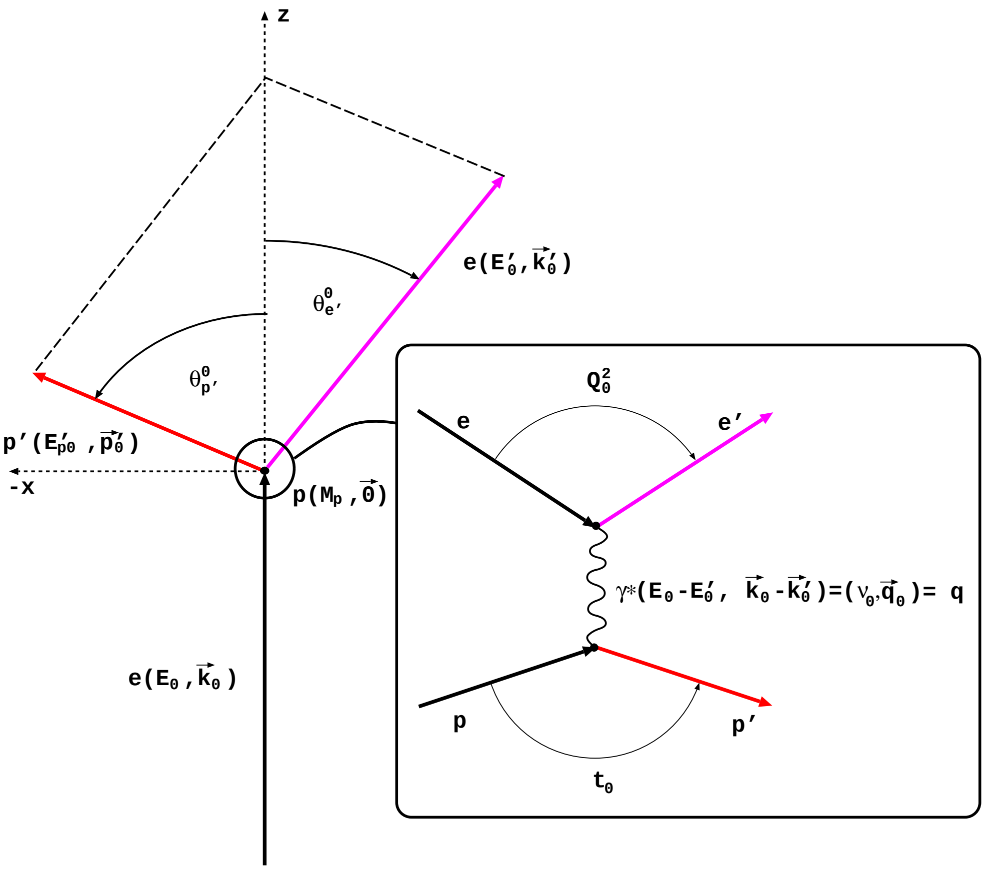

Figure D.1: ***Elastic Kinematics (^{1}H(e, e′p) Scattering):*** *Definitions of the quantities used in the formulation of the problem. x and z axes correspond to the target frame. y axis is perpendicular to the plane of this page.*

Moreover, the knowledge of the beam energy and the angle of the scattered electron completely determines the energy of the scattered electron,

$$E_0' = \frac{E_0}{1 + (2E_0/M_p)\sin^2(\theta_{e'}/2)} \tag{D.8}$$

Energy and momentum conservation provides other constraining relations,

$$P_{\text{initial}} \;=\; k + p \;=\; (E_0 + M_p, \vec{k}_0\,) \tag{D.9}$$

$$P_{\text{final}} \;=\; k' + p' \;=\; (E_0' + E_{p0}, \vec{k}_0' + \vec{p}_0\,) \tag{D.10}$$

$$(E_m, \vec{P}_m\,) \;\stackrel{\text{def}}{=}\; P_{\text{final}}^{\text{detected}} - P_{\text{initial}} \;\stackrel{\text{ep}\to\text{ep}}{=}\; P_{\text{final}} - P_{\text{initial}} \;=\; 0 \tag{D.11}$$

Therefore,

$$\boxed{E_{m0} = E_0 - E_0' - E_{p0} + M_p = 0} \tag{D.12}$$

$$P_m = |\vec{k}_0 - \vec{k}_0' - \vec{p}_0| = 0 \tag{D.13}$$

The magnitude of a vector vanishes only when all three of its components are equal to zero, in a given frame of reference, so that the expression D.13 is equivalent to three linearily independent equations. Decomposition of $\vec{P}_m$ in the target frame (see Figure D.1) yields,

$$\boxed{P_{m0}^{\parallel} = E_0 - \vec{k'}_0^{\parallel} - \vec{p}_0^{\parallel} = 0} \tag{D.14}$$

$$\boxed{P_{m0}^{\perp} = \vec{k'}_0^{\perp} - \vec{p}_0^{\perp} = 0} \tag{D.15}$$

Here the out-of-plane (y) component has been omitted since it is not coupled to any of the used quantities, W, E_m, $P_m^{\parallel}$ and $P_m^{\perp}$, and as such would eventually not contribute to overconstraining the fitting problem. Equations D.7, D.12, D.14 and D.15 are not yet sufficient to formulate a well-defined five parameter fitting procedure.

Mandelstam Variables in 2-body Scattering

The elastic reaction forces also other correlations. To identify them the definition of Mandelstam variables is needed (see Figure D.2). In 2-body scattering one can define three Lorentz invariant quantities (only two of them are independent - see Eqn D.19),

$$s = (p_a + p_b)^2 = (p_1 + p_2)^2 \tag{D.16}$$

$$t = (p_a - p_1)^2 = (p_b - p_2)^2 \tag{D.17}$$

$$u = (p_a - p_2)^2 = (p_b - p_1)^2 \tag{D.18}$$

$$s + t + u = 2M_p^2 + 2m_e^2 \tag{D.19}$$

An immediate consequence of these definitions is that the two 4-momentum transfers t and q^2 are equivalent,

$$t_0 - q_0^2 = t_0 + Q_0^2 = 0 \tag{D.20}$$

by the virtue of D.17. Moreover the invariant u can be calculated using both definitions in D.18. The difference between these two results will provide the final constraint,

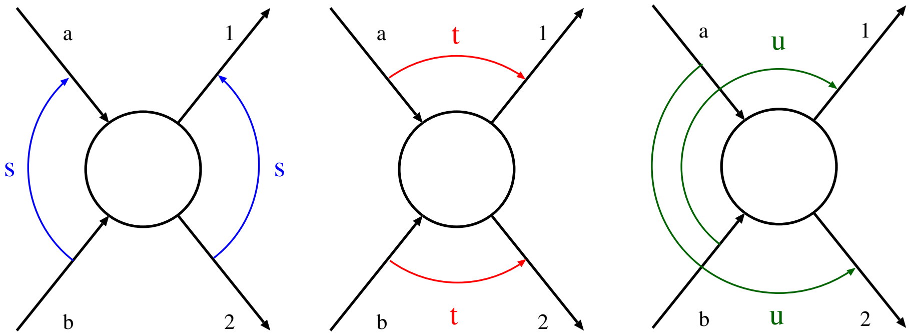

Figure D.2: ***Invariants in 2-body Scattering:*** *Definitions of the Mandelstam variables used in the formulation of the problem.*

$$\begin{aligned} u^0_{\mathrm{pe}'} &= (p-k')^2 = M_p^2 + m_e^2 - 2E_0E^0_{p'} + 2E_0p'_0 cos\theta^0_{p'} \\ u^0_{\mathrm{ep}'} &= (p'-k)^2 = M_p^2 + m_e^2 - 2M_pE'_0 \end{aligned} \tag{D.21}$$

$$\boxed{u^0_{\mathrm{pe}'} - u^0_{\mathrm{ep}'} = 2M_pE'_0 - 2E_0E^0_{p'} + 2E_0p'_0\cos\theta^0_{p'} = 0} \tag{D.22}$$

This set of six equations, D.7, D.12, D.14, D.15, D.20 and D.22, with five unknowns will now be used to determine the influence of the offests on shitfs from nominal values in the reconstructed quantities (see Figure D.3),

$$W^2 = W_0^2 + \Delta W^2 \tag{D.23}$$

$$E_m = E_{m0} + \Delta E_m \tag{D.24}$$

$$P_m^{\parallel} = P_{m0}^{\parallel} + \Delta P_m^{\parallel} \tag{D.25}$$

$$P_m^{\perp} = P_{m0}^{\perp} + \Delta P_m^{\perp} \tag{D.26}$$

$$t + Q^2 = t_0 + Q_0^2 + \Delta\left(t + Q^2\right) \tag{D.27}$$

$$u_{\mathrm{pe'}} - u_{\mathrm{ep'}} = u_{\mathrm{pe'}}^0 - u_{\mathrm{ep'}}^0 + \Delta u \tag{D.28}$$

Offsets

The main idea of the approach presented below is to express W^2, E_m, $P_m^{\parallel}$ and $P_m^{\perp}$, $t+Q^2$ and $u_{\mathrm{pe'}}-u_{\mathrm{ep'}}$ as in equation D.23 through D.28, use the elastic constraints (Eqns D.7, D.12, D.14, D.15, D.20 and D.22) to simplify the relations, linearize the remaining equations and find the offsets by minimizing simultaneously thus resulting deviations. To tackle this task it is important to distinguish the offsets altering the event kinematics from the offsets not capable of doing so. The kinematics of the *ep* scattering is uniquely determined by specifying one quantity in both the initial and the final state. Assuming that the beam energy, E_0, and the scattered electron angle, $\theta_{e'}^0$, are independent, all other quantities can be calculated relative to the kinematics defined by these two quantities. The effect of a beam energy offset from its nominal value is somewhat unique because the beam energy is not measured in the experiment. However any beam energy offset will produce deviations of reconstructed quantities from the elastic constraints. These deviations will be in addition to those resulting in offsets of measured quantities. The following notation convention will be used,

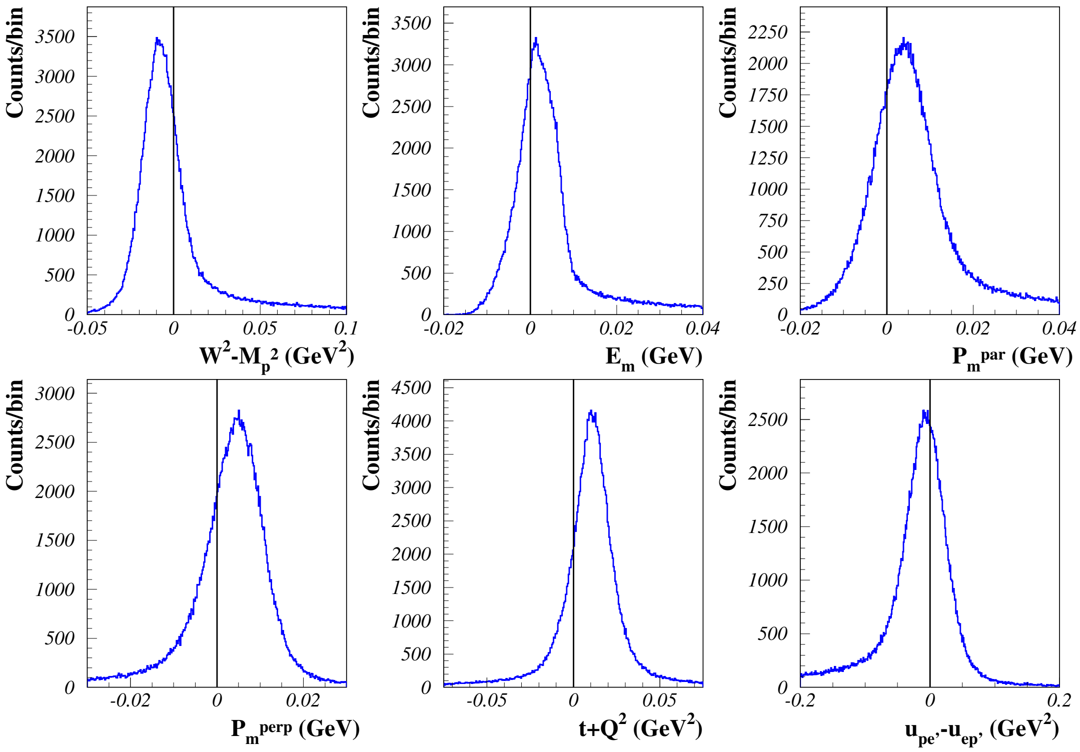

Figure D.3: $^1\mathbf{H}(\mathbf{e}, \mathbf{e}'\mathbf{p})$ ***Data Distributions:*** *Distribution of quantities used in the offset fit. The centroids are clearly shifted from the nominal values represented by the vertical lines.*

nominal (initial) kinematics: E_0 - beam energy, E'_0 - scattered electron energy, $\theta^0_{e'}$ - scattered electron angle, p'_0 - scattered proton momentum and $\theta^0_{p'}$ - scattered proton angle,

true vertex kinematics: E_{vert} - incoming electron energy, E'_{vert} - outgoing electron energy, $\theta^{\text{vert}}_{e'}$ - outgoing electron angle, p'_{vert} - outgoing proton energy and $\theta^{\text{vert}}_{p'}$ - outgoing proton angle,

quantities seen by the spectrometers: E'_{spec} - scattered electron energy, $\theta^{\text{spec}}_{e'}$ - scattered electron angle, p'_{spec} - scattered proton momentum and $\theta^{\text{spec}}_{p'}$ - scattered proton angle,

offsets & shifts: the offsets will be denoted by δ's while the actual changes (shifts) will be denoted by Δ's.

All the offsets are assumed to be negative therefore lowering the actual values. The influence of these offsets on the controid values of the data distributions will be calculated below. The obtained deviation matrix will then be used to develop the `MINUIT` fitting routine.

Invariant Mass Squared- W^2

The calculation for the invariant mass squared, W^2, will be presented in greater detail. The remaining part, because of its length, will be reduced to presenting only neccesary steps of the calculation. How the existence of the offsets can affect the invariant mass squared will be shown separately for each contributing offset and then the final result will be the superpostion of these results.

1. First, assuming that there is only one offset coming into play, the beam energy offset, $\delta E \neq 0$, its effect on the kinematics at the interaction vertex is the following. At the vertex the energy of the incoming electron is smaller by δE so consequently the energy of the outgoing electron will be lowered by $\Delta E'$ (compare Eqn D.8) but measured precisely,

$$E_{\text{vert}} = E_0 - \delta E \tag{D.29}$$

$$E'_{\text{spec}} = E'_{\text{vert}} = E'_0 - \Delta E' \tag{D.30}$$

Using the above the invariant mass squared, W^2, is calculated the way it is being done in the data analysis code,

$$\begin{aligned} W^2 &= M_p^2 + 2M_p(E_0 - E'_{\text{spec}}) - 4E_0E'_{\text{spec}}\sin^2\left(\frac{\theta_{e'}^0}{2}\right) \\ W^2 &= M_p^2 + 2M_p(E_0 - E'_0) - 4E_0E'_0\sin^2\left(\frac{\theta_{e'}^0}{2}\right) \\ &+2M_p\Delta E' + 4E_0\Delta E'\sin^2\left(\frac{\theta_{e'}^0}{2}\right) \end{aligned} \tag{D.31}$$

which, with the aid of the elastic constraint D.7 and D.23, is transformed to,

$$\Delta W^2 = 2M_p\Delta E' + 4E_0\Delta E'\sin^2\left(\frac{\theta_{e'}^0}{2}\right) \tag{D.32}$$

Since only small deviations are expected $\Delta E'$ is expressed as an expansion into Taylor series in the beam energy E around the nominal value E_0 with only the linear term retained,

$$\Delta W^2 = \left(2M_p + 4E_0\sin^2\left(\frac{\theta_{e'}^0}{2}\right)\right)\frac{dE'}{dE}\delta E \tag{D.33}$$

The relation D.33 demonstrates that nonzero beam energy offset implicitly causes a shift in the $W^2 - M_p^2$ centroid (see Eqn D.23).

2. In a similar fashion, if one assumes that the only non-zero offset is the offset in the scattered electron momentum, $\delta E' \neq 0$, then the vertex kinematics corresponds exactly to the nominal one $E_{\text{vert}} = E_0$, $E'_{\text{vert}} = E'_0$ but,

$$E'_{\text{spec}} = E'_0 - \delta E' \tag{D.34}$$

This time, however, the offset $\delta E'$ explicitly enters the calculation because it only alters the measurement but not the kinematics,

$$\begin{aligned} W^2 &= M_p^2 + 2M_p(E_0 - E'_{\text{spec}}) - 4E_0 E'_{\text{spec}} \sin^2\left(\tfrac{\theta^0_{e'}}{2}\right) \\ W^2 &= M_p^2 + 2M_p(E_0 - E'_0) - 4E_0 E'_0 \sin^2\left(\tfrac{\theta^0_{e'}}{2}\right) \\ &\quad +2M_p\delta E' + 4E_0\delta E' \sin^2\left(\tfrac{\theta^0_{e'}}{2}\right) \end{aligned} \tag{D.35}$$

$$\Delta W^2 = 2M_p\delta E' + 4E_0\delta E' \sin^2\left(\frac{\theta^0_{e'}}{2}\right) \tag{D.36}$$

Combination of the above cases gives,

$$E_{\text{vert}} = E_0 - \delta E \tag{D.37}$$

$$E'_{\text{vert}} = E'_0 - \Delta E' \tag{D.38}$$

$$E'_{\text{spec}} = E'_{\text{vert}} - \delta E' \tag{D.39}$$

This gives,

$$\begin{aligned} W^2 &= M_p^2 + 2M_p(E_0 - E'_{\text{spec}}) - 4E_0 E'_{\text{spec}} \sin^2\left(\tfrac{\theta^0_{e'}}{2}\right) \\ W^2 &= M_p^2 + 2M_p(E_0 - E'_0 + \Delta E' + \delta E') \\ &\quad -4E_0(E'_0 - \Delta E' - \delta E') \sin^2\left(\tfrac{\theta^0_{e'}}{2}\right) \end{aligned} \tag{D.40}$$

what amounts to a simple superposition of the first two results,

$$\Delta W^2 = \left(2M_p + 4E_0 \sin^2\left(\frac{\theta^0_{e'}}{2}\right)\right) \frac{dE'}{dE}\delta E + \left(2M_p + 4E_0 \sin^2\left(\frac{\theta^0_{e'}}{2}\right)\right) \delta E' \tag{D.41}$$

3. The remaining offset in the electron scattering angle $\delta\theta_{e'}$ can be treated separately and then added to give the full deviation. Assuming that only $\delta\theta_{e'} \neq 0$, one immediately knows that $E_{\text{vert}} = E_0$, $E'_{\text{vert}} = E'_0$ and $\theta^{\text{vert}}_{e'} = \theta^0_{e'}$. Moreover,

$$\theta^{\text{spec}}_{e'} = \theta^0_{e'} - \delta\theta_{e'} \tag{D.42}$$

If W^2 is recast in the form,

$$W^2 = M_p^2 + 2M_p(E_0 - E'_0) - 2E_0E'_0(1 - \cos\theta^{\text{spec}}_{e'}) \tag{D.43}$$

then the Taylor expansion around the nominal point can be used again. Retaining only linear term simply gives,

$$\cos\theta^{\text{spec}}_{e'} = \cos\theta^0_{e'} + \sin\theta^0_{e'}\delta\theta_{e'} \tag{D.44}$$

this yields the $\delta\theta_{e'}$ contribution to the $W^2 - M_p^2$ centroid shift,

$$\Delta W^2 = 2E_0E'_0 \sin\theta^0_{e'}\delta\theta_{e'} \tag{D.45}$$

Eventually, the total difference of the $W^2 - M_p^2$ from the expected value is given by,

$$\begin{aligned}\Delta W^2 &= \left(2M_p + 4E_0 \sin^2\left(\frac{\theta_{e'}^0}{2}\right)\right)\frac{dE'}{dE}\delta E \\ &+ \left(2M_p + 4E_0 \sin^2\left(\frac{\theta_{e'}^0}{2}\right)\right)\delta E' \\ &+\ 2E_0 E_0' \sin\theta_{e'}^0 \delta\theta_{e'}\end{aligned} \tag{D.46}$$

Missing Energy - E_m

Introducing all the offsets at the same time for the missing energy forces the change in the vertex kinematics and the electron and proton spectrometer momentum mismeasurements at the same time therefore,

$$E_{\text{vert}} = E_0 - \delta E \tag{D.47}$$

$$E'_{\text{vert}} = E'_0 - \Delta E' \tag{D.48}$$

$$p'_{\text{vert}} = p'_0 - \Delta p' \tag{D.49}$$

$$E'_{\text{spec}} = E'_{\text{vert}} - \delta E' \tag{D.50}$$

$$p'_{\text{spec}} = p'_{\text{vert}} - \delta p' \tag{D.51}$$

The missing energy, E_m, can be expressed as,

$$\begin{aligned}E_m &= E_0 - E'_{\text{spec}} - E_{p'}^{\text{spec}} + M_p \\ E_m &= E_0 - (E'_0 - \Delta E' - \delta E') - (E_{p'}^0 - \Delta E_{p'} - \delta E_{p'}) + M_p \\ E_m &= E_{m0} + \left(\frac{dE'}{dE} + \frac{dE_{p'}}{dE}\right)\delta E + \delta E' + \delta E_{p'}\end{aligned} \tag{D.52}$$

This with the aid of Eqn D.24 yields,

$$\Delta E_m = \left(\frac{dE'}{dE} + \frac{dE_{p'}}{dE} \right) \delta E - \delta E' - \delta E_{p'} \tag{D.53}$$

which is yet another straightforward example of the implicit effect of the beam energy offset on the centroid values of the relevant reconstructed quantities.

Missing Momentum (Parallel to $\vec{k}$) - $P_m^{\parallel}$

The parallel component of the missing momentum (in the target frame) involves all five offsets since,

$$P_m^{\parallel} = E_0 - E'_{\text{spec}} \cos \theta_{e'}^{\text{spec}} - p'_{\text{spec}} \cos \theta_{p'}^{\text{spec}} \tag{D.54}$$

Therefore this time the kinematics will be altered and not only momenta of the outgoing particles will be mismeasured but also their angles. Putting down all the shifts and offsets explicitly one arrives at,

$$E_{\text{vert}} = E_0 - \delta E \tag{D.55}$$

$$E'_{\text{vert}} = E'_0 - \Delta E' \tag{D.56}$$

$$p'_{\text{vert}} = p'_0 - \Delta p' \tag{D.57}$$

$$E'_{\text{spec}} = E'_{\text{vert}} - \delta E' \tag{D.58}$$

$$p'_{\text{spec}} = p'_{\text{vert}} - \delta p' \tag{D.59}$$

$$\theta_{e'}^{\text{spec}} = \theta_{e'}^{0} - \delta\theta_{e'} \tag{D.60}$$

$$\theta_{p'}^{\text{vert}} = \theta_{p'}^{0} - \Delta\theta_{p'} \tag{D.61}$$

$$\theta_{p'}^{\text{spec}} = \theta_{p'}^{\text{vert}} - \delta\theta_{p'} \tag{D.62}$$

Using, in addition to D.44, the following Taylor expansion,

$$\cos(\theta_{p'}^{0} - \Delta\theta_{p'} - \delta\theta_{p'}) = \cos\theta_{p'}^{0} + \sin\theta_{p'}^{0}\delta\theta_{p'} + \sin\theta_{p'}^{0}\Delta\theta_{p'} \tag{D.63}$$

yields,

$$\begin{aligned} P_m^{\|} &= E_0 - (E'_0 - \Delta E' - \delta E')\cos(\theta_{e'}^{0} - \delta\theta_{e'}) \\ &\quad -(p'_0 - \Delta p' - \delta p')\cos(\theta_{p'}^{0} - \Delta\theta_{p'} - \delta\theta_{p'}) \end{aligned} \tag{D.64}$$

$$\begin{aligned} P_m^{\|} &= P_{m0}^{\|} - E'_0\sin\theta_{e'}^{0}\delta\theta_{e'} - p'_0\sin\theta_{p'}^{0}\Delta\theta_{p'} - p'_0\sin\theta_{p'}^{0}\delta\theta_{p'} \\ &\quad +(\Delta E' + \delta E')(\cos\theta_{e'}^{0} + \sin\theta_{e'}^{0}\delta\theta_{e'}) + (\Delta p' + \delta p')(\cos\theta_{p'}^{0} + \sin\theta_{p'}^{0}\delta\theta_{p'}) \end{aligned} \tag{D.65}$$

$$\begin{aligned} P_m^{\|} &= P_{m0}^{\|} - E'_0\sin\theta_{e'}^{0}\delta\theta_{e'} - p'_0\sin\theta_{p'}^{0}\delta\theta_{p'} + \cos\theta_{e'}^{0}\delta E' + \cos\theta_{p'}^{0}\delta p' \\ &\quad + \left(\tfrac{dE'}{dE}\cos\theta_{e'}^{0} + \tfrac{dp'}{dE}\cos\theta_{p'}^{0} - \tfrac{d\theta_{p'}}{dE}\sin\theta_{p'}^{0}\right)\delta E \end{aligned} \tag{D.66}$$

In turn $\Delta P_m^{\|}$ reads,

$$\begin{aligned}\Delta P_m^{\parallel} &= -E_0' \sin\theta_{e'}^0 \delta\theta_{e'} - p_0' \sin\theta_{p'}^0 \delta\theta_{p'} + \cos\theta_{e'}^0 \delta E' + \cos\theta_{p'}^0 \delta p' \\ &+ \left(\tfrac{dE'}{dE}\cos\theta_{e'}^0 + \tfrac{dp'}{dE}\cos\theta_{p'}^0 - \tfrac{d\theta_{p'}}{dE}\sin\theta_{p'}^0\right)\delta E\end{aligned} \tag{D.67}$$

Missing Momentum (Perpendicular to $\vec{k}$) - $P_m^{\perp}$

The perpendicular component of the missing momentum (in the target frame) is expressed via,

$$P_m^{\perp} = E'_{\text{spec}} \sin\theta_{e'}^{\text{spec}} - p'_{\text{spec}} \sin\theta_{p'}^{\text{spec}} \tag{D.68}$$

Trigonometric functions in the above equation can be replaced by the Taylor expansions upto linear terms,

$$\sin(\theta_{e'}^0 - \delta\theta_{e'}) = \sin\theta_{e'}^0 - \cos\theta_{e'}^0 \delta\theta_{e'} \tag{D.69}$$

$$\sin(\theta_{p'}^0 - \Delta\theta_{p'} - \delta\theta_{p'}) = \sin\theta_{p'}^0 - \cos\theta_{p'}^0 \Delta\theta_{p'} - \cos\theta_{p'}^0 \delta\theta_{p'} \tag{D.70}$$

Working out this component in the same manner as before gives,

$$P_m^{\perp} = (E_0' - \Delta E' - \delta E')\sin(\theta_{e'}^0 - \delta\theta_{e'}) - (p_0' - \Delta p' - \delta p')\sin(\theta_{p'}^0 - \Delta\theta_{p'} - \delta\theta_{p'}) \tag{D.71}$$

$$\begin{aligned} P_m^{\perp} &= P_{m0}^{\perp} - E_0' \cos\theta_{e'}^0 \delta\theta_{e'} + p_0' \cos\theta_{p'}^0 \delta\theta_{p'} - \sin\theta_{e'}^0 \delta E' + \sin\theta_{p'}^0 \delta p' \\ &- \left(\tfrac{dE'}{dE} \sin\theta_{e'}^0 - \tfrac{dp'}{dE} \sin\theta_{p'}^0 - \tfrac{d\theta_{p'}}{dE} \cos\theta_{p'}^0 \right) \delta E \end{aligned} \tag{D.72}$$

so that the shift of $P_m^{\perp}$ from the centroid value is explicitly given by,

$$\begin{aligned} \Delta P_m^{\perp} &= -E_0' \cos\theta_{e'}^0 \delta\theta_{e'} + p_0' \cos\theta_{p'}^0 \delta\theta_{p'} - \sin\theta_{e'}^0 \delta E' + \sin\theta_{p'}^0 \delta p' \\ &- \left(\tfrac{dE'}{dE} \sin\theta_{e'}^0 - \tfrac{dp'}{dE} \sin\theta_{p'}^0 - \tfrac{d\theta_{p'}}{dE} \cos\theta_{p'}^0 \right) \delta E \end{aligned} \tag{D.73}$$

Momentum Transfers - $t + Q^2$

Equivalence of the momentum transfers t and q^2 is given by,

$$t + Q^2 = 2M_p^2 - 2M_p E_{p'}^{\mathrm{spec}} + 2E_0 E'_{\mathrm{spec}} (1 - \cos\theta_{e'}^{\mathrm{spec}}) \tag{D.74}$$

The contributing offsets are δE, $\delta E'$, $\delta p'$ and $\delta\theta_{e'}$ therefore (compare D.55 through D.62),

$$\begin{aligned} t + Q^2 &= 2M_p(M_p - (E_{p'}^0 - \Delta E_{p'} - \delta E_{p'})) \\ &+ 2E_0(E_0' - \Delta E' - \delta E')(1 - \cos(\theta_{e'} - \delta\theta_{e'})) \end{aligned} \tag{D.75}$$

with the first two terms in the cosine Taylor expansion retained (see D.44) the above is expressed as,

$$t + Q^2 = t_0 + Q_0^2 + 2M_p(\Delta E_{p'} + \delta E_{p'}) - 2E_0 E_0' \sin\theta_{e'}^0 \delta\theta_{e'} -4E_0(\Delta E' + \delta E')\sin^2\left(\frac{\theta_{e'}^0}{2}\right) \tag{D.76}$$

Thus the shift in the momentum transfers $t + Q^2$ due to the existance of offsets is given by,

$$\Delta(t + Q^2) = 2M_p\delta E_{p'} - 2E_0 E_0' \sin\theta_{e'}^0 \delta\theta_{e'} -4E_0\sin^2\left(\frac{\theta_{e'}^0}{2}\right)\delta E' + \left(2M_p\frac{dE_{p'}}{dE} - 4E_0\frac{dE'}{dE}\sin^2\left(\frac{\theta_{e'}^0}{2}\right)\right)\delta E \tag{D.77}$$

Mandelstam variable - u

Ultimately, the deviation in the Mandelstam variable u is used to overconstrain the problem,

$$u_{\mathrm{pe}'} - u_{\mathrm{ep}'} = 2M_p E'_{\mathrm{spec}} - 2E_0 E_{p'}^{\mathrm{spec}} + 2E_0 p'_{\mathrm{spec}} \cos\theta_{p'}^{\mathrm{spec}} \tag{D.78}$$

Here the offsets affecting the centroids are $\delta E'$, $\delta p'$ and $\delta\theta_{p'}$,

$$u_{\mathrm{pe}'} - u_{\mathrm{ep}'} = 2M_p(E_0' - \Delta E' - \delta E') - 2E_0(E_{p'}^0 - \Delta E_{p'} - \delta E_{p'}) +2E_0(p_0' - \Delta p_0' - \delta p_0')\cos(\theta_{p'}^0 - \Delta\theta_{p'} - \delta\theta_{p'}) \tag{D.79}$$

with the aid of the Taylor expansion similar to D.63 one obtains,

$$
\begin{aligned}
u_{\mathrm{pe'}} - u_{\mathrm{ep'}} &= 2M_p E'_0 - 2E_0 p'_0 + 2E_0 p'_0 \cos\theta^0_{p'} \\
&+2\left(E_0\left(\tfrac{dE_{p'}}{dp'}\,\tfrac{dp'}{dE} - \tfrac{dp'}{dE}\cos\theta^0_{p'} + p'_0\tfrac{d\theta_{p'}}{dE}\sin\theta^0_{p'}\right) - M_p\tfrac{dE'}{dE}\right)\delta E \\
&-2M_p\delta E' + 2E_0\left(\tfrac{dE_{p'}}{dp'} - \cos\theta^0_{p'}\right)\delta p' + 2E_0 p'_0 \sin\theta^0_{p'}\delta\theta_{p'}
\end{aligned}
\tag{D.80}
$$

Therefore the total deviation Δu reads,

$$
\begin{aligned}
\Delta u &= 2\left(E_0\left(\tfrac{dE_{p'}}{dp'}\,\tfrac{dp'}{dE} - \tfrac{dp'}{dE}\cos\theta^0_{p'} + p'_0\tfrac{d\theta_{p'}}{dE}\sin\theta^0_{p'}\right) - M_p\tfrac{dE'}{dE}\right)\delta E \\
&-2M_p\delta E' + 2E_0\left(\tfrac{dE_{p'}}{dp'} - \cos\theta^0_{p'}\right)\delta p' + 2E_0 p'_0 \sin\theta^0_{p'}\delta\theta_{p'}
\end{aligned}
\tag{D.81}
$$

Deviation Matrix

The equations of constraints can be formally expressed through the matrix equation,

$$
\begin{bmatrix} \Delta W^2 \\ \Delta E_m \\ \Delta P^{\parallel}_m \\ \Delta P^{\perp}_m \\ \Delta_{tQ^2} \\ \Delta u \end{bmatrix} = \mathcal{A} \begin{bmatrix} \delta E \\ \delta E' \\ \delta\theta_{e'} \\ \delta p' \\ \delta\theta_{p'} \end{bmatrix}
\tag{D.82}
$$

with the deviation matrix given by,

$$\mathcal{A} = \begin{bmatrix} (2M_p + 4E_0 s_{e2})\frac{dE'}{dE} & (2M_p + 4E_0 s_{e2}) & 0 & 2E_0 E_0' s_e & 0 \\ \left(\frac{dE'}{dE} + \frac{dE_{p'}}{dE}\right) & 1 & \frac{dE_{p'}}{dp'} & 0 & 0 \\ \left(\frac{dE'}{dE} c_e + \frac{dp'}{dE} c_p - \frac{d\theta_{p'}}{dE} s_p\right) & c_e & c_p & -E_0' s_e & -p_0' s_p \\ -\left(\frac{dE'}{dE} s_e - \frac{dp'}{dE} s_p - \frac{d\theta_{p'}}{dE} c_p\right) & -s_e & s_p & -E_0' c_e & p_0' c_p \\ \left(2M_p \frac{dE_{p'}}{dE} - 4E_0 \frac{dE'}{dE} s_{e2}\right) & -4E_0 s_{e2} & 2M_p \frac{dE_{p'}}{dp'} & -2E_0 E_0' s_e & 0 \\ 2E_0\left(\frac{dE_{p'}}{dE} - \frac{dp'}{dE} c_p + p_0' \frac{d\theta_{p'}}{dE} s_p\right) - 2M_p \frac{dE'}{dE} & -2M_p & 2E_0\left(\frac{dE_{p'}}{dp'} - c_p\right) & 0 & 2E_0 p_0' s_p \end{bmatrix}$$

where $s_{e2} \equiv \sin^2(\theta^0_{e'}/2)$, $s_e \equiv \sin\theta^0_{e'}$, $c_e \equiv \cos\theta^0_{e'}$, $s_p \equiv \sin\theta^0_{p'}$ and $c_p \equiv \cos\theta^0_{p'}$.

Worth noting is the fact that the inclusion of the beam energy offset is implicit (through the changes it forces on the elastic kinematics at the interaction vertex) and results in nontrivial expressions.

All the derivatives are calculated at the nominal kinematics using D.8 and,

$$p' = \left(E_0^2 + E'^2 - 2E_0 E' \cos\theta_{e'}\right)^{1/2} \tag{D.83}$$

$$\theta_{p'} = \arccos\left(\frac{E_0^2 + p'^2 - E'^2}{E_0 p'}\right) \tag{D.84}$$

and they are given by,

$$\left(\frac{dE'}{dE}\right)_{E=E_0} = \left(1 + \frac{2E_0}{M_p}\sin^2\left(\frac{\theta^0_{e'}}{2}\right)\right)^{-1} \tag{D.85}$$

$$\left(\frac{dp'}{dE}\right)_{E=E_0} = \frac{(E_0 - E'_0\cos\theta^0_{e'}) + (E'_0 - E_0\cos\theta^0_{e'})\left(\frac{dE'}{dE}\right)_{E=E_0}}{p'_0} \tag{D.86}$$

$$\left(\frac{dE_{p'}}{dp'}\right)_{E=E_0} = \frac{p'_0}{E^0_{p'}} \tag{D.87}$$

$$\left(\frac{d\theta_{p'}}{dE}\right)_{E=E_0} = \frac{p'_0\cos\theta^0_{p'} \; - \; E_0 \; + \; E'_0\left(\frac{dE'}{dE}\right)_{E=E_0} + \quad (E_0\cos\theta^0_{p'} - p'_0)\left(\frac{dp'}{dE}\right)_{E=E_0}}{E_0 p'_0 \sin\theta^0_{p'}} \tag{D.88}$$

Results

Using `MINUIT` the search for the best combination of offsets was performed by minimizing the χ^2-like function,

$$\chi^2 = \sum_{i=1}^{6} \frac{(\delta f_i^{\text{data}} - \delta f_i^{\text{fit}})^2}{(\sigma_i^{\text{data}})^2} \tag{D.89}$$

where $\vec{f} = (\,W^2 - M_p^2\,,\, E_m\,,\, P_m^{\parallel}\,,\, P_m^{\perp}\,,\, t + Q^2\,,\, u_{\text{pe}'} - u_{\text{ep}'}\,)$, δf_i^{data} are the observed deviations from the elastic constraints and δf_i^{fit} are the expected deviations from the elastic constraints and should come from a reliable Monte Carlo simulation to account for any non-offset related deviations from the calculated values (e.g. energy losses, radiative effects, beam angle at the target, *etc*...). The results of application of this method are shown on Figure D.4.

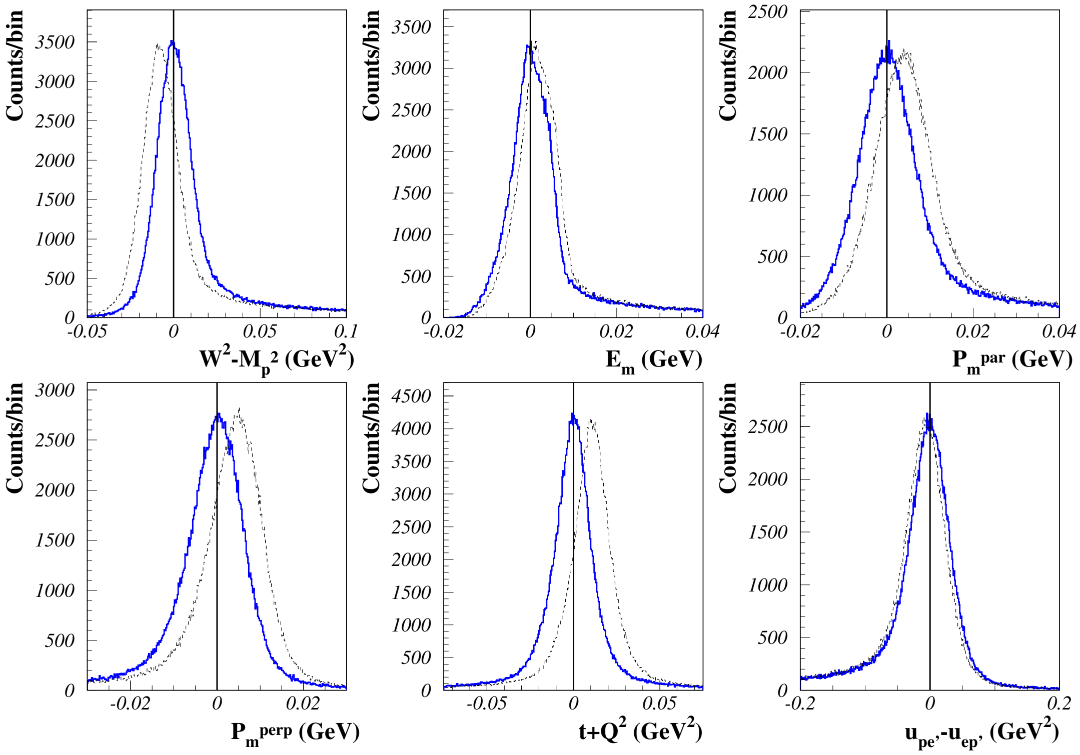

Figure D.4: $^{1}\mathbf{H}(\mathbf{e},\mathbf{e'p})$ ***Data Distributions:*** *The offsets found by optimization of the deviation matrix (refer to Page 226) were applied in generating the data distributions. The resulting centroid values coincide with the prediction (vertical lines) for the nominal elastic kinematics (compare with D.7, D.12, D.14, D.15, D.20 and D.22). The original raw data distributions are shown here in dashed line.*